Electrochemical Nanotechnology

In-situ Local Probe Techniques at Electrochemical Interfaces

Edited by
W. J. Lorenz and W. Plieth

A Publication Initiated by
IUPAC

WILEY-VCH

Keep up to date with WILEY-VCH's books and series ...

E. Budevski, G. Staikov, W. J. Lorenz
Electrochemical Phase Formation and Growth
1996. Hardcover. ISBN 3-527-29422-8

Advances in Electrochemical Science and Engineering

Edited by R. C. Alkire, H. Gerischer†, D. M. Kolb, C. W. Tobias†
ISSN 0938-5193

Volume 1 with contributions from Brusic, J. Horkans, D. J. Barclay, D.-T. Chin, G. P. Evans, T. Iwasita-Vielstich, R. Kötz, J. Winnick
1990. Hardcover. **Sold**

Volume 2 with contributions from C. Deslouis, B. Tribollet, A. Hammou, G. L. Richmond, S. Trasatti
1992. Hardcover. ISBN 3-527-28273-4

Volume 3 with contributions from W. P. Gomes, H. H. Goossens, Y. Okinaka, T. Osaka, J. O. Dukovic, H. Lehmkuhl, K. Mehler, U. Landau, P. C. Andricacos, L. T. Romankiw
1994. Hardcover. ISBN 3-527-29002-8

Volume 4 with contributions from P. Allongue, P. C. Searson, T. Iwasita, F. C. Nart, Z. Galus, Z. Samec, K. Kakiuchi, P. Tatapudi, J. M. Fenton
1995. Hardcover. ISBN 3-527-29205-5

Volume 5 with contributions from A. Kapturkiewicz, O. A. Petrii and G. A. Tsirlina, D. D. Macdonald and L. B. Kriksunov, S. Gottesfeld, and F. Beck
1997. Hardcover. ISBN 3-527-29385-X

Electrochemical Nanotechnology

In-situ Local Probe Techniques at Electrochemical Interfaces

Edited by
W. J. Lorenz and W. Plieth

A Publication Initiated by IUPAC

WILEY-VCH

Weinheim · New York · Chichester · Brisbane · Singapore · Toronto

Editors:
Prof. Dr. Wolfgang J. Lorenz
Institut für Physikalische Chemie
und Elektrochemie
Universität Karlsruhe
Kaiserstraße 12
D-76131 Karlsruhe

Prof. Dr. Waldfried Plieth
Institut für Physikalische Chemie
und Elektrochemie
Universität Dresden
Mommsenstraße 13
D-01062 Dresden

Cover illustration: Pb-Nanoclusters on n-type Si (111); Size: 50 x 50 x 2 nanometers.

Library of Congress Card No.: applied for.

British Library Cataloguing-in-Publication Data:
A catalogue record for this book is available from the British Library.

Die Deutsche Bibliothek – CIP Einheitsaufnahme
Electrochemical nanotechnology : in situ local probe techniques at electrochemical interfaces / prepared for publ. by W. J. Lorenz and W. Plieth. - Weinheim ; New York ; Chichester ; Brisbane ; Singapore ; Toronto : Wiley-VCH, 1998
(IUPAC monography)
ISBN 3-527-29520-8

Printing: Strauss Offsetdruck GmbH, D-69509 Mörlenbach
Bookbinding: Wilhelm Osswald & Co., D-67433 Neustadt/Weinstraße

Printed in the Federal Republic of Germany

Preface

The development of local probe techniques such as Scanning Tunneling Microscopy (STM) or Atomic Force Microscopy (AFM) and related methods during the past fifteen years (Nobel price for physics 1986 to H. Rohrer and G. Binning) has opened a new window to locally study of interface phenomena on solid state surfaces (metals, semiconductors, superconductors, polymers, ionic conductors, insulators etc.) at an atomic level. The in-situ application of local probe methods in different systems (UHV, gas, or electrochemical conditions) belongs to modern nanotechnology and has two different aspects.

First, local probe methods are applied to characterize thermodynamic, structural, and dynamic properties of solid state surfaces and interfaces and to investigate local surface reactions. These investigations represent the analytical aspect of nanotechnology.

Second, tip and cantilever can be used for preparative aspects to form defined nanoobjects such as molecular or atomic clusters, quantum dots, etc., as well as to structure or modify solid state surfaces in the nanometer range. Such studies belong to the preparative aspect of nanotechnology, which is still in the beginning.

In-situ local probe investigations at solid/liquid interfaces can be performed under electrochemical conditions if both phases are electronic and ionic conducting. In this case, electrochemistry offers a great advantage in comparison to local probe studies under UHV or gas environmental conditions since the Fermi levels of both substrate and tip (or metallized cantilever) can be adjusted precisely and independently of each other. This Fermi level control to defined surface properties at tip and substrate and, therefore, to defined tunneling conditions in STM studies.

Electrochemical phase formation, phase transition and dissolution processes play an important role in the preparative aspect of electrochemical nanotechnology. Under electrochemical conditions, super- or undersaturation can be exactly controlled and rapidly changed via the electrode potential, providing a further great advantage of the application of local probe techniques under electrochemical conditions.

The current state of knowledge on the application of in-situ local probe techniques to study electrochemical interfaces is comprehensively treated in this IUPAC-monograph by contributions of international well-recommended experts working in different fields: development of new in-situ methods, theoretical considerations, structural

characterization of solid state surfaces, interfacial nucleation and growth processes, surface structuring and modification, properties of oxide layers, corrosion phenomena, etc..

The aim of this monograph is to direct the attentions of scientists, industry, economy and politics to modern nanotechnology which certainly will have a strong impact in many fields such as surface chemistry and physics, materials science, electronics, sensor technology, biology, medicine, etc.. IUPAC is interested that R & D nanoprojects should be supported financially by national and international foundations as already done in USA, Japan and Switzerland.

The contents of the separate contributions were put into eight subtitles, General aspects, Roughness and Mesoscopic Structure, Interface Structure, Surface Modification, Nucleation and Growths, Oxide layers and Corrosion, Semiconductors, STM and Complementary Methods. This structure symbolizes the broad application of the new technology.

One important aspect of this collection of different researchers in the field of nanotechnology is the question for the future developments. In this context one author writes "the technology has concentrated so far on the long lasting questions of electrochemistry". This can be emphasized with the statement that many of the results were already assumed on the basis of classical integral measurements. However, many STM or AFM results are completely unexpected and surprizing. Discrepancies between classical integral and local information have to be cleared up by independent measurements. In this context many authors mention that the new technique must be considered as only one method of the entire ensemble of in-situ and ex-situ surface methods. This is an important statement, since different surface spectroscopic methods such as in-situ X-ray, Raman, NMR, etc. may act as such independent methods.

Another aspect mentioned is the question of the relevance of a nanoscale information applied to an electrode behaviour in the micrometer or even meter range. It was emphasized again that the comparison of results of local probe techniques with integral techniques is one way to avoid this problem.

Several times spectacular results were reported of nanostructuring of solid surfaces. However, one author writes "the technique is still in a prelimanary stage". Therefore, the preparative aspect of electrochemical nanotechnology might be the dominant one even in the first years of the 21st century.

IUPAC is a body to look for wide spread international implications of scientific developments. It has selected the topic of local probe techniques of nanoscale dimensions as one of the outstanding technological developments of the last decade. The broad impact of the new technology on surface chemistry, surface physics, materials science, nano-electronics, sensorics, medicine etc. is generally accepted. The present collection of contributions with different individual statements should be a guide for future decisions and developments in the field.

The editors greatfully acknowledge the cooperation of Mrs. S. Hehme and Mr. Gunther Sandmann in the preparation of this volume.

The editors

Contents

Preface V

Part I General Aspects

Local Probing of Electrochemical Processes at Non-ideal Electrodes 1
E. Ammann, P. I. Oden, H. Siegenthaler

Electrochemistry and Nanotechnology 13
G. Staikov, W. J. Lorenz

Imaging of Electrochemical Processes and Biological Macromolecular Adsorbates by in-situ Scanning Tunneling Microscopy 27
J. E. T. Andersen, J. Ulstrup, P. Møller

Beyond the Landscapes: Imaging the Invisible 45
A. A. Kornyshev, M. Sumetskii

Part II Roughness and Interface Structure

Roughness Kinetics and Mechanism Derived from the Analysis of AFM and STM Imaging Data 57
R. C. Salvarezza, A. J. Arvia

Electrodes with a Defined Mesoscopic Structure 73
U. Stimming, R. Vogel

In-situ Stress Measurements at the Solid/Liquid Interface Using a Micromechanical Sensor 87
T. A. Brunt, E. D. Chabala, T. Rayment, S. J. O'Shea, M. E. Welland

Surface Structure and Electrochemistry: New Insight by Scanning Tunneling Microscopy 101
G. Aloisi, L. M. Cavallini, R. Guidelli

Part III **Surface Modification**

STM and AFM Studies of the Electrified Solid-Liquid Interface: Monolayers, Multilayers, and Organic Transformations 113
A. A. Gewirth, B. K. Niece

Scanning Probe Microscopy Studies of Molecular Redox Films 125
J. E. Hudson, H. D. Abruña

New Aspects of Iodine-modified Single-crystal Electrodes 137
K. Itaya

The Growth and the Surface Properties of Polypyrrole on Single Crystal Graphite Electrodes as Studied by in-situ Electrochemical Scanning Probe Microscopy 149
Chr. Froeck, A. Bartl, L. Dunsch

Part IV **Nucleation and Electrodeposition**

Nucleation and Growth at Metal Electrode Surfaces 159
O. M. Magnussen, F. Möller, M. R. Vogt, R. J. Behm

STM Studies of Electrodeposition of Strained-Layer Metallic Superlattices 171
T. P. Moffat

Part V **Oxide Layers and Corrosion**

STM Studies of Thin Anodic Oxide Layer 185
P. Marcus, V. Maurice

Local Probing of Electrochemical Interfaces in Corrosion Research 199
A. Schreyer, T. Suter, L. Eng, H. Böhni

Morphology and Nucleation of Ni-TiO_2 LIGA Layers 215
M. Strobel, U. Schmidt, K. Bade, J. Halbritter

SPM Investigations on Oxide-covered Titanium Surfaces: Problems and Possibilities 225
C. Kobusch, J. W. Schultze

Part VI Semiconductors

Electrochemical Surface Processing of Semiconductors at the Atomic Level 241
P. Allongue, C. H. de Villeneuve

In-situ Electrochemical AFM Study of Semiconductor Electrodes in Electrolyte Solutions 253
K. Uosaki, M. Koinuma

Part VII STM and Complementary Methods

In-situ STM and Electrochemical UHV Technique: Complementary, Noncompeting Techniques 267
M. P. Soriaga, K. Itaya, J. L. Stickney

Growth Morphology and Molecular Orientation of Additives in Electrocrystallization Studied by Surface-enhanced Raman Spectroscopy 277
B. Reents, W. Plieth

Instrumental Design and Prospects for NMR-Electrochemistry 291
J. B. Day, J. Wu, E. Oldfield, A. Wieckowski

List of Contributors 303

List of Abbreviations 309

Symbol List 311

Subject Index 315

Part I

Electrochemical Nanotechnology
In-situ Local Probe Techniques at Electrochemical Interfaces
Edited by W. J. Lorenz and W. Plieth

Local Probing of Electrochemical Processes at Non-ideal Electrodes

E. Ammann, P.I. Oden, H. Siegenthaler

Contents

1 Introduction 1
2 STM Investigation of Pb and TI Underpotential Deposition at Non-ideal Ag(111) Electrodes 3
2.1 Experimental Techniques and Surface Morphology of the Non-ideal Ag(111) Electrodes 3
2.2 Local Progress of Pb and TI Adsorbate Formation 4
2.2.1 Fast adsorption and desorption of Pb 4
2.2.2 Fast adsorption and desorption of TI 7
2.3 Adsorbate-Substrate Rearrangement Phenomena 8
3 Conclusions and Outlook 10
4 References 11

Summary. The potential of in-situ scanning probe techniques for the local investigation of surface properties and reactions at "nonideal" electrodes is presented in a typical example: in the field of metal underpotential deposition, the essential role of the step dislocations for the local progress of adsorbate formation and also for the longterm adsorbate stability is shown and discussed for the adsorption of Pb and Tl monolayers at stepped Ag(111) electrodes.

1 Introduction

In the past years, the combined characterization of electrodes and electrode reactions by electrochemical methods and by local probing techniques has been advanced

significantly by the progress and experimental refinement achieved in the field of in-situ scanning probe microscopy (SPM) techniques, especially scanning tunneling microscopy (STM) and scanning force microscopy (SFM) [1]. In a variety of systems, these two methods now enable nanometer- and atomic-scale imaging of the surface structure and morphology of electrode surfaces, of monolayer and bulk metal deposits, and of organic adsorbates and conducting polymer electrodes [2].

A specially attractive aspect of the mentioned SPM techniques consists in their capability to image also nonperiodic features at the electrode-electrolyte interface, and to characterize locally selected domains with lateral extensions ranging from the micrometer-scale to nanometer dimensions. This is of particular interest in view of the investigation of "real" electrode systems applied in electrochemical technology (e.g., galvanotechnical applications and battery technology), and encountered in corrosion problems. Such electrodes exhibit usually pronounced structural and morphological heterogeneities (e.g., monoatomic or polyatomic steps, islands and pits, surface defects and dislocations, grain boundaries) and chemical heterogeneities (e.g., foreign adsorbates, heterogeneous alloy electrodes, passive layers), whose electrochemical characterization implies the correlation of the global electrochemical system response with the local monitoring of electrode properties and processes.

In order to investigate the effects of atomic-scale morphology (e.g., density of atomic steps, number and local distribution of atomic-scale islands and pits) upon the local progress of electrochemical reactions, the use of "non-ideal" single-crystal electrodes has proved to be a very interesting tool towards further elucidation of the electrochemical properties of real electrodes. Especially in the field of metal underpotential deposition, our own investigations in the system Tl^{+}/Ag(111) [3] and Pb^{2+}/Ag(111) [4], presented in more detail in this paper, as well as investigations by other groups [5, 6], have revealed the essential role of step dislocations for the local progress of adsorbate formation and also for the long-term adsorbate stability, and are further discussed in a recent publication [7].

In the field of chemically heterogeneous electrodes, the combined electrochemical and local probe investigation of conducting polymers has become an important technique for elucidating possible influences of electrolyte composition and polarization dynamics upon the electropolymerization process, to investigate the film morphology dependence on film oxidation/reduction, and to study possible effects of morphological and electronic film inhomogeneities upon the electrochemical properties of these compounds. Earlier studies by *Bard et al.* [8] and by *Nyffenegger et al.* [9] have demonstrated the application of STM for the study of film growth and morphology, and more recent reports have presented STM- and SFM-based methods for measuring film thickness [10] and monitoring film thickness changes [11]. With regard to SFM imaging of such "soft" samples, it is shown below that significant

progress can be expected in the application of non-contact mode (e.g., tapping mode) techniques involving weaker mechanical interactions with the film than in the conventional contact mode.

In the present contribution, the possibilities of local in-situ STM and SFM probing at non-ideal electrodes are illustrated with recent SPM work performed in the electrochemistry group of the University of Bern: STM studies of underpotential deposition of Pb^{2+} and Tl^{+} at non ideal (chemically polished) Ag(111) electrodes are presented to show the influence of the nanometer-scale morphology of the non-ideal Ag(111) substrate upon the local progress of adsorbate formation and the long-term stability of the resulting adsorbates. More detailed reports of the experiments are given elsewhere [3,4].

2 STM-Investigation of Pb and Tl Underpotential Deposition at non-ideal Ag(111) Electrodes

2.1 Experimental Techniques and Surface Morphology of the Non-ideal Ag(111) Electrodes

A detailed description of the experimental methods and applied measurement techniques is given elsewhere [3, 4]. The reported experiments were performed in 0.01M $HClO_4$ containing 0.005 M Pb^{2+} or Tl^{+}. Commercial Ag(111) electrodes were prepared by mechanical polishing (diamond polish of decreasing grain size), followed by chemical chromate polishing. The electrode was transferred under electrolyte cover first into a conventional electrochemical cell for test voltammetric measurements, then transferred into the electrolytic STM cell. The STM measurements were performed in a commercial Nanoscope II instrument equipped with a homebuilt electrolytic cell [3]. Electrochemically etched Pt/Ir tunneling tips insulated laterally with Apiezon wax were used for the STM experiments.

The STM images were recorded at constant tunneling currents applied in the range between 3 and 30 nA. Time-dependent local changes were specially monitored either by calculating the difference between 2 scan windows of the same substrate domain, recorded at different times, or by monitoring a selected part of the surface continuously in a one-dimensional scan and recording the scan dependence on time [4].

Figure 1 shows a typical example of the surface morphology of a chemically polished Ag(111) electrode. The following characteristic morphological features can be observed:

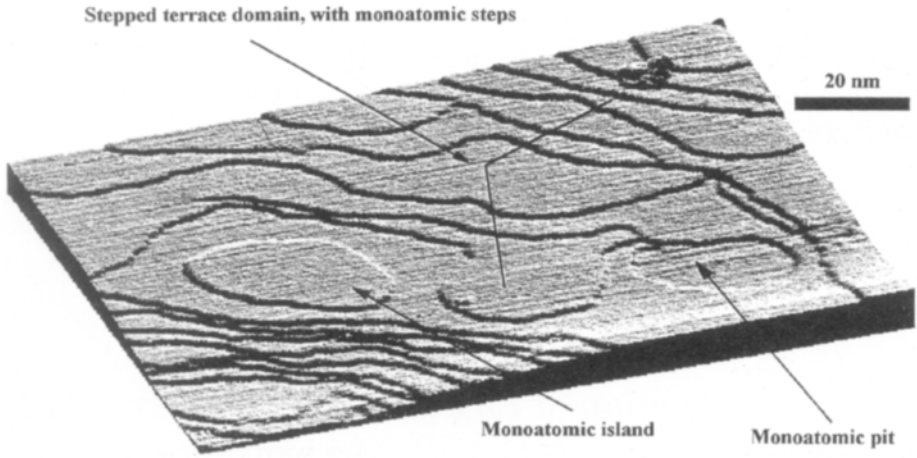

Fig. 1. STM image of a chemically polished Ag(111) electrode in 0.01 M $HClO_4$, showing stepped terrace domains with monoatomic steps, a monoatomic island, and a monoatomic pit [4].

- The largest part of the surface consists of stepped terrace domains composed of "stacks" of monoatomic terraces. The width of the terraces in these stacked parts varies between ca. 2 nm and more than 20 nm. Exceptionally, terrace widths up to 100 nm have been observed.

- Monoatomic islands and monoatomic pits are observed regularly, with typical average
  widths of ca. 25 nm.

2.2 Local Progress of Pb and Tl Adsorbate Formation

2.1.1 Fast adsorption and desorption of Pb

Based on the presented typical substrate morphology shown in Fig. 1, the local progress of Pb adsorption has been systematically studied at the three morphologically different substrate domains, using a special dynamic line-scan technique described

elsewhere [4] and *step polarization* into the various parts of the voltammetric curve investigated.

The results of this STM study, presented in more detail elsewhere [4], are summarized schematically in Fig. 2 in correlation with the typical cyclic voltammogram of Pb underpotential deposition observed at macroscopic, chemically polished Ag(111) electrodes in perchlorate-containing electrolyte [12].

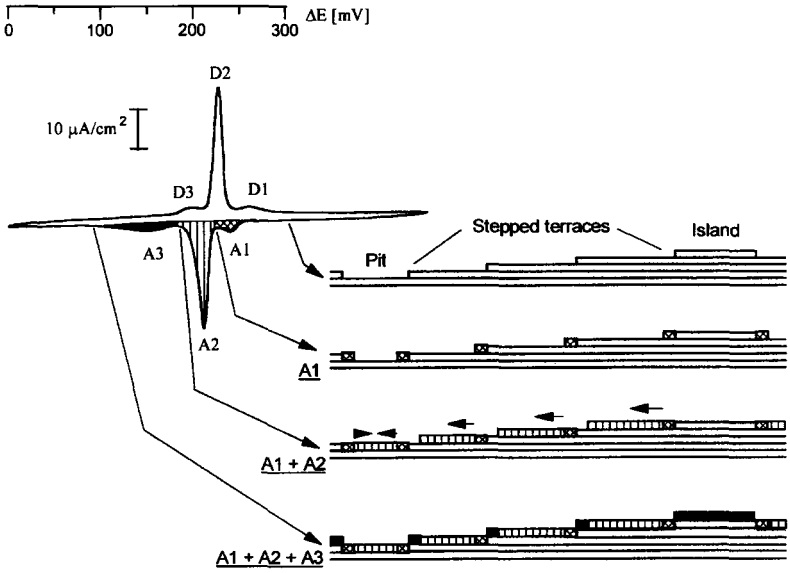

Fig.2. Schematic presentation of the local progress of Pb underpotential deposition at monoatomic pits, monoatomic islands, and stepped terrace domains of non-ideal chemically polished Ag(111) electrodes [4]. For further explanation see the text.

The formation of a Pb monolayer occurs in three distinct potential ranges associated with the voltammetric adsorption/desorption peaks A1/D1, A2/D2, and A3/D3. The local progress of adsorbate formation at the morphologically different domains of the non-ideal Ag(111) substrate can be described as follows:

(a) The first adsorption stage, associated with the *voltammetric peak A1,* consists in a decoration of the steps by a spatially delimited adsorbate extending laterally ca. 1-3 nm from the step edge. As indicated in Fig. 2, this phenomenon is observed at all

three morphological domains. Although the lateral extension of this initial coverage is remarkably stable in time scales up to several hours, it has not been possible, up to now, to resolve a stable atomic structure. It can therefore not be excluded that the adsorbate consists of a locally delimited coverage with a temporally unstable (fluctuating) structure.

(b) In the *voltammetric peak A2*, the growth of the adsorbate layer proceeds in the following way:

- At the *stepped terrace domains*, adsorption proceeds from the decorated step edges and leads to the formation of a "partial" adsorbate coverage, which does not completely cover the terraces, but extends only to within 1-3 nm of the peripheral terrace boundaries. The widths of these adsorbate-free peripheral domains at the external terrace boundaries conform strikingly with the widths of the step decoration coverage formed in peak A1. This "partial" adsorbate formed after the adsorption in peak A2 has a hexagonally close-packed structure that can be imaged during a time scale of ca. 100s, before the onset of slow structural transformations (see below).

- In the *monoatomic pits*, the adsorbate coverage grows inwards from the decorated pit boundaries, leading to a hexagonally close-packed (hcp) monolayer that covers the pit completely.

- On the *monoatomic islands*, no adsorbate layer growth has been observed up to now after step polarization into the potential range of peak A2. However, in one experiment a sequence of local formation and subsequent disappearance of a cluster-like adsorbate domain has been observed within peak A2 on an island.

(c) In the most cathodic *voltammetric peak A3*, the monolayer formation is completed as follows:

- At the *stepped terrace domains*, the adsorbate-free peripheral parts are completely covered, leading to a "complete" hcp adsorbate that is stable over several hours.

- In the *monoatomic pits*, that are already covered in peak A2 by a complete adsorbate coverage, no further reaction occurs.

- On the *monoatomic islands*, step polarization into the range of peak A3 leads to

the (presumably nucleative) formation of a complete adsorbate coverage.

As observed previously in an STM study by *Obretenow et al.* [13], the resulting complete monolayer has a hexagonally close-packed structure with Pb-Pb interatomic distances that are compressed with regard to the values in the Pb bulk phase. In addition, a higher-periodicity Moiré pattern has been observed in this system by Müller et al. [14, 15] that has been interpreted in terms of the electronic or geometric superposition of an incommensurate Pb adlayer with the topmost substrate layer. A systematic study of the dependence of the periodicity of this Moiré superstructure on the undervoltage has revealed an approximately linear decrease of the Pb-Pb nearest-neighbor distance in the hcp adlayer with decreasing undervoltage, in good agreement with the results of an in-situ GIXS study by *Toney et al.* [16].

Desorption of the complete Pb adlayer within the three distinct desorption peaks D3, D2 and D1 (see Fig. 2) by step polarization proceeds in an analogous way to the adsorption sequence, except on the monoatomic islands: in contrast to the complete adsorbate formation at the islands in peak A3, desorption in peak D3 only involves the outermost part of the monolayer at the island periphery, whereas the remaining adsorbate coverage is completely desorbed in peak D2. Desorption on the monoatomic islands occurs thus in the same way as at the stepped terrace domains, except for the missing step decoration coverage desorbed in D1.

2.2.2 Fast adsorption and desorption of Tl

In earlier voltammetric experiments [17] it has been found that Tl underpotential deposition occurs in two distinctly separated potential intervals that have been associated with the successive formation of two monolayers prior to Tl bulk deposition, whereby the voltammogram in the more anodic potential range (assigned to the formation of a first monolayer) exhibits a very similar splitting into three distinct peaks A1/D1, A2/D2, A3/D3 as observed in the system Pb/Ag(111) (see Fig. 2).

In a recent STM study by *Carnal et al.* [3], these assumptions have been confirmed by the observation that a hexagonally close-packed adlayer with slightly compressed Tl-Tl interatomic distances is formed at more anodic potentials, followed by the formation of a second hcp adlayer with slightly disordered domains at small undervoltages. The progress of the formation of the first adsorbate layer was studied in that work by more conventional STM imaging techniques and was restricted to investigations at the stepped terrace domains. As shown in detail in [3], the formation of the first adsorbate layer at the stepped terrace domains follows the same scheme as shown in Fig. 2 for the system Pb/Ag(111), i.e.

- Peak A1: Decoration of the steps at a lateral width of ca. 1-3 nm.
- Peak A2: Formation of an hcp adlayer on the stepped terraces, except for the peripheral terrace boundaries that remain adsorbate-free over a width of ca. 1-3 nm.
- Peak A3: Completion of the adsorbate coverage at the peripheral terrace boundaries.

The progress of adsorbate formation in the monoatomic pits and at monoatomic islands has not been investigated yet. In contrast to the system Pb/Ag(111), a higher-periodicity superstructure imaging the adsorbate-substrate registry has been resolved only faintly [18].

2.3 Adsorbate-Substrate Rearrangement Phenomena

In both systems, it has been shown previously [12, 17] that the voltammetric peaks A2/D2 decrease continuously, if the "incomplete" adsorbate coverage obtained in peaks A1 + A2 (see Fig. 2) is submitted to long-term polarization, either at constant potential between peaks A2 and A3, or by continuous cyclic polarization within the entire potential range of peaks (A1 + A2) / (D1 + D2). In the system $Tl^+/Ag(111)$ thin-layer studies [17] have shown that Tl^+ is desorbed into the electrolyte during this long-term polarization, and the changes in the voltammetric properties observed in both systems after the complete disappearance of peaks A2/D2 have been interpreted tentatively by the formation of structurally different residual Tl or Pb coverages.

These previously anticipated structural changes occurring at incomplete Pb or Tl coverages during long-term polarization have been studied in detail by STM [3], and are summarized in Fig. 3: Fig. 3(a) depicts a surface area from a *stepped terrace domain* (see Fig. 1) in the system $Pb^{2+}/Ag(111)$ after formation of a Pb adsorbate coverage in the peaks A1 + A2, and 600 s polarization at constant potential between peaks A1 and A2. As discussed in Section 2.2 and shown schematically in Fig. 2, the initial Pb coverage obtained at stepped terrace domains after adsorption in the peaks A1 + A2 consists of a "partial" hcp adlayer extending only to within 1-3 nm from the peripheral terrace boundaries, whereas a complete hcp adlayer is formed only in the monoatomic pits, and the monoatomic islands remain 1adsorbate-free. The STM image of Fig. 3(a) depicts the surface in the neighborhood of a monoatomic step crossing the substrate outside the picture window near its lefthand bottom corner. The image shows the boundary between the originally formed hcp adsorbate layer (recognized in Fig. 3(a) also by the higher-periodicity Moiré pattern) and a well-ordered hexagonal structure with Pb-Pb interatomic distances of 0.51 0.01 nm. From the observed interatomic distances and the orientation with regard to the substrate, the transformed coverage is assigned to a rearranged Pb layer with a $[\sqrt{3} \times \sqrt{3}]$ R30° - atomic structure

(schematic picture in Fig. 3(a)) which is assumed to be formed by exchange of every third Ag atom of the substrate by a Pb atom and desorption of the excess Pb into solution, thus resulting in a "surface alloy" involving only the topmost layer of the substrate atoms. Recent studies [4] have given strong evidence that these slow structural rearrangements start at the boundary between the original hcp layer and the adsorbate-free domain at the periphery of the stepped terraces, and propagate on the terraces inwards from the periphery. Desorption of the surface alloy occurs at higher undervoltages than the peak ranges D2 and D1 assigned to the desorption of the initially formed hcp coverage, and leads to the fast recuperation of the initial voltammetric behavior, in contrast to the system Tl/Ag(111), described below.

A very similar transformation of the original hcp adlayer to a surface alloy coverage with the same Tl-Tl interatomic distances and $[\sqrt{3} \times \sqrt{3}]R30°$ symmetry has been observed in the system Tl/Ag(111) during extended polarization of the incompletely formed first Tl adsorbate layer. As in the system Pb/Ag(111), there is strong evidence that the transformations proceed from the boundaries of the peripheral adsorbate-free domains inwards on the terraces. However, in contrast to the system Pb/Ag(111), the transformed coverages include both ordered and disordered domains, and their desorption results in the formation of monoatomic pits in the substrate with widths of ca. 3 to 10 nm [3]. These pits diminish and finally vanish within a few minutes by coalescence and lateral displacement, at a rate that can be increased markedly by positive shift of the substrate potential.

Under the experimental conditions prevailing in both systems in the STM investigations of the slow transformation phenomena, the onset of the "surface alloy" formation has been imaged only in the potential range between peaks A2 and A3 at the boundary between an hcp Pb or Tl coverage and the narrow adsorbate-free substrate domains remaining at the terrace edges after adsorption in peaks A1 + A2, hence relating the slow transformation with the presence of steps. Although the line scan imaging results discussed in Section 2.2 indicate that the adsorbate formation in peak A2 proceeds from the decorated step edges, the lack of atomic resolution within the peak interval A2 has prevented, up to now, direct STM-based evidence being obtained for surface alloy formation at small and intermediate coverages in peak A2, or even at decorated steps within peak A1. Whether, and how, surface alloy formation also takes place at low and intermediate coverages far from the step edges therefore remains a subject for further studies.

Kinetic studies of the slow structural rearrangements have been performed by *Vitanov and co-workers* [19] in the system Pb^{2+}/Ag(111), ClO_4^-, using real and quasiperfect Ag(111) substrates with varying step densities, and investigating the rate of transformation at both low adsorbate coverages (i.e., between adsorption peaks A1

and A2) and high coverages (i.e., between adsorption peaks A2 and A3). As discussed in more detail in [7], at low coverages, the authors observed relatively high

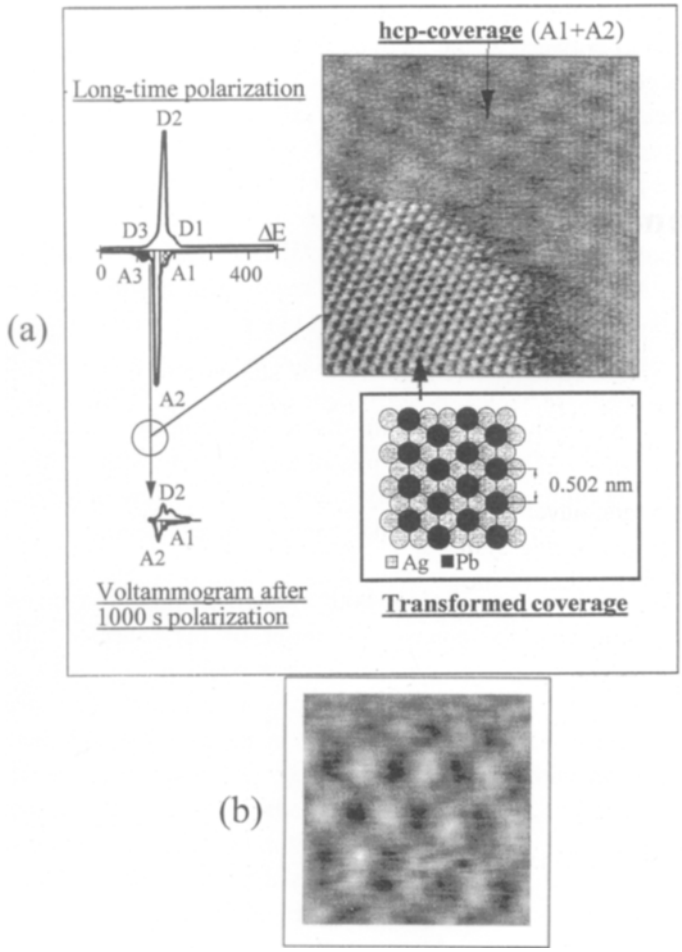

Figure 3. Slow adsorbate-substrate rearrangement phenomena after adsorption of incomplete monolayer (peaks A1 + A2) and subsequent extended polarization at constant potential between peaks A2 and A3. STM-images recorded in 0.01 M $HClO_4$ + 0.005M Pb^{2+} or Tl^{+}.(a) STM image recorded in the system Pb^{2+}/Ag(111) after 600 s extended polarization. Window size 12 nm; grayscale range 0.07 nm. The voltammograms represent the voltammetric behavior before and after 600 s polarization. (b) STM image of the transformed coverage in the system Tl^{+}/Ag(111) after 3000 s extended polarization. Window size 1.93 nm; gray scale range 0.07 nm.

transformation rates that were independent of the step densities, whereas a strong dependence of the rates of the step densities was found at high coverages, corresponding to the conditions of the STM studies described above. The measurements were related to kinetic site exchange models including surface inhomogeneities at low adsorbate coverages, and choosing a one-dimensional diffusion model without consideration of surface inhomogeneities for high coverages. However, there remain uncertainties about the dependencies of the transformation rates on the surface inhomogeneities that require further elucidation [7].

3 Conclusions and Outlook

The presented results demonstrate the relevance of the nanometer-scale morphology (stepped terrace domains, monoatomic islands and monoatomic pits) for the local progress of adsorbate formation and adsorbate stability. The stepwise formation of the Pb and Tl adsorbate coverages, combined with the slow formation of a surface alloy coverage, illustrates experimentally thermodynamic and kinetic aspects of various growth modes of metal deposits discussed recently [7, 20]. In the two systems presented, the complete hcp monolayer coverages formed during fast adsorption of Pb and Tl represent obviously *metastable systems*, whereas the surface alloy coverage formed during extended polari-zation of incomplete adsorbate layers is considered to be the thermodynamically stable coverage. The experiments described indicate that in-situ STM is specially suitable for local measurements. Further insight into the role of atomic-scale inhomogeneities in the local progress of electrochemical processes can be expected, e.g., from the use of nanostructured model electrodes.

Acknowledgements. The authors acknowledge gratefully the financial support by the Schweiz. Nationalfonds, and they thank F. Niederhauser for technical support.

4 References

[1] A.A. Gewirth, H. Siegenthaler (Eds.), Nanoscale Probes of the Solid/Liquid Interface, NATO Series E, Applied Sciences, Vol. 288, Kluwer Academic Publishers, Dordrecht, 1995.

[2] Scanning Tunneling Microscopy II, R. Wiesendanger, H.-J. Güntherodt (Eds.), Springer Series on Surface Sciences, Vol. 28, Springer-Verlag, Berlin, 1995.

[3] D. Carnal, P.I. Oden, U. Müller, E. Schmidt, H. Siegenthaler, Electrochim. Acta 40, 1223 (1995).
[4] E. Ammann, Diploma Thesis, University of Bern, 1995; E. Ammann H. Siegenthaler, submitted to J. Electrochem. Soc.
[5] U. Schmidt, S. Vinzelberg, G. Staikov, Surf. Sci. 348, 261 (1996).
[6] J.X. Wang, R.R. Adzic, O.M. Magnussen, B.M. Ocko, Surf. Sci. 344, 11 (1995).
[7] E. Budevski, G. Staikov, W.J. Lorenz, Electrochemical Phase Formation and Growth - An Introduction to the Initial Stages of Metal Deposition. VCH, Weinheim, 1996.
[8] Y.T. Kim, H. Yang, A.J. Bard, J. Electrochem. Soc. 138, L71 (1991).
[9] R. Nyffenegger, C. Gerber, H. Siegenthaler, Synth. Metals 55-57, 402 (1993).
[10] H.Yang, F.-R.Fan, Sh.-L.Yau, A.J.Bard, J. Electrochem. Soc. 139, 2182 (1992).
[11] R. Nyffenegger, E. Ammann, H. Siegenthaler, R. Kötz, O. Haas, Electrochim. Acta 40, 1411 (1995).
[12] H. Siegenthaler, K. Jüttner, Electrochim. Acta 24, 109 (1979).
[13] W. Obretenow, M. Höpfner, W.J. Lorenz, E. Budevski, G. Staikov, H. Siegenthaler, Surf. Sci. 271, 191 (1992).
[14] U. Müller, D. Carnal, H. Siegenthaler, E. Schmidt, W.J. Lorenz, W. Obretenow, U. U.Schmidt, G. Staikov, E.Budevski, Phys. Rev. B 46, 12899 (1992).
[15] U. Müller, D. Carnal, H. Siegenthaler, E. Schmidt, W.J. Lorenz, W. Obretenow, U. Schmidt, G. Staikov, E. Budevski, Phys. Rev. B 49, 7795 (1994).
[16] M.F. Toney, J.G. Gordon, G.L. Borges, O.W. Melroy, D. Yee, L.B. Sorensen, Phys. Rev.B 45, 9362 (1992).
[17] H. Siegenthaler, K.. Jüttner, E. Schmidt, W.J. Lorenz, Electrochim. Acta 23, 1009 (1978).
[18] P.I. Oden, unpublished results.
[19] A. Popov, N. Dimitrov, D. Kashchiev, T. Vitanov, E. Budevski, Electrochim. Acta 38, 2173 (1992), and references by the same authors cited therein.
[20] W.J. Lorenz, G. Staikov, submitted.

Electrochemical Nanotechnology
In-situ Local Probe Techniques at Electrochemical Interfaces
Edited by W. J. Lorenz and W. Plieth

Electrochemistry and Nanotechnology

G. Staikov, W. J. Lorenz

Contents

1	Introduction		13
2	Analytical Nanoelectrochemistry		15
	2.1	Substrate Surfaces	15
	2.2	Growth Modes of 2D and 3D Metal-Phase Formation Processes	17
3	Preparative Nanotechnology		22
4	Conclusions		24
5	References		24

Summary. Electrochemical nanotechnology and its analytical and preparative aspects using local probe techniques such as STM and AFM are described. Typical examples for in-situ application of local probe methods in different electrochemical systems are discussed: UPD and OPD of metals and nanostructuring of metal, semiconductor, and superconductor surfaces.

1 Introduction

Future aspects of science and technology in many fields such as physics, chemistry, materials science, electronics, sensor technology, biology, medicine, etc., are characterized by miniaturization down to an atomic level. "Nanotechnology" dealing with single atoms, molecules or small clusters will take the place of the "micrometer technology" predominating during the last 150 years. In surface nanotechnology, the surfaces of solid-state materials such as metals, semiconductors, superconductors, and insulators have to be analyzed, structured, and modified in the nanometer range. This is only possible using local probe techniques such as STM, AFM and related methods which were developed during the last decade and are generally denoted as scanning probe microscopy (SPM) [1 - 9].

Analytical and preparative aspects of modern nanotechnology can be distinguished. Local probe investigations of surface thermodynamics, structure, dynamics, and reactions belong to the analytical aspect. On the other hand, surface nanostructuring or surface modification and the preparation of defined "nanoobjects" by local probe techniques represent the preparative aspect.

Local probe techniques are carried out "ex-situ", "non-situ" or "in-situ" with respect to applied environmental conditions. Ex-situ local probe investigations are performed under UHV conditions on well-defined substrates, e.g., single-crystal surfaces. Such ex-situ measurements are often made in far from real conditions, which are characterized by adsorption and film formation. Therefore, ex-situ UHV techniques are usually combined with appropriate transfer devices to switch substrates from the real environment to UHV and vice versa. Non-situ local probe measurements are also started under UHV conditions to characterize the bare substrate surface, but they are continued under a finite vapor pressure in order to form adsorbates or mono- or multi-atomic (-molecular) films modeling real environmental conditions. In-situ local probe measurements are carried out at solid/liquid or solid/gas interfaces under defined real conditions involving adsorption and film formation.

In-situ local probe investigations at solid/liquid interfaces can be performed by electro-chemical means if both phases are electronically and ionically conducting. In this case, electrochemistry offers a great advantage since the Fermi levels [10], E_F, of both substrate and tip (or metallized cantilever) can be adjusted precisely and independently of each other using bipotentiostatic control in a four-probe technique (substrate as working electrode; tip or conducting cantilever as local probe „sonde"; reference and counter electrodes) [8]. In STM studies, this Fermi level control leads to defined surface properties at tip and substrate and, therefore, to defined tunneling conditions for distance tunneling spectroscopy (DTS) and voltage tunneling spectroscopy (VTS). Without bipotentiostatic conditions, only the potential difference between tip and substrate, i.e., the tunneling voltage $E_t = E_{tip} - E$, can be held constant without control of the surface properties and, therefore, of the tunneling conditions.

A further advantage of electrochemical in-situ SPM studies of two- and three-dimensional phase formation processes is the possibility of controlling accurately the supersaturation or undersaturation, $\Delta\mu$, which can be correlated, in the absence of other kinetic hindrances with overpotential and underpotential, respectively [11]:

$$\Delta\mu \overset{\text{def}}{=} \mu_{i,\,\text{ads}}(E) - \mu_{i,\,\text{ads}}(E_{\text{Me/Me}^{z+}}) = -zF(E - E_{\text{Me/Me}^{z+}}) \qquad (1)$$

where $\mu_{i,ads}(E)$ and $\mu_{i,ads}(E_{Me/Me}{}^{z+})$ denote the chemical potentials of the adsorbed electroactive species i at the actual electrode potential E and at the Nernst equilibrium potential E_{rev}, respectively. The potential difference $E - E_{Me/Me}{}^{z+}$ is defined as:

$$E - E_{Me/Me}{}^{z+} \overset{\text{def}}{=} \begin{cases} \Delta E \text{ (underpotential)} & > 0 \quad \text{for } E > E_{Me/Me}{}^{z+} \\ \eta \text{ (overpotential)} & < 0 \quad \text{for } E < E_{Me/Me}{}^{z+} \end{cases} \qquad (2)$$

Consequently, under- or supersaturation can be adjusted precisely and varied rapidly under electrochemical conditions, in contrast to gas-phase investigations.

The combination of in-situ local probe techniques and classical steady-state and non-steady-state electrochemical measurements gives new information on the local and global behavior of electrified solid/liquid interfaces with respect to analytical and preparative nanotechnological aspects.

The electrochemistry group at the University of Karlsruhe, Germany, introduced in-situ local probe techniques in order to get more information about substrate surfaces and Faradaic reactions occurring at substrate/liquid electrolyte interfaces under different conditions. Single-crystal faces of metals and semiconductors as well as eptiaxially grown thin films of superconductors are used as substrates. Underpotential deposition (UPD) and overpotential deposition (OPD) of metals were used as Faradaic model reactions for 2D and 3D phase formation processes, respectively. First attempts are being made to use these processes and application of in-situ STM and AFM for a local structuring of solid-state surfaces. Current results will be briefly summarized in terms of analytical and preparative aspects.

2 Analytical Nanoelectrochemistry

2.1 Substrate Surfaces

The surface structure of single-crystal faces of noble metals such as Ag(*hkl*) and Au(*hkl*) were found to be unreconstructed under defined electrochemical conditions. For example, a unreconstructed Ag(111) surface domain on a terrace in contact with perchloric acid solution is shown in Fig. 1. Surface reconstruction changing the inter-atomic distance and symmetry of surface atoms can be induced thermally or by potential, as observed by other authors [12]. This phenomenon can be lifted by potential or by adsorption processes. Surface defects such as monatomic steps and

screw dislocations can be directly observed by in-situ SPM, as demonstrated in Fig. 2 [13].

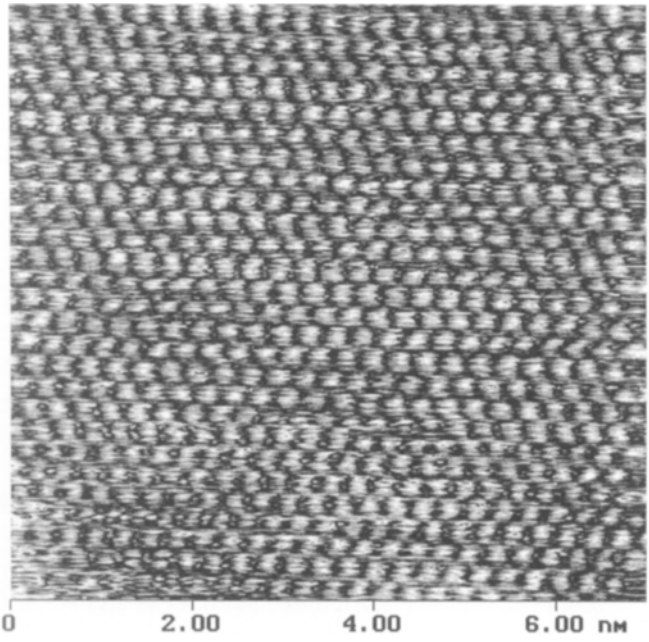

Fig. 1. In-situ STM image of an Ag(111) surface under electrochemical conditions. System: Ag(111)/10^{-2} M $HClO_4$ at E_{H/H^+} = 350 mV and T = 298 K with I_t = 10 nA and Pt-Ir tip.

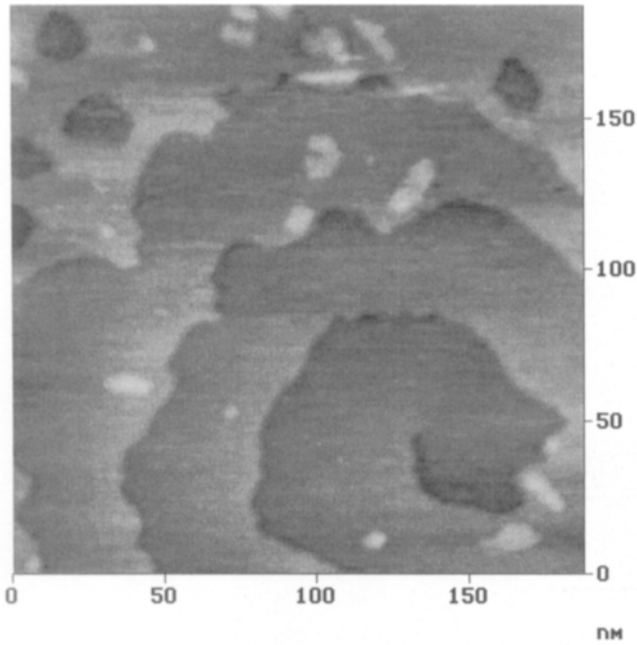

Fig. 2. In-situ STM image of an Au(111) surface under electrochemical conditions. System: Au(111)/5 x 10^{-3} M $AgClO_4$ + 5 x 10^{-1} M $HClO_4$ at ΔE = 200 mV and T = 298 K. I_t = 10 nA, Pt-Ir tip.

2.2 Growth Modes of 2D and 3D Metal Phase Formation Processes

Three different growth modes (Volmer-Weber, Frank-van der Merwe, and Stranski-Krastanov) can be distinguished, depending on the vertical binding energy between a metal adatom, Me_{ads}, on a foreign substrate, S, and on the crystallographic Me-S misfit, as schematically illustrated in Fig. 3.

In the case of weak vertical Me-S interaction, only 3D Me cluster formation takes place in the OPD range according to the Volmer-Weber growth mode (Fig. 3(a)), as found experimentally in the system highly oriented pyrolytic graphite HOPG(0001)/Ag^+) [14].

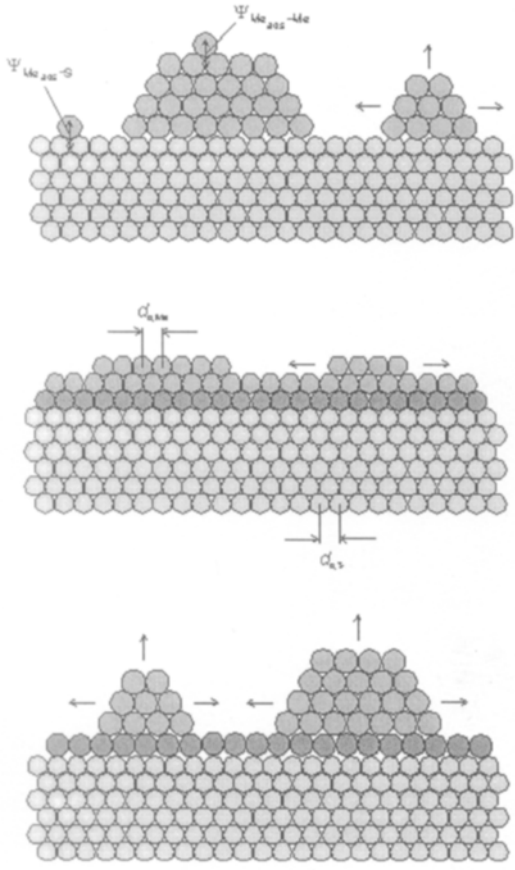

Fig. 3. Schematic representation of different growth modes in metal (Me) deposition on foreign substrate (S) depending on the binding energy ($\leftrightarrow$) of Me_{ads} on S, $\Psi_{Me_{ads}-S}$, compared with that that of Me_{ads} on native substrate Me, $\Psi_{Me_{ads}-Me}$, and on the crystallographic misfit characterized by the interatomic distances $d_{o,Me}$ and $d_{o,S}$ of 3D Me and S bulk phases, respectively. (a) "Volmer-Weber" growth mode (3D Me island formation) for $\Psi_{Me_{ads}-S} << \Psi_{Me_{ads}-Me}$ independent of the ratio $(d_{o,Me} - d_{o,S})/d_{o,S}$. (b) "Franck-van der Merwe" growth mode (Me layer-by-layer formation) for $\Psi_{Me_{ads}-S} >> \Psi_{Me_{ads}-Me}$ and ratio $(d_{o,Me} - d_{o,S})/d_{o,S} \approx 0$. (c) "Stranski-Krastanov" growth mode (3D Me island formation on top of predeposited 2D Me_{ads} overlayers on S for $\Psi_{Me_{ads}-S} >> \Psi_{Me_{ads}-Me}$ and $(d_{o,Me} - d_{o,S})/d_{o,S} > 0$ (positive misfit) or $(d_{o,Me} - d_{o,S})/d_{o,S} < 0$ (negative misfit).

Strong vertical Me-S interaction (Figs. 3(b) and 3(c)) leads to the formation of two-dimensional Me phases in the UPD range prior to the formation of 3D Me phase in the OPD range. The systems Au(*hkl*)/Ag^+ [11,13,15,16], Au(*hkl*)/Pb^{2+} [11,16,17], and Ag(*hkl*)/Pb^{2+} [11,17,18] are typical examples of strong Me-S interaction. No Me-S misfit exists in the first system, whereas the second and third systems are characterized by a significant positive Me-S misfit .

2D Me_{ads} UPD overlayers were found to be formed stepwise [11]. At high ΔE, decoration of monatomic steps takes place. Expanded Me_{ads} overlayers with commensurate structures coexisting with bare substrate domains are observed at high and medium ΔE, as shown in Fig. 4 [11,17]. At relatively low ΔE, 2D phase transitions take place and expanded Me_{ads} overlayers are found to be transformed into condensed 2D Me overlayers, which are higher-order commensurate or incommensurate depending on the crystallographic Me-S misfit. Figure 5 shows a compressed and internally strained incommensurate hcp 2D Pb overlayer structure on Au(111) giving rise to a moiré pattern of the surface structure [11, 16]. A 2D phase transition process at relatively low ΔE in the system Au(100)/Pb^{2+} is illustrated in Fig. 6 [11, 17].

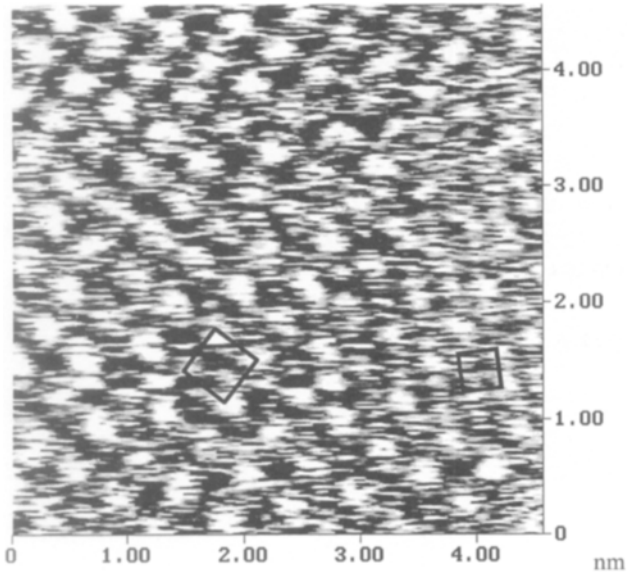

Fig. 4. In-situ STM image of an Ag(100) -c(2 x 2) Pb domain together with bare substrate in the system Ag(100)/5 x 10^{-3} M $Pb(ClO_4)_2$ + 10^{-2} M $HClO_4$ at T = 298 K. ΔE = 175 mV, I_t = 5 nA, Pt-Ir tip.

2D Me overlayers formed at low ΔE are observed to act as precursors for subsequent 3D Me phase formation in the OPD range [11,13,15-18].

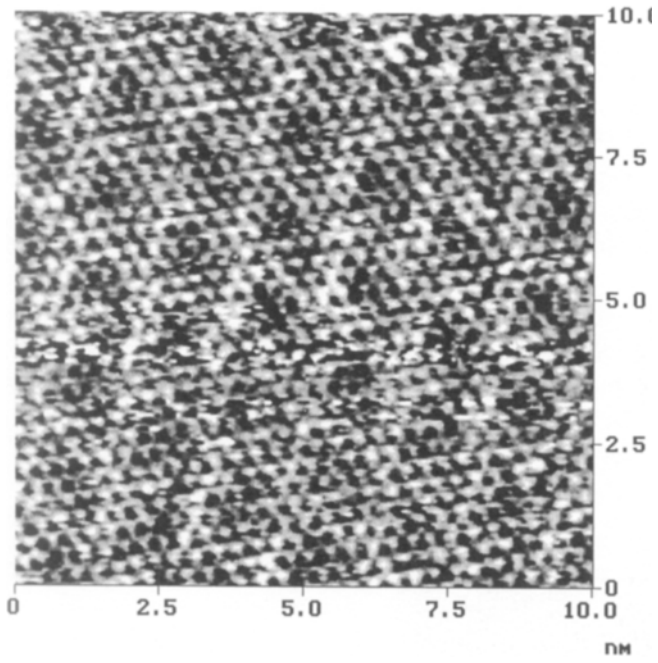

Fig. 5. In-situ STM image of a compressed 2D hcp Pb_{ads} overlayer showing a higher-order superstructure with moiré pattern in the system Au(111)/5 x 10^{-3} M $Pb(ClO_4)_2$ + 10^{-2} M $HClO_4$ at $\Delta E = 0$ mV and $T = 298$ K, $I_t = 40$ nA, Pt-Ir tip.

Tabel 1. Epitaxy of 2D and 3D Me Phases

System	2D Me_{ads} overlayer	3D Me phase
Au(*hkl*)/Ag^+	Au(100)-(1x1)Ag	Au(100) [110] || Ag(100) [110]
	Au(111)-(1x1)Ag	Au(111) [110] || Ag(111) [110]
Ag(*hkl*)/Pb^{2+}	Ag(100) [110] || 2D hcp Pb [110]	Ag(100) [110] || Pb(111) [110]
	Ag(111) [110] || 2D hcp Pb [110] R 4.5°	Ag(111) [110] || Pb(111) [110]R 4.5°

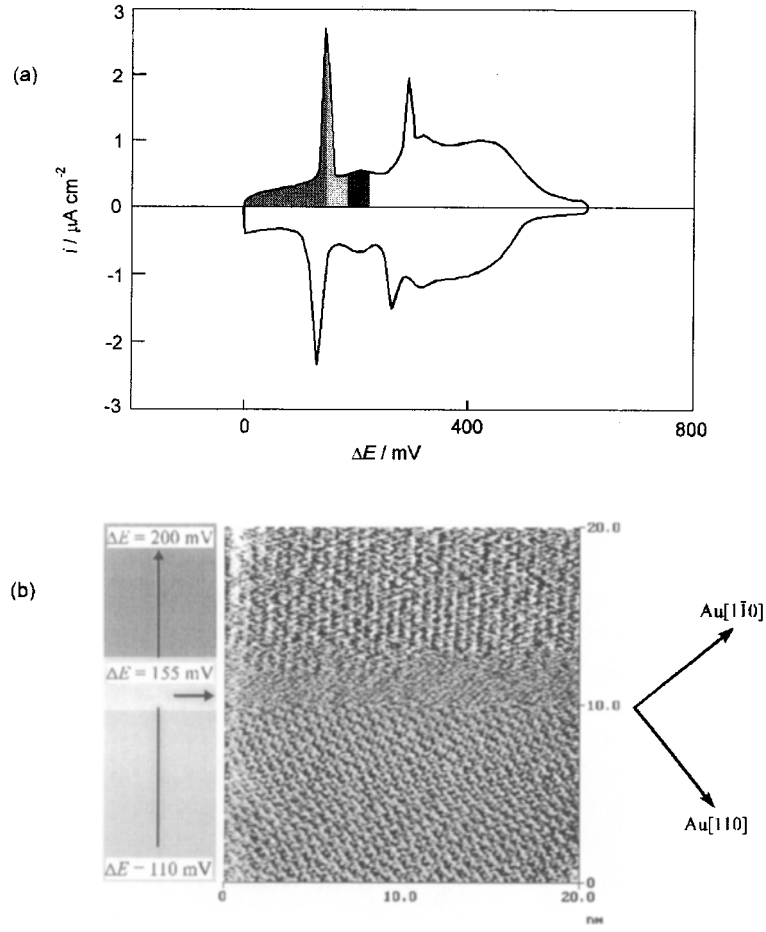

Fig. 6. In-situ STM image of a first-order phase transformation of a condensed 2D Pb overlayer into an expanded one on Au(100) during anodic polarization in the system Au(100)5x10^{-3} M Pb^{2+} + 0.01 M $HClO_4$ at T = 298 K. (a) cyclic voltammogram $|dE/dt| = 10\ mVs^{-1}$, (b) in-situ STM image, $I_t = 40$ nA, Pt-Ir tip, ■ Au(100) - c(3√2 x √2) R 45° Pb, □ bare Au(100) substrate, ■ Au(100) - hcp 2D Pb overlayer.

This means, that the epitaxy of 2D Me overlayer is reflected in the epitaxy of 3D Me crystallites, as summarized in Table 1 [11,18]. The structural and energetic properties of 2D Me overlayers are found to determine the nucleation and growth kinetics of 3D Me phases [11, 15, 18].

3 Preparative Nanoelectrochemistry

Local structuring and modification of solid-state surfaces by electrodeposition of metals are of great practical importance. However, the realization of these processes requires an exact knowledge of UPD and OPD of Me at an atomic level. At present, first attempts have been started to develop appropriate polarization routines for a defined nanostructuring or nanomodification of solid-state surfaces (metals, semiconductors, superconductor films) using in-situ STM and AFM.

For example, 3D Ag crystallites cathodically deposited on HOPG(0001) decorate preferentially monatomic steps and other surface imperfections at relatively low $|\eta|$, as shown in Fig. 7. In the OPD range -35 mV $\leq \eta \leq$ -10 mV, the number of atoms in critical Ag clusters is found to be $N_{crit} = 4$. Ag clusters can be deposited on flat terraces only at much higher $|\eta|$ or by special polarization routines as demonstrated in Fig. 8 [11,14].

Investigations of local Me deposition on Si(100) in the OPD range are more difficult due to the band gap of the semiconductor, which influences the process itself as well as the tunneling conditions for in-situ STM [18].

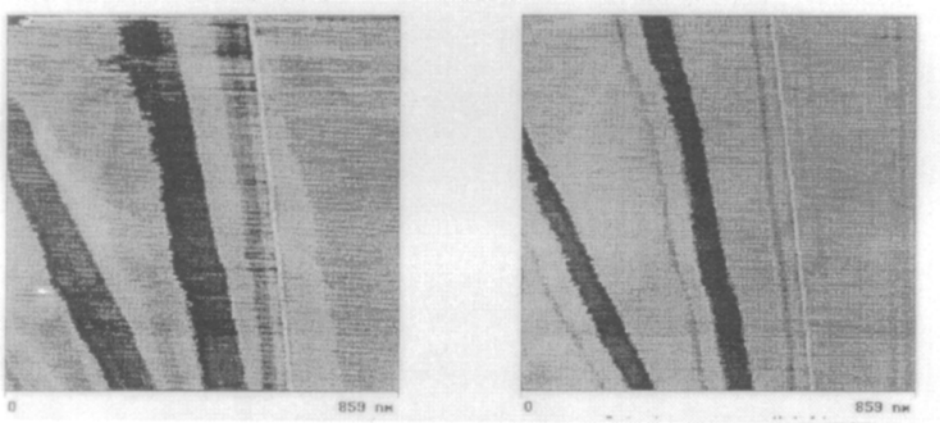

Fig. 7. In-situ STM images of a stepped HOPG (0001) surface in the system HOPG(0001)/10^{-2} M $AgClO_4$ + 1 M $HClO_4$ at $T = 298$ K. Left image: bare substrate surface at $\Delta E = 100$ mV. Right image: after Ag deposition at $\eta = -125$ mV. $I_t = 5$ nA, Pt-Ir tip.

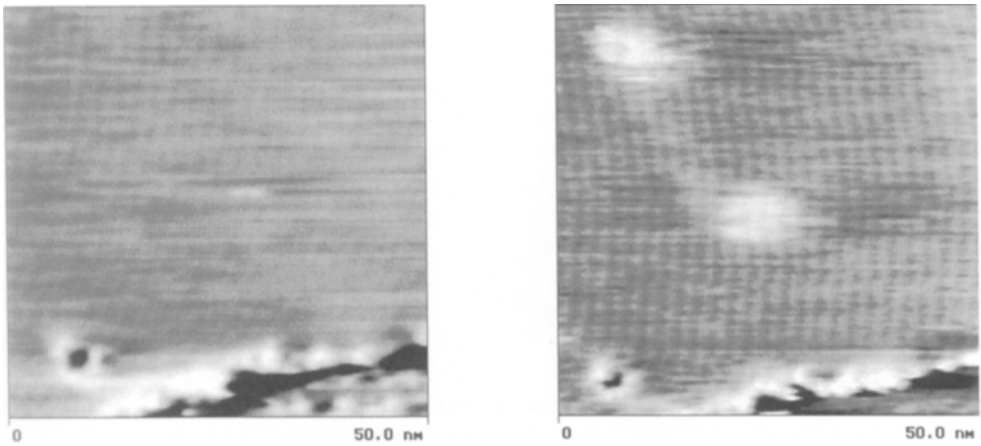

Fig. 8. In-situ STM images in the system HOPG(0001)/10^{-2} M $AgClO_4$ + 1 M $HClO_4$ at T = 298 K. Left image: bare substrate surface. Right image: Ag clusters locally deposited on a flat substrate terasse applying tip-positive 6 V bias with 0.1 ms duration. I_t = 5 nA; Pt-Ir tip.

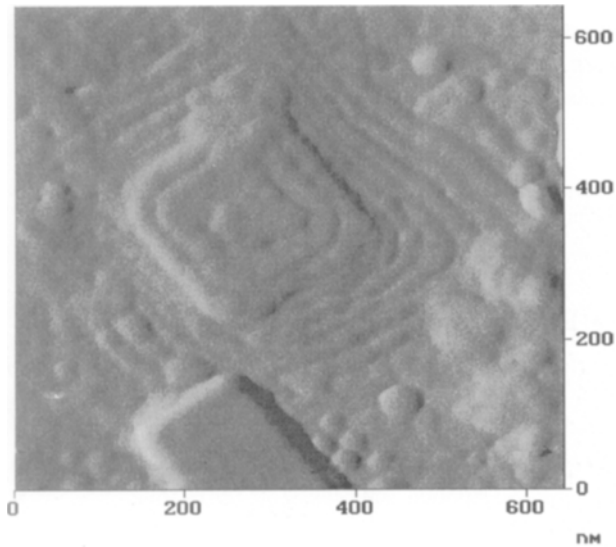

Fig. 9. In-situ AFM image of a $YBa_2Cu_3O_{7-\delta}$ thin-film surface (c-axis oriented) under electrochemical conditions in the system $YBa_2Cu_3O_{7-\delta}$/3.3x10^{-3} M $[CH_3COCH{=}COCH_3]_2$ Cu + CH_3CN + 0.1 M $C_{16}H_{36}ClNO_4$ at T = 298 K, contact mode.

Surfaces of superconducting $YBa_2Cu_3O_{7-\delta}$ thin films, which are epitaxially grown on $SrTiO_3$ single-crystal substrates, exhibit terraces separated by monatomic steps as shown in Fig. 9. The surface morphology is also suitable for nanostructuring by local Me deposition in the OPD range.

Local Cu OPD on Au(111) is already successfully accomplished using a modified AFM technique with a special polarization routine [20]. First experiments have been started to use a similar technique for the nanostructuring of semiconductor and superconductor surfaces.

4 Conclusions

Investigations of UPD and OPD of metals leading to 2D and 3D Me phase formation are of great interest for electrochemical nanotechnology. Application of in-situ local probe techniques in this field gives new analytical information on an atomic level and offers possibilities for a defined nanostructuring of solid-state surfaces.

Acknowledgments. The authors thankfully acknowledge financial support of this work given by Deutsche Forschungsgemeinschaft (DFG), Arbeitsgemeinschaft Industrieller Forschungsvereinigungen (AIF), Bundesministerium für Wirtschaft (BMWi) and Fonds der Chemischen Industrie. The following coworkers contributed to the results presented: W. Obretenov, U. Schmidt, S. Vinzelberg, S. G. Garcia, D. Salinas, R. T. Pötzschke, A. Froese, C. Gervasi, and A. Bary.

5 References

[1] G.Binnig, H.Rohrer, C.Gerber, E.Weibel, Phys. Rev. Lett. 49, 57 (1982).
[2] G.Binnig, H.Rohrer, IBM J. Res. Dev. 30, 355 (1986).
[3] G.Binnig, C.F.Quate, C.Gerber, Phys. Rev. Lett. 56, 930 (1986).
[4] 10 Years of STM, Ultramicroscopy 42-44 (1992).
[5] R.J.Behm, N.Garcia, H.Rohrer (Eds.),Scanning Tunneling Microscopy and Related Methods, NATO ASI Series E, Applied Sciences, Vol. 184, Kluwer Academic Publishers, Dordrecht, 1990.
[6] H.D.Abruna (Ed.), Electrochemical Interfaces: Modern Techniques for In-situ Interface, VCH, Weinheim, 1991.
[7] J.Lipkowski, P.N.Ross (Eds.), Structure of Electrified Interfaces, VCH, Weinheim,1993.

[8] R.Wiesendanger, H.-J.Güntherodt (Eds.), Scanning Tunneling Microscopy II, Springer Series in Surface Sciences, Vol. 28, Springer-Verlag, Berlin, 1992.

[9] N.John Di Nardo, Nanoscale Characterization of Surfaces and Interfaces, VCH, Weinheim, 1994.

[10] $E_{e^-}^{(j)} = \tilde{\mu}_{e^-}^{(j)} = \mu_{e^-}^{(j)} - F\phi^{(j)}$ where $\tilde{\mu}_{e^-}^{(j)}$ and $\mu_{e^-}^{(j)}$ denote the electrochemical and chemical potentials of electrons in phase j, respectively, and $\phi^{(j)}$ is the inner or Galvani potential of phase j which can be measured as electrode potential E vs. a reference electrode.

[11] E.Budevski, G.Staikov, W.J.Lorenz, Electrochemical Phase Formation and Growth - An Introduction to the Initial Stages of Metal Deposition,W-VCH, Weinheim,1996.

[12] D.M.Kolb, A.S.Dakkouri, N.Batina, The Surface Structure of Gold Single-Crystal Electrodes, in Proc.of NATO Advanced Study Institute on Nanoscale Probes of the Solid/lLiquid Interface, Sophia Antipolis, France, July 10-20, 1993, H.Siegenthaler, A. Gewirth (Eds.), Kluwer Academic Publishers, Dordrecht, 1995, p.263.

[13] S.G.Garcia, Electrochemical and in-situ STM investigations in the system Au(*hkl*)/Ag^+, PhD Thesis, University of Bahia Blanca, Argentina, 1997; S. Garcia, D. Salinas, C. Mayer, E. Schmidt, G. Staikov, and W. J. Lorenz, Electrochim. Acta, submitted.

[14] R.T.Pötzschke, C.A.Gervasi, S.Vinzelberg, G.Staikov, W.J.Lorenz, Electrochim. Acta 40, 1469 (1995).

[15] S.G.Garcia, D.Salinas, C.Mayer, J.R. Vilche, H.-J.Pauling, S.Vinzelberg, G.Staikov, W.J. Lorenz, Surface Sci. 316, 143 (1994).

[16] S.Vinzelberg, Elektrochemische 2D und 3D Phasenbildung aus atomarer Sicht - Rastertunnelmikroskopische und -tunnelspektroskopische Untersuchungen in den Modellsystemen Au(*hkl*)/Ag^+ und Au(*hkl*)/Pb^{2+}. PhD Theses, Universität Karlsruhe, 1995.

[17] U.Schmidt, S.Vinzelberg, G.Staikov, Surface Sci. 348, 261 (1996).

[18] W.Obretenov, U.Schmidt, W.J.Lorenz, G.Staikov, E.Budevski, D.Carnal, U.Müller, H. Siegenthaler, E.Schmidt, J. Electrochem. Soc. 140, 692 (1993).

[19] R.T.Pötzschke, Nanostrukturierung elektronenleitender Festkörperoberflächen, PhD Thesis, University of Karlsruhe, 1997, in preparation.

[20] A.Froese, Elektrochemisches Phasengrenzverhalten von Supraleitern, PhD Thesis, University of Karlsruhe, 1996.

Electrochemical Nanotechnology
In-situ Local Probe Techniques at Electrochemical Interfaces
Edited by W. J. Lorenz and W. Plieth

Imaging of Electrochemical Processes and Biological Macromolecular Adsorbates by in-situ Scanning Tunneling Microscopy

Jens E.T. Andersen, Jens Ulstrup, Per Møller

Contents

1	Introduction		28
2	Imaging electrochemistry by in-situ scanning tunneling microscopy (in-situ STM/electrochemical STM)		29
	2.1	Pure gold surfaces in electrolyte solutions	29
	2.2	Metal deposition and metal dissolution	31
3	STM of adsorbed metalloproteins		37
	3.1	In-situ STM patterns of cytochrome *c* and other metalloproteins	38
	3.2	In-situ tunneling through metalloproteins as a three-center multiphonon electron transfer process	40
4	References		42

Summary. In-situ scanning tunneling microscopy (STM) has provided intriguing new information about electrocrystallization, corrosion, and the surface dynamics of metall proteins.

Repetive cycles of copper deposition on gold have been found to lead to surface alloy formation where nucleation occurs during the first cycle, followed by growth of the alloy phase in subsequent cycles. Bulk metal crystallites nucleate and grow on top of the alloyed surface at cathodic overpotentials. The entire process can be followed in time and the surface morphology mapped while cyclic voltammograms are simultaneously recorded. This has led to a new understanding of surface atom mobility, mechanisms of electrocrystallization, and electrosorption. It has also been shown that the potentials of copper deposition and dissolution on gold are separated by exactly 59 mV. This is not reflected in the cyclic voltammograms but

indicates that copper electrodeposition is indeed a single-electron process such as predicted by the Bockris-Mattson model.

In other investigations in-situ STM imaging has shown that the single-center metalloproteins cytochrome *c* (Fe) and azurin (Cu) are strongly adsorbed on gold at low ionics strength. In contrast, the multicenter copper oxidase laccase, surprisingly, appears to be weakly adsorbed on pyrolytic graphite in spite of good electrochemistry. Cytochrome *c* (cyt *c*) and azurin assemble in flat aggregates, organized in a heterophase, and corresponding in lateral size (≈50 nm x 50 nm) to about 100 molecules. The organized aggregates evolve in time, and pinholes open and split. Further investigation of cyt *c* has revealed smaller structures, of the size of individual molecules, between the larger aggregates. This holds interesting perspectives for in-situ characterization of protein structure and dynamics on solid surfaces.

A theory of in-situ STM of large adsorbates, based on inelastic tunneling, strong electronic vibrational coupling, and molecular electron transfer theory, has been developed.

1 Introduction

By introduction of electrochemical control of both the tip and the working electrode, conventional STM has been developed to image surfaces in-situ, i.e. with both surface and tip in contact with electrolyte [1-4]. Key factors in high-quality images are potentiostatic control [1, 2] and tip coating [1-5]. The tip in contact with the electrolyte acts as an additional working electrode. The system therefore needs independent potentiostatic control of the two working electrodes with respect to a common reference electrode. This is most frequently achieved by a bipotentiostat [1-4, 7] but other methods are also encountered [3]. Faradaic current densities at the tip or working electrode may then be kept within pre-determined limits. The uncoated tip in contact with electrolyte usually results in a Faradaic current density which exceeds the tunnel current by orders of magnitude [8] and prevents meaningful imaging. The Faradaic current at the tip is, however, minimized by coating the tip with an insulating film [9, 10]. Our in-situ STM research has followed two lines. One addresses electrochemical metal deposition, the other the structural surface organization and functional mechanisms of adsorbed metall proteins.

2 Imaging Electrochemistry by in-situ Scanning Tunneling microscopy (in-situ STM/electrochemical STM)

In contrast to conventional microscopy, in-situ STM affects the electrochemical process imaged. Although the tip is well coated and only small currents (nA) are conducted, the tip is still important. A linear relation between the tip potential and the electrochemical potential for copper deposition on polycrystalline gold was found recently [11]. The potential was swept to a point where the surface was just covered by copper as observed by in-situ STM, i.e., the potentials (E_{ON}, E_{tip}) for the onset of copper electrodeposition were registered. Similarly, the potentials (E_{OFF}, E_{tip}) where the bare surface was recovered during copper dissolution were registered. Both potential relations follow a linear behaviour in a wide range of tip potentials (Fig. 1). The parallel lines are separated by 59 mV, which indicates that copper electrodeposition/dissolution is a one-electron process [11]. An implication of this is that cyclic voltammetry cannot directly relate voltammetry features to in-situ STM images. The procedure is rather to record in-situ STM at several tip potentials and extrapolate all the data to zero tip potential in comparison with voltammetry. Alternatively, the tip potential should be kept at the value zero.

2.1 Pure Gold surfaces in electrolyte solutions

Atomic structures on crystalline surfaces in electrolytes have been identified [1-8]. It is essential that the surface is kept under electrochemical control [3-8]. Figure 2 shows images of a crystalline gold surface prepared by flame annealing [12] and instantly subjected to potentiostatic control (E = 180 mV vs. Cu^{2+}/Cu). Individual gold atoms are readily identified (Fig. 2). Imaging may be maintained for many hours provided that the potential is kept at a sufficiently large anodic value to prevent underpotential deposition (UPD) [13] but not so large that surface oxidation begins [14].

Davenport et al. [14] have shown that a worm-like structure of gold oxide appears on a crystalline gold surface oxidized electrochemically. By comparing in-situ STM images with electrochemical data it was evident that monolayers of gold oxide were formed at anodic potentials and that a slow reduction of the gold oxide at cathodic potentials recovered the bare surface. The gold surface, however, is not oxidized solely by electrochemical methods.

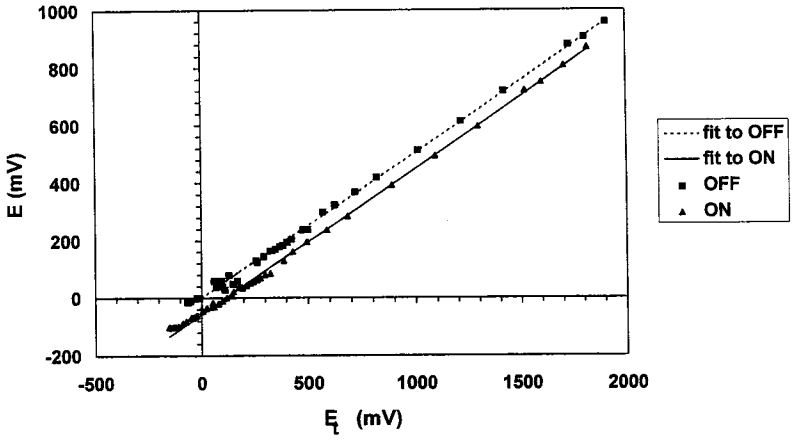

Fig.1. The electrochemical potential of copper electrodeposition (▲ , E_{ON}) and of copper electrodissolution (■, E_{OFF}) on a gold polycrystalline working electrode as imaged by in-situ STM. The separation between the two straight lines fitted to the data are parallel and separated by 59 ± 2 mV. Electrolyte: 0.01 M $CuSO_4$ and 0.01 M H_2SO_4 in Millipore water.

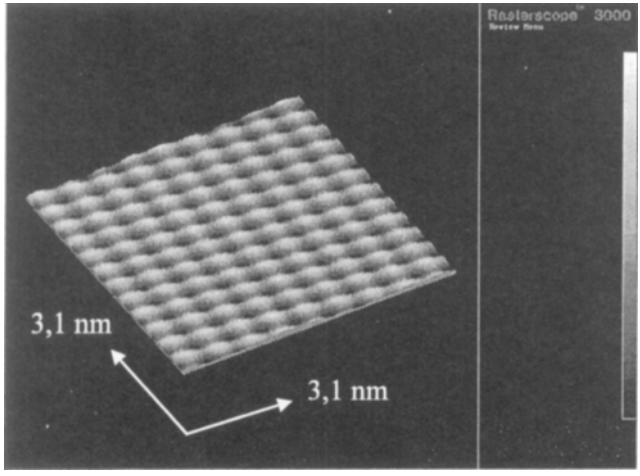

Fig.2. Gold crystalline surface imaged at atomic resolution by in-situ STM in 0.01 M $CuSO_4$ and 0.05 M H_2SO_4 in Millipore water with E = 200 mV and E_t = -110 mV (filtered), d = 0.02 nm, I_t = -3 nA.

Figure 3 illustrates surface oxidation by contact with ambient atmosphere for 24 h, i.e., ex-situ. Figure 3 is recorded by installing the oxidized sample in the in-situ STM system, keeping it under slightly acidic conditions and anodic potentials. Under these conditions the atomic surface structure is visible (Fig. 3, center) together with a few layers of gold oxide (Fig. 3, upper left). A growing oxide layer is observed to the lower right of Fig. 3 as evidenced by blurring of the atomic structure.

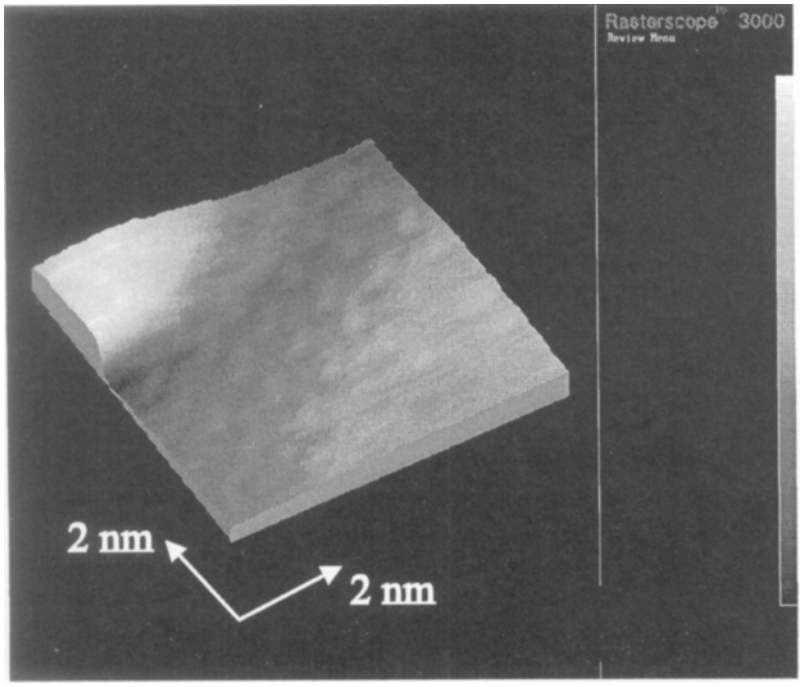

Fig. 3. Gold crystalline surface oxidized ex-situ at ambient pressure for 24 h. Two layers of gold oxide are seen to the upper left, and to the lower right the gold was only partially oxidized. Along the mid-diagonal, rows of individual atoms are observed. In-situ STM images, electrolyte: 0.01 M $CuSO_4$ and 0.05 H_2SO_4 in Millipore water, E = 400 mV, E_t = -91 mV, d = 0.5 nm, I_t = 1.2 nA.

2.2 Metal deposition and metal dissolution

In-situ STM offers unique high resolution of the dynamics of atoms and molecules at surfaces in solution [15]. The technique applies, however, also to bulk phenomena at

lower magnification in the whole range from optical microscopic to atomic resolution [16-18]. At lower magnifications, e.g., with image dimensions in the micron range, the results may be compared with results obtained by methods such as ex-situ electron diffraction [6]. Intermediate resolution has provided much new information about electrochemical mechanisms of bulk electrocrystallization and -dissolution. The mechamism of growth during metal electrocrystallization is classically divided into three major categories: layer-by layer growth (Frank-van der Merwe) [19], monolayer

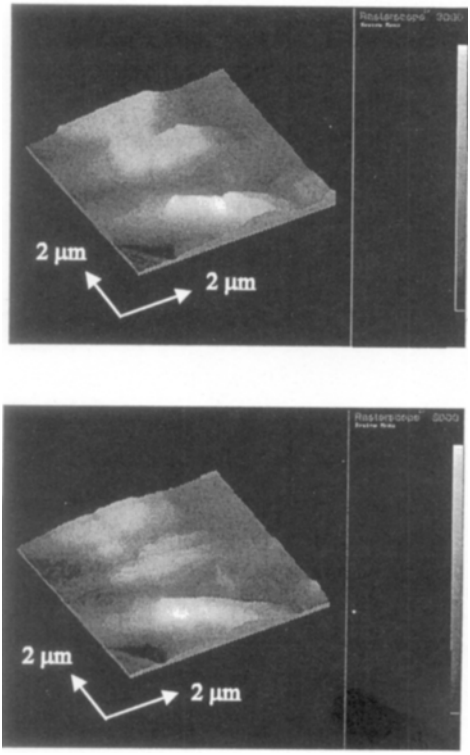

Fig. 4. In-situ STM images of copper crystallites electrodeposited on gold. Electrolyte: 0.001M $CuSO_4$ and 0.01 M H_2SO_4 in Millipore water. (a) Electrodeposition terminated at E = -100 mV, E_t = -58 mV, d = 216 nm, I_t = 2.1 nA. (b) Electrodissolution initiated at E = 0 mV, E_t = 42 mV, d = 186 nm, I_t = 2.1 nA.

and island formation (Stranski-Krastanov) [20], and pure islanding (Volmer-Weber) [21]. Metal ions in solution typically grow on the surface at cathodic overpotentials by the latter two mechanisms [8, 19, 22-24]. Growth by the layer-by-layer mechanism proceeds only for a single-monolayer UPD. Excellent atomic resolution of the growth of metal monolayers on metal working electrodes for a number of systems has been obtained by in-situ STM [6, 7, 13, 14, 22-27]. The gold surface reconstructs when small amounts of halides are added [6, 28], lifting the potential-induced (1 x 23) surface reconstruction. These results agree well with results obtained under UHV conditions [6, 28] even though water adsorption is different in the two cases.

Nucleation in bulk deposition occurs near surface imperfections. Steps and kinks are observed for copper on copper [16], gold [22], platinum [23], and graphite [29]. Nucleation continues at cathodic overpotentials until the surface is covered. New results indicate that several layers of equally sized nuclei are formed initially whereas crystallites are formed only when the surface concentration of nuclei exceeds a certain limit [11], possibly determined by the surface atom density. Growth proceeds to become three-dimensional, nucleation is then terminated, and crystallites of micron dimensions cover the surface (Fig. 4(a)). If the overpotential is fixed at values small enough to induce bulk nucleation but prevent bulk deposition, the system may enter a state of equilibrium between electrodeposition and -dissolution [11]. The amount of metal electrodeposited may thus be controlled with great precision so as to maintain a fraction of the number of metal ions in solution with a corresponding number resting on the surface at small overpotentials. This situation is established at potentials at the leading edge of the cathodic branch of a cyclic voltammogram [11].
By comparing cyclic voltammetry with in-situ STM recorded simultaneously it seems that the cathodic current peak of bulk metal electrodeposition reflects the termination of metal deposition rather than a potential of maximum metal growth [11].

The morphology of the copper deposit has been studied also in the presence of organic additives. Organic additives do not appear in the images but their effect is striking. They adsorb onto defect sites, steps, and kinks, and prevent copper from nucleation at these sites. Copper nucleates in a more random manner and when adequate coverage is reached the copper crystallites merge and form a compact layer [22]. The overall effect of additives is thus to induce lateral growth (2D), as opposed to island formation by 3D growth which dominates in the absence of additives.

As observed by in-situ STM the metal is also dissolved before the maximum current is reached in the voltammogram when the potentials are swept from cathodic to anodic values [11]. Figure 4(b) shows the first stages of copper dissolution (vs. Cu^{2+}/Cu) where copper gradually enters the ionic state from the top layers. When copper dissolves, a small fraction remains and alloys with the gold polycrystalline surface to from nanometer-scale crystallites (Fig. 5(a, b)). In Figure 5(a) the alloy nuclei form

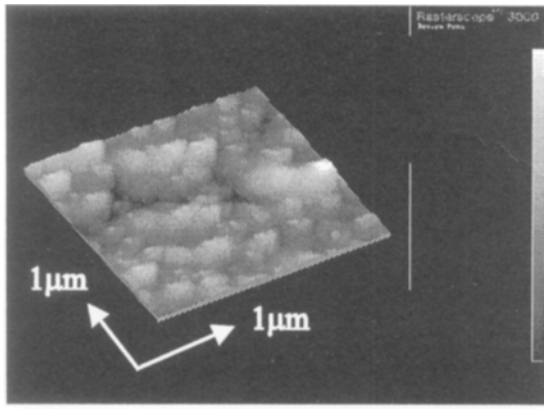

a)

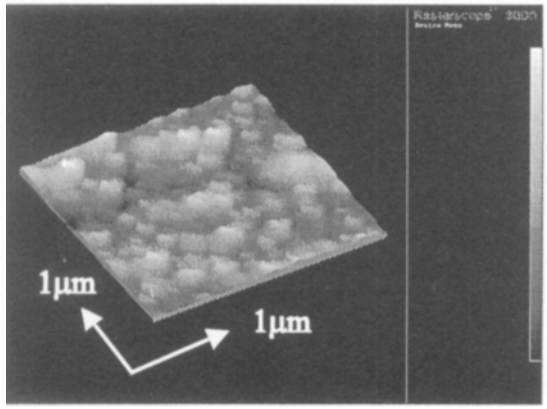

b)

Fig.5. Gold polycrystalline surface with copper-gold alloy crystallites grown by performing cycles of copper electrodeposition and dissolution. (a) After first cycle: $E = 400$ mV, $E_t = 442$ mV, d = 44 nm, $I_t = 1.8$ nA. (b) After second cycle. In-situ images: d = 42 nm, $I_t = 2.1$ nA. Electrolyte: 0.001 M $CuSO_4$ and 0.05 M H_2SO_4 in Millipore water, $E = 400$ mV, $E_t = 442$ mV.

after one cycle of copper electrodeposition and -dissolution [30]. After the second cycle the dimensions of the nuclei have increased by 3D growth. Copper-gold alloy surfaces have been investigated by in-situ STM as models for corrosion [31] and results concord with ex-situ electron microscopy data [32]. A critical potential exists below which migrating gold atoms prevent copper dissolution. Above the critical

potential, copper dissolves selectively because fresh sites are exposed to the electrolyte by increased migration of gold atoms [31, 32].

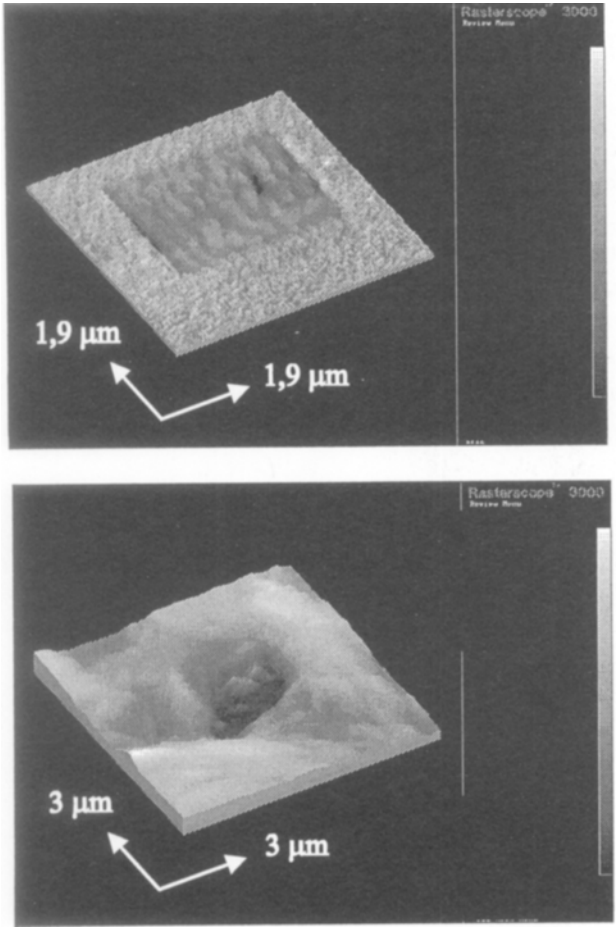

Fig.6. In-situ STM images of gold surfaces with figures machined into the surface by electrochemical methods. (a) Square produced by a sweep of cell potential from 0 to -100 mV five times in a diluted MES (2-(N-morpholino)ethanesulfonic acid) buffer electrolyte. E = 500 mV, E_t = 546 mV, d = 24 nm, I_t = 2.5 nA. (b) Cavity in the surface produced by performing 40 copper electrodepositions and sub-sequent dissolutions with potentials between -500 mV and 500 mV.
Electrolyte: 0.001 M $CuSO_4$ and 0.05 M H_2SO_4 in Millipore water, E = 200 mV, E_t = 235 mV, d = 282 nm, I_t = 7.1 nA.

The surface mobility is induced by potential gradients in the electrified interface and estimated to be ca. 10^{-12} cm^2/s [32, 33]. A consequence is that the tip action on the surface atoms should be considered in in-situ STM [11]. In Figure 6(a) is seen the influence of sweeping the cell voltage at constant bias voltage in a 2-(N-morpholino)ethanesulfonic acid (MES) buffer solution. Under such conditions the tip potential was swept together with the gold surface potential with respect to the common reference potential. A transition of the surface morphology was observed during the sweep and simultaneous imaging (Fig. 6(a). However, when the image area was subsequently enlarged it was evident that the surface flattened markedly owing to the tip action, as seen in Figure 6(a) by a square engraved in the surface. The surface morphology also undergoes a transition in metal electrodeposition and -dissolution. In Figure 6(b), is shown a cavity created by the tip action. After approximately 40 cycles the imaging area was increased to reveal the cavity (-500 mV < E < 500 mV and sweep rate 1-10 mV/s). Accordingly, copper grows and dissolves on the gold surface simultaneously with gold atom migration and the final surface imaged possibly contains small amounts of copper [17, 30].

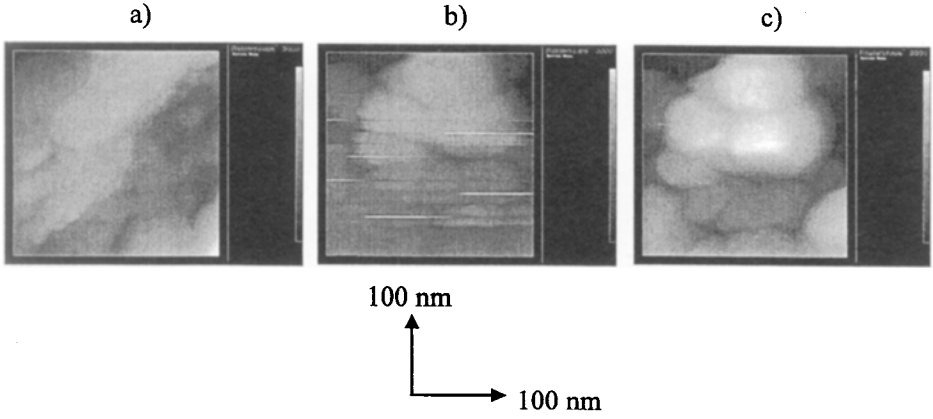

Fig.7. In-situ STM images of copper potentiostatic pulse plating on gold. Electrolyte: 0.001 M $CuSO_4$ and 0.05 M H_2SO_4 in Millipore water. (a) Clean surface, d = 9 nm. (b) Ten pulses of 0/-100 mV, each 500 ms duration (stripes), d= 44 nm. (c)Copper crystallites created by the process, E = 0 mV, E_t = 42 mV, d = 29 nm, I_t = 4.2 nA.

In studies of electrochemical processes on gold imaged by in-situ STM the surface mobility introduces complications in theoretical modeling [33]. In technical

applications of in-situ STM the ability of the tip to create well-defined patterns on the surface might be useful in „nanotechnology" or „nanoelectronics". In-situ STM and AFM (atomic force microscopy) have succesfully been introduced in technologically important contexts such a electronic circuit boards, polymer-metal interfaces [34] and pulse plating [35]. An example is shown in Fig. 7(a)-(c). A clean surface was subjected to 10 cycles of square pulses of E = -100 mV for 0.5 s followed by E = 0 mV for 0.5 s. When potentiostatic cycling was activated, imaging was temporarily disturbed (the middle of Fig. 7(b) where 10 horizontal lines appear). However, as the scanning is from below towards the top, it is possible to image the growth of copper between the lines of Fig. 7(b). The final result of the pulse plating process is copper crystallites (Fig. 7(c)). It is well known that potentiostatic or galvanostatic pulse shapes have a profound influence on the morphology of the deposit and the mechanical properties of the coating [36]. The imaging of the process may prove useful in developing metal surface coatings but the image features have yet to be related to macroscopic properties.

3 In-situ STM of adsorbed metalloproteins

Chemical and biological *homogeneous electron tunneling* (ET) has been mapped in considerable detail [37-43], based on elaborate synthetic work, characterization of many new redox proteins, and new theoretical achievements. Concepts and physical properties in focus have been: (a) the distance and orientation of the donor and acceptor centers, and the nature of the intermediate molecular groups; (b) supramolecular organization in multi-ET patterns; (c) vibrational coherence and (d) fluctuation-induced tunneling and critical phenomena. Interfacial *electrochemical* ET has not witnessed a parallel evolution due to less feasible structural and theoretical characterization of the heterogeneous, field-exposed, interfacial region. Perspectives for more precise characterization are opening, however, rooted in the availability of new, stable, self-assembled films, and precise deconvolution of the tunnel and nuclear activation factors over broad potential ranges [44, 45], supported by new construction of dielectrically screened energy functionals [46, 47] and interfacial ET rate constants [48]. At the same time in-situ STM has opened exciting perspectives for direct imaging of the two-dimensional adsorbate organization. Our research has recently focused on mapping of biological macromolecules by in-situ STM, with reference to concepts and formalism of long-range ET of solute metalloproteins. The activity is prompted by the inherent perspectives of protein mapping at surfaces and by the fact that metalloproteins in homogeneous solution offer some of the most detailed tunnel features.

3.1 In-situ STM patterns of cytochrome c and other metalloproteins

Structural mapping of adsorbate molecules by STM and AFM has been extended to biological macromolecules [49]. These include DNA [50], proteins, and protein complexes [51, and references therin). The natural medium for biological macromolecules is, however, aqueous solution, and water constitutes an integrated element of three-dimensional structure. High-resolution in-situ STM imaging of DNA [50], DNA bases [52], and metalloporphyrins [53] has been achieved recently, but obstacles arise for proteins:

(a) Solute proteins are conformationally labile.
(b) Proteins are collectively mobile on the substrate surface. The mobility patterns are interesting but immobilization is needed to achieve molecular resolution.
(c) Protein mobility, together with the large tunnel distance, poses a risk of mechanical dislodging by the tip during the scanning process.
(d) Metallic surfaces reconstruct in certain potential ranges, resulting in structural features interfering with adsorbate dynamics.

We have investigated in-situ STM of the small single-metal redox proteins cytochrome *c* (MW ≈ 12 kDa) and azurin (≈ 14 kDa), and the larger four copper-enzyme laccase (MW ≈ 64 kDa), all involved in natural ET [51, 54, 55]. The choice rested on the following considerations:

(1) Key structural elements of the proteins are transition-metal atoms which are easily reduced or oxidized. The metal atoms provide favourable tunnel routes either as local tunnel barrier indentations, or by accomodating the electron or hole in inelastic STM modes [56, 57].
(2) The proteins are well characterized electrochemically, indicative of facile electron exchange with metallic surfaces of ET through the protein.
(3) Cyt *c* and azurin are structurally and in other respects very well characterized, and in-situ STM can be referred to many other structural, spectral, and kinetic data. No three-dimensional structure of laccase is available, but the structure of the closely related enzyme ascorbate oxidase is available with high resolution and supports a view of facile ET *through* the protein, involving all the copper atoms.

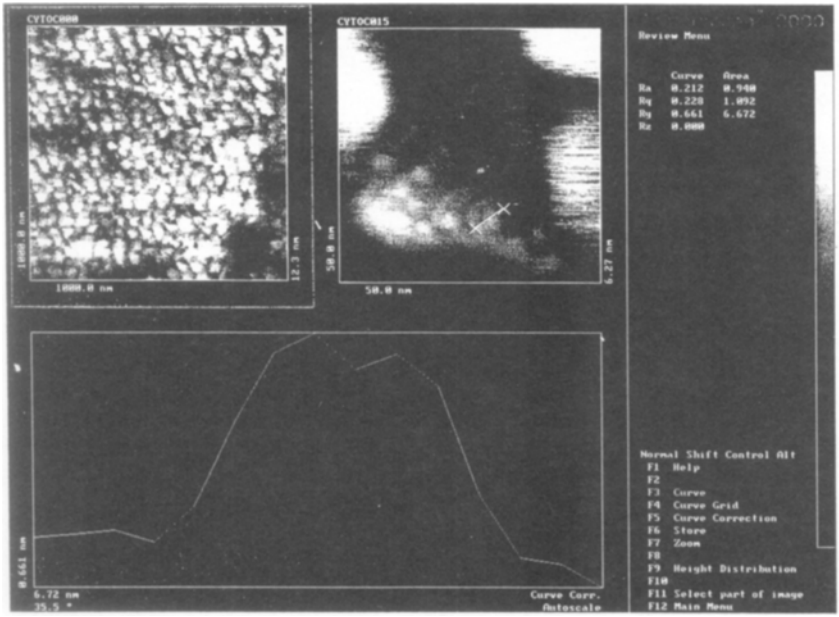

Fig.8. Cyt *c* on gold adsorbed from 10^{-5} M cyt *c* and 20 mM MES buffer (pH = 7). Upper left: Organized arrays of ≈50 nm lateral extent. Constant current mode, I_t = 1.8 nA. Structures resembling individual cyt *c* moleculesadsorbed on gold between larger cyt *c* aggregates. Bottom: Height profile of the structures at the upper right.

Figure 8 shows representative images of polycrystalline or flame-annealed gold surfaces in contact with 10^{-3} M cyt *c* in 20 mM MES buffer (pH = 7.0) [51]. The surface structure is quite different from the structure in the absence of cyt *c*. The view shows arrays of individual structural elements about 50 nm in lateral extent, corresponding to ≈100 molecules. Similar patterns are observed for azurin. The structures are fluctuationally mobile. This mobility impedes molecular resolution but, subject to adequate persistence, much smaller structures of the size of individual molecules are clearly visible *between* the larger structures (Fig. 8). The smaller structures have not so far been found for azurin for which, on the other hand, ex-situ AFM on flame-annealed gold has shown structures of similar size [55]. The height (0.5 $\pm$ 0.1 nm) and lateral extent (3.3 $\pm$ 0.5 nm) for the molecular-size cyt *c* structures are close enough to the crystallographic dimensions to indicate that Fig. 9 could well show molecular resolution.

In-situ STM of laccase has so far been attempted using only basal-plane pyrolytic graphite surfaces [54]. No adsorption could be detected. This is perhaps not surprising as laccase voltammetry requires edge-plane graphite and/or pre-adsorption of promoters. Low-resolution ex-situ micron-scale laccase structures could be recorded during evaporation of laccase solution where individual molecular-size structures, possibly dislodged by mechanical tip contact, could also be observed.

3.2 In-situ tunneling through metalloproteins as a three-center multiphonon electron transfer process

In-situ STM has been approached theoretically. Focus has been on (a) solvent polarization effects on the metallic electronic structure [58, 59]; (b) local pseudopotentials [59]; (c) electron tunnel routes through networks of „quantum dots" [60]; (d) time correlation effects and noise [60]; (e) resonance tunneling [62, 63], and (f) tunneling through intermediate local molecular levels as in other three-level coherent thermal and optical processes [56, 57, 64].

We discuss briefly the latter view. The intermediate state is representative of the metal centers in metalloproteins or large transition-metal complexes, spatially separated from the electrodes by protein or intramolecular ligand frames. The electron- or hole-transferring redox level has also much lower energy than surrounding protein or solvent. Figure 9 shows the level dynamics. The local level, at the equilibrium nuclear configuration $q = 0$, is initially well above the Fermi level of both tip and substrate. Nuclear fluctuations take the level close to the Fermi level of the negatively biased electrode. This lowers the tunnel barrier, even to the extent of temporary population but at the expense of nuclear activation. A variety of three-level STM patterns then arise of which the following are particularly important:

(1) The populated level begins to relax vibrationally after the first ET step, but the second step, i.e., electron transfer from the populated intermediate level to the positively biased electrode, occurs before full relaxation. This pattern corresponds to *coherent* two-step ET, of which strictly resonating three-level transfer would be a limiting case.
(2) The tunnel interactions may be weak so that full vibrational relaxation occurs after the first step. Renewed fluctuations induce the second step so that the overall process turns into two sequential independent single-ET processes.

The view in Fig. 9 can be given a quantitative frame which incorporates distance and voltage relations [56, 57, 64]. In-situ STM here offers an additional dimension

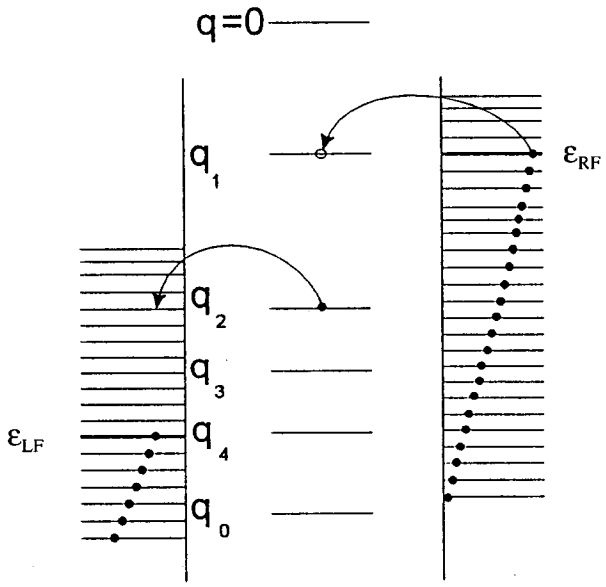

Fig. 9. Molecular adsorbate level between two continuous metallic-level distributions. Tunneling is from the negatively (right) to the positive (left) biased electrode and feasible when nuclear fluctuations take the adsorbate level from the initial location *above* both Fermi levels, ε_{RF} and ε_{LF}, respectvely, to a location *between* the Fermi levels. *q* with different subscripts indicates nuclear configurations at which tunneling in the coherent two-step ET mode can occur [53, 55].

compared with electrochemical ET. STM can thus be monitored at variable *bias* voltage, but fixed *overpotential.* The latter is the substrate-molecule potential difference relative to a reference potential. The tunnel current can also be recorded at variable overpotential and fixed bias potential. In the latter case the electrode potentials vary in parallel. It has been noted [64] that the current-overpotential relation exhibits close formal relations to the *excitation profile* of resonance Raman spectroscopy while the current-bias voltage relation correspondingly resembles the resonance Raman *spectrum* [64].

The view discussed above offers frames for in-situ STM phenomena once uniform adsorbate organization can be achieved. This is not at present the case for metalloproteins but a recent investigation of in-situ current-voltage relations of protoporphyrin IX and Fe-protoporphyrin IX at highly oriented pyrolytic graphite is extremely illuminating [53]. In particular, the current-overpotential relation has anmaximum when the local molecular level passes the Fermi levels at small bias voltage. This is in line with vibrationally coherent two-step ET and different from both electrochemical single-step ET and sequential two-step ET as a current plateau would be expected at high overvoltage in either of these limits.

Acknowledgments. The financial support from the National Danish Research Foundation is gratefully acknowledged.

7 References

[1] R. Sonnenfeld, P.K. Hansma, Science 232, 211 (1986).
[2] J. Schneir, R. Sonnenfeld, P.K. Hansma, J. Tersoff, Phys. Rev. B 34, 4979 (1986).
[3] P. Lustenberger, H. Rohrer, R. Christoph, H. Siegenthaler, J. Electroanal. Chem. 243, 225 (1988).
[4] J. Wiechers, T. Twomey, D.M. Kolb, R.J. Behm, J. Electroanal. Chem. 248, 451 (1988).
[5] R.V. Coleman, B. Drake, P.K. Hansma, G. Slough, Phys. Rev. Lett. 55, 394 (1985).
[6] O.M. Magnussen, J. Hotlos, R.J. Nichols, D.M. Kolb, R.J. Behm, Phys. Rev. Lett. 64, 2929 (1990).
[7] K. Itaya, E. Tomita, Surface Sci. Lett. 201, L507 (1988).
[8] D.M. Kolb, R.J. Nichols, R.J. Behm, R. Guidelli (eds.), Electrified Interfaces in Physics, Chemistry and Biology, NATO ASI Series C, Kluwer Academic Publishers, Dordrecht, Netherlands, 1992, p. 275-292.
[9] C.E. Bach, R.J. Nichols, W. Beckmann, H. Meyer, A. Schulte, J.O. Besenhard, P.D.Jannakoudakis, J. Electrochem. Soc. 140, 1281 (1993).
[10] C.E. Bach, R.J. Nichols, H. Meyer, J.O. Besenhard, Surf. Coat. Technol. 67, 139 (1994).
[11] J.E.T. Andersen, G. Bech-Nielsen, P. Møller, J.C. Reeve, J. Appl. Electrochem. 26, 161 (1996).
[12] J. Clavier, R. Faure, G. Guinet, R. Durand, J. Electroanal. Chem. 107, 205 (1980).

[13] W. Obretenov, U. Schmidt, W.J. Lorenz, G. Staiikov, E. Budevski, D. Carnal, U. Müller, H. Siegenthaler, E. Schmidt, J. Electrochem. Soc. 140, 692 (1993).
[14] C.M. Vitus, A.J. Davenport, J. Electrochem. Soc. 141, 1291 (1994).
[15] A.A. Gewirth, K.J. Hanson, Interface (Spring 1993) 37.
[16] X.G. Zhang, U. Stimming, J. Electroanal. Chem. 291, 273 (1990).
[17] R.J. Nichols, D.M. Kolb, R.J. Behm, J. Electroanal. Chem. 313, 109 (1991).
[18] J.E.T. Andersen, G. Bech-Nielsen, P. Møller, Surf. Coat. Technol. 70, 87 (1994).
[19] F.C. Frank, J.H. van der Merwe, Proc. R. Soc. A (London) 198, 205 (1949).
[20] J.N. Stranski, L. Krastanov, Ber. Akad. Wiss. (Wien 146, 797 (1938).
[21] M. Wolmer, A. Weber, Z. Phys. Chem. 119, 277 (1926).
[22] R.J. Nichols, W. Beckmann, H. Meyer, N. Batina, D.M. Kolb, J. Electroanal. Chem. 330, 381 (1992).
[23] M. Wünsche, R.J. Nichols, R. Schumacher, W. Beckmann, H. Meyer, Electrochim. Acta 38, 647 (1993).
[24] M.P. Green, K.J. Hanson, R. Carr, I. Lindau, J. Electrochem. Soc. 137, 3493 (1990).
[25] W.J. Lorenz, L.M. Gassa, U. Schmidt, W. Obretenov, G. Staikov, V. Bostanov, E. Budevski, Electrochim. Acta 37, 2173 (1992).
[26] N. Batina, T. Will, D.M. Kolb, Faraday Discuss 94, 93 (1992).
[27] K. Sashikata, N. Furuya, K. Itaya, J. Electroanal. Chem. 316, 361 (1991).
[28] D.M. Kolb, *Structure of Electrified Interface* Ch. 3, J. Lipkowski, P.N. Ross (eds.), VCH, New York, 1993.
[29] N. Breuer, U. Stimming, R. Vogel, Surf. Coat. Technol. 67, 145 (1994).
[30] J.E.T. Andersen, P. Møller, J. Electrochem. Soc. 142, 2225 (1995).
[31] T.P. Moffat, F.-R.F. Fan, A.J. Bard, J. Electrochem. Soc. 138, 3224 (1991).
[32] J.D. Fritz, H.W. Pickering, J. Electrochem. Soc. 138, 3209 (1991).
[33] C. Alonso, R.C. Salvarezza, J.M. Vara, A.J. Arvia, Electrochim. Acta 35, 1331 (1990).
[34] R.J. Nichols, D. Schröer, H. Meyer, Scanning 15, 266 (1993).
[35] J.E.T. Andersen, G. Bech-Nielsen, P. Møller, Surf. Coat. Technol. 67, 151 (1994).
[36] P.T. Tang, T. Watanabe, J.E.T. Andersen, G. Bech-Nielsen, J. Appl. Electrochem. 25, 347 (1995).
[37] H. Sigel, A. Sigel (eds.), Metal Ions in Biological Systems, Vol. 27, M.Dekker, New York, 1991.
[38] H.B. Gray, J.R. Winkler, Chem. Rev. 92, 369 (1992).
[39] Contributions in: Chem. Phys.176, 289-649 (1993), Special issue on Electron Transfer.
[40] Contributions in: Chem. Phys. 197, 223-472 (19995), Special issue on Photosynthesis and the Bacterial Reaction Center.

[41] H.E.M. Christensen, L.S. Conrad, K.V. Mikkelsen, M.K. Nielsen, J. Ulstrup, Inorg. Chem. 29, 2808 (1990).
[42] P. Siddarth, R.A. Marcus, J. Phys. Chem. 94, 2985 (1990).
[43] A.A. Kornychev, A.M. Kuznetsov, U. Stimming, J. Ulstrup, J. Phys. Chem., submitted.
[44] H.O. Finklea, D.D. Handshuh, J. Am. Chem. Soc. 114, 3173 (1992).
[45] J.F. Smalley, S.W. Feldberg, C.E.D. Chidsey, M.R. Lindford, M.D. Newton, J. Phys. Chem., in press.
[46] A.A. Kornyshev, in: The Chemical Physics of Solvation. Part C. Solvation in Specific Physical, Chemical and Biological Systems, R.R. Dogonadze, E.Kálmán, A.A. Kornyshev, J.Ulstrup (eds.), Elsevier, Amsterdam, 1988, p. 355.
[47] A.A. Kornyshev, A.M. Kuznetsov, J. Mol. Liquids 61, 103 (1994).
[48] A.A. Kornyshev, A.M. Kuznetsov, J. Ulstrup, J. Phys. Chem. 98, 3832 (1994).
[49] O. Marki, M. Arnrein (eds.), STM and AFM in Biology, Academic Press, San Diego, 1993.
[50] N.J. Tao, J.A. DeRose, S.M. Lindsay, J. Phys. Chem. 97, 910 (1993).
[51] J.E.T. Andersen, P. Møller, M.V. Pedersen, J. Ulstrup, Surf. Sci. 325, 193 (1995).
[52] M.H. Hölzle, T. Wandlowski, D.M. Kolb, Surf. Sci. 335, 281 (1995).
[53] N.J. Tao, Phys. Rev. Lett., in press.
[54] J.E.T. Andersen, M.H. Jensen. P. Møller, J. Ulstrup, Electrochim. Acta 41, 2005 (1996).
[55] J.E.T. Andersen, E. Friis, L.L. Madsen, P. Møller, J. Ulstrup, in preparation.
[56] A.M. Kuznetsov, P. Sommer-Larsen, J. Ulstrup, Surf. Sci. 275, 52 (1992).
[57] A.M. Kuznetsov, J. Ulstrup, Surf, Coat. Technol. 67, 193 (1994).
[58] W. Schmickler, D. Henderson, J. Electroanal. Chem. 290, 283 (1990).
[59] A. Mosyak, A. Nitzan, R. Kosloff, J. Chem. Phys., in press.
[60] M. Sumetskij, J. Phys. C: Condensed Matter 3, 2651 (1991).
[61] M. Sumetskij, A.A .Kornyshev, Phys. Rev. B 48, 17493 (1993).
[62] L.I. Glazman, R.I. Shekhter, Sov. Phys. JETP 94, 282 (1987).
[63] W. Schmickler, Surf. Sci. 295, 43 (1993).
[64] J.E.T. Andersen, A.A. Kornyshev, A.M. Kuznetsov, L.L. Madsen, P. Møller, J. Ulstrup, Electrochim. Acta 42, 819 (1997).

Electrochemical Nanotechnology
In-situ Local Probe Techniques at Electrochemical Interfaces
Edited by W. J. Lorenz and W. Plieth

BEYOND THE LANDSCAPES: IMAGING THE INVISIBLE

A.A. Kornyshev, M. Sumetskii

Contents

1	Introduction		45
2	Adatom diffusion from STM noise		46
	2.1	Assumptions and basic equations	48
	2.2	Temporary current correlation function and low-frequency noise for adatom diffusion	50
	2.3	How and where to use these formulas	52
	2.4	Distinguishing isotropic and anisotropic diffusion	52
	2.5	First experimental observations	53
3	STM and molecular reorientations		53
4	What is the true shape of the cluster for a given shape of the tip?		54
5	References		54

Summary. In-situ scanning probe microscopy: how to see the „invisible", e.g., sluggish adsorbed atoms moving along the surfaces, water molecules, etc.? What is the true shape of atomic cluster on the surface studied by a nanoprobe? These and other „nonconventional" questions are discussed in this short overview, covering ideas, the main difficulties in their realization, and the first experimental examples.

1 Introduction

Imaging the landscapes of solid surfaces ex-situ and in-situ is nowadays an established method for gaining information about their local structure. Reliable data about the structure of adsorbate overlayers on top of the substrate can also be obtained by this technique (see other papers in this volume), if the atoms are strongly adsorbed. What to

do, however, with the sluggish adsorbed species, solvent, and any other molecules moving in the vicinity of or under the tip? They remain invisible in the conventional scanning probe methods, contributing to the noise. Noise in STM current is something that one usually tends to depress, get rid of or subtract as a factor obscuring the main signal. However, an alternative strategy may be followed, based on the theory of elastic tunneling including the current fluctuations due to motions of particles between the tip and the sample [1]. The latter suggests new ways for the study of local dynamics of weakly adsorbed species on metallic substrates. The ideas of the program, „Noise: from an enemy to a friend", are discussed in this paper.

The second question we tackle here is how to restore the true shape of the adsorbate nanometer-scale clusters from the images drawn by a tip that is not atomically sharp.

These „exotic" ideas for nanoprobe imaging are not pure speculations: some progress in their experimental realization is briefly discussed.

2 Adatom diffusion from STM noise

Adatoms moving along the substrate surface under an STM tip introduce an additional current noise [2, 3]. Random jumps of adatoms under an STM tip and the current dependence on time, $I(t)$, caused by these jumps, are shown schematically in Fig. 1. The random function $\tilde{I}(t)$ found experimentally can be used to obtain information about the diffusion process. It is the task of the theory to connect $I(t)$ with the parameters of the system under investigation, in particular with the diffusion coefficients of adatoms and their density.

Gomer in his pioneering work [4] solved this problem (in the context of field emission spectroscopy) for the case of weak interaction between tunneling electrons and adsorbed atoms, i.e., when the current enhancement due to the appearance of an adsorbed atom under an STM tip is small. However, in experiments [2] one finds the opposite situation: the current peaks that appear when adsorbate is passing the region under an STM tip is several times larger than the stationary current. The solution of the indicated problem for the case of relatively strong electron-adatom interaction was obtained by Sumetskii et al. [5], where the strict asymptotic approach for finding the transparency of potential barriers with nonseparable variables [5, 6] and the ideas of Sumetskii and Kornyshev [1] were combined. We briefly discuss the main ideas and results of this work.

The idea of noise spectroscopy is to determine for a measured $\tilde{I}(t)$ the average current, $\bar{I} \equiv <\tilde{I}(t)>$, and also the temporary current correlation function,

$$K(t) = <\tilde{I}(t+\tau)\tilde{I}(\tau)>_{\tau} - <\tilde{I}>^2 \quad (1)$$

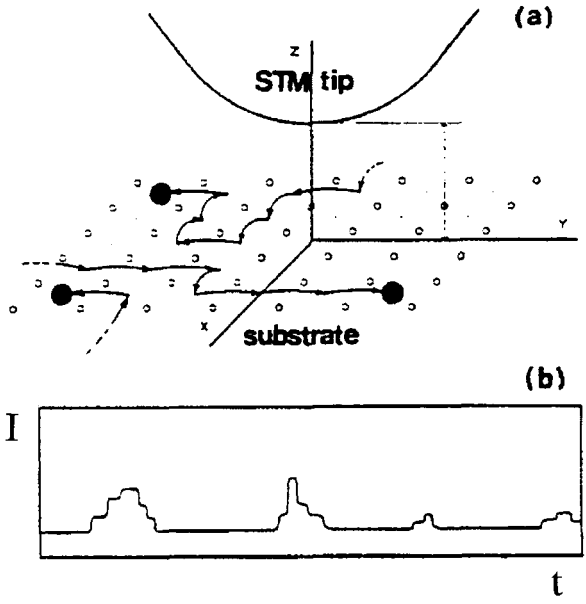

Fig. 1. (a) Random jumps of adatoms (black dots) along the substrate surface under STM tip. (b) Sketch of the current I as a function of time t caused by adatom diffusion. The peaks correspond to individual adatoms passing near the STM tip. Steps in each peak correspond to the elementary jumps of the adatom.

In the course of the measurement, the tip is positioned at a place of interest above the sample. Having obtained enough t-points to perform the time averaging, one may move to another space point in order to end up with the maps of $\bar{I}$ (**u**) and $K(t;\mathbf{u})$ [**u**≡(x,y) is the lateral coordinate along the surface]. Another important characteristic would be the current noise spectral density $S(\omega)$, the Fourier transform of $K(t)$:

$$S(\omega) = \int_{-\infty}^{\infty} dt\, e^{i\omega t} K(t) \quad (2)$$

and its spatial map $S(\omega,\mathbf{u})$

Which information, can be extracted from the measured $<I>$, $K(t)$, and $S(\omega)$? This is the question that the theory is required to solve. The answer can be given for a specified type of random process and some simplifying assumptions. The process of random diffusion was studied by Sumetskii et.al. [5] and assumptions were made that allowed expression of the introduced functions via the parameters of the tunneling gap and of the moving atoms. The central result was the analytical expression for the correlation function $K(t)$, found for a relatively small adsorbate density.

2.1 Assumption and basic equations

Having ignored the lattice structure of the flat substrate surface, the barrier between the STM tip and the substrate was modeled by a *bare* potential $V_0(\mathbf{r})$. The absolute value of electron momentum in the empty tunneling gap is then given by

$$p(\mathbf{r}) = \sqrt{2m_e\left[V_0(\mathbf{r}) - E_F\right]} \tag{3}$$

where E_F is the Fermi energy.

The adatom j, disposed in the barrier region at a point $\mathbf{r}_j$, is modeled by a potential well, $U(\mathbf{r}-\mathbf{r}_j)$, so that the potential barrier between the tip and the substrate, $V(\mathbf{r})$, is the sum of the bare barrier and the atom potentials:

$$V(\mathbf{r}) = V_0(\mathbf{r}) + \sum_{j=1}^{N} U\left(\mathbf{r} - \mathbf{r}_j\right) \tag{4}$$

Different approaches were used by Sumetskii and Kornyshev [1] in order to solve the Schrödinger equation with potential (Eq. (4)) having a rectangular form for the strong and relatively weak electron-atom interaction, $U(\mathbf{r}-\mathbf{r}_j)$, respectively. When applied to the problem of diffusion along the flat. surface, these approaches give similar results expressing $<I(t)>$ and $K(t)$ through the scattering cross-section σ of the tunneling electron on an adsorbed atom. The results of Ref. [1] were generalized [5] by means of the semiclassical perturbation theory with respect to, $U(\mathbf{r}-\mathbf{r}_j)$, to the case of an arbitrary semiclassical potential $V_0(\mathbf{r})$. For this the scattering cross-section

$$\sigma = \int du \left[\exp\left(\frac{2m_e}{\hbar} \int_{-\infty}^{\infty} dz \frac{U(\mathrm{u},z)}{p(z)} \right) - 1 \right] \tag{5}$$

was introduced, where $U(\mathbf{u},z) = U(\mathbf{r})$ and $p(z)=p(0,0,z)$ (see Fig. 1). Usually, the scattering cross-section σ has the order of atom "geometrical" cross-section $\pi b^2 \cong 10$ Å^2.

The analytical expression for the current through the tunneling gap was obtained and then averaged over the positions of atoms assuming that they move *independently*. The latter is valid for relatively low adsorbate density. Similarly to [1], the average current is then:

$$< I > = I_0 \left(1 + N_{\mathrm{sd}}\, \sigma\right) \tag{6}$$

where I_0 is the tunneling current through the empty gap, N_{ad} is the density of adatoms, and $N_{\mathrm{ad}}\sigma \cong N_{\mathrm{ad}} b^2 << 1$. Thus, adatoms in the low coverage limit introduce only a small correction to the average current.

The basic quantity which determines surface diffusion is the adatom distribution function $f(\mathbf{u}_0, \mathbf{u}_1, t)$, i.e., the density of probability that the atom which is initially at a point $\mathbf{u}_0$ appears at time t at the point $\mathbf{u}_1$. For the assumed low adsorbate density N_{ad}, the expression for the correlation function $K(t)$ through $f(\mathbf{u}_0, \mathbf{u}_1, t)$ reads [5]:

$$K(t) = \frac{N_{\mathrm{ad}}\, \sigma^2 Q^2}{\pi^2} I_0^2 \int d\mathrm{u}_0 d\mathrm{u}_1\, f(\mathrm{u}_0, \mathrm{u}_1, t) \exp\left[- Q\left(u_0^2 + u_1^2\right) \right], \tag{7}$$

where Q is the parameter characteristic of the bare gap. There is a defined system of equations for its determination [5] which we do not reproduce here. In the simplest case of a rectangular barrier when $p(\mathbf{r}) = p_0 =$ constant in the barrier region, it gives

$$Q = p_0 / d \tag{8}$$

where d is the width of the tunneling gap. For the general form of the potential barrier, one can use the following approximate expression for Q [6]:

$$Q = \left[\frac{z_m}{p(z_m)} + \int_{z_m}^{d} \frac{dz}{p(z)} \right]^{-1} \tag{9}$$

where z_m is the coordinate of the maximum of the potential barrier. This expression is good for estimates of Q but, for a fixed value of d, one would rather treat Q as the free parameter of the tip sample configuration. Equation (7) is the basis for further calculations.

2.2. Temporary current correlation function and low-frequency noise for adatom diffusion

Let us use the distribution function which corresponds to the (generally) anisotropic surface diffusion of adatoms:

$$f(\mathbf{u}_0, \mathbf{u}_1, t) = \frac{1}{4\pi|t|\sqrt{D_x D_y}} \exp\left[-\frac{(x_1 - x_0)^2}{4D_x|t|} - \frac{(y_1 - y_0)^2}{4D_y|t|} \right] \tag{10}$$

where D_x and D_y are the diffusion coefficients along axes x and y of the surface, the atomic structure of which is ignored.

The integral of Eq. (7) with distribution function in Eq.(10) gives:

$$K(t) = \frac{K(0)}{\sqrt{\left(1 + |t|/t_c^{(x)}\right)\left(1 + |t|/t_c^{(x)}\right)}}, \quad K(0) = \frac{N_{ad} Q \sigma^2 I_0^2}{2\pi} \tag{11}$$

where the two characteristic correlation times,

$$t_c^{(x)} = \frac{1}{2QD_x}, \quad t_c^{(y)} = \frac{1}{2QD_y} \tag{12}$$

are the times needed for an adatom to cross the current tube of tunneling along the x or y direction. In the case of isotropic diffusion $D_x = D_y = D$, $t_c^{(x)} = t_c^{(y)} = t_c$, and Eq. (11) reduces to:

$$K(t) = \frac{K(0)}{1+|t|/t_c} \tag{13}$$

In the opposite case of strongly anisotropic (one-dimensional) diffusion with negligible D_y,

$$K(t) \cong \frac{K(0)}{\sqrt{1+|t|/t_c^{(x)}}} \tag{14}$$

Noise spectral density (Eq. (2)) can be expressed through special functions. Since there is no problem in numerical calculation of $S(\omega)$ using Eqs. (11) and (2), we will not set it out here. We present, however, simple results for the low-frequency noise. In the case of comparable $t_c^{(x)}$ and $t_c^{(y)}$):

$$S(\omega) \cong -\frac{1}{\pi} K(0) \sqrt{t_c^{(x)} t_c^{(y)}} \ln(\omega \hat{t}_c) \quad for \quad \omega t_c << 1 \tag{15}$$

where $\hat{t}_c = \max\left[t_c^{(x)}, t_c^{(y)}\right]$.

Equation (15) diverges logarithmically. In the case of one-dimensional diffusion, the divergence is stronger: for $t_c^{(x)} << \omega^{-1} << t_c^{(y)}$ it follows $1/\sqrt{\omega}$ law:

$$S(\omega) \cong \frac{K(0)\sqrt{2\pi t_c^{(x)}}}{\sqrt{\omega}} \quad for \quad \omega t_c^{(x)} << 1, \quad D_y = 0 \tag{16}$$

In contrast to what has been assumed by Gomer [4], the electron-adatom interaction must not he small. This can change the instant current by an order of magnitude.

However, the form of time dependence of the temporary current correlation function appears to be similar to the one obtained in [4]. The difference is in the values of coefficients in these expressions.

2.3 How and where to use these formulas

The analytical results, presented above, are valid for the diffusion of adatoms independently moving along the flat substrate surface. At a first glance, the account for the lattice structure of the surface could significantly change the resulting equations. However, it is not the case when a large number of adatom sites contribute to a current peak as shown e.g., in Fig 1(a), i.e., the tip is not too sharp. Substituting the flat surface for the lattice is then somewhat similar to substituting the integral for the sum when there are many terms with a slow dependence on their number. In the case when only a few sites contribute to the current peak, Eqs. (7) and (1) could also be applied but to $<I>$ and $K(t)$ averaged over the lateral coordinates of the tip within an area larger than the surface unit cell.

The treatment of random $I(t)$ dependence found from experiment can give the average current, $<I>$, and the correlation function, $K(t)$. The current through the bare barrier, I_0, coincides with the value of *I(t) outside peaks* (see Fig. 1(b)). Therefore I_0 can be directly measured. The conventional method make it possible to determine the absolute value of wave numbers in the barrier region, and the width of the tunneling gap, d giving thereby an estimate for Q. Then the values for $\sigma^2 n$ can be found from $K(0)$; with an estimate for σ this gives the adatom density n. The values D_x and D_y might be found by treating the curve $K(t)/K(0)$, using an estimate for Q. However, this is usually too much! We do not need to estimate Q if we are interested only in the activation energies of surface diffusion, but not in pre-exponential factors, if the tip-sample configuration is temperature-independent.

2.4 Distinguishing isotropic and anisotropic diffusion

Using the data for $K(t)$ we could distinguish between isotropic and strongly anisotropic (one-dimensional) diffusion: linear t-dependence should be obtained for $1/K(t)$ or $1/K(t)^2$ for isotropic or one-dimensional diffusion, respectively. Alternatively, one may judge the kind of diffusion from the low-frequency spectra: $-\ln(\omega)$ dependence is typical of isotropic diffusion, while $1/\sqrt{\omega}$ is a fingerprint of strongly anisotropic diffusion. These simple recipes can be used to gain this valuable qualitative information.

2.5 First experimental observations

Theory [1] shows that the noise due to surface diffusion can be distinguished at the background of the fundamental thermal and shot noises. This conclusion is supported by experimental indications on oxygen diffusion on Ni manifested in STM current fluctuations [2]. The first quantitative analysis of the STM current fluctuation spectra, along the lines discussed above, has been published in [8], where the ex-situ oxygen diffusion on stepped Si(111) was studied. The method used followed exactly the ideas discussed above: the fluctuations of the tunneling current were monitored with the tip stationary over the surface and the feedback loop suspended. The time-current correlation function was analyzed with a frequency spectrum analyzer with account taken for high- and low-frequency cut-offs imposed by electronics. The very high sensitivity to the presence of oxygen atoms (the results are compared to the noise spectra on the clean, oxygen-free Si) was found, which allowed the authors to attribute the fluctuation pattern to the current spikes induced by surface diffusion. The mode of fluctuations observed seemed to follow the Fourier transform of Eq.(13) with a definite logarithmic divergence at low frequencies (Eq.(15)), indicative of *isotropic* diffusion. The problem of exact evaluation of Q did not emerge here: after obtaining $t_c \sim D$ the authors focused not on the absolute values of D but on the evaluation of the activation energy of surface diffusion using the Arrhenius plots ($\log t_c$ versus $1/T$).

Similar in-situ data in electrolytes have not been published so far, though preliminary results [9] on the diffusion events in the region of the so-called „frizzy" steps on Ag(111) [1] have been reported. Signature of $1/\sqrt{\omega}$ was found, indicative of fast anisotropic diffusion of silver surface atoms along the step edges.

A number of methods exist for the study of surface diffusion ex-situ [11-13]. The STM noise method, discussed above, has its own advantages (or shortcomings) as the local probe method. However, for the electrochemical interface it seems to be unique. (The impedance measurements [14] may not always be unambiguously interpreted, and nor do they give the „local" information about the surface.) We thus expect that the STM noise method will be widely used for in-situ study of surface diffusion, as long as the resolution of the high frequency noise measurements improves. Then the maps of local adatom diffusivity on metal electrodes will become a reality.

3 STM and molecular reorientations

We are much less optimistic, however, about the prospects, of probing in the immediate future the orientational dynamics of the solvent or molecular adsorbates from STM noise spectra. Though the model expressions for the noise spectra induced

by molecular reorientation have been obtained [15], much higher frequencies are to be probed here, and it is a very long way to it from the technique currently available. Suggestions to study possible orientational order-disorder transitions, where the critical slowing down may lead to rather slow relaxation times [16], may appear to be more realistic.

4 What is the true shape of the cluster for a given shape of the tip?

Fabrication of nano-sized metallic clusters on the surfaces and the study of their catalytic properties are a hot topic in electrocatalysis, for both tailoring new catalysts and understanding the interplay between the structure and catalytic activity (including possible mesoscopic effects) in the existing catalysts. From the dreams about the „invisible" we may thus come back to earth, and ask ourselves whether the images of these clusters represent the reality. The question is motivated by often-met differences in the shapes of the clusters prescribed by STM and by transmission electron microscopy (TEM), by miraculous double clusters, etc.

A mathematical routine has been developed which relates the true shapes of the nano-sharp tip and the nano-scaled cluster and the image of the latter [17]. In many cases the shape of the tip is poorly known. Thus, the solution of the inverse problem [17] suggests how to restore the shape of the tip from the image of the spherical cluster of a given radius, or by averaging images of different clusters distributed along the surface and having typical radius and a given dispersion. Such samples, calibrated by TEM, could be a tool to calibrate the tip.

Acknowledgments. The authors are thankful to U.Stimming and R.Vogel for useful discussions. The support given to M.S. by the Alexander von Humboldt Stiftung is gratefully acknowledged.

5 References

[1] M. Sumetskii, A.A. Kornyshev, Phys.Rev.B 48, 927 (1993).
[2] G. Binnig, H. Fuchs, E. Stoll, Surf.Sci. 169, L95 (1986).

[3] J.C. Dunphy, P. Sautet, D.F.Ogletree, O.Dabbousi, M.B.Salmeron, Phys.Rev.B 47, (1993).
[4] R. Gomer, Appl.Phys.A 39, 1 (1986).
[5] M. Sumetskii, A.A. Kornyshev, U. Stimming, Surf.Sci. 307-309, 23 (1994).
[6] M..Yu. Sumetskii, G.V. Dubrovskii, Sov.Phys.Dokl. 24(3), 171 (1979).
[7] M.Yu. Sumetskii, Sov.Phys.JETP 67, 438 (1988).
[8] M.L. Lozano, M.C. Tringides, Europhys.Lett. 30, 537 (1995).
[9] D.M. Kolb, Report on Symposium "Atomic and Molecular Perspectives in Interfacial Electrochemistry", 46 ISE Meeting, Xiamen, China, 1995.
[10] M. Dieterle, T. Will, D.M. Kolb, Surf.Sci. 327, L495 (1995).
[11] R. Gomer, Rep.Prog.Phys. 53, 917 (1990).
[12] A.G. Naumovetz, Yu.S.Vedula, Surf.Sci.Rep. 4 , 365 (1985).
[13] J.W.M. Frenken, B.J. Hinch, in He Scattering, A Gentle and Sensitive Tool in Surface Science, E.Hupke, A.M.Lahee (Eds.), Springer-Verlag, Heidelberg, 1992.
[14] Impedance Spectroscopy, J. Ross Macdonald (Ed.), Wiley, New York, 1987.
[15] A.A. Kornyshev, J. Electroanal. Chem. 376, 9 (1994).
[16] A.A. Kornyshev, I. Vilfan, Electrochim. Acta 40, 109 (1995).
[17] M. Sumetskii, A.A. Kornyshev, U. Stimming, Appl. Phys. Lett. 68, 2436 (1996).

Part II

Electrochemical Nanotechnology
In-situ Local Probe Techniques at Electrochemical Interfaces
Edited by W. J. Lorenz and W. Plieth

Roughness Kinetics and Mechanism Derived from the Analysis of AFM and STM Imaging Data

R.C. Salvarezza, A.J. Arvia

Contents

1 Introduction 58
2 The growth of a solid thin film 59
2.1 Growth models 59
2.2 The dynamic scaling theory 60
2.3 Prediction of Dynamic Scaling Parameters from Growth Models 62
3 Application to real surfaces 63
3.1 The electrochemical formation of columnar-structured gold surfaces 64
3.2 Roughness relaxation at columnar-structured gold surfaces 66
3.3 Topographic changes during silver electrodissolution in aqueous 1 M $HClO_4$ 67
4 Conclusions 69
5 References 70

Summary. The analysis of in situ and ex-situ STM and AFM images of irregular surfaces by using the dynamic scaling theory provides kinetic data of processes occurring far from equilibrium involving either the formation or disappearance of a solid phase under non-steady and stationary conditions. Parameters derived from the above-mentioned procedure can be interpreted using either continuum or atomistic models for the interface evolution. This approach has been successfully applied to investigate a number of processes such as vapor deposition, electrodeposition, chemical vapor deposition, and molecular beam epitaxis, and has been extended to the coarsening of gold crystals and silver and copper electrodissolution in acid solution by in-situ STM imaging.

1 Introduction

The topography of real solid surfaces plays an important role in defining the electronic energy distribution at surface sites, particularly when irregularities at the atomic level, i.e. in the substrate crystallography, are considered. Likewise, surface irregularities at the micrometer level, which are usually related to the surface roughness, determine the accessibility of particles interacting at surface sites. Therefore, for solid catalysts or electrocatalysts, the compromise between these types of irregularities regulates the efficiency of a solid surface for a particular reaction as they represent the quality and quantity of reaction sites, and the surface topography, respectively.

Real solid surfaces always involve some kind of irregularity. Until the advent of nanoscopy [1], i.e., scanning tunneling microscopy (STM) and atomic force microscopy (AFM), the experimental approach to the study of those irregularities was extremely limited, and consequently reliable data on the matter were available but only very scarce to compare with theories related to the formation, relaxation, and stability of irregular surfaces. In recent years, however, this situation has changed considerably as the possibility of imaging irregular solid surfaces from the nanometer scale upwards, in both real space and time, offers a new and broader approach to understanding the behavior of surfaces in materials science.

This paper covers some relevant applications of STM and AFM to investigate three main aspects of those irregular metal electrode surfaces which can be described as anisotropic surfaces. These surfaces are grown under conditions far from equilibrium, usually at rates in the range 0.1 - 300 nm s^{-1}. The growth kinetics of irregular surfaces when either a new phase is formed or a phase is eroded, the qualitative and quantitative approach to the degree of surface disorder, and the relaxation of those surfaces are the main subjects of in this report.

The approach presented in this paper is of a universal character as it applies equally to all irregular interfaces, irrespective of their composition, solid growth or solid attack procedure. Hence, its application to electrocatalysis and corrosion processes appears to be of great practical relevance as it comprises the effect of the dynamics of solids on their shape, their crystalline quality and consequently, on their electronic and mechanical properties.

2 The Growth of a Solid Thin Film

2.1 Growth Models

The growth of a solid thin film can occur under two extreme kinetic conditions involving either the neighborhood of thermodynamic equilibrium or a situation far from equilibrium.

Growth modes based on thermodynamics imply a local equilibrium at the growing surface, and mass transport processes parallel to the growing surface which are much faster than the flux of arriving particles. Growth modes observed during solid thin film growth are described by the Volmer-Weber (VW) model involving an initial nucleation and three-dimensional (3D) growth [2], the Frank-van der Merwe model (FM), which describes a monolayer-by-monolayer growth [3], and the Stranski-Krastanov (SK) model comprising the formation of the initial two-dimensional (2D) growth up to a critical thickness followed by a 3D island growth [4]. The application of these models to phase growth is, however, constrained to situations such as metal underpotential deposition and overpotential deposition of metals on metals, semiconductors and superconductor surfaces under certain conditions as described by Staikov and Lorenz (pp 13-25). Conversely, for many processes of technical relevance occurring far from equilibrium at relatively high rates, thermodynamic models had to be modified to account for their kinetic limitations.

Growth models developed for phase growth far from equilibrium comprise a flux of arriving particles which is much faster than the mass transport processes along the growing surface, such as surface diffusion and other surface-tension-like relaxation processes. Then, the stochastic arrival of depositing particles is film-growth-determining. These models can be described as discrete (atomistic) models by using molecular dynamics and Monte Carlo calculations or by continuous motion equations. Among the simplest discrete models the random deposition model, the random deposition with surface relaxation model, the ballistic deposition model and the Eden model can be considered [5, 6]. A reasonable explanation of this type of growth is provided by continuum models in which the growth of the solid film implies a competition between a roughening and a smoothening contribution. Roughening is caused by the stochastic arrival of depositing particles through a white noise of arriving particles, whereas smoothening results from surface diffusion and other surface-tension-like relaxation processes. For homodeposition processes, these concepts are considered in those motion equations proposed by Kardar, Parisi and Zhang (KPZ) [7],

Wolf and Villain (WV) [8], Villain, Lai, and Das Sarma (VLD) [9] and others [10]. The rate equations for the film growth resulting from these models are modified versions of the Langevin stochastic equation [10] for the variation with time of the interface height.

2.2 The Dynamic Scaling Theory

The concept of scaling was introduced in the field by Family and Vicsek in 1985 [10] to provide a framework for understanding fractal-like topologies of nonequilibrium surfaces.

The dynamic scaling theory describes the development of a contour ($D_{TOP} = 2$, where D_{TOP} is the topological dimension), on a flat surface of size L on the x-axis at time $t = 0$ (Fig. 1), and roughness surface growth proceeds in a single direction normal to L (z-axis) increasing in height, h, without overhangings. The instantaneous surface mean height, $\bar{h}_S(t)$, can be described by $h(x,t)$, a function of the x-coordinate and time. Then, $\omega(L,t)$, the instantaneous surface width, can be taken as a measure of the surface roughness. The value of $\omega(L,t)$ is given by the root mean square of the interface height fluctuations.

According to the scaling theory, the discreteness of the depositing material is the main factor in turning the growing surface into a self-affine fractal surface. The standard deviation of the interface height can be expressed as

$$\omega(L,t) = L^{\alpha} f(t/L^{z}) \tag{1}$$

where $f(t/L^z)$ denotes a function of the t/L^z ratio, resulting in $f(t/L^z)$ = constant for $t/L^z \to \infty$, and $f(t/L^z) = (t/L)^{\alpha/z}$ for $t/L^z \to 0$. Likewise, $z = \alpha/\beta$, where α and β are the roughness exponent and the growth exponent, respectively, and z is the coarsening exponent. Then, for small L and $t \to \infty$, eq. (1) becomes

$$\omega(L) \sim L^{\alpha} \tag{2}$$

which corresponds to a quasi-steady-state regime for the roughness development. It implies the appearance of a saturation roughness in the growth process. On the other hand, for $L \to \infty$ and $t \to 0$,

$$\omega(L,t) \sim t^{\beta} \tag{3}$$

Equation (3) represents the nonsteady-state roughness growth regime. The transition from the nonsteady- to the steady-state regime implies the existence of a transition time, t_x which is given by the proportionality

$$t_x \sim L^z \tag{4}$$

For $t > t_x$ the surface becomes a scale-invariant self-affine fractal. The value of α is related to D_{FRAC}, the local fractal dimension of the surface [11], as $D_{FRAC} = 3 - \alpha$. It should be noted that due to the fact that $\bar{h}_S$, is proportional to t, Eqs. (3) and (4) can be formulated indistinctly in terms of these variables depending on the available experimental data.

Key parameters α, β, and z can be derived from the analysis of surface profiles resulting from adequate imaging procedures. In fact, those profiles from the STM and AFM images are adequate for the dynamic scaling analysis of solid topographies because STM and AFM provide high lateral resolution 3D images in real space. For this purpose, Eqs. (1) - (4) can be applied to nanomicroscopy imaging data, taking $\omega(L,t) = \omega_{nM}(L_S,t)$, where $\omega_{nM}(L_S,t)$ represents the root-mean-square average roughness determined from image profiles scanned in either the x- or y-direction. The determination of $\omega_{nM}(L_S,t)$, the fluctuation of h over each profile size $L = L_S$ along both the x- and y-directions, allowed the calculation of α, β, and z, starting from the relationship:

$$\omega_{nM}(L_S,t) \approx \left[\frac{1}{L_S}\sum_{i=1}^{L_S}\left[\left(h(i,t) - < h_S(t) >\right)\right]^2\right]^{1/2} \tag{5}$$

and considering equations (1) -(4) for $\omega(L,t) = \omega_{nM}(L_S,t)$. In Eq. (5) $<h_S(t)>$ stands for the instantaneous average height of the surface profile of size L_S measured from either STM or AFM images in the x- and y-directions. A detailed discussion on methods for the dynamic scaling analysis of nanomicroscopy image analysis is given elsewhere [12].

2.3 Prediction of Dynamic Scaling Parameters from Growth Models

Let us consider the scaling behavior of growth models under equilibrium conditions. It is clear that for those models involving a surface which remains flat, as is the case in the FM model and in the early stages of growth in the SK model, this results in $\alpha = 0$ and $\beta = 0$ [13]. The situation is more complex for the VW and advanced stages of the SK models which yield values of α in the range $0.5 \leq \alpha \leq 0.6$ and time-dependent values of β as the growth results in these cases from the coalescence of islands.

Surface scaling parameters for a number of nonequilibrium atomistic models have also been established [6, 10]. Continuum equations for the surface motion have to be used to find a solution for discrete models. Thus, for ballistic deposition [14] and the Eden model [15] the interface saturates, resulting in $\alpha = 1/2$ and $\beta = 1/3$ for $D_{TOP} = 2$, and $\alpha \approx 0.35$ and $\beta \approx 0.21$ for $D_{TOP} = 3$. Conversely, from the random deposition model $\beta = 1/2$ and, since the correlation length is always zero, the interface does not saturate and, therefore, α is not defined. Depending on the rules used in the simulations, for the atomistic model including surface diffusion $\alpha = 3/2$ and $\beta = 3/7$ [6], $\alpha = 3/2$ and $\beta = 0.34$ [7] for $D_{TOP} = 2$ or $\alpha = 1$ and $\beta = 0.25$ [6] and $\alpha = 0.66$ and $\beta = 0.20$ [7] for $D_{TOP} = 3$. Furthermore, when energy barriers at step edges are included in these models, the value of β increases from $\beta \cong 0.2$ to $\beta \cong 0.5$ [16].

As far as continuous models are concerned, the simplest one is represented by the Edwards-Wilkinson equation [17] for the local rate of increase in column heights. The corresponding rate equation contains the contribution of a smoothening term and a roughening term, i.e.,

$$\partial h(x,t)/\partial t = \nu \nabla^2 h + \eta(x,t) \tag{6}$$

The first term on the r.h.s. of eq. (6) can be assimilated to a surface-tension-like smoothening term; η(x,t), the roughening term, represents the white noise in the flux of arriving particles and it would be responsible by itself for the production of a Poisson surface. For a correlated surface it results in $\langle \eta(x,t) \rangle \neq 0$, whereas for a surface formed by a random deposition mechanism it corresponds to $\langle \eta(x,t) \rangle = 0$. The solution of Eq. (6) yields $\alpha = (3-D_{TOP})/2$, $\beta = (3-D_{TOP})/4$ and $z = 2$ [10].

To account for lateral effects in the solid film growth, the KPZ equation adds a new term to eq. (6), leading to [8]:

$$\partial h(x,t)/\partial t = \nu \nabla^2 h + \lambda(\nabla h)^2 + \eta(x,t) \tag{7}$$

where ν and λ are proportionality constants which can be interpreted physically [6]. The solution of eq. (7) results in $\alpha = 0.5$ and $\beta = 0.33$ for $D_{TOP} = 2$, $\alpha \approx 0.4$ and $\beta \approx 0.25$ for $D_{TOP} = 3$, and $(\alpha + \alpha/\beta) = 2$ for all D_{TOP}.

On the other hand, according to the VW model [8] when smoothening is produced by surface diffusion, the equation of motion becomes

$$\partial h(x,t)/\partial t = -\nu_1 \nabla^4 h + \eta(x,t) \tag{8}$$

where $\eta(x,t)$ has a Gaussian distribution. Equation (8) leads to $\alpha = 3/2$ and $\beta = 3/7$ for $D_{TOP} = 2$ and $\alpha = 1$ and $\beta = 0.25$ for $D_{TOP} = 3$.

The VLD model [10] included a surface diffusion term in Eq. (7). Thus, it follows that

$$\partial h(x,t)/\partial t = -\nu_1 \nabla^4 h + \lambda_1 \nabla^2 (\nabla h)^2 + \eta(x,t) \tag{9}$$

where ν_1 and λ_1 are proportionality constants. Equation (9) leads to $\alpha = 3/2$ and $\beta = 0.34$ for $D_{TOP} = 2$ and to $\alpha = 2/3$ and $\beta = 1/5$ for $D_{TOP} = 3$.

Values of α, β, and z are suitable quantities for the comparison of experimental data and theoretical models. Therefore, the preceding summary of the dynamic scaling approach provides a way for determining the dominant mechanism for the rough surface growth mode, irrespective of whether the development of the rough surface results from the accumulation or the dissolution of the solid phase.

The equations derived from the dynamic scaling theory are valid for self-affine and self-similar surfaces. Accordingly, the theory provides information about fractal properties and growth mechanisms of rough surfaces.

3 Application to Real Surfaces

Changes in solid surfaces occur either during the formation of a new phase as in vapor deposition, molecular beam epitaxis, chemical vapor deposition and metal electrodeposition, or during a phase disappearance as is the case of metallic corrosion and material erosion. Similar changes occur in roughness relaxation, a process which plays a relevant role in establishing, for instance, the lifetime of solid catalysts.

Practical growth of solid material phases, such as by vapor phase metal deposition, electrodeposition, etc., occurs away from the idealized thermodynamic models.

3.1 The Electrochemical Formation of Columnar-structured Gold Surfaces

Representative 1000x1000 nm^2 ex-situ STM images of rough gold films of different average thicknesses ($\bar{h}_s$) show the development of a typical columnar structure (Fig.1(a)-(c)) [18]. These films are produced by electroreducing, at 100 nm s^{-1} in 0.5 M H_2SO_4 at 298 K, gold oxide layers formed on gold plates by anodization at 2.4 V (vs a saturated hydrogen reference electrode) in the same acid solution. Columnar-structured gold film surfaces exhibit a self-affine fractal behavior as the result of the type of aggregation process involved in the oxide layer electroreduction [19].

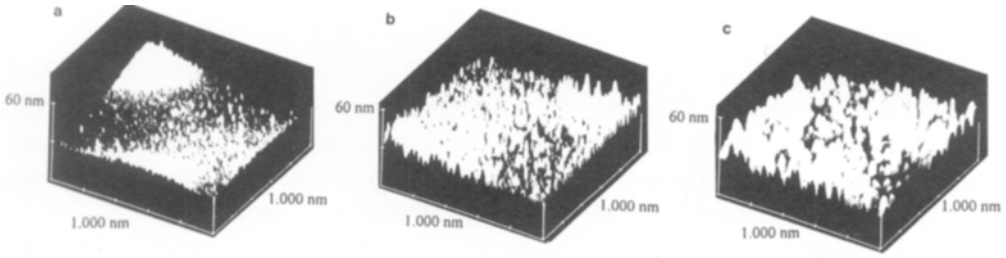

Fig. 1. Constant current (1000x1000 nm^2) 3D STM images of gold electrodeposits grown at 100 nm s^{-1} on gold at $T = 298$ K. (a) $\bar{h}_S(t) = 35$ nm; (b) $\bar{h}_S(t) = 175$ nm; (c) $\bar{h}_S(t) = 318$ nm.

Data resulting from STM imaging were plotted as log ω_{nM} vs. log $<L_S>$ (Fig.2(a)) and log ω_{nM} vs. log $\bar{h}_S(t)$ (Fig.2(b)) to derive the value of exponents α and β included in Eqs. (2) and (3). These plots exhibit two sets of exponents, each one of them being valid within a certain scale length L_S, i.e., the microscope imaging resolution. Those plots also define a crossover point at a certain critical distance which coincides with d_s, the average size of the column cross-section. Thus, when $L_S < d_S$, it results in $\alpha(I) = 0.90 \pm 0.06$ and $\beta(I) = 0.31 \pm 0.06$, whereas for $L_S > d_S$, it yields $\alpha(II) = 0.49 \pm 0.05$ and $\beta(II) = 0.51 \pm 0.08$.

It should be noted that for $L_S < d_S$, the value of α is close to those predicted by atomistic models incorporating surface diffusion, and a continuum model described by

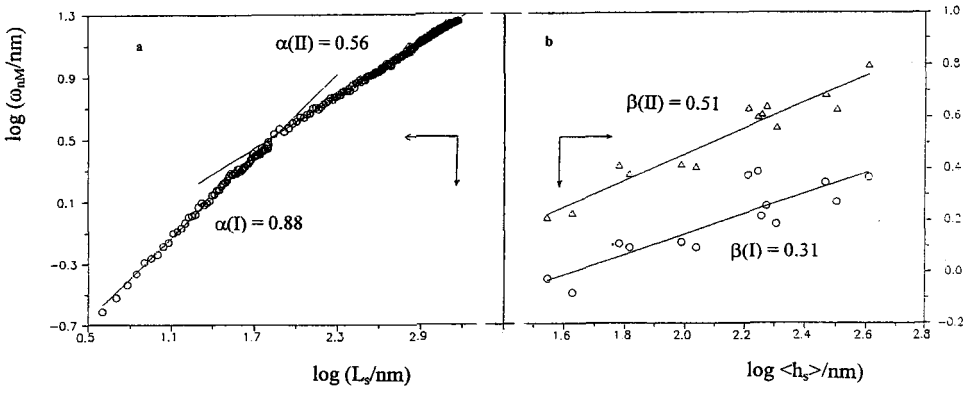

Fig. 2. (a) Log ω_{nM} vs log L_S plot. Gold electrodeposits with $\bar{h}_S(t)$ = 886 nm. (b) log ω_{nM} vs log $\bar{h}_S(t)$ plot. (o) L_S = 35 nm; (Δ) L_S = 398 nm.

Eq. (8). The value of β is, however, slightly greater than the predictions of these models. This difference is presumably caused by nonlocal effects produced by the electric field operating at the growing interface [20]. Likewise, the difference in the value of β leads to $z \approx 3$, and a coarsening exponent $1/z \approx 0.33$.

The set of exponents obtained for $L_S > d_S$ involve crystal-crystal interaction terms which characterize solid grained-structures. These terms are not considered in the physical background representing any of the available growth models. Theoretical work is in progress to provide a deeper understanding of these exponents [21]. Nevertheless, the main conclusions derived from these results are the existence of two distinguishable domains of roughness at columnar-structured metal electrodes, and the dominant participation of surface atom diffusion in the smoothening of the columnar surface.

3.2 Roughness Relaxation at Columnar-structured Gold Surfaces

The kinetics of particle coarsening was followed by applying the dynamic scaling analysis to sequential in-situ and ex-situ STM images of columnar-structured Pt and Au films on conducting substrates.

Columnar-structured Au films, prepared as described in section 3.1, were immersed in NaCl-containing 0.5 M aqueous H_2SO_4 at 298 K and held at a constant potential in the double-layer region of gold. In this potential region, the change in topography (Fig. 3) is mass conservative as neither corrosion nor deposition occurs [22]. Then, large anisotropic gold particles grow at the expense of small ones.

The value of d_S, the size of a growing grain in either the x- or y-direction, respectively, increases as $d_S \propto t^{1/z}$ with $z = 1/4$, as predicted by a surface diffusion controlled coarsening mechanism [8]. Furthermore, the coarsening of gold particles occurs without a significant change in the standard deviation of the gold electrodeposit height. It should be noted that the value of z is the same as that observed for the growth of vapor-deposited gold films at the same temperature [23], although slightly lower than that observed during the growth of these particles [18] under the influence of the electric field between the column tip and the sample.

According to the topographic anisotropy, direction-dependent values of D_S, the surface diffusion coefficient of gold atoms in contact with the acid solution, were derived from the relationship:

$$d_S = (2a^4 \gamma D_S / kT)\, t^{1/4} \qquad (10)$$

where a is the lattice constant, γ is the local surface tension, D_S is the surface diffusion coefficient of the particle, k is the Boltzmann constant and T is the absolute temperature.

The average value in the preferred growth direction is $D_S \approx 10^{-13}$ cm^2 s^{-1}, a figure which is in agreement with previously reported data derived exclusively from electrochemical measurements in aqueous acid solutions at room temperature [24].

These results demonstrate that the mechanism of roughness relaxation at column-structured metal surfaces operates under a surface diffusion control. The anisotropy of coalescence is consistent with an anisotropic surface diffusion process on smooth grains ($\alpha = 1$).

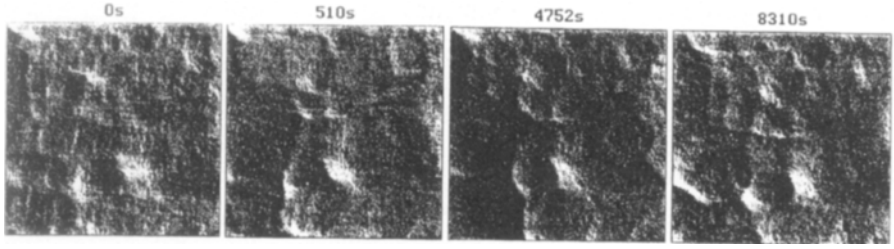

Fig. 3. (a) 100x100 nm^2 in-situ STM images of gold electrodeposits obtained at different t in 0.5 M H_2SO_4 + 0.1 M NaCl. The applied potencial is 0.6 V. 298 K.

3.3 Topographic Changes during Silver Electrodissolution in Aqueous 1 M $HClO_4$

Topographic changes occur at the terrace domain of a silver single crystal immersed in aqueous 1 M perchloric acid at 298 K, and held at constant electrodissolution current density (j) and temperature. These changes can be followed by in-situ STM sequential imaging [25].

At low values of j ($j < 15$ μA cm^{-2}) silver electrodissolution proceeds at step edges (Fig. 4) without roughening (Fig. 5). In this case, the dynamic scaling analysis of STM profiles results in $\beta = 0$, a figure which is consistent with a layer-by-layer dissolution mechanism as established by the FM model [3].

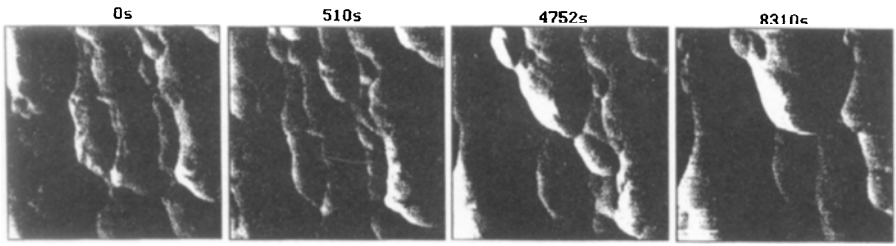

Fig. 4. 85 x 85 nm^2 in-situ STM images obtained during the electrodissolution of silver in 1 M $HClO_4$ at constant current density 4 μA cm^{-2} at 298 K.

Conversely, for $j > 15$ μA cm^{-2}, the silver topography becomes rougher (Fig. 6) to attain the steady roughness regime after a critical time (Fig. 5). In this case, according to the dynamic scaling analysis of STM images, the dissolving metal surface can bedescribed as a self-affine fractal surface with $\alpha = 0.90 \pm 0.06$, and $\beta = 0.36 \pm 0.08$. The value of α, which is in accordance with those expected from growth models including surface diffusion [8], confirms previous conclusions about the electrodissolution mechanism of silver in acid aqueous solutions derived from electrochemical kinetic data, in which a relevant role was played by the surface diffusion of silver atoms at low overpotential.

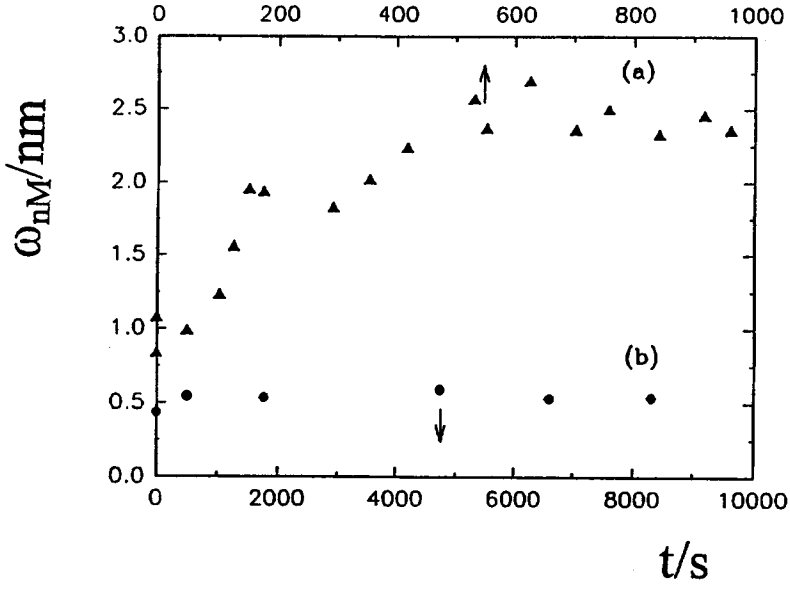

Fig. 5. ω_{hM} vs. t plots for silver electrodissolution. (a) Constant current density 30 μA cm^{-2}. (b) Constant current density 4 μA cm^{-2} at 298 K.

On the other hand, the fact that the experimental value of β is higher than $\beta = 0.20$-0.25 as expected for a simple surface diffusion model [8], may reflect again either the influence of the electric field on surface diffusion processes for metal atoms at the electrochemical interface [20] or the existence of energetic barriers at step edges [16] enhancing the growth of instabilities normal to the electrode surface. Presumably, the presence of additional contributions to the energy barriers at step edges could account

for the dependence of D_S on the potential applied to the working electrode, as in the case of roughness relaxation of column-structured gold electrodes in acids [24].

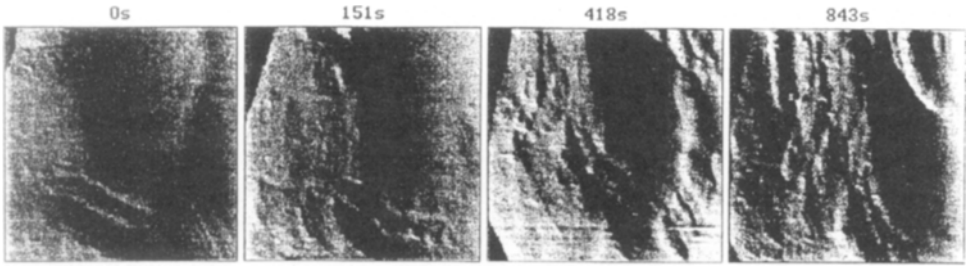

Fig. 6. 85x85 nm^2 in-situ STM images obtained during the electrodissolution of silver in 1 M $HClO_4$. Constant current density 30 $\mu A\ cm^{-2}$ at 298 K.

4 Conclusions

In many cases electrochemical processes such as metal electrodeposition, roughness relaxation and metal corrosion develop self-affine fractal surfaces rather euclidean surfaces due to the presence of non-equilibrium conditions. When this type of surface is formed thermodynamic models can not be strictly applied. The roughness and growth exponents obtained by the dynamic scaling applied to STM imaging give relevant information about processes operating during the interface evolution. Advances in the development of theoretical models related to non-equilibrium growth processes are needed to attain a more complete description of this type of processes.

Acknowledgment. This work was finacially supported by the Consejo Nacional de Investigaciones Científicas y Técnicas (CONICET) of Argentina.

5 References

[1] R.J. Behm, N. García, H. Rohrer (Eds.), Scanning Tunneling Microscopy and Related Methods, NATO ASI Series E, Applied Sciences, Vol. 184, Kluwer Academic Publishers Dordrecht, 1990.
[2] M. Volmer, A. Weber, Z.Phys.Chem. 119, 277 (1926).
[3] F.C. Frank, J.H. van der Merwe, Proc. R. Soc. London A 198, 205 (1949).
[4] J.N. Stranski, L. Krastanov, Ber. Akad. Wiss. Wien 146, 797 (1938).
[5] C. Godreche (Ed.), Solids far from Equilibrium, Cambridge University Press, Cambrige, 1992.
[6] A.L. Barabási, H.E. Stanley, Fractal Concepts in Growth Phenomena, Cambridge University Press, Cambridge, 1995.
[7] M. Kardar, G. Parisi, Y.C. Zhang, Phys. Rev. Lett. 56, 889 (1986).
[8] D. Wolf, J. Villain, Europhys. Lett. 13, 389 (1990); J. Villain, J. Phys. I 1, 19 (1992).
[9] Z.W. Lai, S. Das Sarma, Phys. Rev. Lett. 66, 2348 (1991).
[10] F. Family, T. Vicsek (Eds.), Dynamics of Fractal Surfaces, World Scientific, Singapore, 1991; F. Family, Physica 168A, 561 (1990), and references therein.
[11] B. Mandelbrot, *The Fractal Geometry of Nature*, Freeman, San Francisco, 1982.
[12] L. Vázquez, R.C. Salvarezza, P. Herrasti, P. Ocón, J.M. Vara, A.J. Arvia, Chaos, Solitons and Fractals 6, 569 (1995).
[13] W.M. Tong, R. Stanley Williams, A. Yanase, Y. Segawa, M.S. Anderson, Phys. Rev. Lett. 72, 3374 (1994).
[14] P. Meakin, P. Ramanlal, L.M. Sander, R.C. Ball, Phys. Rev. A 34, 509 (1986).
[15] M. Eden, in Proc.of the 4th Berkeley Symposium on Mathematical Statics and Probability, F. Neyman (Ed.), University of California Press, Berkeley, 1961.
[16] Z. Zhang, J. Decht, H. Metiu, Phys. Rev. B 48, 4972 (1993); H.J. Ernst, F. Fabre, R. Folkerts, J. Lapujoulade, Phys. Rev. Lett. 72, 112 (1994).
[17] S.F. Edwards, D.R. Wilkinson, Proc. R.Soc. London A 381, 17 (1982).
[18] L. Vázquez, R.C. Salvarezza, P. Herrasti, P. Ocón, J.M. Vara, A.J. Arvia, Phys. Rev. B 52, 2032 (1995).
[19] M.E. Vela, S.L. Marchiano, R.C. Salvarezza, A.J. Arvia, J. Electroanal. Chem. 388, 133 (1995).
[20] A. Iwamoto, T. Yoshinobu, H. Iwasaki, Phys. Rev. Lett. 72, 4025 (1994).
[21] E.V. Albano, R.C. Salvarezza, A.J. Arvia, in preparation.
[22] G. Andreasen, M. Nazzarro, J. Ramirez, R.C. Salvarezza, A.J. .Arvia, J. Electrochem. Soc. 143, 466 (1996).

[23] L. Vázquez, R.C. Salvarezza, P. Herrasti, P. Ocón, J.M. Vara, A.J. Arvia, Surf. Sci. 345, 17 (1996).

[24] M.P. García, M.M. Gómez, R.C. Salvarezza, A.J. Arvia, J. Electroanal. Chem. 347, 237 (1993).

[25] M.E. Vela, G. Andreasen, A. Hernández Creus, R.C. Salvarezza, A.J. Arvia, Phys. Rev. B 53, 10217 (1996).

Electrochemical Nanotechnology
In-situ Local Probe Techniques at Electrochemical Interfaces
Edited by W. J. Lorenz and W. Plieth

Electrodes with a defined mesoscopic structure

U. Stimming, R. Vogel

Contents

1	Introduction	73
2	Average mesoscopic properties	74
3	Local mesoscopics properties	79
4	Electrochemical nanotechnology	82
5	Conclusions and future prospects	84
6	References	85

Abstract. The possibility of characterizing the real-space morphology of electrode surfaces on the nanometer scale using scanning probe microscopy (SPM) gives access to the influence of mesoscopic structures on electrochemical processes. Various possibilities of creating defined mesoscopic structural properties of electrode surfaces are discussed. Special emphasis is put on structure and behavior of supported metal clusters, which can be regarded as model systems for electrocatalysts used in technological processes.

1 Introduction

The influence of the surface structure of electrodes on electrochemical processes has been a central topic of basic electrochemical research in recent years. Advances were mainly achieved due to the utilization of structurally defined electrodes, usually low-index single-crystal surfaces, and to the development of surface-sensitive analytical techniques for the in-situ characterization of electrodes [1, 2]. Most of the advances can be attributed to the application of the latter, the new techniques, to the former, namely the well-defined surfaces. This approach has proven very powerful and its

exploitation is still in the beginning, but it is already clear that structural effects on electrochemical processes in general can not be related to the local atomic scale order alone, but are also to a large extent affected by mesoscopic structural properties. Control of the mesoscopic structural properties is required in order to elucidate their influence on electrochemical reactivity.

The atomic surface order is described in terms of a simple unit cell and techniques for the preparation of surfaces with defined atomic order are well established. The description of mesoscopic structures is not as straightforward; for a single-crystal surface mesoscopic properties can be, e. g., terrace widths and step densities, for dispersed electrodes the size and distribution of particles. Real-space information under in-situ electrochemical conditions is required for the characterization of such mesoscopic properties. This information can only be derived from the application of scanning probe techniques, which were introduced to electrochemistry in the mid-1980s and give high-resolution real-space images of electrode surfaces under in-situ electrochemical conditions.

We want to focus on the modification of substrate electrodes with metal particles of mesoscopic dimensions and their characterization with STM. For such chemically heterogeneous surfaces, the chemical information complementing the structural investigation is required. The different chemical compositions of the constituents, namely the substrate and the deposit, is often manifest in different characteristic mesoscopic structures of both. Thus, although the chemical selectivity of STM is rather poor, this chemical information can often be concluded from the mesoscopic structure.

2 Average mesoscopic properties

A structural surface characterization with high resolution is always restricted to a small fraction of the total surface area. The question of how representative the characterized fraction is for the whole sample is thus crucial. The utilization of well-defined substrate electrodes facilitates the interpretation of local structural information to a large extent. Starting from well-defined substrate surfaces, composite model electrodes with defined mesoscopic structures can be prepared. Out of the various approaches two examples will be discussed, one describing the nanometer-scale modification of Pt(111) surfaces by ruthenium, the other the modification of conductive surfaces by nanometer-sized particles.

The first example addresses ruthenium-modified platinum electrodes, which show an enhanced electrochemical activity for the oxidation of H_2/CO gas mixtures as compared with pure platinum [4, 5]. This makes them interesting electrocatalysts for low-temperature fuel cell applications. Here we discuss the mesoscopic structure of

Ru/Pt(111) electrodes only; the catalytic implications are described elsewhere [6]. The current efficiency of Ru deposition from $RuCl_3$ solutions is low. This allows an easy tuning of the amount of deposition in the submonolayer regime. The amount of electrodeposited Ru cannot be directly derived from integration of the charge during the deposition process (low current efficiency), but a phenomenological approach was developed for its determination by potentiodynamic electrodissolution of the previously deposited Ru [4]. From this approach, which can only be applied to polycrystalline platinum substrates, a relation between coverage and deposition potential was derived. Deposition for 5 min on polycrystalline platinum from a 5 mM solution of $RuCl_3$ in 0.1 M H_2SO_4 resulted in coverages of $\theta \approx 0.3$ and $\theta \approx 0.7$ of a monolayer at 0.6 V and 0.3 V (RHE), respectively.

STM results related to these conditions are shown in Fig. 1. The electrode surfaces for this sequence were prepared in a standard electrochemical glass cell then, protected with a drop of water, transferred to the STM cell. Figure 1(a) shows in a blank experiment the surface of the Pt(111) electrode without any Ru deposit. The terrace structure of the (111) surface is clearly recognized. The islands on the terraces can be attributed either to insufficient flame annealing of the surface or to contamination during the transfer of the electrode. Fig. 1(b) and (c) show two examples of Ru-modified Pt(111) electrodes. In Fig. 1(b), a considerable density of islands is observed on the surface. The islands are between 2 and 5 nm in diameter and their height is close to the height of a monatomic step of the substrate. From the evaluation of several STM images it was derived that the coverage of the surface with islands varies between 0.25 and 0.38. This is consistent with a Ru coverage of 0.3, which was determined by electrochemical techniques for a polycrystalline platinum electrode subjected to the same deposition conditions. These results confirm the approach of Watanabe and Motoo [4], and they allow the conclusion that the observed islands represent the Ru deposit, which was recently also supported by X-ray surface diffraction data. In addition, it indicates that the deposition of Ru is comparable for polycrystalline platinum and Pt(111). In order to cross-check the results, a Ru-modified Pt(111) electrode was prepared under conditions, where a coverage of $\theta \approx 0.7$ is expected. An image of this surface is shown in Fig. 1(c). The surface is densely covered with structures similar to those in Fig. 1(b). The coverage is, however, too high for a detailed evaluation, but the image is in reasonable agreement with a coverage of $\theta \approx 0.7$.

The second example concerns an important class of technical electrodes which are based on dispersed catalyst particles. For those, the relation between structure and reactivity is important [7], but its elucidation is hampered by the problem that reactivity is usually referred to a macroscopic sample while the structural characterization gives local information. For fundamental investigations it would be

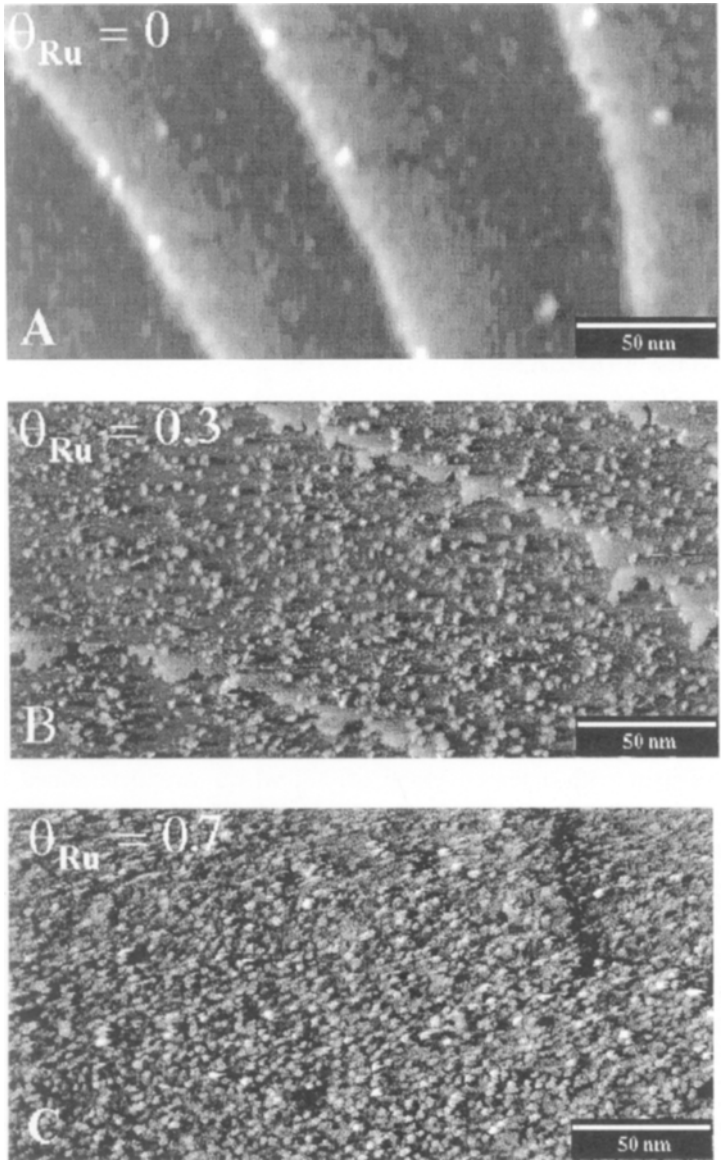

Fig. 1. Ru-modified Pt(111) electrodes in 0.1 M $HClO_4$ at $E = 0.5$ RHE, $E_t = 0.8$ V, $I_t = 0.4$ nA (A) without Ru deposit, (B) after Ru deposition at 0.6 V, (C) after Ru deposition at 0.3 V; deposition time 5 min for (B) and (C).

desirable to control the average mesoscopic structure of such electrodes, i.e., to control the size and distribution of the catalyst particles on the substrate surface.

Recently a technique for the preparation of catalyst particles with a narrow size distribution was developed [8], yielding colloidal metal clusters stabilized by a shell of surfactants. By adsorbing these clusters on substrate surfaces, model electrodes for dispersed electrocatalysts can be prepared [9]. Figure 2 compares two samples prepared from different colloidal solutions of such clusters adsorbed on a gold surface. It is evident that both samples differ significantly with respect to their mesoscopic structure.

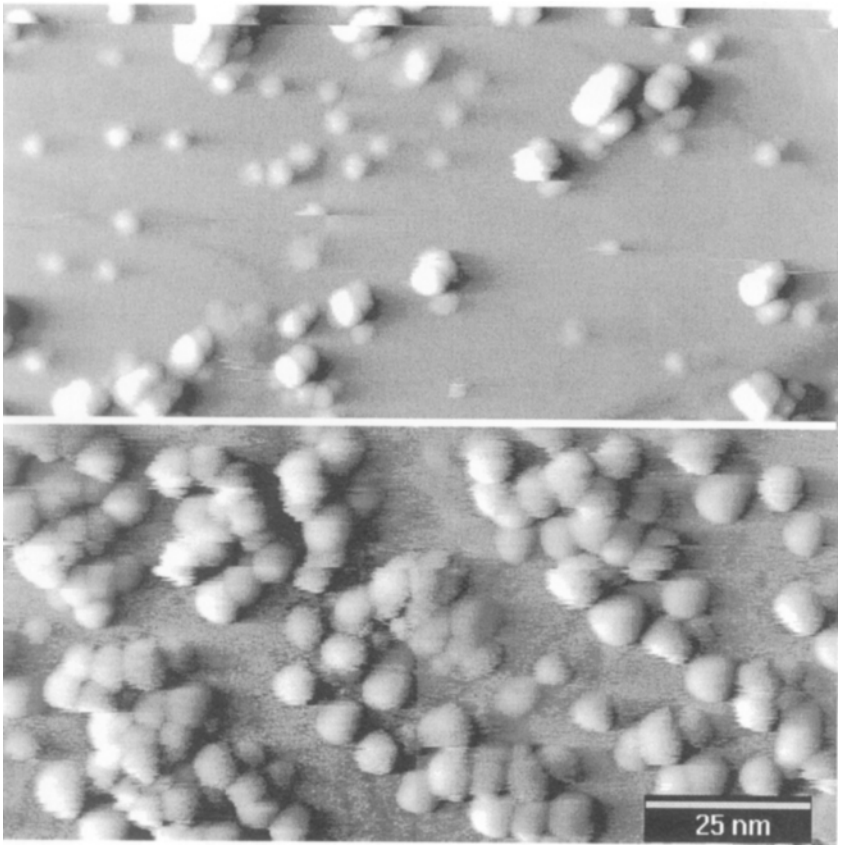

Fig. 2. Surfactant-stabilized Pd clusters on Au(111); surfactant, $N(n\text{-}C_8H_{17})_4Br$. Upper panel: average diameter d_{STM} = 4 nm. Lower panel: aveage diameter d_{STM} = 6.9 nm.

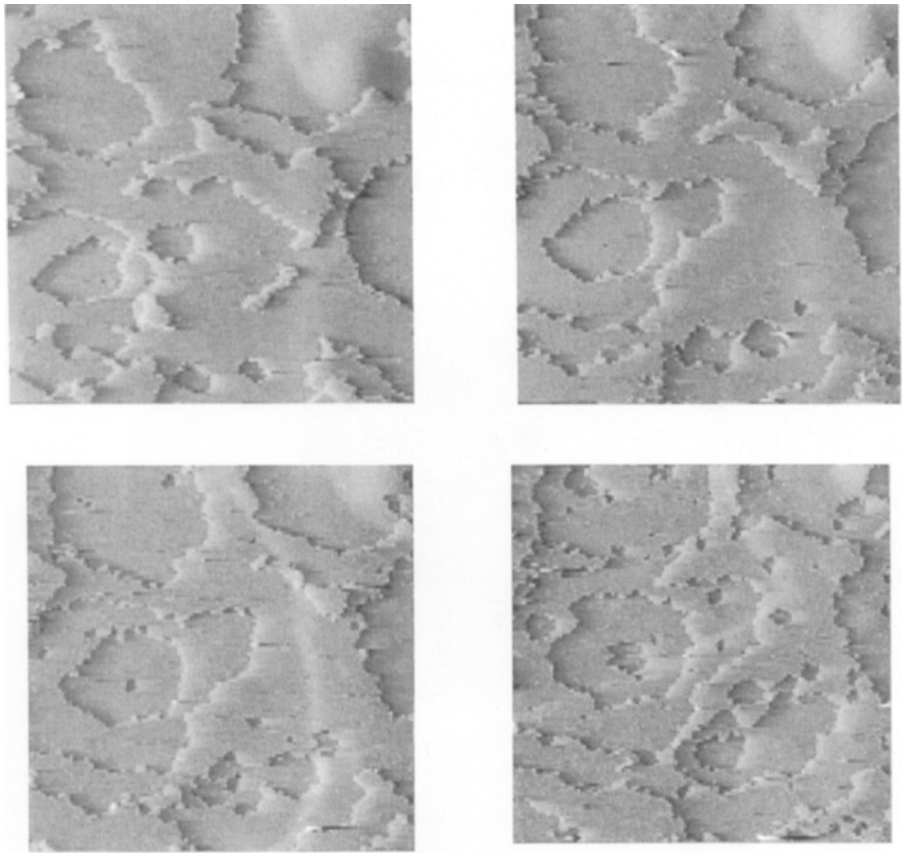

Fig. 3. HOPG oxidation in 0.1 M $HClO_4$ at 1.9 V RHE after 2, 4, 6 and 8 min (from left to right). Scan size 255 nm x 255 nm.

Similar model electrodes were prepared using highly oriented pyrolytic graphite (HOPG) as a substrate. On these electrodes, imaging of clusters was only possible when they were attached to defects, which are rather sparse on a freshly cleaved HOPG surface. There was some evidence that clusters were also present on the defect-free terraces, but these were apparently easily swept away by the tunneling tip [10]. Since the defect density was concluded to be crucial for such model electrodes, possibilities for its manipulation were investigated. It was found that electrochemical oxidation of the surface at high potentials increases the defect density. Since the respective process is controlled by the electrochemical potential and can be followed with STM in real

time, as shown in Fig. 3, it allows direct interactive control on the surface morphology of the substrate.

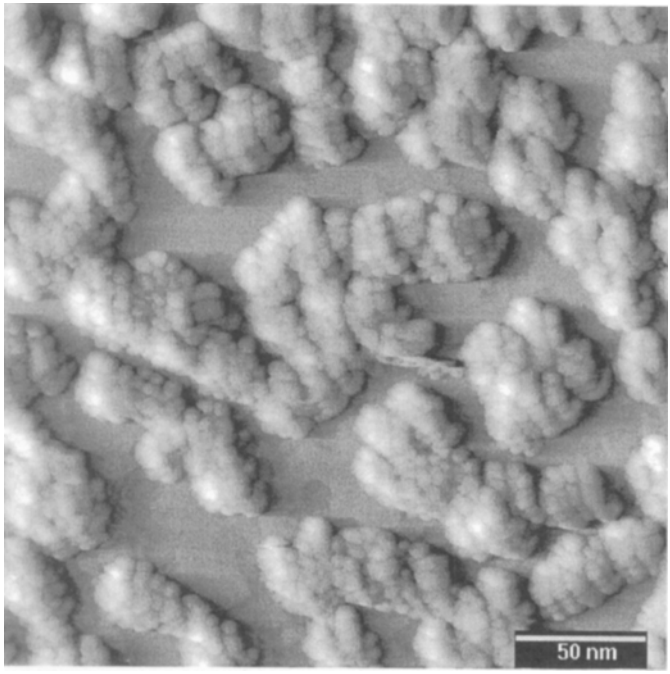

Fig. 4. Pt clusters on preoxidized HOPG; metal core diameter d_{TEM} = 4 nm; surfactant, $N(C_4H_9)_4Br$; sample prepared by electrophoretic deposition from a colloidal solution in THF at $U = 5$ V for 30 s.

On such defective surfaces the adhesion of particles is improved as compared with freshly cleaved graphite, but force interactions between tip and sample are still evident in the measurements. An example for a model electrode, which was prepared by electrophoretic deposition of a platinum colloid onto a defective HOPG surface, is shown in Fig. 4.

3 Local mesoscopic properties

The utilization of well-defined surfaces facilitates the interpretation of local structural information, but the application of STM is not restricted to such model systems. When irregular surfaces are investigated with STM, the local character of the measurement

has to be emphasized and a clear-cut distinction between the well-characterized local morphology and the average surface morphology has to be made.

An example for the variation of the local topography is given in Fig. 5, which shows two images of a flame-annealed polycrystalline gold electrode. Figure 5 a shows a region which exhibits a smooth hill-and-valley structure, while another region, fig. 5 b, shows pronounced crystalline features with monatomic steps, atomically smooth terraces, and islands of monatomic height[11]. Both kinds of topography were quite often observed on flame annealed gold foils.

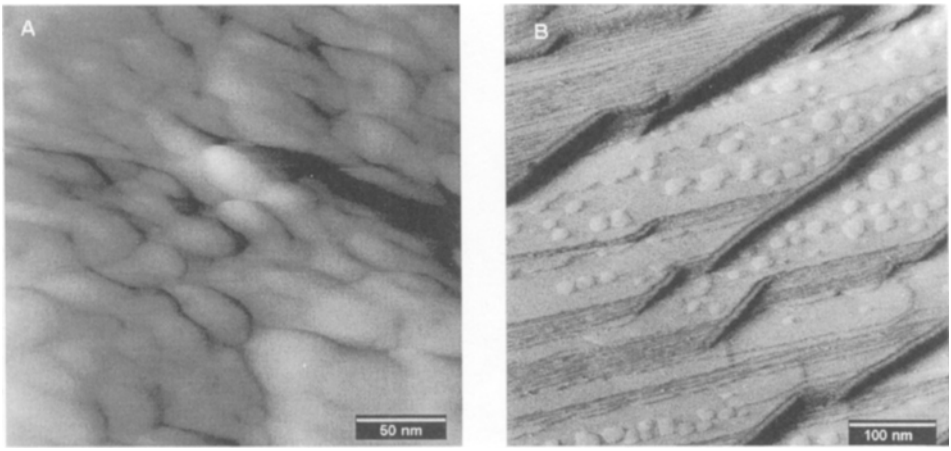

Fig. 5. Two different types of morphology of the same flame-annealed polycrystalline gold electrode.

This example is intended to highlight the scaling problem, which is inherent in the correlation of structure and reactivity. The structural characterization is performed on an almost negligible fraction of the sample surface while the reactivity usually refers to the integral sample surface and is an average quantity. In general, mesoscopic structural information can thus not be correlated with the overall electrochemical behavior of an electrode in a straightforward way. STM allows, however, to probe the real local electrochemical behavior of a real sample area with well-characterized mesoscopic topography.

This is visualized in Fig. 6, which shows the bulk deposition of copper on a flame-annealed polycrystalline gold electrode. The experiment was performed on an approximately 100 nm-wide, rather well-ordered microfacet, which is bordered by relatively rough regions of the sample surface. The orientation of the facet is presumably (100), as indicated by the rectangular shapes of islands and supported by

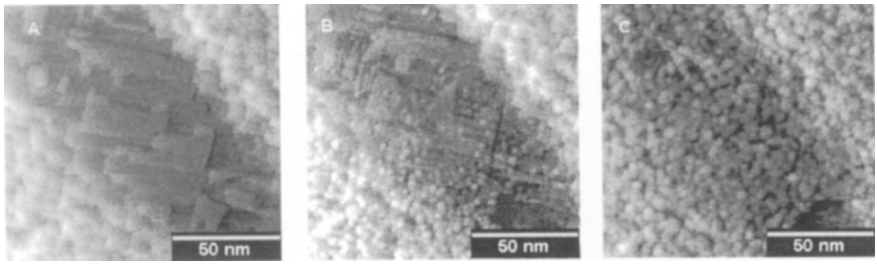

Fig. 6. Copper deposition on polycrystalline gold in 0.01 M $HClO_4$ + 0.1 M $NaClO_4$ + 0.1 mM Cu^{2+} (A) E = 0.1 V vs. Cu/Cu^{2+} in the range of UPD, (B) E = -0.1 V in the range of bulk deposition, and (C) E = -0.1 V during continuing bulk deposition

more detailed investigations of the substrate surface [11]. The first image of the sequence, Fig. 6 A, was recorded at a potential of +0.1 V versus the Cu/Cu^{2+} equilibrium potential, where a monolayer of copper is adsorbed on the surface due to the so-called underpotential deposition (UPD). Upon lowering the potential into the region of bulk-copper deposition, E = -0.1 V, after an induction period of approximately 20 s the formation of copper nuclei becomes visible (Fig. 6(B)). The nuclei are about 3 nm in diameter and one to three monolayers in height, and their density is considerably higher in the rough region than on the ordered facet. This gives rise to an inhomogeneous distribution of the deposit on the polycrystalline substrate resulting from the mesoscopic structural properties of the sample. In the course of continuing deposition, Fig. 6(C), the substrate influence is smeared out and the deposit distribution becomes homogeneous.

The dissolution of previously electrodeposited copper clusters from a polycrystalline gold electrode is addressed in Fig. 7. The particles are rather large, ranging from 10 to 50 nm in diameter and 0.5 to 5 nm in height. From a macroscopic point of view a continuous shrinking of the clusters would be expected under the given experimental conditions. Such a continuous shrinking has indeed been observed for cases where the distance between clusters is large [12]. For more densely packed arrangements, however, the size of an individual cluster remains more or less stable for a certain time and then decreases rather fast (on the time scale of the imaging process) until the cluster vanishes. For an agglomerate of clusters this individual behavior averages to an approximately exponential decrease of the number of clusters with time. For the measurement, which is represented in Fig. 7 by six out of a sequence of 25 images,

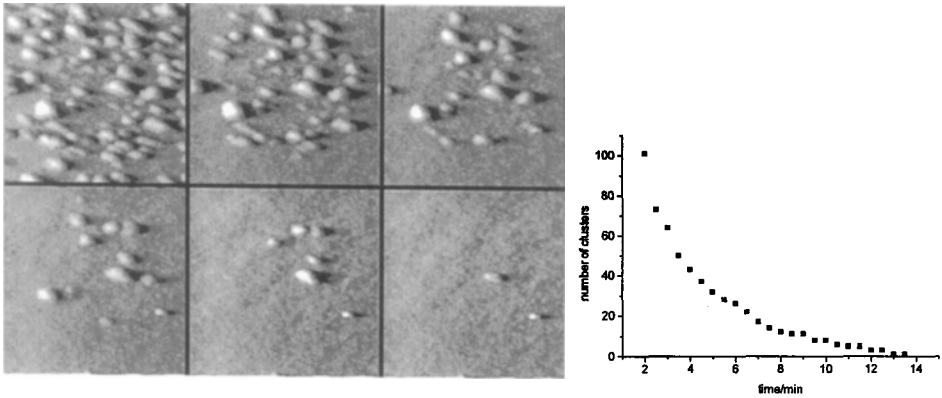

Fig. 7. Dissolution of copper from a polycrystalline gold electrode at $E = +25$ mV vs. Cu/Cu^{2+} in 0.01 M $HClO_4$ + 0.1 M $NaClO_4$ + 10 mM Cu^{2+}. (A) STM images; time interval between images: 3 min. Image size: 255 nm x 255 nm. (B) Number of particles as a function of dissolution time.

roughly 50% of the clusters disappear every two minutes.

The above examples of copper deposition and dissolution represent local experiments. They address the deposition on one section of the substrate and the dissolution of a specific distribution of copper clusters. These local processes can be related to the overall process, since information on the latter is available from the Faradaic current measured in the course of an experiment. Significant discrepancies between local and average kinetics are often but not always observed [13, 14]. This reflects the stochastic nature of electrochemical kinetics on the mesoscopic scale, but there are also systematic deviations, which indicate that the local kinetics may be influenced by the tunneling tip. The elucidation of this influence, which has up to now only been addressed qualitatively, is crucial for the understanding of electrochemical processes on the mesoscopic scale.

4 Electrochemical nanotechnology

In addition to analytical applications for monitoring surface structures and dynamics STM can also be used as a tool for the deliberate modification of electrode surfaces on the mesoscopic scale. By applying appropriate signals to an STM tip, local metal-deposition reactions can be induced from metal-ion-containing solutions [12, 15, 16]. As an example, Fig. 8 shows a platinum particle on an HOPG surface, which was

produced by pulsing the voltage between tip and sample in a Pt^{4+}-containing solution. The image thus represents a highly defined model electrocatalyst, since there is only one catalyst particle with known morphology on the electrode. In principle, the reactivity of the particle could be measured by conventional electrochemical techniques, but a reaction which is ten orders of magnitude faster on platinum than on graphite would be required to compensate the ratio of the surface areas of substrate and catalyst. Nevertheless this approach is supposedly realistic: by preparation of arrays of catalyst particles the surface area of the catalyst can be increased in a controlled way, and the application of scanning electrochemical microscopy (SECM) [17] for the investigation of the reactivity can reduce the influence of the substrate area to a large extent. Experiments in this direction are, however, still in their initial stages.

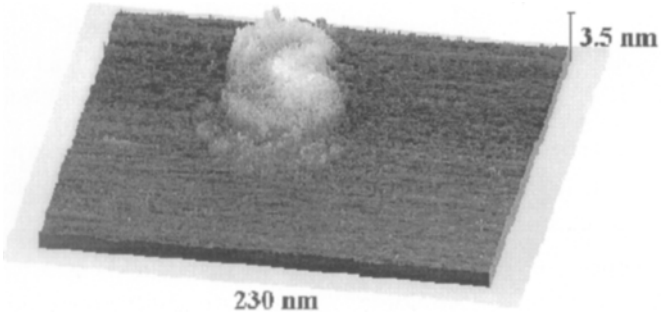

Fig. 8. Pt cluster on HOPG, prepared by a pulse $\Delta U = 6$ V (tip positive) for 10 μs in 1 mM H_2PtCl_6.

Interesting questions regarding material stability can also be addressed by nanotechnology. This is demonstrated in Fig. 9, which shows the dissolution of a tip-induced platinum particle on a polycrystalline gold electrode. It should be noted that the process occurs at a potential of 1.7 V (RHE), where vigorous oxygen evolution occurs on platinum electrodes. Due to this gas evolution it is impossible to image electrodes containing substantial amounts of platinum under the same conditions. For a Pt nanoelectrode like that in Fig. 9 the dissipation of the evolved oxygen occurs under hemispherical diffusion conditions with a high rate and thus does not interfere with the imaging process [18]. The local current density of the oxygen evolution reaction is supposedly several milliamps per square centimeter at the Pt nanostructure, three orders of magnitude higher than that of the substrate. The contribution of the nanostructure to the total current is, however, negligible, since it is on the scale of femtoamps whereas while the measured overall current is 5 μA.

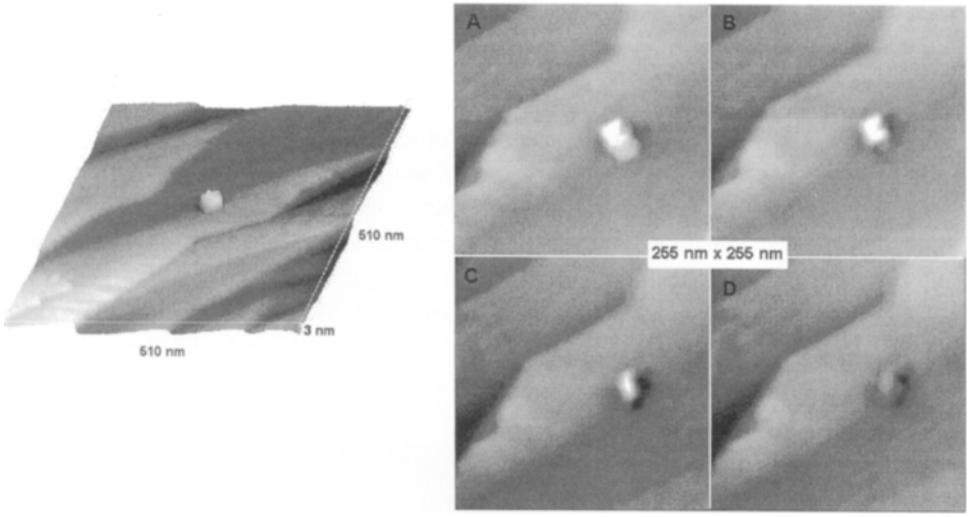

Fig. 9. Dissolution of tip-induced Pt nanostructure from polycrystalline Au substrate. The left-hand image shows the initial morphology. The sequence on the right visualizes the dissolution in 0.1 M $HClO_4$ at 1.7 V with time intervals of 5 min.

5 Conclusions and future prospects

The structural characterization of electrode surfaces on the mesoscopic scale is a prerequisite for the elucidation of mesoscopic effects on electrochemical reactivity. The most straightforward approach to access the mesoscopic scale is the application of scanning probes under in-situ electrochemical conditions. Three different applications of STM have been discussed, namely the structural characterization of model electrodes, the visualization of dynamic processes on the nanometer-scale, and the defined modification of electrode surfaces.

For the structural characterization of model electrodes it was shown that on the base of well-defined substrates, composite electrodes with defined mesoscopic structure can be prepared. Rather different methods such as low-efficiency electrochemical deposition or adsorption of colloidal particles can be employed for this purpose, and the effect on the surface morphology can be adequately characterized with STM. Knowledge of the mesoscopic surface properties facilitates the interpretation of results obtained from other techniques, e. g., conventional electrochemical methods or infrared spectroscopy [6], since these are affected by the surface structure but do not contain detailed information about the morphology.

Electrochemical processes which involve structural changes of the electrode morphology, such as deposition and dissolution reactions, can be directly monitored in real time with STM. Such measurements give a visualization of the reactivity of the sample area under investigation. Well-defined substrate surfaces are not required for this approach. In principle, the local experiment can be performed on sections of the substrate surface with interesting structural features. An important point is that the measurement may also give mesoscopic chemical information; structures, which grow and shrink at potentials negative and positive, respectively, of the Cu/Cu^{2+} equilibrium potential can be identified as copper.

The application of STM is not restricted to analytical applications, but it can also be applied for a defined modification of electrode surfaces on the nanometer scale. At present the creation and manipulation of mesoscopic structures are still at an exploratory stage, but they gain increasing attention and may soon develop to an established nanotechnology. The stability of such structures, which is crucial for technical applications, can be investigated with STM under in-situ electrochemical conditions. Regarding the correlation of structure and reactivity, a synthetic approach can be envisaged since defined distributions of defined catalyst particles are accessible.

6 References

[1] A.J. Bard, et al., J. Phys. Chem., 97, 7147 (1993).

[2] D.M. Kolb, Ber.Bunsenges. Phys. Chem., 98, 1421 (1994).

[3] B. Drake, R. Sonnenfeld, J. Schneir, P.K. Hansma, Surf. Sci., 181, 92 (1987).

[4] M. Watanabe, S. Motoo, J. Electroanal. Chem., 60, 267 (1975).

[5] P.N.Ross, K.Kinoshita, A.J.Scarpellino, P.Stonehart, J. Electroanal. Chem., 63, 97 (1975).

[6] K.A. Friedrich, K.-P. Geyzers, U. Stimming, J. Stumper,R. Vogel, First International Symposium on Proton Conducting Membranes, S. Gottesfeld (Ed.), Electrochem. Soc. Proc., Vol. 95-23, 299 (1995).

[7] S. Mukerjee, J. Appl. Electrochem. 20, 537 (1990).

[8] M.T. Reetz, W. Helbig, J. Am. Chem. Soc. 116, 7401 (1994).

[9] M.T. Reetz, W. Helbig, S.A. Quaiser, U.Stimming, N.Breuer, R.Vogel, Science 267, 367 (1995).

[10] N. Breuer, U. Stimming, R. Vogel, Surf. Coat. Technol. 67, 145 (1994).

[11] N. Breuer, A.M. Funtikov, U. Stimming, R. Vogel, Surf. Sci. 335, 145 (1995).

[12] N. Breuer, U. Stimming, R. Vogel, in: Nanoscale Probes of the Liquid-Solid Interface, A. Gewirth and H. Siegenthaler (Eds.), NATO ASI Series E: Applied Sciences, Vol. 288, (Kluwer Academic Publisher, Dordrecht, 1995), p. 121.

[13] U. Stimming, R. Vogel, D.M. Kolb, T. Will, J. Power Sources 43, 169 (1993).
[14] N. Breuer, U. Stimming, R. Vogel, Electrochim. Acta 40, 1401 (1995).
[15] W. Li, J.A. Virtanen, R.M. Penner, Appl. Phys. Lett. 60, 1181 (1992).
[16] R. Ullmann, T. Will, D.M. Kolb, Chem. Phys. Lett. 209 238 (1993).
[17] A.J. Bard, F.R.F. Fan, A. Kwak, O. Lev, Anal. Chem. 61, 132 (1989).
[18] A. Marmann, U. Stimming, R. Vogel, *in preparation.*

Electrochemical Nanotechnology
In-situ Local Probe Techniques at Electrochemical Interfaces
Edited by W. J. Lorenz and W. Plieth

In-situ Stress Measurements at the Solid/Liquid Interface Using a Micromechanical Sensor

T.A. Brunt, E.D. Chabala, T. Rayment, S.J O'Shea, M.E. Welland

Contents

1	Introduction		88
2	Experimental		90
3	Results and discussion		92
	3.1	Electrocapillary curves	92
	3.2	Silver underpotential deposition	94
4	Conclusions		97
5	References		98

Summary. Scanned probe methods for imaging electrochemical deposition on surfaces are now well established. For such methods the surface structure at the atomic scale can be measured so that surface strains may be inferred. Here we demonstrate how extremely sensitive and fast stress sensors can be constructed from atomic force microscope (AFM) cantilevers for studies of interfacial processes such as adsorption and reconstruction. The surface stress sensor has submonolayer sensitivity for use in electrochemistry, whereby simultaneous cyclic voltammograms and stress changes can be recorded. This is demonstrated with measurements of the electrocapillary curve of gold, and stress changes associated with the underpotential deposition of silver on gold (111).

1 Introduction

Recently, the structure of the solid/liquid interface has been studied with a wide range of in-situ structural techniques. In particular, scanned probe microscopes [1-5] and synchrotron-based methods [6-9] have yielded a wealth of structural information. The ultimate goal of this work is an understanding of the structure and reactivity of the electrode surface at the atomic level. One of the most extensively studied processes is metal underpotential deposition (UPD) [10], which involves the formation of one or more metal monolayers at a potential positive of the reversible Nernst potential for bulk deposition.

One of the most interesting structural aspects of adsorption in an electrochemical environment is the formation of very open ordered structures. For instance, the UPD of copper on gold (111) in sulfuric acid exhibits a honeycomb structure [11-12], and the silver on gold (111) UPD system displays a range of open adlayer structures in different electrolytes [13-15]. These surface structures are markedly different from the UHV metal monolayers found for copper and silver on gold (111) [16-18] in which close-packed surface adlayers are the norm. There are a number of explanations for these structural differences. Firstly, the metal species in several UPD adlayers has been shown to retain a partial positive charge after adsorption [19-21]. These partially charged species will tend to repel one another and consequently prefer a more open adlattice. Alternatively, co-adsorption of negatively charged anions, which is known to occur from coulometric measurements[11, 12, 20], SPM [13], and extended X-ray absorption fine structure (EXAFS) [9], also tends to favor the formation of a similar adlattice arrangement. In both of these cases the surface is thought to be subject to a compressive stress mediated via Coulombic charge-charge repulsive forces.

Formation of open adlayers via UPD is not a universal phenomena. Other metals such as lead, thallium and bismuth form close-packed incommensurate monolayers and exhibit an effect which has been termed electrocompression. This refers to a gradual compression of the monolayer in the region between the monolayer deposition and bulk deposition regions. There is a slow reduction of the monolayer lattice parameter until it is about 3% compressed with respect to the bulk metal [22 - 23]. This type of behavior is expected for close-packed commensurate monolayers on the basis of effective medium theory [24].

In all of these systems, reduction of surface stress is thought to be one of the most important factors in the structure adopted. In the past some confusion has arisen because of the tendency in ordinary language to mix stress and strain. Only *direct* measurements of the stress changes on deposition and stripping of metal monolayers and bulk deposits can give information about the lateral forces in the plane of the

surface. These stress change measurements are complementary to other structural probes which provide information about the geometry of the surface structure. The stress changes can also be related to the thermodynamics of the interface via the electrocapillary equation [12].

The most commonly used direct method for determination of surface stress is the bending beam method in which a lever bends when subjected to a change in surface stress in one of its faces in order to minimize its stored strain energy. The relationship between the deflection of a cantilever and the different stresses in its surfaces was first determined by Stoney [25] and in surface science it has been used to measure the stress changes associated with the reconstructions of semiconductor surfaces [26 - 27].

Within the electrochemical environment, bending-beam stress measurements have been used to determine the electrocapillary curves for gold and platinum surfaces [28 - 29]. This serves as a useful test of the sensor performance and calibration procedure. A number of other methods have also been applied to study interfacial stress changes in an electrochemical environment. For instance, Haiss and Sass [30] have used a STM to measure the stress changes occurring during the UPD of copper on gold (111). Simultaneous mass and surface stress changes have also been made for the lead and thallium UPD processes on gold using a quartz crystal microbalance combined with interferometric measurement of the surface stress change [31].

Semiconductor fabrication processes permit construction of small, sensitive, stress sensors. In fact the levers used in atomic force microscopes are almost ideal for this purpose. The combination of the mechanical properties of silicon nitride and the geometry of the cantilever mean that the lever has a high resonant frequency and a low spring constant [32]. The low spring constant is beneficial for sensor applications because it means that a small applied force can be transduced to a measurable deflection, which lies at the heart of any sensor [33]. When combined with the highly sensitive optical lever AFM detection system, both of these factors mean that this arrangement is a fast and highly sensitive stress sensor.

The sensor can in principle be used to detect stress changes as small as 10^{-5} Nm^{-1} although here the stress changes are several orders of magnitude larger than this. This means that other possible sources of lever deflection such as thermal drift or heating of the electrode can be neglected. Already, several AFM-based sensor devices which measure mass changes [34] humidity changes [35], and surface stress changes [36] working at the lever resonance frequency in air have been designed. A thermal sensor based on bimetallic bending working in a direct current (dc) mode [37], has also been developed for use in air.

2 EXPERIMENTAL

A schematic diagram of the stress sensor is shown in Fig. 1. In essence it is an optical-deflection AFM without a sample [33]. The housing for the sensor is machined from a single block of aluminum. The electrochemical cell is made from Teflon with a glass window through which the optical beam passes. The gold-coated lever itself is the working electrode and reference and counter electrodes are positioned within the cell for electrochemical control. Electrical contact to the lever is made via a thin insulated wire which is glued to the lever holder with conducting epoxy resin. This connection is then insulated with an inert, insulating epoxy resin. The quality of the voltammograms that we have obtained indicates that there is minimal contamination caused by the epoxy resin.

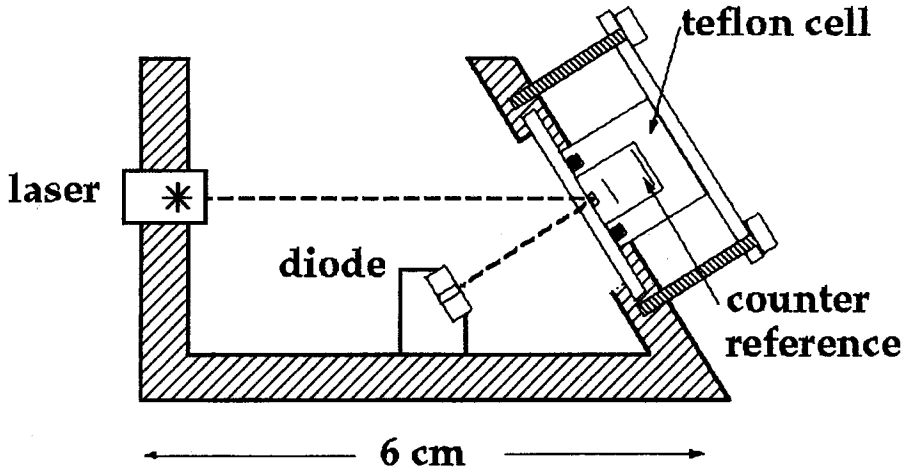

Fig. 1. Schematic diagram of the experimental arrangement.

The gold coating on the as-supplied silicon nitride cantilevers is stripped with aqua regia and a clean (111) oriented gold surface is then deposited by vacuum evaporation on the tip side of the lever. The gold film deposition is carried out at a pressure of less than 10^{-7} mbar and at a temperature of 270°C and the films are then annealed at the same temperature for 4 h before being allowed to cool down slowly (Balzers UTT400

UHV evaporation system). This procedure is similar to that used for the vacuum evaporation of well-oriented gold (111) films on mica substrates [38]. The (111) orientation of the films was then determined by X-ray diffraction.
The stress change can be determined directly from the optical-beam deflection signal. The stress change is given by Stoney's equation:

$$\sigma_1 - \sigma_2 = \frac{\mathbf{E}t^2}{6(1-\nu)r} \tag{1}$$

where σ_1 and σ_2 are the surface stresses in the two faces of the cantilever, **E** the Young's modulus of the lever, t the thickness of the lever, n the Poisson ratio of the lever and r the radius of curvature of the bent cantilever. The values of **E** (1.5×10^{11} Nm^{-2}) and n (0.3) are those of bulk amorphous silicon nitride. In order to interpret these lever deflections it is necessary to assume that the surface stress of the silicon nitride face is constant. The voltages applied to the working electrode are small (not more than ±1V). This has been shown not to alter the electrical characteristics of silicon nitride [29], so the stress changes can be regarded as surface stress changes of the gold electrode surface. The quoted thickness of the levers is 0.6mm. This was confirmed by measuring the lever resonant frequency. The photocurrents are proportional to the measured output voltages A and B. However, care must be taken to consider the effect of a reflected beam from the glass/solution boundary also impinging upon the detector. To take this into account we measure the $A+B$ signal when the beam is just missing the tip of the lever. This is then subtracted as the background signal $(A+B)_{off}$. By considering the geometry of the measurement system and applying Stoney's formula (above), the stress change $\Delta\sigma$ can be written as:

$$\Delta\sigma = \frac{\mathbf{E}t^2 L}{18(1-\nu)sl}\left[\frac{\Delta(A-B)_{on}}{(A+B)_{on} - (A+B)_{off}}\right] \tag{2}$$

where $(A+B)_{on}$ is the signal from the detector when the laser beam is focused on the lever. From Eq. (2) it is clear that using this approach only changes in the surface stress are experimentally accessible rather than the absolute surface stress value, because there is no reference point of known stress.

The linearity of the photodiode detector was checked using neutral density filters and over the range of operation the output voltages are proportional to the incident beam

intensity. Some care is required in the beam alignment to ensure that all of the reflected beam impinges upon the detector compared to the earlier error term, this is negligible.

The photodiode-lever separation can be measured sufficiently accurately to ensure that it is a negligible source of error. The value of this distance varies slightly from scan to scan, depending on the beam alignment, but is typically 12.0 mm. Finally one must consider the geometrical and mechanical properties of the cantilever. Because the stoichiometry of the cantilevers can vary from that of bulk amorphous silicon nitride, the values of the Young's modulus and Poisson ratio are not very accurately known. We have used quoted values for bulk silicon nitride, but the accuracy of these values is hard to assess. As mentioned earlier, the quoted thickness of the levers was checked by measuring the lever resonant frequency, and the width of the levers is accurately known (10 μm).

The error in the effective cantilever length corresponds to a percentage error in the stress changes of ~6%. Furthermore, there could also be some variation in the measured stress changes because of differences in the surface roughness and morphology of individual gold films.

Electrochemical control was provided by an Eco-Chimie PSTAT10 potentiostat, which facilitated the simultaneous measurement of current and the lever deflection signal. For the silver UPD work a clean silver wire was used as the reference electrode, and for the electrocapillary curve a silver/silver chloride reference electrode was used. In all cases a platinum coil served as the counter electrode. All the electrolyte solutions were made with 18.2MW water (Elga). Silver sulfate (Specpure, Johnson Matthey), silver fluoride (99.9+%, Aldrich), potassium chloride (99.999%, Aldrich), perchloric acid (Aristar 70%, BDH) and sulfuric acid (Aristar, BDH) were used for making the electrolyte solutions. All the electrolytes were de-aerated with high-purity nitrogen prior to use.

3 RESULTS AND DISCUSSION

3.1 Electrocapillary Curves

The electrocapillary curve of a solid metal electrode is more difficult to measure than that of a liquid electrode, because of problems of surface cleanliness. The most widely used approach has been the bending-beam method, which was originally developed by Fredlein et al. [28] using large samples. More recently Raiteri and Butt [29] have used gold electrodes deposited on an AFM cantilever to record electrocapillary curves.

As a calibration of our instrument we have recorded electrocapillary curves for a gold (111) electrode surface (Fig.2), vacuum-evaporated onto a standard silicon nitride AFM cantilever.

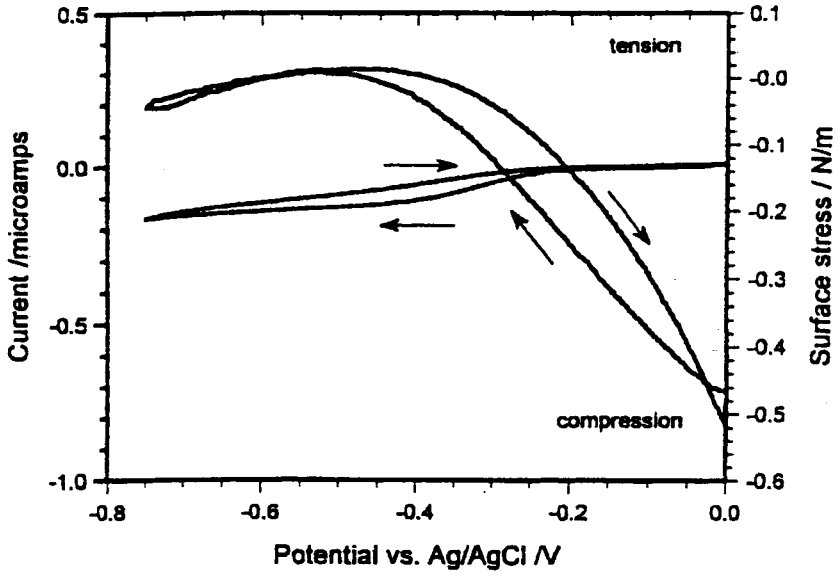

Fig. 2. Cyclic voltammogram/stress curves of electrocapillary effects on a gold(111)-coated cantilever in 0.1 M KCl. Scan rate $10 mVs^{-1}$.

The cantilever deflection results from a change in the surface stress as the electrode potential is varied. The surface stress is related to the surface energy by the Shuttleworth equation:

$$\sigma = \gamma + \frac{d\gamma}{d\varepsilon} \tag{3}$$

where σ is the surface stress, γ the surface energy and ε the surface strain. For liquid electrodes the second term is identically zero. However, this is not the case for solid surfaces because the surface energy required to form unit area of a strained surface is different from that required to form unit area of an unstrained surface. Despite this complication, Mohilner and Beck [40] have shown that typical values of this term are several orders of magnitude smaller (10^{-4} Nm^{-1}) than the measured surface stress changes associated with electrocapillary curves or UPD processes, which are greater than 0.1 Nm^{-1}. So for the purposes of this work the surface stress and surface energy can be regarded as approximately equal.

There is considerable variation in the quoted values of the potential of zero charge (pzc) or electrocapillary maximum for gold. For instance the quoted pzc values for gold in 0.1 M KCl range from 0 to -0.6 V [28 - 29] versus the standard hydrogen electrode (SHE). This must be due to the sensitivity of the pzc to the surface crystallinity and the fact that these studies were carried out on polycrystalline gold surfaces . The pzc is also known to be highly sensitive to surface contaminants.

The pzc of our well-defined gold (111) surface was in all cases between -0.2 and -0.3 V with respect to the SHE (Fig.2). Despite the wide range of pzc values, the relative stress changes in this work and that in the literature are all in good agreement. That is to say that the measured stress changes between the pzc and some other potential are similar. The electrocapillary curve is therefore a good diagnostic test of the stress sensor and our calibration procedure.

There is some hysteresis associated with the electrocapillary curves. This is shown in the difference between the pzc values for cathodic and anodic scan directions (scanning to more negative and positive values respectively). This has been observed in other stress-voltage measurements. This hysteresis shows some scan rate dependence and is reduced at lower scan rates, suggesting that some kinetic factor may be involved.

3.2 Silver Underpotential Deposition

The stress-voltage curve for the silver UPD process in sulfuric acid (Fig. 3) shows a clear change in the lever deflection signal corresponding to the first silver monolayer peak. This is apparent in both deposition and stripping. This indicates that there is a change in surface stress which occurs when a silver monolayer is deposited onto or stripped from the gold surface. The direction of the lever deflection shows that as the silver monolayer is deposited there is a reduction in the compressive surface stress. Then as the potential is scanned in the cathodic direction, the compressive stress is gradually restored. The general form of the variation shows several similarities to that shown for copper UPD on Au (111) in sulfuric acid [30], a comparable UPD system.

At high positive potentials prior to the deposition of the first silver monolayer, the gold surface is covered with an ordered sulfate lattice [41]. Repulsive anion-anion interactions give rise to a compressive surface stress. On formation of the first silver monolayer some of the sulfate species must be displaced from the surface. According to AFM studies [13], the resulting adlattice consists of an open (3x3) arrangement of the silver atoms with some remaining co-adsorbed sulphate, and STM studies find a ($\sqrt{3}$ x $\sqrt{3}$)R30° adlayer [15]. Irrespective of the apparent disagreement between these AFM and STM studies, this phase is under less compressive stress than the sulfate arrangement, because of the reduction in anion-anion repulsions and the presence of partially discharged cations.

There are three possible explanations for the gradual increase in the compressive stress as the potential is scanned towards the bulk silver deposition region. The first is that the silver monolayer enhances further adsorption of sulphate anions (this has been demonstrated on polycrystalline gold by radiotracer measurements [42 - 43]). Consequently there is a gradual build-up in compressive stress which continues until further silver deposition occurs near the bulk silver deposition region.

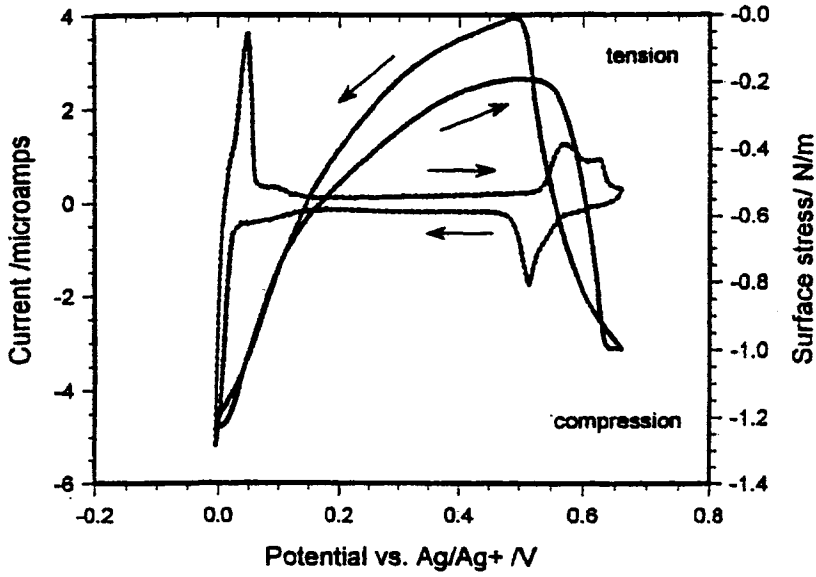

Fig. 3. Stress-voltage curve for UPD of silver onto a gold (111) coated cantilever.

The second possibility is based on electrochemical quartz crystal microbalance results. Uchida et al. [44] suggest that following the first silver monolayer deposition process, there is a gradual deposition of more Ag atoms and that the monolayer coverage increases from around 1/3 to around 2/3, at which point the final epitaxial monolayer is formed at a potential near the bulk deposition region. This gradual filling of the first open monolayer does not, they claim, alter the extent of anion adsorption, so this process could be responsible for the slow increase in compressive stress in this region, particularly if the silver atoms retain a partial charge as has been suggested.

Finally, the observed decrease in the surface stress could arise from an electrocapillary-type effect. In this case the gradual increase in compressive stress occurs as the potential moves further away from the pzc, just as was seen for the electrocapillary curve of gold. This clearly depends on the value of the pzc of a gold (111) surface covered with a partial silver monolayer, which is not known. Electrocapillary curves of this type of system have been calculated from coulometric data [12] but the agreement between these calculations and experimental measurements [30] is not very good.

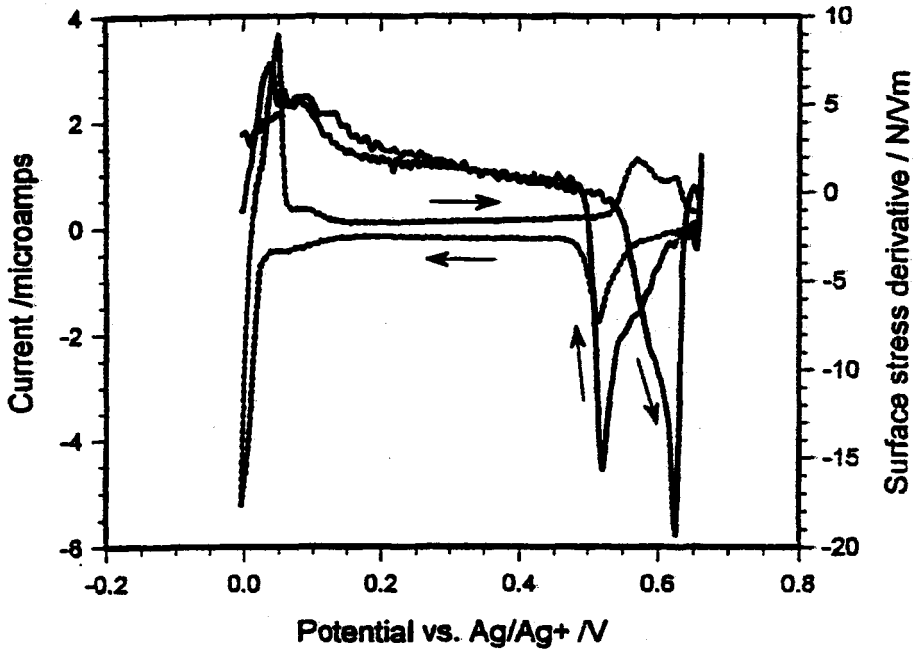

Fig. 4. Derivative of the stress with respect to voltage of Ag on Au(111).

It is clear that the electrocapillary curve exhibits gradual stress changes with changes in potential, whereas the gradient of the stress changes associated with the silver monolayer deposition process is much greater. Taking the derivative of the stress-voltage curve for the silver UPD process illustrates this (Fig. 4). This effectively diminishes the contribution from the potential region between the first monolayer and bulk deposition. There is a very clear correlation between the peaks in this derivative curve and those in the cyclic voltammogram in both scan directions. This derivative curve is less affected by the gradual electrocapillary-type

4 CONCLUSIONS

The AFM-based cantilever stress sensor is a highly sensitive device. We have used the sensor to obtain information about processes occurring at the solid/liquid interface in an electrochemical environment with submonolayer sensitivity. This work has shown the importance of lateral surface interactions in determining adlayer structures. In particular the repulsive charge-charge interactions, unique to the electrochemical environment, are clearly important in UPD and presumably in other surface electrochemical processes. These forces are predominantly responsible for the open adlattice structures which are frequently observed at this interface compared with the close-packed metal monolayers that are associated with the metal/vacuum interface. The extent to which these interactions are related to the co-adsorption of negatively charged ions requires further investigation for a variety of UPD systems.

As well as the sensitivity of this device, which could clearly be advantageous in more stringent sensor applications, the high resonant frequency of the cantilever means that it is ideally suited to applications where fast lever response is needed. In this work potential scan rates of several hundred mVs^{-1} shave been used. We have started studies of fast electrochemical processes using potential-step methods, since the fast dynamic response of the cantilever is its primary advantage over other stress sensors. Additionally one may ultimately expect a combined instrument so that the tip of a scanning tunneling microscope can be used to image the sensor surface in-situ, allowing for real-space surface-strain imaging in addition to surface stress.

5 REFERENCES

[1] S. Manne, P.K. Hansma, J. Massie, V.B. Elings, A.A. Gerwirth, Science 251, 183 (1991).
[2] T.R.I. Cataldi, I.G. Blackham, I.A.D. Briggs, J.B. Pethica, H.O.A. Hill, J. Electroanal. Chem. 290, 1 (1990).
[3] A.J. Bard, F-R. Fan, Faraday Discuss. 94, 1 (1992).
[4] F.A. Möller, O.M. Magnussen, R.J. Behm, Phys. Rev. B 51, 2484 (1995).
[5] O.M. Magnussen, J. Hotlos, R.J. Nichols, D.M. Kolb, R.J. Behm, Phys. Rev. Lett. 64, 2929 (1990).
[6] O.R. Melroy, M.F. Toney, G.L. Borges, M.G. Samant, J.B. Kortright, P.N. Ross, L. Blum, Phys. Rev. B 38, 10962 (!988).
[7] M.F. Toney, J.G. Gordon, M.G. Samant, G.L. Borges, O.R. Melroy, D. Yee, L.B. Sorensen, Phys. Rev B 45, 9362 (1992).
[8] O.R. Melroy, M.G. Samant, G.L. Borges, J.G. Gordon, L. Blum, J.H. White, M.J. Albarelli, M. McMillan, H.D. Abruña, Langmuir 4, 728 (1988).
[9] J.H. White, M.J. Albarelli, H.D. Abruña, L. Blum, O.R. Melroy, M.G. Samant, G.L. Borges, J.G. Gordon, J. Phys. Chem. 92, 4436 (1988).
[10] D.M. Kolb in Advances in Electrochemistry and Electrochemical Engineering, H. Gerischer and C. Tobias (Eds.), Wiley-VCH, New York, Vol. 11.
[11] M.F. Toney, J.N. Howard, J. Richer, G.L. Borges, J.G. Gordon, O.R. Melroy, D. Yee, L.B. Sorensen, Phys. Rev. Lett. 75, 4472 (1995).
[12] Z. Shi, J. Lipkowski, J. Electroanal. Chem.365, 289 (1994).
[13] C. Chen, S.M. Vesecky, A.A. Gerwirth, J. Am. Chem. Soc. 114, 451 (1992).
[14] C. Chen, A.A. Gerwirth, Ultramicroscopy 42-44, 437 (1992).
[15] T. Hachiya, K. Itaya, Ultramicroscopy 42-44, 445 (1992).
[16] Y. Nakai, M.S. Zei, D.M. Kolb, G. Lehmpfuhl, Ber. Bunsenges. Phys. Chem. 88, 340 (1984).
[17] D.D. Chambliss, R.J. Wilson, J. Vac. Sci. Technol. B 9, 928 (1991).
[18] M.M. Dovek, C.A. Lang, J. Nogami, C.F. Quate, Phys. Rev. B 40, 11973 (1989).
[19] A. Tadjeddine, D. Guay, M. Ladouceur, G. Tourillon, Phys. Rev. Lett. 66, 2235 (1991).
[20] Z. Shi, J. Lipkowski, J. Electroanal. Chem. 365, (1994).
[21] P. Zelenay, L.M. Rice-Jackson, A. Wieckowski, Surf. Sci. 256, 253 (1991).
[22] M.F. Toney, J.G. Gordon, M.G. Samant, G.L. Borges, O.R. Melroy, D. Yee, L.B. Sorensen, J. Phys. Chem. 99, 4733 (1995).
[23] C. Chen, K. Kepler, A.A. Gerwirth, J. Wang, B. Ocko, J. Phys. Chem. 97, 7290 (1993).
[24] K. Jacobsen, J. Norskov, M. Puska, Phys. Rev. B 35, 7423 (1987).
[25] A.J. Schell-Sorokin, R.M. Tromp, Surf. Sci. 319, 110 (1994).
[26] A.J. Schell-Sorokin, R.M. Tromp, Phys. Rev. Lett. 64, 1039 (1990).
[27] R.E Martinez, W.M. Augustyniak, J.A. Golovchenko, Phys. Rev. Lett. 65, 1035 (1990).

[28] R.A. Fredlein, A. Damjanovic, J.O'M. Bockris, Surf. Sci.25, 261 (1971).
[29] R. Raiteri, H-J. Butt, J.Phys. Chem.99, 15728 (1995).
[30] W. Haiss, J.K. Sass, J. Electroanal. Chem. 386, 267 (1995).
[31] L. Jaeckel, G. Làng, K.E. Heusler, Electrochim. Acta 39, 1081 (1994).
[32] D. Sarid, Scanning Force Microscopy, with Applications in Electric, Magnetic and Atomic Forces, Oxford University Press, Oxford, 1991
[33] S.J. O'Shea, M.E. Welland, T.A. Brunt, A.R. Ramadan, T. Rayment, J. Vac. Sci. Technol. B, in press
[34] T. Thundat, E.A. Wachter, S.L. Sharp, R.J. Warmack, Appl. Phys. Lett. 66, 1695 (1995).
[35] T. Thundat, G.Y. Chen, D.P. Allison, Appl. Phys. Lett. 64, 519 (1994).
[36] G.Y. Chen, T. Thundat, E.A. Wachter, R.J. Warmack, J. Appl. Phys. 77, 3618 (1995).
[37] J.R. Barnes, R.J. Stephenson, M.E. Welland, Ch. Gerber, J.K. Gimzewski, Nature (London) 372, 79 (1994).
[38] J.A. DeRose, D.B. Lampner, S.M. Lindsay, N.J. Tao, J. Vac. Sci. Technol. A 11, 776 (1993).
[39] J.E. Sader, I. Larson, P. Mulvaney, L.R. White, Rev. Sci. Instrum.66, 3789 (1995).
[40] D.M. Mohilner, T.R. Beck, J. Phys. Chem.83, 1160 (1979).
[41] O.M. Magnussen, J. Hageböck, J. Hotlos, R.J. Behm, Faraday Discuss. 94, 329 (1992)
[42] G. Horanyi, E.M. Rizmayer, P. Joo, J. Electroanal. Chem. 152, 211 (1983).
[43] P. Zelenay, L.M. Rice-Jackson, J. Gawlowski, A. Wieckowski, Surf. Sci. 256, 253 (1991).
[44] H. Uchida, M. Miura, M. Watanabe, J. Electroanal. Chem.386, 261 (1995).

Electrochemical Nanotechnology
In-situ Local Probe Techniques at Electrochemical Interfaces
Edited by W. J. Lorenz and W. Plieth

Surface structure and electrochemistry: new insight by scanning tunneling microscopy

Giovanni Aloisi, Massimiliano Cavallini, Rolando Guidelli

Contents

1	Introduction	102
2	Corrosion	102
3	Adsorption	103
	3.1 Atoms	103
	3.2 Molecules	107
4	Structure and interaction with light	107
5	Future developments	109
6	Conclusions	110
7	References	111

Summary. The importance of the electrode surface structure in electrochemistry is briefly described. Examples are given in which the structural information provided by scanning tunneling microscopy (STM) is of assistance in clarifying the electrochemical behavior. The importance of surface structure in the photoelectrochemical response of metals is illustrated by an STM application. Finally, the potentialities of new scanning microprobe techniques suitable for mapping local photoelectrochemical properties of metal surfaces are briefly discussed.

1 Introduction

The electrochemistry of single-crystal electrodes, pioneered by Clavilier et al. [1], clearly shows that the electrochemical behavior of metal surfaces depends not only on their chemical composition but also, to a large extent, on their surface structure. The understanding of the importance of the latter factor has introduced into electrochemistry concepts such as surface reconstruction, epitaxy, etc., which were originally peculiar to ultrahigh-vacuum (UHV) surface science. At the same time, a notable effort has been devoted to the application of experimental techniques typical of UHV to electrochemical systems [2]: one of the most successful applications has certainly consisted in the use of the electrochemical STM which, only six years after its introduction as a UHV tool [3], proved able to yield atomic resolution on the surface of polarized electrodes, i.e. in-situ [4, 5]. Nowadays, even if further in-situ techniques have been developed, such as low-angle X-ray diffraction [6] and atomic force microscopy (AFM) [7], STM remains the most widespread technique, in view of its ability to determine the structure of surface features in the range of micrometers and on the atomic scale as well. STM is particularly useful in the investigation of surface defects, which are often responsible for electrochemical effects of importance in electrochemical applications. Some examples are given and briefly discussed below.

2 Corrosion

Figure 1 shows two consecutive images of an Au(111) terrace immersed in an acidic solution containing traces of Cl^- ions and polarized at positive potentials. The progressive growth of the holes, one atomic diameter deep, provides clear evidence that the corrosive attack takes place preferentially at their edges, probably because the simultaneous binding of more than one chloride ion to the same gold atom is required to cause the formation and desorption of the water-soluble $AuCl_4^-$ complex.

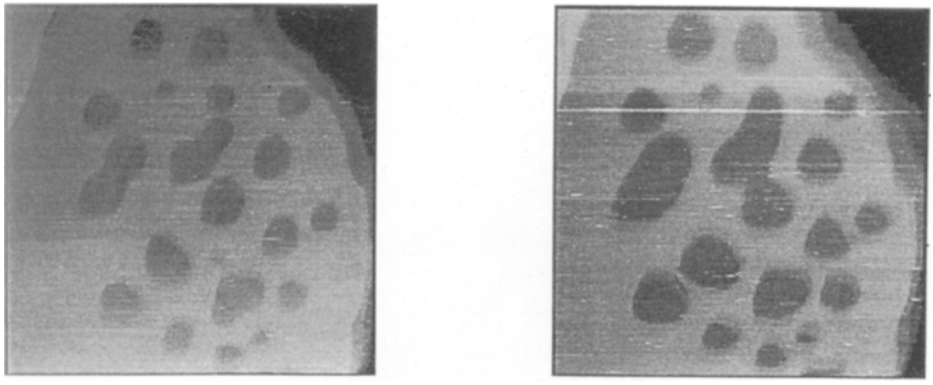

Fig. 1. Two consecutive images of the same 267 nm x 267 nm area of an Au(111) electrode in 10 mM H_2SO_4 + 10 μM NaCl under conditions of anodic corrosion. E=0.95 V/SCE and E_{tip} = -650 mV with I_t = 2 nA and a W tip.

3 Adsorption

3.1 Atoms

The atomic resolution of STM is widely exploited for the structural investigation of overlayers on metal substrates. Achieving atomic resolution requires not only a good instrument, but also a careful elimination of vibrations and thermal gradients as well as the preparation of single crystals with a minimum of surface defects.

Figure 2 shows the stage immediately preceding the formation of an iodine overlayer on an Ag(111) surface [8, 9] . This STM image, which reveals the presence of the first few isolated iodine atoms, was obtained at polarization potentials positive to the most negative adsorption peak, as recorded by cyclic voltammetry. This permits us to locate the most negative potential at which partial charge transfer between the adsorbed anion and the metal substrate starts to become strong enough as to immobilize the anion, making it "visible" by STM: only at more negative potentials does iodide adsorption become reversible enough to allow the determination of the relative adsorption isotherm via a thermodynamic analysis of capacitive charge data obtained by chronocoulometry [10].

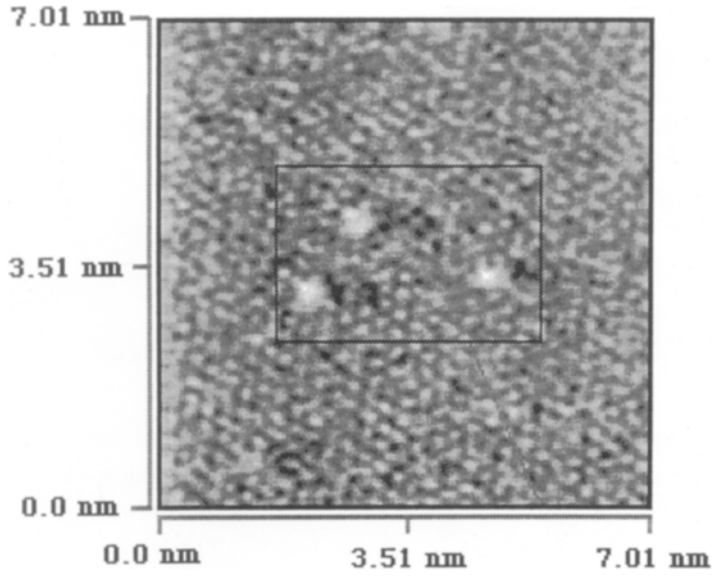

Fig. 2. STM image of an Ag(lll) surface in 10 mM NaF + 0.I mM NaI. E = 0.835 V/SCE and E_{tip} = +50 mV with I_t = 1.5 nA and a W tip.

To the authors' knowledge this is the first case in which isolated atoms have been imaged on an electrode surface: at submonolayer coverages only ordered islands of adatoms are normally imaged on the substrate, as in the case of bromide adsorption on Ag(l11) [8, 9]. At more positive potentials iodide anions also give rise to the formation of islands with a ($\sqrt{3}$ x $\sqrt{3}$)R30° symmetry with respect to the substrate, as shown in Fig. 3. Sulfide ion is chemisorbed on Ag(lll) from neutral and alkaline solutions starting from the most negative accessible potentials [11]. Proceeding towards less negative potentials, it is first chemisorbed randomly, then undergoes a disorder/order two-dimensional (2D) phase transition whose kinetics is controlled by nucleation and growth, and finally it undergoes a further 2D phase transition yielding a more compact overlayer, before giving rise to a bulk deposition of elemental sulfur. The first 2D phase transition takes place at about -1.0 V/SCE and yields a ($\sqrt{3}$ x $\sqrt{3}$)R30° overlayer, as shown in Fig. 4.

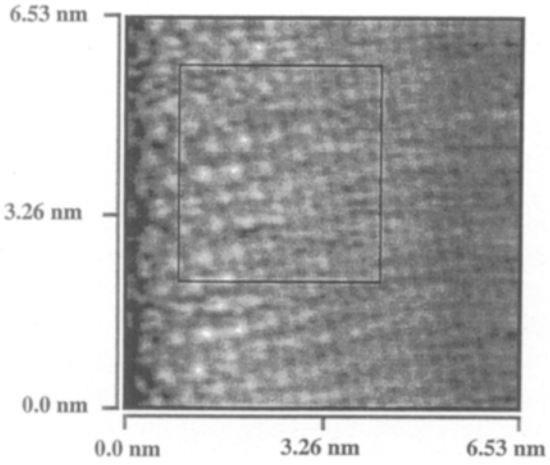

Fig. 3. STM image of an Ag(111) surface in 10 mM NaF + 0.1 mM NaI. E = -0.74 V/SCE and E_{tip} = +100 mV with I_t = 0.9 nA and a W tip.

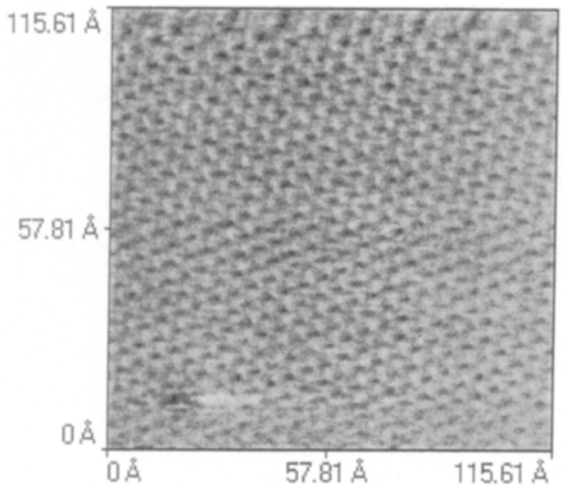

Fig. 4. STM image of an Ag(111) surface in 0.2 M NaOH + 0.8 mM Na_2S. E = -1.03 V/SCE and E_{tip} = 250 mV with I_t = 1.5 nA and a W tip.

The chemisorption of sulfide ions involves a total charge transfer, as indicated by the perfect correspondence between the ordered structures revealed by the STM images and the flow of charge which accompanies their formation and which was estimated both by cyclic voltammetry and by chronocoulometry [12].

In investigating the behavior of silver electrodes in sulfide solutions, it was observed that the aging of the solution is accompanied by a progressive irreproducibility of the cyclic voltammograms. Thus, if the sulfide solution is exposed to the light for a sufficently long time, long polysulfide chains are observed on the Ag(111) surface; these are strongly adsorbed even at far negative potentials and are clearly revealed STM, as shown in Fig. 5.

The underpotential deposition of sulfur on Ag(111) is just the first step towards the realization of mono- and multilayers of semiconducting sulfides, such as CdS and PbS, by the alternated underpotential deposition of S and Cd (or Pb) atomic monolayers on the low-index faces of silver. This procedure, called electrochemical atomic layer

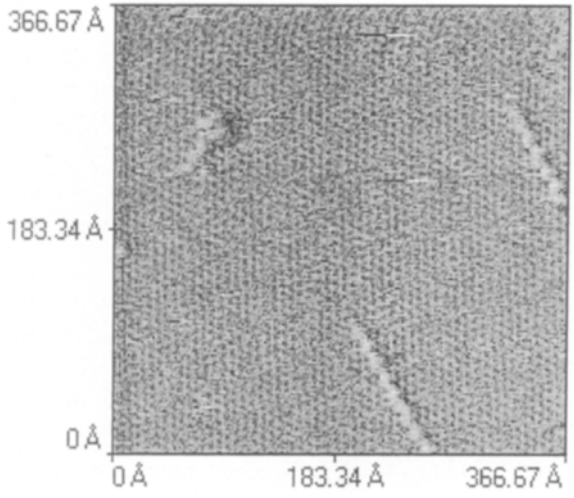

Fig.5. STM image of an Ag(111) surface in 10 mM NaF +0.1 mM Na_2S. E = -0.75 V/SCE and E_{tip} = 250 mV with I_t = 1.5 nA and a W tip.

epitaxy [13], is the electrochemical analogue of atomic layer epitaxy. STM is invaluable in the elucidation of the structures resulting from these alternate underpotential depositions.

3.2 Molecules

In recent years particular attention has been devoted to the investigation of 2D phase transitions of electroinactive organic compounds at single-crystal electrodes from a kinetic point of view, using electrochemical techniques such as cyclic voltammetry, chronoamperometry, chronocoulometry, and the phase-sensitive lock-in technique. Among the systems so far investigated we can mention coumarin on Au(111) and Au(100)-(hex) [14], uridine on Au(111) [15, 16], uracil on Au(100), Au(100)-(hex) [17], Ag(111) [18, 19], and Ag(100) [18], thymine on Ag(111) and Ag(100) [20], and cytosine on Au(111) [21]. Ordered adlayer structures have also been reported for thymine, cytosine, guanine and adenine on Au(111) employing in-situ STM [22].

Practically all these organic compounds are purine and pyrimidine derivatives which are present as components of DNA and RNA, where they encode genetic information; their molecules have both proton-donor and proton-acceptor groups, and are therefore likely to form intermolecular hydrogen bonds in the adsorbed state [23]. Many of these systems [18, 21] exhibit both an ordered, liquid-like physisorbed state which shows the typical behavior of 2D condensed films at the mercury/water interface and, at more positive potentials, a further ordered, chemisorbed state which shows an extreme stability even at relatively high temperatures and is relatively insensitive towards the surface crystallographic orientation. While STM images of chemisorbed adlayers of uracil [17] and of cytosine [21] on Au(111) have been obtained, no STM images of physisorbed adlayers have so far been reported. This is quite probably due to the high mobility of the physisorbed molecules and to their inability to alter the electron density profile of the metal substrate to a detectable extent.

2D condensation of uracil on Ag(111) in the chemisorbed state shows both a short- and a long-time behavior [19]. STM images of chemisorbed uracil on Ag(111) are now under investigation in our laboratory in an attempt to monitor their evolution in time.

4 Structure and interaction with light

Another field in which the electrode surface structure plays a fundamental role is photoelectrochemistry. It is well known that electronically conducting surfaces are characterized by collective excitations of the conduction electrons relative to the

corresponding fixed positive charges, called surface plasmons [24, 25]. Because of the requirements of momentum conservation, these excitations cannot couple directly with light, either incoming (absorption) or outgoing (emission). Nonetheless, a coupling is possible by diffraction if the surface is not smooth but rather exhibits a grating structure (grating coupling). Now, any bidimensional profile can be decoupled into simple sine Fourier components, i.e. any surface roughness can be treated as a linear superposition of diffraction gratings [24]: hence, surface roughness enables the coupling of surface plasmons with light.

The most striking effects are observed in surface-enhanced Raman scattering (SERS) [26], but other effects such as second-harmonic generation [27] and photocurrents [28] are also strongly affected by surface roughness. The most effective metal for this kind of investigations is silver, whose surface is normally roughened by an oxidation-reduction cycle (ORC). In-situ STM was of assistance in showing that surface roughness is stabilized at far negative potentials, but decays rapidly at potentials positive to the point of zero charge as shown in Fig. 6 [29]. In turn, this relaxation in roughness is responsible for an irreversible quenching of the photoelectrochemical response of the electrode [30].

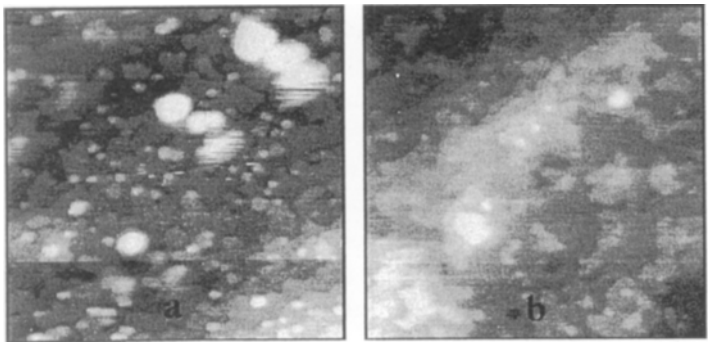

Fig. 6. 80 nm x 80 nm images of a silver electrode surface after an ORC in 10 mM $KClO_4$. (a) E = -1.2 V/SCE, E_{tip} = 1 V . (b) E = -0.5 V/SCE, E_{tip} = 0.3 V with I_t = 1 nA and a W tip.

5 Future Developments

A natural extension of the investigation of the correlation between the surface roughness of electrodes and their photoelectrochemical response consists in studying how the photo-electron coupling is affected by the local surface structure. A possible way to achieve this goal consists in mapping the feeble photoemission associated with electron tunneling on metals [31] by collecting the photoemission from the gap between the STM tip and the sample by the use of an optical fiber. Connecting the fiber to a photomultiplier and the resulting signal to an auxiliary input of the STM, as shown in Fig. 7, allows a map of the intensity of emission throughout the surface to be recorded.

The preliminary results reported in Fig. 8 clearly show a correlation between the photoemission intensity and the surface "bumps" which are the site of radiative localized surface plamons [32].

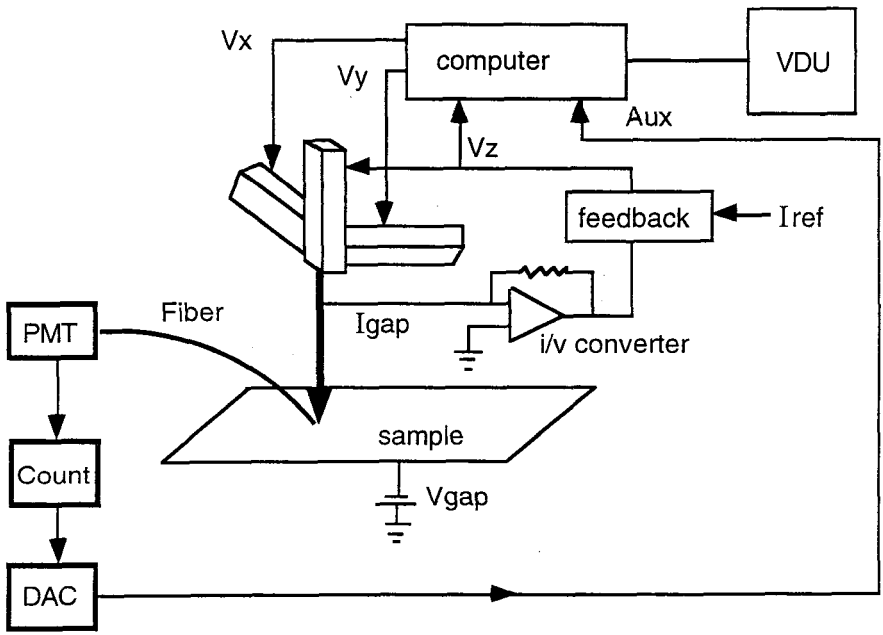

Fig.7. Scheme of the instrumentation for mapping tunneling-induced photoemission on a metal surface. DAC = digital/analog converter; PMT = photomultiplier; VDU = video display unit; Aux = auxiliary input; I_{ref} = reference current.

A complete description of the local photoelectrochemical response (albeit with a lower resolution) can be achieved using a near-field scanning optical microscope (SNOM), in which the end of a tapered optical fiber scans the metal surface [33]; using very small fiber apertures it is possible to obtain a resolution higher than the half-wavelength limit of classical optics. In addition, the exponential decay of the electromagnetic field at the probe aperture allows a direct excitation of surface plasmons, as in Otto's configurations [24; 25]: this makes the SNOM ideally suitable for the investigation of the topography of surface excitations.

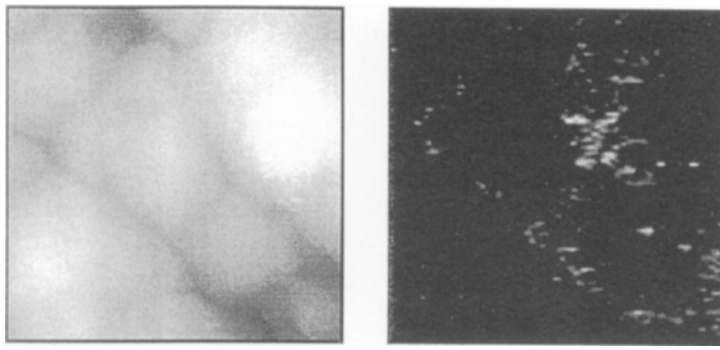

Fig.8. Two consecutive scans on the same 97 nm x 97 nm area of a polycrystalline silver surface in 10 mM NaF solution, with the first scan mapping the structure (z piezo signal) and the second the emission intensity (Aux signal; see Fig. 7). E = - 1.2 V/SCE and E_{tip} =2.3 V with I_t =5 nA and an Au tip.

6 Conclusions

STM makes information on the surface structure of electrodes readily available, and hence turns out to be extremely helpful when tackling problems related to electrocatalysis and photoelectrochemistry. The development of further scanning probe microscopies is still an open and stimulating field of research in electrochemistry as well as in surface science.

Acknowledgments. The financial support of the Consiglio Nazionale delle Ricerche and of the Ministero dell'Universita' e della Ricerca Scientifica e Tecnologica is grateful acknowledged.

7 References

[1] A. Hamelin, in: Modern Aspects of Electrochemistry, B.E. Conway, R.E. White, J.O.M. Bockris (Eds.), Vol. 16, pp. 1-102, Plenum, New York, 1985.
[2] D.M. Kolb, in: Advances in Electrochemistry and Electrochemical Engineering, H. Gerischer, C.W. Tobias (Eds.), Vol. 11, Wiley, New York, 1978.
[3] G. Binnig, H. Rohrer, Ch.Gerber, E. Weibel, Phys. Rev. Lett. 49, 57 (1982).
[4] P. Lustenberg, H. Rohrer, R. Cristoph, H. Siegenthaler, J. Electroanal. Chem. 243, 225 (1988).
[5] J. Wiechers, T. Twomey, D.M. Kolb, R.J. Behm, J. Electroanal. Chem. 248, 451 (1988).
[6] J. Wang, A.J. Davenport, H.S. Isaacs, B.M. Ocko, Science 255, 1416 (1992).
[7] S. Manne, P.K. Hansma, J. Massie, V.B. Elings, A.A. Gewirth, Science 251, 183 (1991).
[8] M. Cavallini , G. Aloisi, J. Phys. Chem., submitted.
[9] M.L. Foresti, G. Aloisi, M. Innocenti, H. Kobayashi, R. Guidelli, Surface Sci. 335, 241 (1995).
[10] M.L. Foresti, M. Innocenti, H. Kobayashi, in preparation.
[11] D.W. Hatchety, X. Gao, S.W. Catron, S. White, J. Phys. Chem. 100, 331 (1996).
[12] G. Aloisi, M. Cavallini, M.L. Foresti, R.Guidelli, M. Innocenti, G. Pezzatini, unpublished results.
[13] D. Wayne Suggs, J. Stickney, Surface Sci. 290, 375 (1993).
[14] M.H. Hölzle, D.M. Kolb, Bunsenges. Ber. Phys. Chem. 98, 330 (1994).
[15] M. Scharfe, A.Hamelin, C. Buess-Herman, Electrochim. Acta 40, 61 (1995).
[16] C.Buess-Herman, Prog. Surf. Sci. 46, 335 (1994).
[17] M.H. Hölzle, Th. Wandlowski, D.M. Kolb, Surface Sci. 335, 281 (1995).
[18] Th. Wandlowski, J. Electroanal. Chem. 395, 83 (1995).
[19] R. Guidelli, M.L. Foresti, M. Innocenti, J. Phys. Chem.100, 18491 (1996).
[20] M.H. Hölzle, D. Krznaric, D.M.Kolb, J. Electroanal. Chem. 386, 235 (1995).
[21] Th.Wandlowski, D. Lampner, S.M. Lindsday, J. Electroanal. Chem. 404, 215 (1996).
[22] N.J. Tao, J.A. de Rose, S.M.Lindsday, J. Phys. Chem. 97, 910 (1993).
[23] R. de Levie, Th.Wandlowski, J. Electroanal. Chem. 366, 265 (1994).
[24] H. Raether, Surface Plasmons , Springer Tracts in Modern Physics No. 111, Springer Verlag, Berlin, 1988.
[25] D.M. Kolb, in: Spectroelectrochemistry, R.J.Dale (Ed.), Plenum, New York, p.87.
[26] R.K. Chang, T.E.Furtak, Surface Enhanced Raman Scattering, Plenum, New York, 1982.

[27] G.L. Richmond, in: Electrochemical Interfaces, Modern Techniques for in-situ Interface Characterization, H.D. Abruña (Ed.), VCH, New York, 1991, 256.
[28] A.M. Funtikov, S.K. Sigalaev, V.E. Kazarinov, Elektrokhimiya 25, 762 (1989)
[29] G. Aloisi, A.M. Funtikov, R. Guidelli, Surface Sci. 296, 291 (1993).
[30] G. Aloisi, M. Muniz-Miranda, R. Guidelli, A.M .Funtikov, V.E. Kazarinov, Mendelejev Commun., 1, 244 (1993).
[31] R. Berndt, J.K. Gimzewski P. Johansson, Phys. Rev. Lett. 67, 3796 (1991).
[32] J.I.Gersten, A. Nitzan, J. Chem. Phys. 73, 3023 (1980).
[33] U. Ch.Fischer, D. W.Pohl, Phys. Rev. Lett. 62, 458 (1989).

Part III

Electrochemical Nanotechnology
In-situ Local Probe Techniques at Electrochemical Interfaces
Edited by W. J. Lorenz and W. Plieth

STM and AFM Studies of the Electrified Solid-Liquid Interface: Monolayers, Multilayers, and Organic Transformations

Andrew A. Gewirth, Brian K. Niece

Contents

1	Introduction	113
2	Underpotential deposition	114
3	Cu electrode surfaces	117
4	Molecular adsorbates	121
5	Conclusion	123
6	References	123

Summary. We describe work from our group utilizing in-situ scanning tunneling microscopy and atomic force microscopy in conjunction with additional surface characterization techniques. Systems described include catalytically active monolayers on electrode surfaces, oxygen or hydroxide adlattices on Cu, enhanced and additive-modified deposition of Cu, and molecular adsorbates on Au and Ag electrodes.

1 Introduction

The application of the scanning tunneling microscope (STM) and the atomic force microscope (AFM) to electrochemical problems over the past seven years has greatly enlivened electrochemical surface science. The salient feature of these techniques is their ability to obtain real-space images of electrode surfaces with atomic resolution. The facility of obtaining this kind of direct structural information has both confirmed

previously held ideas and provided new directions in the study of electrode surfaces. The direct structural information now available has also moved the entire field forward at a considerable pace. As seen in this volume, systems studied include those involving deposition, corrosion, monolayers, catalysis, and surface structural transformations. These systems are central to the core of electrochemical science and the scanning probe work is thus of the highest importance.

While the high real-space resolution and the ability to operate on surfaces under potential control in redox-active solutions are strengths of the scanning probe methods, there are also a number of drawbacks. The probe microscopies do not provide any discrimination between different chemical species present on the surface. To be sure, the STM can certainly distinguish between conducting, insulating, and semiconductor surfaces and the AFM can distinguish between soft and hard specimens. However, they provide no information about the specific chemical identity of the features observed. This lack should be contrasted to the plethora of chemical information available from such techniques as vibrational spectroscopy or potential-step chronocoulometry, which lack the fine spatial resolution. The scanning probe methods also lack the very high resolution available from surface x-ray scattering, but this technique requires access to a synchrotron light source, is somewhat insensitive to defects, and appears to work best on high-atomic-weight systems. Therefore, to address electrochemical systems most appropriately, a combination of techniques should be utilized.

In the early days of in-situ scanning probe microscopy (SPM) work, results were hard won and often of poor quality. As practical knowledge has accumulated in the community, this difficulty has lessened, and the large number of groups represented in this volume is only one indication of the popularity and efficacy of the techniques. In what follows, we describe some of the research areas in the Gewirth group, and indicate what we feel are directions for the future.

2 Underpotential Deposition

As indicated in several chapters in this volume, many groups have studied underpotential deposition (UPD). UPD is an electrochemical process in which monolayers or submonolayers of a foreign metal adatom are deposited on a surface at potentials positive of the reversible or Nernst potential. The UPD monolayer can be thought of as deriving from a relatively strong adatom-substrate bond formed using less energy than the subsequent adatom-adatom bonds formed during bulk deposition. The attraction of many groups to studying UPD stems not only from the relative experimental simplicity of the process and the tendency of UPD adlattice structures to

exhibit considerable structural complexity, but also from the importance of the UPD process in deposition, catalysis, and fundamental studies of monolayers [1]. We have used STM and AFM to examine several UPD lattice structures and to correlate these structures with electrochemical reactivity.

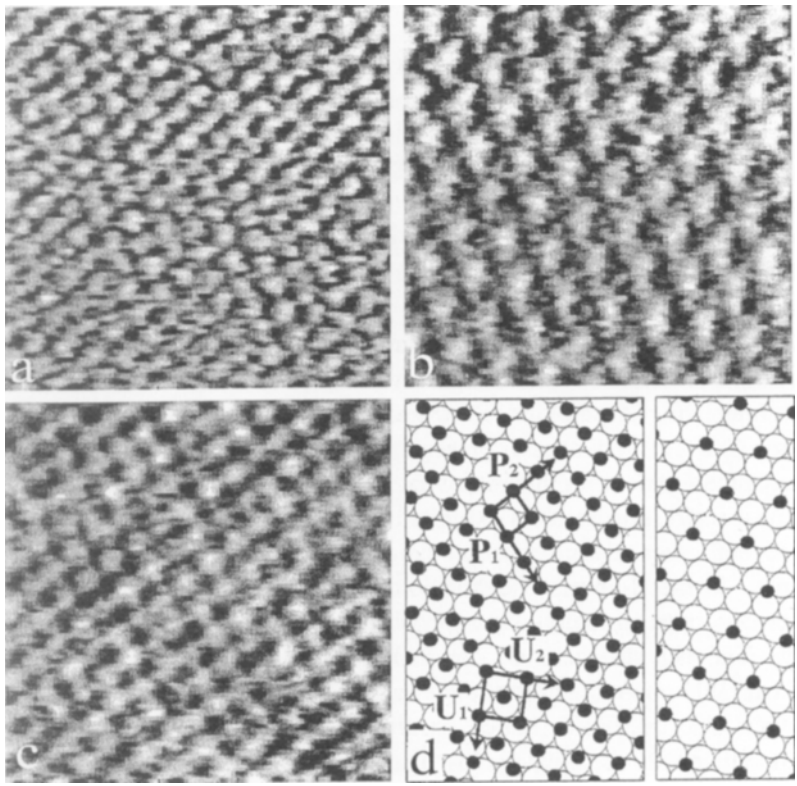

Fig. 1. AFM images (5 nm x 5 nm) of Bi UPD on Au(111) in 0.1 M $HClO_4$. (a) Au(111) surface found positive of Bi UPD. Atom-atom distance is 0.29 nm. (b) (2 x 2) Bi adlattice found at 200 mV vs $E^{\circ}_{Bi/Bi^{3+}}$. Atom-atom distance is 0.75 ± 0.02 nm. (c) Uniaxially commensurate, rectangular Bi adlattice found at 100 mV. Atom-atom distance is 0.3 ± 0.02 nm. (d) Schematic of Bi structures: left, rectangular lattice where p and p_1 are primitive and nonprimitive (designated with U in the figure) unit cell vectors, respectively; right, (2 x 2) Bi adlattice showing open Au and Bi sites. The Bi adatoms are larger than Au; They are shown smaller here for clarity. Other arrangements with the Bi in bridging ar atop sites are also possible.

A favorite example is the underpotential deposition of Bi onto Au(111). Monolayers of Bi formed through UPD on Au(111) act as catalysts for the two-electron electroreduction of H_2O_2 to H_2O in acid solutions. However, this catalytic activity occurs only in a narrow potential region [2]. There are three different lattices observed in the UPD range by AFM [3]. The first of these, obtained at the most positive potentials and shown in Fig. 1(a), exhibits a 0.29 nm atom-atom spacing and a hexagonal structure. This is the bare Au(111) lattice which should be observed at these potentials. Moving into the UPD region, a different structure is observed (Fig. 1(b)). This first monolayer of Bi on Au(111) has a 0.58 nm spacing, hexagonal structure, and exhibits no rotation relative to the underlying Au. The structure corresponds to a (2 × 2) Bi adlattice shown at the right of Fig. 1(d). Finally, the third structure seen prior to bulk deposition of Bi is shown in Fig. 1(c). The lattice has now changed to a "uniaxially commensurate" (p × $\sqrt{3}$) structure which exhibits a $\sqrt{3}$ spacing in one direction (p_2 in Fig. 1(d) (left)) but is incommensurate in the p_3 direction. These structures have been confirmed by the completely independent Surface X-ray scattering technique [4]. Interestingly, peroxide electroreduction occurs only in the potential region where the (2 × 2) Bi adlattice is present. This suggests that both substrate and adatom sites are a requirement for this reactivity.

One of the most interesting features exhibited in the UPD process described above and found in several other adatom-substrate pairs is the existence of "open" adatom lattice structures. In metal-on-metal depositions performed in the ultrahigh-vacuum (UHV) environment, open structures are never observed in the absence of formation of a surface alloy. Yet such structures are common in the electrochemical environment. In the case of Cu UPD on Au(111) in the presence of sulfate, considerable effort has shown that the ($\sqrt{3}$ × $\sqrt{3}$)R30° lattice exhibited by this system forms due to coadsorption of sulfate with the UPD Cu [5]. The sulfate forms a ($\sqrt{3}$ × $\sqrt{3}$)R30° lattice with 1/3 monolayer coverage, while the Cu atoms are arranged in a honeycomb lattice exhibiting a 2/3 surface coverage [6]. UPD of Ag on Au(111) exhibits packing densities which correlate inversely with the size of the anion, with smaller anions giving rise to higher packing densities [7]. In the Bi case described above the same (2 × 2) lattice structure forms, regardless of the anion present in solution. We first thought that this behavior implied that the open structure resulted not from anion coadsorption, but rather from electrostatic repulsion between putatively partially discharged Bi adatoms. However, recent chronocoulometric measurements performed in our laboratory clearly indicate that the Bi adatom is fully discharged [8]. These measurements also indicate that hydroxide is co-adsorbed with the Bi in a 1:2 ratio. Thus the open adlattice structure is again due to anion co-adsorption although in this case the anion is not deliberately added to the solution but rather originates from the

solvent itself. The presence of hydroxide in the potential region exhibiting maximal catalytic activity has important consequences for the mechanism of this activity [9]. More importantly, this example shows that the SPM techniques are most powerful when utilized in conjunction with other techniques providing more quantitative information about the number and type of species present on the electrode surface.

3 Cu Electrode Surfaces

Although the focus of UPD work is often on single-crystal surfaces of Au, Ag, or Pt, much important electrochemistry occurs on more technically relevant materials and materials which are less easily prepared. Work in the Gewirth group has focused on Cu surfaces with the goals of understanding aspects of Cu surface chemistry and developing relationships between this surface chemistry and the subsequent Cu bulk deposition behavior. The focus on bulk deposition of Cu is important because of the use of this process in industry.

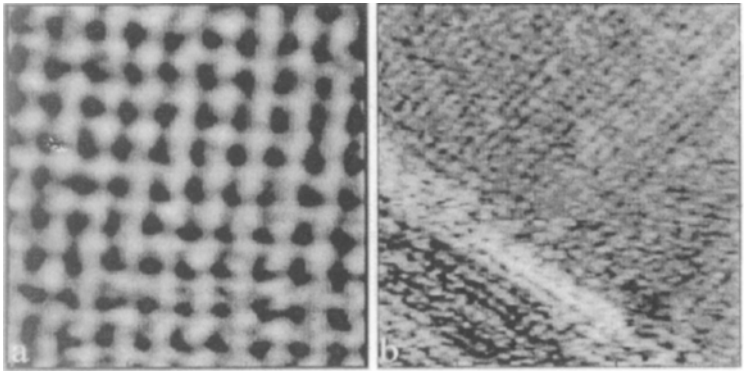

Fig. 2. (a) 3 nm × 3 nm AFM image of electropolished Cu(100) in 0.1 M $HClO_4$ at -0.45 V vs. Hg_2SO_4. The structure is square with an interatomic spacing of 0.36 nm.
(b) 9 nm × 9 nm AFM image of two-domain region with Cu(110) (upper right) and (2 × 1) rows (lower left) observed at E^o after a potential of -550 mV was applied.

Initial work examined structures formed on Cu(*h,k,l*) surfaces in the acid electrochemical environment. Figure 2 shows adlayer structures formed on the Cu(100) [10] and Cu(110) [11] electrode surfaces as imaged by in- situ atomic force microscopy. On the Cu(100) surface a $(\sqrt{2} \times \sqrt{2})R45°$ adlattice structure was observed at all but the

most negative potentials. This ($\sqrt{2} \times \sqrt{2}$)R45° structure was anion independent and appeared even when rigorous measures were taken to exclude Cl^- from the electrolyte. The structure was thus associated with O or OH^- adsorbed on the surface. However, the same ($\sqrt{2} \times \sqrt{2}$)R45° structure appeared when Cl^- was deliberately added to the solution, which complicated definitive assignment of these features. On Cu(111) surfaces, only a diffuse structure was observed, which is considerably different from the ($\sqrt{3} \times \sqrt{3}$)R30° adlattice formed on the surface following deliberate addition of Cl^- [12]. In order to show definitively that the adlattice structures were not associated with Cl^-, we imaged Cu(110) single crystals in aqueous solutions during the initial stages of oxidation. Images obtained in pH 2.5-2.7 $HClO_4$ and H_2SO_4 solutions revealed the growth of oxide monolayers consisting primarily of [001] oriented chains (Fig. 2(b)). A majority of these chains (ca. 70%) were arranged in (2 × 1) and (3 × 1) structures. Images obtained following addition of Cl^- yielded a completely different structure. These observations strongly indicate that the adlattices observed on the Cu(100) and Cu(110) surfaces are not related to ad-ventitious Cl^-, but rather are associated with O or OH^- as an adsorbate. The (n × 1) structures found on the Cu(110) surface are in

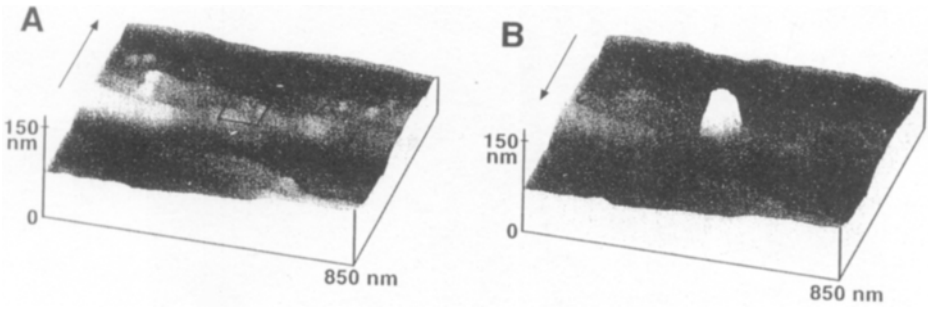

Fig. 3. 850 nm × 850 nm AFM images showing the Cu surface before and after enhanced electrochemical deposition of Cu. (A) The Cu(110) surface under open-circuit conditions in an $HClO_4$ solution (pH = 2.45) prior to deposition. The black square outlines the region in which the AFM tip was scanned during deposition. (B) After the deposition caused by a potential step of -70 mV, a single 60 nm-high feature was evident on the surface.

addition strongly reminiscent of the structures formed in the UHV environment following exposure of the surface to small amounts of oxygen. However, definitive identification of these adlattices must await interrogation of these surfaces with a chemically sensitive probe. Both the ($\sqrt{2} \times \sqrt{2}$)R45° and the chain structures were

observed in the thermodynamically forbidden region for copper oxide in the pH-potential phase diagram, which indicates that stable oxide monolayers develop prior to bulk oxide formation. In turn, this has important consequences for interaction of Cu surfaces with bulk plating additives and other adsorbates.

During the course of our work on Cu adsorbate systems, we discovered that the AFM tip-sample interaction could enhance Cu electrodeposition on Cu single-crystal electrodes [13, 14]. Figure 3 shows a sequence of AFM images taken before and after electrodeposition of Cu with concurrent scanning of the AFM tip at high force in a restricted spatial region. The image in Fig. 3(b) clearly shows that Cu deposition occurs preferentially in the area in which the AFM tip was scanning; the magnitude of this enhancement is approximately 15-folg. The magnitude of the enhanced deposition effect depends primarily on tip-sample force, crystallographic orientation, and solution pH. Enhanced Cu deposition is stronger on Cu(110) than CU(111) which correlates with the reactivity of these orientations towards oxide monolayer formation, described above. For a specific orientation, enhanced Cu deposition becomes less pronounced with decreasing solution pH. These results are consistent with a modification mechanism in which partially passivating oxide layers mediate both normal and enhanced Cu deposition. The AFM tip-sample force physically creates defects in these adlayers, thus forming active sites for Cu adsorption.

Finally, we have examined bulk Cu electrodeposition from acidic solutions both with and without organic additives [15]. The electrodeposited surfaces were analyzed quantitatively by scaling analysis of electrodeposited surface roughness during the course of deposition and by modeling the spectral power density (SPD) of the surface shape evolution. These analyses provide insight into the specific mechanisms giving rise to the observed textures. Deposition from additive-free solutions (Fig. 4(a)) leads to rough surface textures due to roughening originating from surface diffusion. Addition of benzotriazole (BTA), a commonly used organic additive, acts to smooth the deposit (Fig. 4(b)) by diminishing surface diffusion. Deposits grown from thiourea-containing solutions (Fig. 4(c)) exhibit formation of three-dimensional islands atop initially flat plates, reflecting a two-stage growth mechanism. These results emphasize the close interplay between molecular functionality and gross topology of the growing electrodeposit.

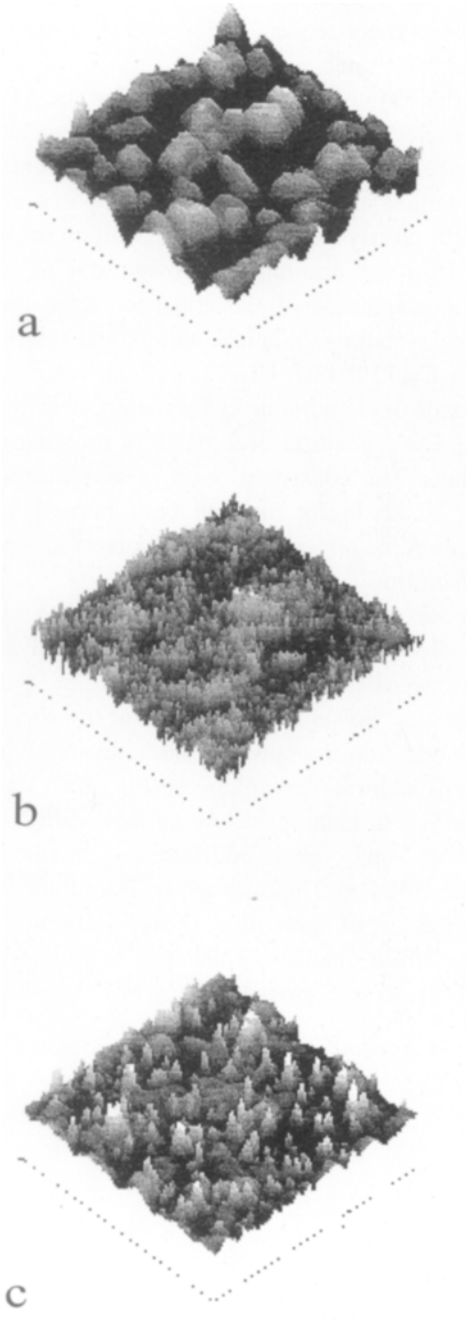

Fig. 4. 15 μm x 15 μm AFM images of electrodeposition of Cu on Au(111) at a current density of 0.8 mA/cm^2 for a coverage of 0.375 C from solutions of 0.05 M $CuSO_4$ in (a) 0.25 M H_2SO_4 + 100 μM BTA;(c) 0.25 M H_2SO_4 + 100 μM thiourea.

4 Molecular Adsorbates

The results shown above indicate a rich interplay between adsorbates and the electrode surface. Early efforts directed at imaging organic molecules on surfaces were hampered by ill-defined surface chemistry and agglomeration of adsorbates. However, within the past two years, several groups, many of which are represented in this volume, have reported images of a variety of adsorbates on electrode surfaces. Because the diversity of organic and inorganic adsorbates is so large and because molecular transformations are crucial to devices as important as sensors and fuel cells, these studies will continue to have importance for some time.

We used the STM to monitor the electrooxidation of phenoxide to oligophenol on Au(111) in alkaline solutions [16]. Prior to oxidation, phenol associates as phenoxide to Au(111) in a $(\sqrt{3} \times \sqrt{3})R30^{o}$ structure with the molecule oriented end-on through the O atom (Fig. 5(a), 5(b)). After oxidation, a disordered, close-packed array of oxidation products consisting of monomers, dimers, trimers, and a few higher oligomers is observed (Fig. 5(c)). The oxidation products are oriented with the ring roughly parallel to the electrode surface. Complementary IR studies conducted prior to oxidation confirmed the nonparallel orientation of the ring relative to the electrode surface and showed that the orientation of the molecule does not change with potential through the double-layer region of the voltammetry. These results provide structural insight into one of the transformations that organic molecules can undergo on electrode surfaces.

We have also examined adsorption of inorganic molecules on electrode surfaces [17]. Figure 6 shows the $c(5 \times 3\sqrt{3})$ structure formed by the self-assembly of α-dodecatungstosilicate, α-$Si_{12}O_{40}^{4-}$. These molecules spontaneously form adherent, passivating, monolayer-thick, ordered molecular arrays on Ag(111) surfaces upon immersion of the surfaces into an aqueous solution of the acid. These monolayers represent the first example of inorganic monolayer self-assembly and provide a way to derivatize surfaces with inorganic functionality. Polyoxometalates are known to function not only as superacids in cases like α-$H_4SiW_{12}O_{40}$ but also as ion exchangers, corrosion inhibitors, electron transfer reagents, catalysts, and photochemical oxidants. Since they can accommodate a wide range of organic, organometallic, and inorganic functional groups, we anticipate widespread interest in these and other classes of inorganic molecules as self-assembled monolayers.

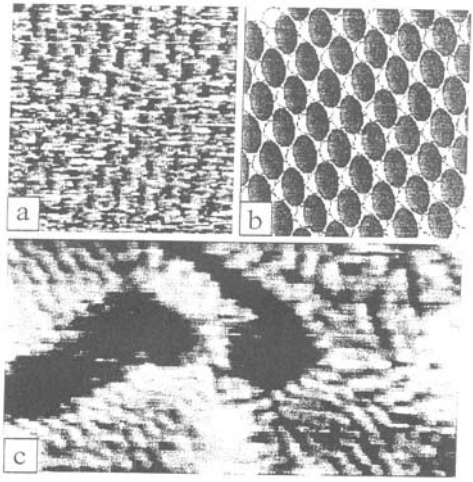

Fig. 5. (a) 4.5nm × 4.5nm STM image of the phenoxide structure on Au(111) at +50 mV vs. NHE. Spacing is 0.5 ± 0.02 nm and corresponds to a $(\sqrt{3} \times \sqrt{3})R30°$ overlayer. I_{tip} = 2 nA, E_{tip} = 28 mV. (b) Model of the phenoxide overlayer showing the underlying Au(111) lattice. Open circles represent Au, while filled ovals represent phenoxide. (c) 10 nm × 20 nm STM image of oligomers on Au(111) at +340 mV vs. NHE, following the electrooxidation of phenoxide by sweeping potential to +600 mV. Molecule width is 0.72±0.1 nm and length varies from 0.8 to 2.5 nm. I_{tip} = 2 nA, E_{tip} = 355 mV.

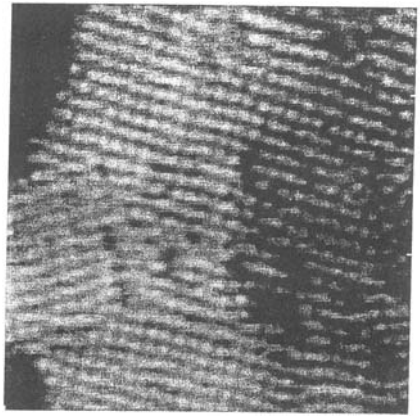

Fig. 6. 28 nm × 28 nm STM image of a monolayer of α-$SiW_{12}O_{40}^{4-}$ on an Ag(111) surface in 0.1 M $HClO_4$. I_{tip} = 2.7 nA, E_{tip} = 100 mV.

5 Conclusion

The results presented above, and in the other chapters in this volume, show that SPM studies of electrode surfaces have progressed into maturity. The probe methodology provides important structural information so that many salient issues surrounding the electrified solid-liquid interface can be addressed. The novelty of in -itu imaging with atomic resolution is no longer as great as it was and it is clearly appropriate now to focus on overriding problems in electrochemical surface science. Addressing these problems will require the use of many complementary techniques. Present-day studies focus on problems that are longstanding in electrochemistry. These include the structure of UPD adlayers and their correlation with reactivity, the texture of bulk deposits following addition of standard additives, and adsorption of small model molecules to surfaces. Except through serendipity, successful completion of these studies will not yield technologically relevant advances such as room-temperature direct-methanol-oxidation fuel cells or a universal, robust plating additive. Future efforts must therefore use the structural insight gained from these studies to directly address these important technological goals. These can only be resolved through surface synthetic programs which will make real contributions to electrochemical surface science.

Acknowledgment. This work was funded by the Department of Energy (DE-FG02-91ER45349) through the Frederick Seitz Materials Research Laboratory at the University of Illinois.

6 References

[1] D.M. Kolb in Advances in: Electrochemistry and Electrochemical Engineering; (H. Gerischer, C.W.Tobias (Eds.)), Wiley, New York, 1978, Vol. 11, pp. 125-271.
[2] S.M. Sayed, K. Jüttner, Electrochim. Acta 28, 1635-1641 (1983).
[3] C.H. Chen, A.A. Gewirth, J. Am. Chem. Soc. 114, 5439-5440 (1992).
[4] C.H. Chen, K.D. Kepler, A.A. Gewirth, B.M. Ocko, J. Wang, J. Phys. Chem. 97, 7290-7294 (1993).
[5] Z. Shi, J.Lipkowski, J. Electroanal. Chem. 365, 303-309 (1994) and references therein.
[6] M.F. Toney, J.N. Howard, J. Richer, G.L. Borges, J.G. Gordon, O.R. Melroy, Phys. Rev.Lett. 75, 4472-4475 (1995).
[7] C.-H. Chen, S.M. Vesecky, A.A. Gewirth, J. Am. Chem. Soc. 114, 451-458 (1992).

[8] B.K. Niece, A.A. Gewirth, Langmuir 12, 4909 (1996).
[9] R.R. Adzic, in: Proc. Workshop on Structural Effects in Electrocatalysis and Oxygen Electrochemistry, D.Scherson, D.Tryk, M.Daroux, X.Xing (Eds.), The Electrochemical Society, Inc., Pennington, NJ, 1992, Vol. 92-11, pp. 419-433.
[10] B.J. Cruickshank, D.D. Sneddon, A.A.Gewirth, Surf. Sci. Lett.. 281, L308-L314 (1993).
[11] J.R.LaGraff, A.A.Gewirth, Surf. Sci. Lett. 326, L461-L466 (1995).
[12] W. Suggs, A.J. Bard, J. Am. Chem. Soc. 116, 10725 (1994).
[13] J.R. LaGraff, A.A. Gewirth, J. Phys. Chem. 98, 11246 (1994).
[14] J.R. LaGraff, A.A. Gewirth, J. Phys. Chem. 99, 10009 (1995).[15]
[15] W.U. Schmidt, R.C. Alkire, A.A. Gewirth, J. Electrochem. Soc. 143, 3122 (1996).
[16] K.M.Richard, A.A. Gewirth, J. Phys. Chem. 99, 12288-12293 (1995).
[17] M. Ge, B. Zhong, W. Klemperer, A.A. Gewirth, J. Am. Chem. Soc. 118, 5812 (1996).

Electrochemical Nanotechnology
In-situ Local Probe Techniques at Electrochemical Interfaces
Edited by W. J. Lorenz and W. Plieth

Scanning Probe Microscopy Studies of Molecular Redox Films

James E. Hudson, Héctor D. Abruña

Contents

1	Introduction		125
2	Structural studies of molecular redox films		126
	2.1	Covalent binding	127
	2.2	Polymerization	129
	2.3	Self-assembly	130
3	Electrochemical force spectroscopy		132
4	Conclusions		134
5	References		135

Summary. Scanning probe microscopy studies of electrodes chemically modified with electroactive transition metal complexes are described. Emphasis is placed on scanning tunneling microscopy and electrochemical scanning tunneling microscopy studies of their structure and dynamics of formation and on electrochemical force spectroscopy studies of their electrochemical potential dependent chemical properties.

1 Introduction

Nanotechnology is a burgeoning field which strives to push electronic and mechanical devices to their ultimate lower limit, the atomic scale. The explosive growth of research in this field over the past decade has proliferated the development of a variety of interdisciplinary approaches to molecular engineering and molecular electronics [1]. Electrochemistry, as a bridge between chemistry and electronics, is uniquely positioned

to advance the development of nanotechnology, particularly molecular electronics [2]. Electroactive molecules show considerable promise as nanotechnological building blocks due to the fact that the electrode potential can be employed as a means to induce transformations in their chemical, electronic, and/or structural properties. The ability to adsorb or chemically bind electroactive molecules to the surface of electrodes, the focus of considerable research effort over the past 25 years, represents an important first step toward molecular electronics [3 - 5].

Molecular redox films have already been incorporated into the design of thin-film batteries and electrochromic displays and are being developed for use in a variety of additional technologies including drug delivery, chemical sensing, and catalysis. Also, diode and field-effect transistor behavior has been demonstrated in systems integrating redox films with different electronic properties [6 - 7]. However, despite the many advances in the design and synthesis of molecular redox films, comparatively little is known about their electronic or molecular structure. The clear need for a deeper understanding of these systems necessitates the use of ultra-high resolution techniques such as scanning probe microscopy (SPM).

Since its inception, SPM has revolutionized the field of surface science and has provided an extraordinary impetus to nanotechnology by enabling the visualization of molecular structures with resolution at or approaching the atomic level [8 - 10]. The ability to operate this class of techniques in the presence of electrolyte solution has further benefited the interfacial sciences by facilitating in-situ studies of potential dependent variations of surface morphology [11]. In this brief account, we present a general overview of our efforts using scanning tunneling microscopy (STM), electrochemical scanning tunneling microscopy (electrochemical STM), and electrochemical force spectroscopy to study structural and chemical properties of molecular redox films.

2 Structural Studies of Molecular Redox Films

A vast literature exists describing numerous strategies for the adsorption and binding of electroactive molecules to electrode surfaces. Of those, the most commonly employed are covalent binding, polymerization, and self-assembly [2 - 5]. In this section, we briefly discuss the utility of these three immobilization techniques for studying redox-active species by STM and electrochemical STM, and present examples from our own studies.

For STM of molecular redox films, theoretical models predict enhanced tunneling through redox-active centers via resonant tunneling modes; specifically, reorganizations of the inner-sphere vibrational modes should significantly contribute to

the tunneling current [12 - 14]. It is notable, however, that the observation of anomalous molecular corrugation for several electroactive self-assembling monolayers by Kim et al. [15] and our own observation of weak contrast for a self assembling redox-active osmium complex [16] suggest that the contrast mechanism is the result of several factors.

2.1 Covalent Binding

A convenient method of preparing molecular redox films is by covalently bonding them directly to an electrode surface. These techniques typically yield stable, disordered molecular films at coverages close to a monolayer. Numerous chemical strategies exist to covalently immobilize electroactive molecules to an electrode surface. A common one utilizes 1,3-dicyclohexylcarbodiimide (DCC), a dehydrating agent developed for peptide synthesis which facilitates amide bond formation between a primary amine and a carboxylic acid [17]. In a typical approach, the electrode is first chemically treated to generate a chemically reactive surface (with either the amine or carboxylic acid) and subsequently immersed into a solution containing DCC and a reactive redox molecule with a complementary pendant amine or carboxylic acid. Examples of covalent immobilization on Au(111) and highly oriented pyrolytic graphite (HOPG) electrodes using DCC are detailed below

Figure 1(A) shows a typical electrochemical STM image for an Au(111) electrode which was first modified with a monolayer of 3-mercaptopropionic acid (to form a carboxylate-terminated surface) followed by immersion overnight in a solution containing DCC and [Os(2,2'-bipyridine)$_2$ [4-(aminomethyl)pyridine]Cl] (Fig. 1(B)). The high-contrast regions, commonly observed in these systems, most likely correspond to aggregates of the transition-metal complex, though it is not clear why aggregation occurs. A disadvantage of using this immobilization technique for STM studies is that it gives rise to disordered, chemically inhomogeneous surfaces which make image interpretation difficult.

Sample homogeneity can be somewhat assured by using thermally oxidized HOPG as a substrate. Upon heating in the presence of oxygen, ketogenic oxidation causes the formation of pits and defects on the HOPG surface [18], enabling electroactive species to be directly bound to the step edges and defects using DCC. The disadvantage of this approach lies in image validation, since molecular species immobilized onto a step edge are often indistinguishable from the step itself. However, it is possible to find isolated molecular species which are bound directly to defects (or small, incipient pits). Figure 2(A) shows a single Fe(CN)$_5$[4-(aminomethyl)pyridine] molecule (Fig. 2(B))

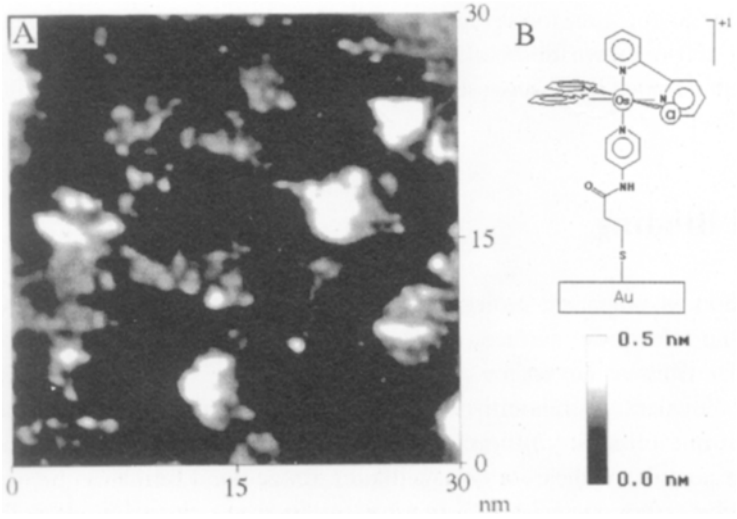

Fig. 1. (A) Unfiltered electrochemical STM image, taken in 0.1 M $KClO_4$ electrolyte solution, of an Au(111) electrode modified with $[Os(bpy)_2[4\text{-(aminomethyl)pyridine}]Cl](PF_6)$ using 3-mercapto-propionic acid and DCC. Tip bias = -50 mV, tunneling current = 1.0 NA, scan rate 5.1 Hz. (B) Structure and proposed binding mode of the covalently immobilized osmium complex.

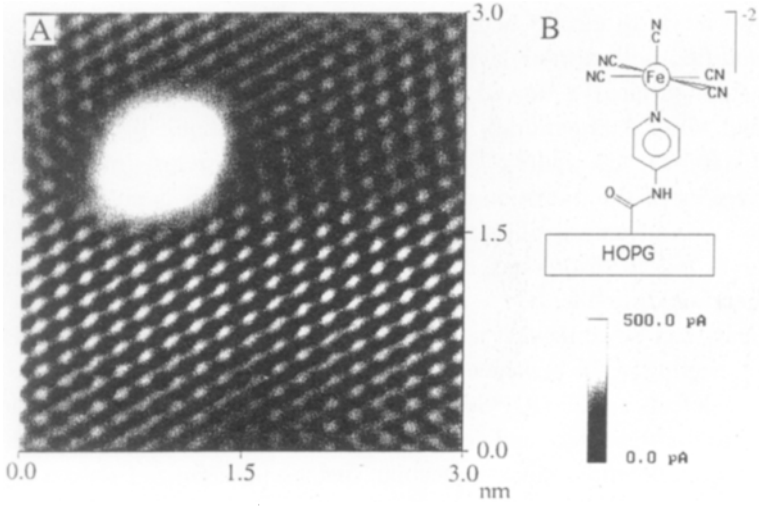

Fig. 2. (A) Fourier filtered ex-situ STM image, taken in constant-height mode, of a thermally oxidized HOPG electrode modified with $K_2[Fe(CN)_5$ [4-(aminomethyl)pyridine]] using DCC as a coupling reagent. Tip bias = -50 mV, tunneling current = 1.0 nA, scan rate = 30.5 Hz. (B) Structure and proposed binding mode of the covalently immobilized iron complex.

which was immobilized onto a thermally oxidized HOPG surface using DCC. The diameter of the imaged molecule (~10 Å) is somewhat larger than the calculated diameter of the transition metal heads group (~7 Å). We ascribe this difference to molecular motions by the tethered molecule. Similar effects have been reported by other investigators [19].

2.2 Polymerization

Electrode modification through electrochemical or chemical deposition of redox-active polymers is another area of active research since these methods typically produce highly stable films which can be prepared in thicknesses varying from nanometers to microns [20]. Polymer films are, however, not well suited for study by STM since the resulting structures are molecularly rough and often poorly conducting, especially at high coverages. Also, as is common for weakly bound molecular adsorbates, polymer films often have high surface mobility (compared with the time required to obtain an STM image) and are susceptible to tip induced interactions [21].

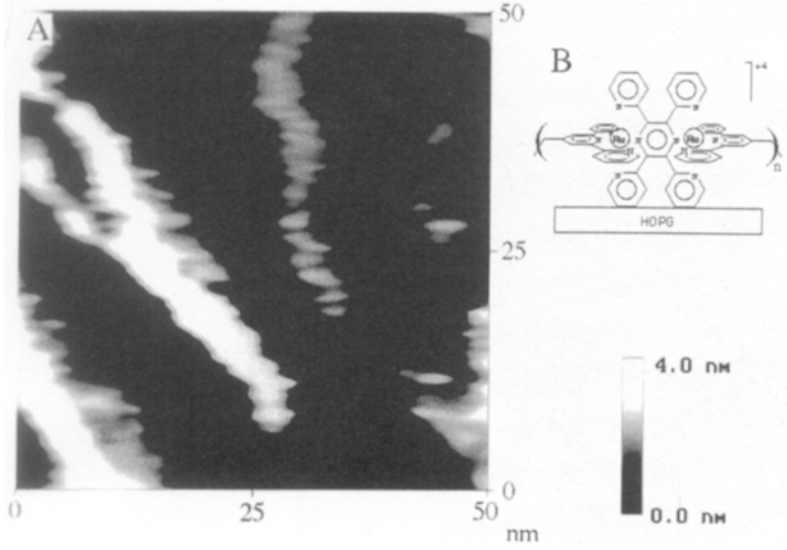

Fig. 3. (A) Unfiltered ex-situ STM image of an HOPG electrode modified with an electropolymerized film of $[[(v\text{-}tpy)Ru]_2(tppz)](PF_6)_4$. Tip bias = 100 mV, tunneling current = 500 pA, scan rate = 60.3 Hz. (B) Structure of the symmetric ruthenium polymer.

This is exemplified in Fig. 3(A), which shows a representative STM image of [((v-tpy)Ru)$_2$(tppz)](PF$_6$)$_4$ (v-tpy is 4'-vinyl-2,2':6',2"-terpyridine, tppz is 2,3,5,6-tetrakis(2-pyridyl)pyrazine; Fig. 3(B)) electropolymerized onto an HOPG substrate according to a previously published procedure (coverage of approximately 75% of one equivalent monolayer). The poor resolution and streaking in the image, probably the result of tip-induced interactions, prevent the visualization of any discernible atomic structure. As a final note, image validation can be difficult for these systems since surface features such as defects and step edges can mimic molecular aggregates and polymer strands under certain conditions in the STM [23].

2.3 Self-assembly

The incorporation a redox-active transition metal head group into a self-assembling molecule provides a ready means for the immobilization of transition-metal complexes onto an electrode surface [13, 24]. Unlike other approaches to immobilization which generally yield rough, unordered arrays of molecules, self-assembly techniques can produce well-ordered, atomically smooth molecular arrays.

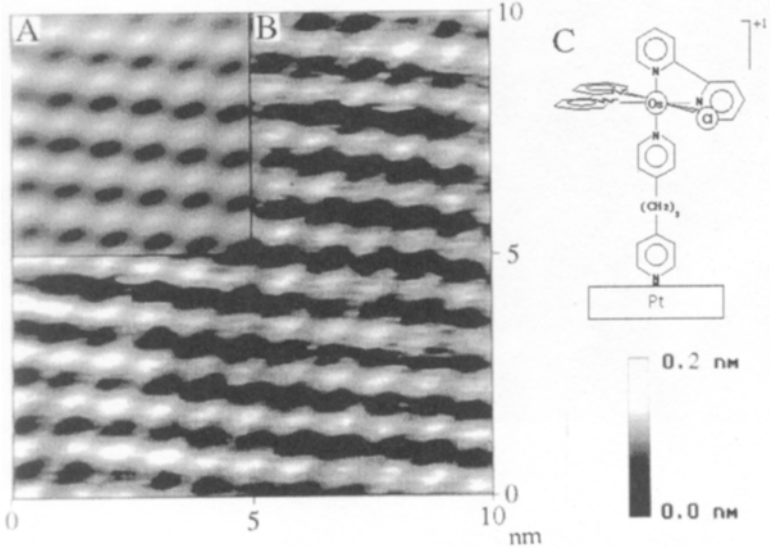

Fig. 4. Molecularly resolved ex-situ STM image of an Osdipy monolayer adsorbed onto a Pt(111) electrode: (A) Fourier-filtered and (B) unfiltered. Tip bias = -150 mV, tunneling current = 500 pA, scan rate = 20 Hz. (C) Chemical structure and proposed binding mode of the Osdipy complex.

The self-assembling complex $[Os(bpy)_2(dipy)Cl](PF_6)$ (bpy is 2,2'-bipyridine, dipy is trimethylene-4,4'-bipyridine; abbreviated as Osdipy; Fig. 4(C)) chemisorbs onto platinum and gold surfaces through a dangling pyridine ring with a free energy of adsorption of the order of -50 kJ/mol to form well-ordered, redox-active monolayers

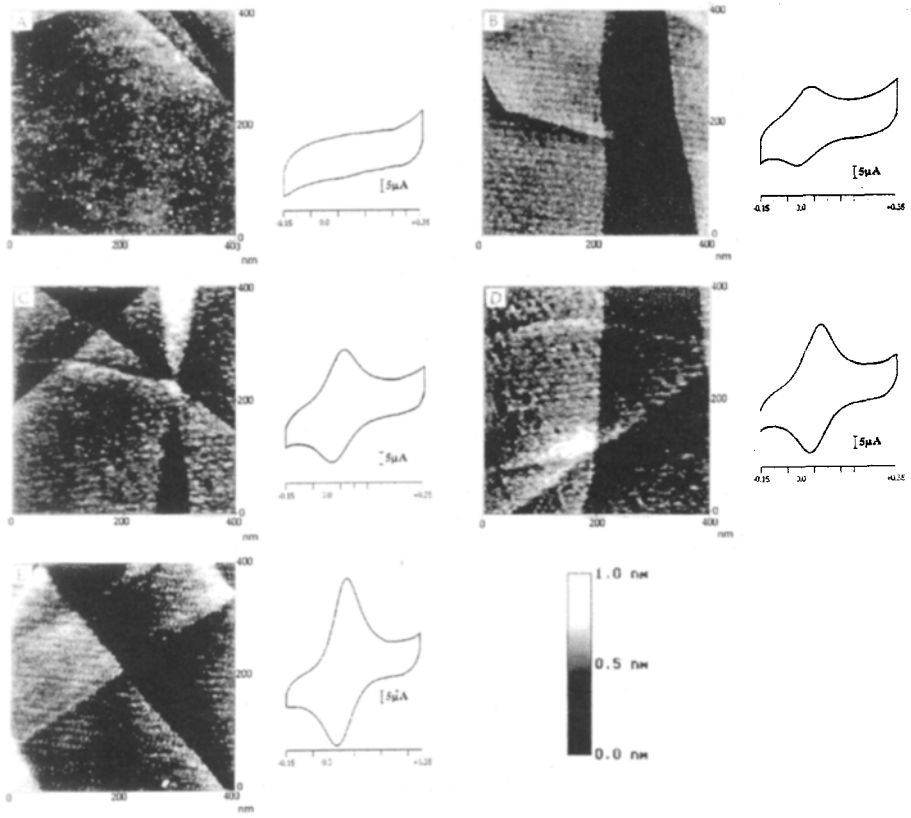

Fig. 5. electrochemical STM images of a Pt(111) surface during the deposition of Osdipy from a 0.1 M $KClO_4$ electrolyte solution with corresponding cyclic voltammograms taken immediately upon withdrawing the tip from the electrode surface. The integrated charge corresponds to (A) 0%, (B) 25%, (c) 49%, (D) 66%, and (E) 100% of a full monolayer. Tip bias = 50 mV, tunneling current = 2.5 nA, scan rate = 8.3 Hz.

which are stable on the electrode surface in a wide range of solvents and electrolytes [25 - 27]. A representative unfiltered ex-situ STM image, taken in air, of an adsorbed

Osdipy monolayer deposited onto a Pt(111) substrate is shown in Fig. 4(B). The image clearly shows molecular-scale features in a rectangular close packed array with unit cell dimensions of 9.3Å by 12.4Å. These dimensions were found to be in excellent agreement with model calculations which assume that the head groups preferentially line up along their dipole [16].

The reversible redox activity enables the straightforward determination of adsorbate coverage at any point during the deposition process by integration of the charge under the voltammetric wave. In an effort to elucidate the mechanism of Osdipy monolayer formation, we utilized electrochemical STM to monitor simultaneously the coverage and structure of the depositing Osdipy layer. A typical series of electrochemical STM images with corresponding cyclic voltammograms (which exhibit the characteristic reversible metal-based oxidation of the transition-metal head group of Osdipy) are shown in Fig. 5.

Combining our electrochemical STM data with the results of previous voltammetric studies, we were able to determine that the monolayer forms through the random decoration of the electrode surface by the Osdipy adsorbate. The electrostatic repulsions between neighboring adsorbate molecules (each molecule carries a net positive charge), combined with the high mobility across the sample surface, causes the submonolayer to spread uniformly across the sample surface. At higher coverages, regions of the adsorbate layer lose part of their solvation to accommodate the increasing coverage (and perhaps counter ions) and become more tightly packed. This leads to the possible formation of domains within the submonolayer structure which appear as recessed defects. The high-density regions continue to grow, possibly by coalescing, until the full monolayer is formed. These observations are supported by electrochemical quartz crystal microbalance studies which show a large decrease in Osdipy solvation at high coverages [28]. Due to the rapid reordering of the adsorbate on the electrode surface, it was not possible to obtain molecularly resolved images of the full monolayer in electrolyte solution.

3 Electrochemical Force Spectroscopy

Force spectroscopy, though originally conceived as a tool for calibrating the atomic force microscope, has become an invaluable tool for studying adhesive interactions on the nanometer scale [29 - 31]. In force spectroscopy the deflection of an atomic force microscopy (AFM) tip is measured as a sample is moved into and then out of contact with the tip. The characteristic hysteresis observed as the sample is retracted is due to adhesion between the tip and sample. The point at which the adhesion is broken and the AFM tip pulls off the sample surface is characterized by a sharp discontinuity in the

force plot. The magnitude of this discontinuity provides a direct measure of the adhesion force between the tip and the sample with near-piconewton resolution.

We have utilized force spectroscopy in electrolyte solution to perform the first study of the potential-dependent adhesion between two electroactive polymer films immobilized onto electrode surfaces. A schematic of the experimental apparatus is shown in Fig. 6(A). A gold foil and gold-coated AFM tip, modified with a 35 nm-thick film of poly(vinylferrocene) (PVF) [32, 33], were grounded together and kept under potential control in a 0.10 M aqueous $KClO_4$ solution. Force measurements were performed while holding the potential of the tip and substrate either negative or positive of the PVF oxidation wave (E = +0.05 V vs. polished silver) corresponding to the neutral and oxidized forms of the polymer film respectively.

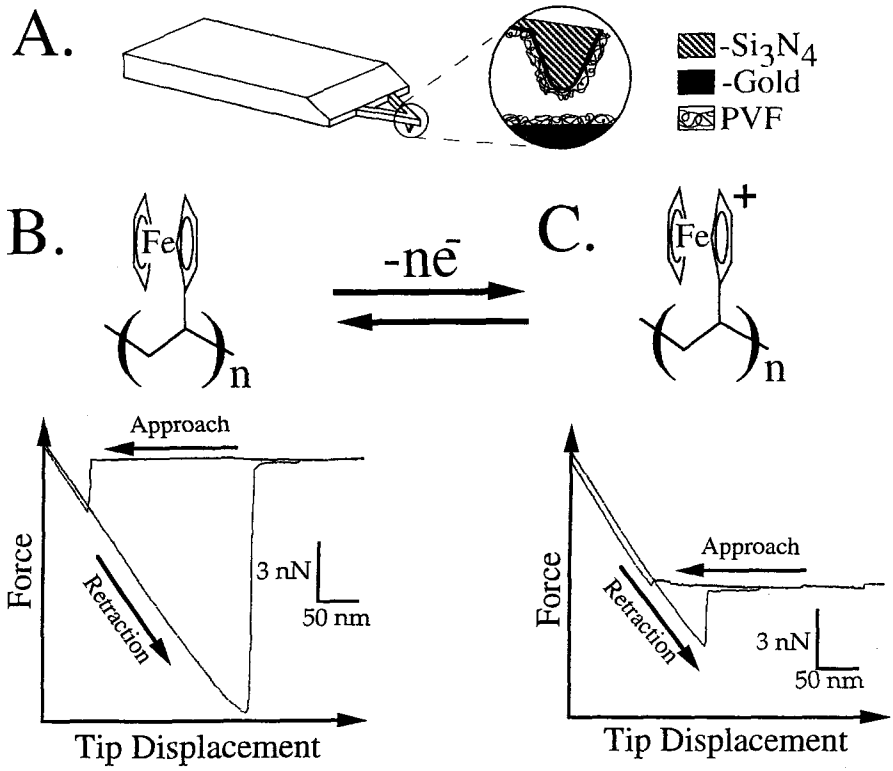

Fig. 6. (A) Schematic representation of a gold substrate and gold-coated AFM tip, modified with a thin film of poly(vinylferrocene) (PVF). The tip and film were mounted inside a glass fluid cell in an atomic force microscope and held under potential control. Also shown are typical force curves for (B) the interaction between neutral polymer films and (C) interactions between oxidized polymer films.

Force spectroscopy measurements between neutral polymer films (Fig. 6(B)) show significantly higher adhesion than do measurements between oxidized polymer films (Fig. 6(C)). Statistical analysis of over 100 consecutive force curves for each type yielded an average adhesion force of 12.2 ± 0.3 nN for the neutral polymer films and 3.2 ± 0.4 nN for the oxidized polymer films. The large difference in adhesion force was ascribed primarily to differences in solvation energies and electrostatic interactions. The unique ability to control the degree of adhesion at an AFM tip was exploited in the construction of a novel nanoscale mechanical switch [34]. By carefully closing the scan range of a continuous force plot between neutral polymer films, the AFM tip could be positioned into the region of the force plot immediately prior to where the tip pulls off the sample surface. By stepping the electrochemical potential to oxidize the polymer films, the drastic decrease in adhesion causes the tip to be released from the sample surface. This experiment serves as a model for a unique way to effect a mechanical change by formation of an electrochemically reversible bond. Switches of this type could ultimately be designed to activate under the response of a single electron.

The ability to remotely control the surface chemistry of an AFM tip, as we have done, represents a convenient method for studying potential-dependent chemical properties of molecular redox films and evidences the utility of redox molecules in nanotechnology.

4 Conclusions

Investigations of molecular redox films are of fundamental importance to numerous technologies. Scanning probe microscopy, in combination with electrochemistry, is uniquely suited to provide invaluable information concerning the potential-dependent structural, chemical, and electronic properties on these systems.

Acknowledgments. This work was supported by the Office of Naval Research (AASERT Program) and the National Science Foundation (Grant No. DMR-9107116). We are grateful to the Materials Science Center at Cornell University for the use of their AFM and STM facilities. J.E.H. acknowledges support by a Department of Education Fellowship and an NSF training grant.

5 References

[1] Engineering in a small world: from atomic manipulation to microfabrication, Science 254, 1300 (1991).
[2] A.J. Bard, Integrated Chemical Systems, Wiley-Interscience, New York, 1994.
[3] R.Murray (Ed.), Molecular Design of Electrode Surfaces, Techniques in Chemistry Series No. 22; Wiley-Interscience, New York, 1992.
[4] H.D. Abruña, Coord. Chem. Rev. *86*, 135 (1988)
[5] A.J.Bard, H.D.Abruña, C.E.Chidsey, L.R.Faulkner, S.W.Feldberg, K.Itaya, M.Majda, M. Melroy, R.W.Murray, M.D.Porter, M.P.Soriaga, H.S.White, J. Phys. Chem. 97, 7147 (1993).
[6] G.P. Kittleson, H.S. White, M.S. Wrighton, J. Am. Chem. Soc. *107*, 7373 (1985).
[7] C.E.D. Chidsey, R.W. Murray, Science 231, 25 (1986).
[8] D.R. Louder, B.A. Parkinson, Anal. Chem. 66, 84R (1994).
[9] H.D. Abruña, J. Hossick Schott, J.E. Hudson, S.R. Snyder, H.S. White, Comments Inorg. Chem. 15(3-4), 171 (1994).
[10] J. Frommer, Angew. Chem. Int. Ed. Engl. 31, 1298 (1992).
[11] Nanoscale Probes of the Solid/Liquid Interface; A.A. Gewirth, H. Siegenthaler (Eds.); Kluwer Academic Publishers: Dordrecht, 1995.
[12] S. Richter, S. Y. Manassen, J. Phys. Chem. 98, 2941 (1994).
[13] S.M. Lindsay, O.F. Sankey, Y. Li, Y., C. Herbst, J. Phys. Chem, 94, 4655 (1990).
[14] W. Schmickler, Surf. Sci. 295, 43 (1993).
[15] Y.-T. Kim, R.L. McCarley, A.J. Bard, J. Phys. Chem. 18, 7416 (1992).
[16] J.E. Hudson, H.D. Abruña, J. Phys. Chem. 100, 1036 (1996).
[17] J.C. Sheehan, G.P. Hess, J. Am. Chem. Soc. 77, 1067 (1955).
[18] D.L Patrick, V.J. Cee, T.P. Beebe, Jr., Science 265, 231 (1994).
[19] J. Hossick Schott, C.R. Arana, H.D. Abruña, H. Hurell Petach, C.M. Elliot, H.S. White, J. Phys. Chem. ,5222 (1992).
[20] M. Stamm, Adv. Poly Sci.. 100, 357 (1992).
[21] G.J. Legget, C.J. Roberts, P.M. Williams, M.C. Davies, D.E. Jackson, S.J.B. Tendler, Langmuir 9, 2356 (1993).
[22] C.R. Arana, H.D. Abruña, Inorg. Chem. 32, 194 (1993).
[23] W.M. Heckl, G. Binnig, Ultramicroscopy 42-44, 1073 (1992).
[24] J.D. Swalen, D.L. Allara, J.D. Andrade, E.A. Chandross, S. Garoff, J. Isreaellachvili, T.J. McCarthy, R. Murray, R.F. Pease, J.F. Rabolt, K.J. Wynne, H. Yu, Langmuir 3, 932 (1987).
[25] D. Acevedo, H.D. Abruña, J. Phys. Chem. 95 , 9590 (1991).
[26] D. Acevedo, R.L. Bretz, J.D. Tirado, H.D. Abruña, Langmuir 10, 1300 (1994).

[27] J.D. Tirado, D. Acevedo, R.L. Bretz, H.D. Abruña, Langmuir 10, 1971 (1994).
[28] K. Takada, H.D. Abruña, J. Phys. Chem. 100, 17909 (1996).
[29] Y.I. Rabinovich, R.-H.Yoon., Langmuir 10, 1903 (1994).
[30] E.L. Florin, V.T. Moy, H.E. Gaub, Science 264, 415 (1995).
[31] G.U. Lee, L.A. Chrisey, R.J. Colton, Science 266, 771 (1994).
[32] L. Roullier, E.J. Waldner, Electroanal. Chem 187, 97 (1985).
[33] A. Merz, A.J. Bard, J. Am. Chem. Soc. 100, 3222 (1978).
[34] J.E. Hudson, H.D. Abruña, J. Am. Chem. Soc. 118, 6303 (1996).

Electrochemical Nanotechnology
In-situ Local Probe Techniques at Electrochemical Interfaces
Edited by W. J. Lorenz and W. Plieth

New Aspects of Iodine-modified Single-crystal Electrodes

Kingo Itaya

Contents

1	Introduction	137
2	Atomic structures of iodine adlayers	139
3	Underpotential deposition	142
4	Adsorption of organic molecules	143
5	Conclusion	146
6	References	147

Summary. Structures and properties of iodine adlayers on Pt(111), Au(111), and other single-crystal electrodes are described, based mainly on our recent STM studies. The underpotential deposition of Ag on Pt(111) in the absence and presence of the iodine adlayer is also briefly described. It is shown that the iodine-modified electrodes are promising substrates for the investigation of the adsorption of organic molecules. High-resolution STM allows us to determine molecular arrangements and internal structures of molecules adsorbed on the iodine-modified electrodes in solution.

1 Introduction

The adsorption of anions such as halides, cyanide, and sulfate/bisulfate on electrode surfaces is currently one of the most important subjects in electrochemistry [1 - 3]. It is well known that various electrochemical surface processes such as underpotential deposition of hydrogen and metal ions are strongly affected by co-adsorbed anions. Particularly, structures of the iodine adlayers on Pt, Rh, Pd, Au, and Ag surfaces have

been extensively investigated using ultrahigh-vacuum (UHV) techniques such as low-energy electron diffraction (LEED) combined with electrochemical methods (electrochemical UHV technique) [1, 2]. For example, the commensurate (3x3) and ($\sqrt{7}$ x $\sqrt{7}$)R19.1° adlattices were found to form on the well-defined Pt(111) (1x1) surface, depending on the electrode potential and pH of the solution [4]. More recently, these structures were confirmed by scanning tunneling microscopy (STM) in both air [5] and solution [6-8]. Only one phase of the commensurate ($\sqrt{3}$ x $\sqrt{3}$)R30° structure was observed on Rh(111) and Pd(111) surfaces with ex-situ LEED [2, 9] and in-situ STM [10, 11].

On the other hand, it has recently been recognized that the iodine adlayer structures are more complicated on Au and Ag surfaces. Although several discrepancies concerning the iodine adlayer structure on Au(111) (I/Au(111)) can be found in the literature, surface X-ray scattering studies carried out recently by Ocko et al. revealed structural changes of I/Au(111) in KI solution in detail [12]. They found an increasing degree of compression, so-called electrocompression, of the iodine adlattice with increasing iodine coverage and electrode potential. Instead of commensurate structures found on Pt(111), Rh(111), and Pd(111) as described above, they proposed that the iodine adlayer should be characterized as two distinct series of incommensurate adlattices, a centered rectangular phase and a rotated hexagonal phase [12]. We have recently reported the structures of I/Au(111) in KI solution determined by both ex-situ LEED and in-situ STM [13, 14], which agree with Ocko et al., surface X-ray scattering results. Similar electrocompression was also found recently on Ag(111) using the LEED and in-situ STM techniques [15]. Our results clearly demonstrate that complementary use of LEED and in-situ STM is a powerful technique for determining atomic structures of the iodine adlayers on single-crystal electrodes.

It is important to note that the iodine adlayers are known to protect highly sensitive surfaces of metal single crystals from oxidation and contamination in the ambient atmosphere, providing easy preparation and handling of well-defined surfaces in many aspects during electrochemical measurements [1, 2, 9]. The iodine/CO replacement method is one of the most important usages of the iodine adlayer, to expose well-defined and clean surfaces of such electrodes as Pt and Rh in solution. The adsorbed iodine on these surfaces can be replaced by a CO adlayer. Clean surfaces are then exposed in solution by the electrochemical oxidation of CO from the surface. A further interesting property of the iodine adlayer was demonstrated by Soriaga and co-workers for the anodic dissolution of Pd electrodes [2, 11]. The site-selective anodic dissolution of Pd, so-called digital etching, was found to occur in noncorrosive electrolyte solutions such as H_2SO_4 only when the surfaces of Pd were modified by the iodine adlayer.

Furthermore, we recently disclosed an extremely interesting property of the iodine-modified electrodes for the adsorption of organic molecules. It was surprisingly found that various organic molecules such as water-soluble porphyrin and Crystal Violet were relatively strongly adsorbed and formed highly ordered molecular arrays via self-ordering on the iodine-modified electrodes in solution [16, 17]. The internal molecular structures, orientations, and packing arrangements of the ordered molecular adlayers were determined with near-atomic resolution by in-situ STM. This new finding indicates that the iodine-modified electrodes will become one of the most important and promising substrates for the investigation of the adsorption of organic molecules in solution, whereas graphite and similar layered crystals such as MoS_2 have been almost exclusively used for STM studies of adsorbed organic molecules [18].

The objective of this paper is to describe structures and properties of the iodine-modified Pt(111), Rh(111), Pd(111), and Au(111) based on our recent results obtained by using in-situ STM. The structure of the iodine adlayers, particularly on the Pt and Au electrodes is described first, followed by the underpotential deposition (UPD) of Ag on Pt(111) in the absence and presence of the iodine adlayer with the ($\sqrt{7}$ x $\sqrt{7}$)R19.1° structure, and finally the adsorption of organic molecules on the iodine-modified electrodes.

2 Atomic Structures of Iodine Adlayers

Hubbard and co-workers investigated the structure of adsorbed iodine on a well-defined Pt(111) using a electrochemical UHV technique, demonstrating that the iodine adlayer structure was potential dependent [1, 4]. The adlattices of (3 x 3) (I=4/9) and ($\sqrt{7}$ x $\sqrt{7}$)R19.1° (I=3/7) were found to form at relatively positive and negative potentials, respectively, in the featureless double-layer region. They also found a ($\sqrt{3}$ x $\sqrt{3}$)R30° (I=1/3) adlattice at relatively negative potentials where a partial reductive desorption of the adsorbed iodine took place. Figure l(a) shows a replica of one of their results obtained in a solution (pH 4) containing 0.1 mM KI (Fig.4 in [4]). It has long been expected, at least by us, that the transformation between those structures should take place reversibly when the electrode potential was changed in the potential range shown in Fig. l(a). Although previous in-situ STM studies revealed atomic structures on Pt(111) in air and in solution [5-8], no direct in-situ STM investigation of the potential dependence expected from Fig. l(a) has hitherto been carried out in solutions containing KI. We recently found that two structures of (3 x 3) and ($\sqrt{7}$ x $\sqrt{7}$)R19.1° always coexisted even after the electrode potential was changed greatly in the double-layer region. Figure l(b) shows an example of STM images acquired in a 1 mM KI solution (pH 4). It can be clearly seen that domains with two different structures form

on the terrace of Pt(111). Time-dependent STM images acquired consecutively in the same area after a potential step indicated surprisingly that the structural transformation did occur but was very slow. Two structures could be seen even after 30 min at each potential where only one structure was expected to appear according to the result shown in Fig. l(a) [4]. The result shown in Fig. l(b) directly indicates that the surface

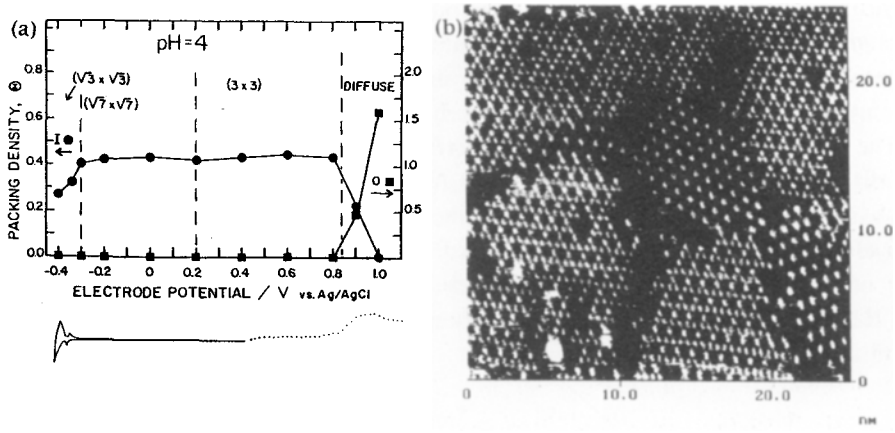

Fig. 1. Cyclic voltammogram of Pt(111) in 0.1 mM KI (pH 4) reported in [4] (a) and atomic STM image of iodine adlayer obtained at 0 V vs. Ag/AgCl. The (3 x 3) and (√7 x √7)R19.1° structures co-existed even after 30 min at the electrode potential of 0 V [19].

mobility of adsorbed iodine atoms is very low on Pt(111), in contrast to that of the iodine on Au(111) [14]. Further investigations [19] are needed to reveal dynamic processes in the iodine adlayers formed on Pt in addition to the simple determination of the structure, even though the I/Pt(111) system has been thought to be well defined and well characterized by many previous investigators.

On the other hand, the structure of the iodine adlayer is more complicated on Au(111). Indeed, various structures were reported for I/Au(111). Bravo et al. using the electrochemical UHV technique found that the iodine adlayer observed upon emersion from CsI solution possessed a (√3 x √3)R30° lattice at a low iodine coverage [20]. A (5 x √3) structure was also found at more positive potentials (high coverage). McCarley and Bard found only the (√3 x √3)R30° structure in their STM studies in air [21]. Haiss et al. reported several structures such as (√3 x √3)R30°, (5 x √3) and (7 x 7)R21.8° in air and in a nonaqueous solvent [22]. These discrepancies strongly suggest that the structure of I/Au(111) is sensitive to electrochemical parameters such as electrode

potential. Using in-situ STM under potential control, Gao and Weaver reported potential-dependent structures on Au(111) in KI solution including (5 x $\sqrt{3}$) and (7 x 7)R21.8° [23]. Under a very similar set of experimental conditions, Tao and Lindsay found a potential-dependent transition only from ($\sqrt{3}$ x $\sqrt{3}$)R30° to (3 x 3) [24].

However, the recent in-situ surface X-ray scattering studies by Ocko et al. revealed a series of I/Au(111) adlattices [12], good agreement with our results obtained by complementary use of LEED and in-situ STM [13, 14]. The adlattice constants varied continuously with the electrode potential in each of the two-dimensional phases designated by Ocko et al., the rectangular (p x $\sqrt{3}$) phase and the rotated hexagonal phase[12]. Figure 2(a) shows a cyclic voltammogram for a well-defined Au(111) in 1 mM KI at a scan rate of 5 mV/s in which the peaks are sharper than those obtained at 20 mV/s as reported in our previous paper [13]. The peaks observed in the potential range between 0 V and -0.5 V correspond to the adsorption-desorption reactions of iodide on Au(111). The small peaks at ca. 0.4 V are associated with the structural transformation of two different phases. The LEED pattern shown in Fig. 2(b) was obtained at an emersion potential of 0.3 V [13]. Three split subspots were clearly seen to move away further from the center and to increase in distance between the split spots when the potential was scanned in the positive direction. The values of p in the rectangular (p x $\sqrt{3}$) phase shown in Fig. 2(c) could be fairly accurately determined by the analysis of the LEED pattern as shown in Fig. 2(b). The p-values obtained as a function of the electrode potential using LEED and in-situ STM [13] were in good agreement with the in-situ surface X-ray scattering results reported by Ocko et al. [12]. The applicability of LEED and in-situ STM was demonstrated in our previous papers for the investigation of continuous structural change [13, 14]. LEED provided the p-values in the (p x $\sqrt{3}$) adlayer precisely enough to describe the structural variation in the electrocompression.

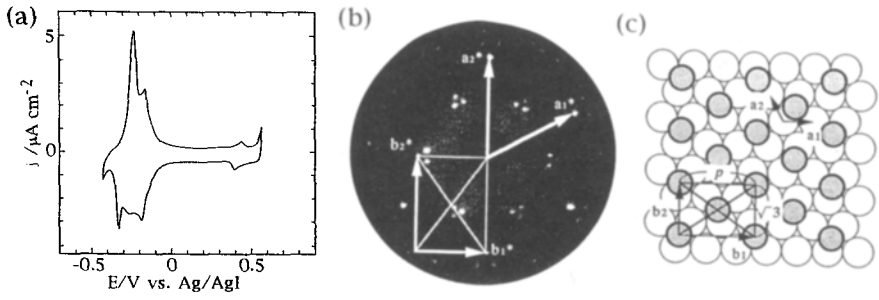

Fig. 2. Cyclic voltammogram of Au(111) in 1 mM KI at 5 mV/s (a), LEED (b), and real-space structure of (p x $\sqrt{3}$) (c) [13].

Although in-situ STM provided overall information of the structural changes in both phases and helped to obtain accurate lattice parameters in the LEED analysis [13, 14], the STM technique alone could not capture such small variations in the adlattice. Our work clearly demonstrates that complementary use of LEED and STM is a powerful technique more easily available in ordinary laboratories compared with surface X-ray scattering to determine accurate structural parameters of adlayers on electrode surfaces. We have recently found that the iodine adlayers on Ag(111) were also continuously compressed with changing electrode potential [15], which is in contrast to the result reported previously [25].

3 Underpotential Deposition

The underpotential deposition (UPD) of hydrogen and metal adlayers on single-crystal electrodes has long been investigated because it is well known that UPD processes are extremely sensitive to the atomic structure of the surface as well as to co-adsorbed anions [1-3]. The UPD of Cu on Au(111) in sulfuric acid is one of the most intensively investigated reactions using STM [26, 27], atomic force microscopy (AFM) [28], and more recently an X-ray scattering technique [29]. The structure of the first adlayer of Cu on Au(111) has recently been confirmed as a $(\sqrt{3} \times \sqrt{3})R30^\circ$ lattice with Cu atoms forming a honeycomb structure with a surface coverage of Cu of 2/3 by crystallographic measurement using x-rays, [29], while in-situ STM and AFM

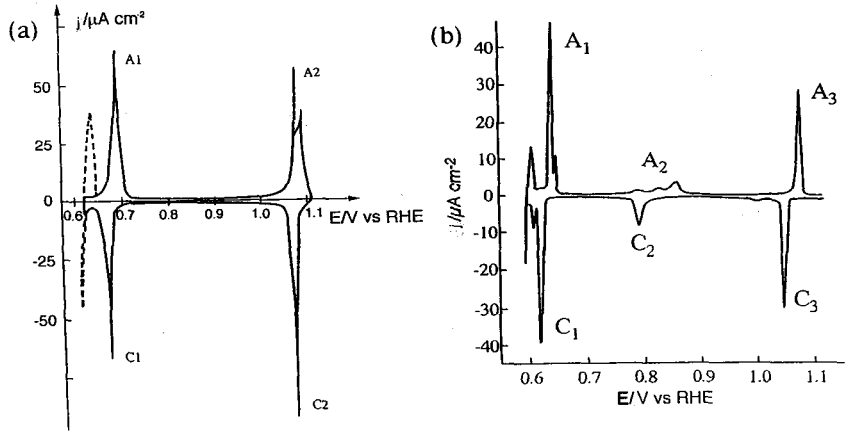

Fig. 3. Cyclic voltammograms of Ag UPD on Pt(111) in sulfuric acid (a) [37] and on I /Pt(111) (b) [8].

consistently showed the image corresponding to a simple ($\sqrt{3}$ x $\sqrt{3}$)R30° structure [26-28]. According to the recent X-ray scattering determination of the first adlayer of Cu, the Cu adatoms form a honeycomb lattice, while a sulfate anion is co-adsorbed at the center of each honeycomb unit cell [29]. Therefore, the bright spots observed by STM and AFM should be considered as being due to adsorbed sulfate ions. Note that the adsorbed sulfate and bisulfate ions form the same structure with a ($\sqrt{3}$ x $\sqrt{7}$) symmetry on Au(111), Pt(111), and Rh(111) [30-33]. It is also noteworthy that in-situ STM also yielded an image of the simple ($\sqrt{3}$ x $\sqrt{3}$)R30° for the first UPD of Cu on Pt(111) in sulfuric acid, as shown in our previous paper [34]. It is also possible to assume in this case that the honeycomb lattice might be formed on Pt(111) as suggested previously by an indirect method [35].

The UPD of Ag on Au and Pt is also an interesting reaction to investigate with surface structure-sensitive techniques. It has clearly been demonstrated that the iodine adlayers on Pt(111) and Au(111) strongly affect the UPD of Ag [1, 8, 36]. For example, Fig. 3 illustrates a clear difference in the electrochemical response of the UPD of Ag on a well-defined Pt(111) in sulfuric acid (a) and on a Pt(111) with the ($\sqrt{7}$ x $\sqrt{7}$)R19.1° iodine adlayer (b), respectively. Two sets of well-defined UPD peaks in the cyclic voltammogram were observed on a well-ordered Pt(111) in sulfuric acid [37]. On the other hand, the UPD of Ag occurred in three steps on the 1/Pt(1 1 1) [1, 8]. The structure of the adlayer formed during the UPD of Ag on 1/Pt(111) has previously been investigated with electrochemical UHV [1, 38]. Our recent preliminary in-situ STM study confirmed that the iodine adlayer structure was converted from ($\sqrt{7}$ x $\sqrt{7}$)R19.1° to (3 x 3) by the formation of the first adlayer of Ag attached directly on the Pt surface [8]. Our result for the effect of the iodine adlayer on the first UPD is in good agreement with that reported by Hubbard et al. [38]. However, STM images acquired after the formations of the second, third, and bulk deposited Ag layers seemed to correspond to a ($\sqrt{3}$ x $\sqrt{3}$)R30° structure. The STM images presented in our previous paper [8] could not explain the LEED patterns with three split spots reported by Hubbard et al., which seem to be similar to the pattern shown in Fig. 3(a), suggesting that the iodine adlayers with Ag layers on Pt(111) might have incommensurate structures similar to those found on Au(111). Nevertheless, further experiments should be carrried out using both LEED and in-situ STM techniques to determine more accurately the structures obtained during the UPD of Ag.

4 Adsorption of Organic Molecules

The adsorption of organic molecules on electrode surfaces in electrolyte solutions has also long been an important subject in electrochemistry for elucidating the role of

molecular properties and the atomic structure of electrode surfaces [39]. In spite of a large number of efforts made to obtain STM images of organic molecules in air and UHV [18], there has not been much success in resolving molecular structures at electrode surfaces with in-situ STM in electrolyte solutions. Although a few recent reports described in-situ STM images of molecular adlayers in electrolyte solutions [40], the resolution achieved by STM imaging in solution seems to be still limited, compared with that in UHV [18].

In the previous work performed mainly in electrochemical UHV technique and in electrolyte solutions, well-defined single-crystal surfaces of metals such as Pt, Rh, Au, and Ag were most frequently used as the substrate for the study of adsorption of organic molecules because of relatively strong tendencies of those surfaces to immobilize organic molecules [l, 2, 39]. However, it was found in our preliminary studies with in-situ STM that the relatively large molecules investigated did not form ordered adlayers on a well-defined Pt(111) nor on Au(111) in solution, probably because of the slow surface mobility of adsorbed molecules. On the other hand, highly ordered pyrolytic graphite (HOPG) and similar layered crystals such as MoS_2 are popular choices as the substrate for the study of adsorbed molecules because of the ease of preparing a clean and atomically flat surface [18, 40]. It is well known that liquid crystals such as alkylcyano-biphenyls form ordered adlayers on HOPG and MoS_2, and they were successfully visualized by STM [18]. These successes can be explained, in our opinion, by relatively weak van der Waals-type interactions of the substrates with adsorbates, allowing self-ordering processes to proceed. However, HOPG is known to exhibit fairly large corrugation amplitudes for the individual carbon atoms in STM images, which sometimes prohibit resolution of small corrugations from adsorbed organic molecules. In fact, in our preliminary experiments, only the atomic structure of HOPG was observed in solutions containing organic molecules.

We have long been interested in finding a more appropriate substrate to investigate the adsorption of various organic molecules in solution, and we recently reported, for the first time, a successful in-situ STM imaging of a highly ordered adlayer of 5,10,15,20-tetrakis(N-methylpyridinium-4-yl)-21H,23H-porphine (TMPyP) on the I-Au(111) in $HClO_4$ [16]. We also obtained recently further evidence that the I-Au(111) electrode can be employed as an ideal substrate for in-situ STM imaging of various adsorbed organic molecules in solution [17]. Organic substances investigated were purposely selected based on their characteristic shapes: square, triangular, and linear. TMPyP hexamethyl-p-rosaniline (Crystal Violet; CV), and 4,4- bis (N-methylpyridinium)-p-phenylenedivinylene (PPV) were all found to form highly-ordered molecular arrays on top of the iodine monolayer adsorbed on Au(111). In-situ STM images shown in Fig. 4 with near-atomic resolution revealed their orientation, packing arrangement, and even the internal structure of each molecule. It is particularly

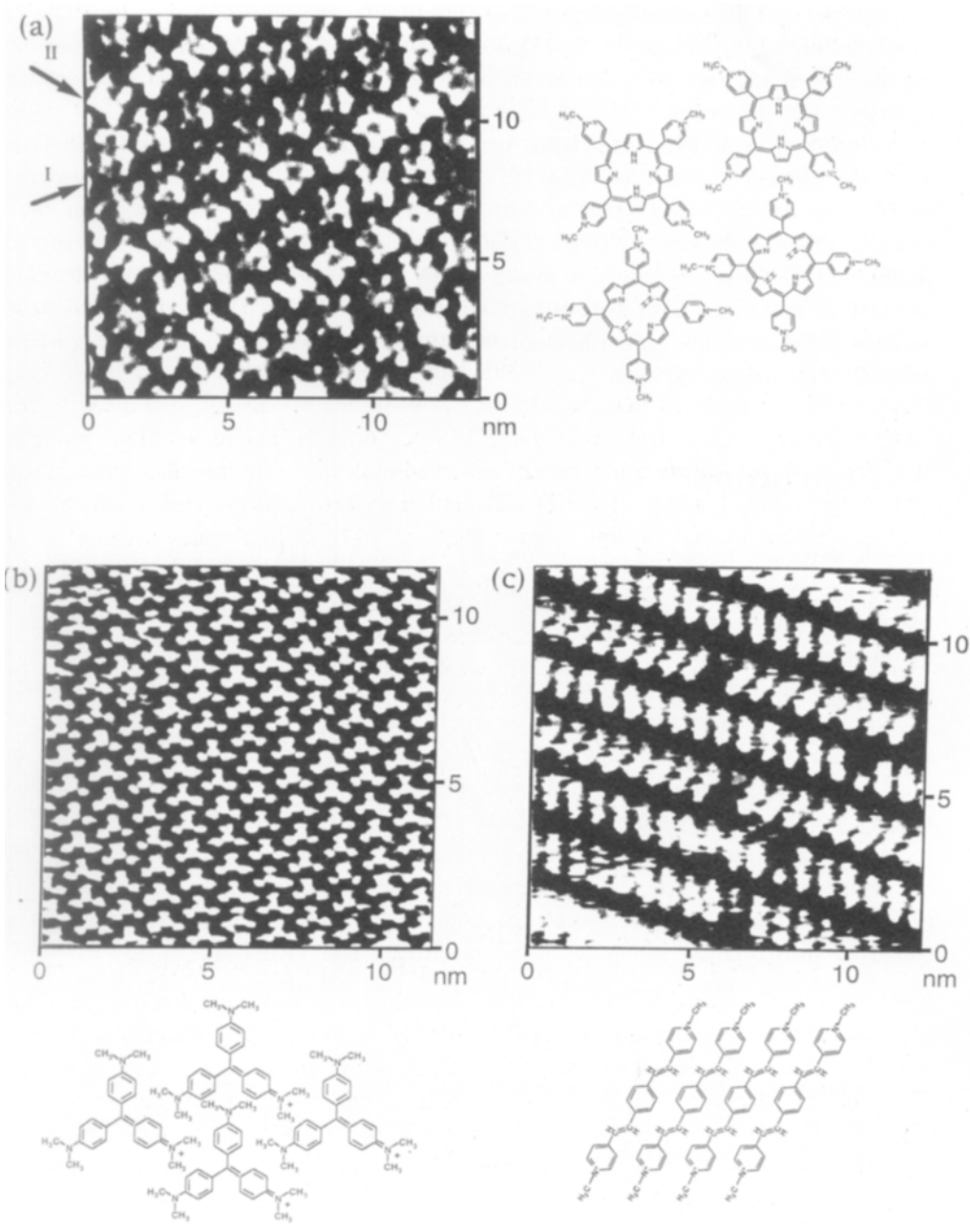

Fig. 4. In-situ STM images of TMPyP (a), CV (b), and PPV (c) on I/Au(111) [16, 17].

emphasized that the iodine layer on Au(111) played a crucial role in the formation of highly ordered TMPYP arrays [16, 17]. Relatively weak van der Waals-type interaction on the iodine adlayers seems to be an important key factor in the formation of the ordered molecular arrays.

The adsorption of these molecules has also been investigated on various iodine-modified electrodes such as I/Ag(111), I/Pt(111) and I/Rh(111). Highly ordered adlayers of TMPyP were found to form on I/Au(111) and I/Ag(111), whereas less-ordered adlayers formed on I/Pt(111) and I/Rh(111) [41]. The surface mobility of iodine on Pt(111) is very slow, as shown in Fig. l(b). TMPyP is adsorbed on I/Pt(111) as isolated molecules with a disordered arrangement. These results suggest that the surface mobility of the iodine adatoms also plays an important role in the ordering process of the organic adlayer.

5 Conclusion

Atomic structures of iodine adlayers on Pt(111) and Au(111), have been described, on our recent results using in-situ STM and ex-situ LEED analysis. The coexistence of two commensurate structures, (3 x 3) and ($\sqrt{7}$ x $\sqrt{7}$)R19.1°, has been found on Pt(111) in the double-layer potential region for a long period of time, indicating that the transformation between the two structures is surprisingly slow. Incommensurate adlayer structures were found to form on Au(111) and Ag(111), and the lattice constant was found to vary continuously with the electrode potential using ex-situ LEED, in good agreement with the recent surface X-ray scattering study. The effect of the iodine adlayer on the underpotential deposition of Ag has been briefly described, and a remaining unsolved problem has been pointed out. Finally, it was demonstrated that the iodine-modified electrodes are appropriate substrates for the investigation of the adsorption of organic molecules in solution. Highly ordered molecular arrays were found to form on the iodine-modified electrodes and visualized by in-situ STM, revealing their packing arrangement and even the internal structure of each molecule.

Acknowledgment. The author gratefully acknowledges the support from Research Development Corporation of Japan (JRDC) as a project (Itaya-Electrochemiscopy Project) of Exploratory Research for Advanced Technology (ERATO).

6 References

[1] A.T. Hubbard, Chem. Rev. 88, 633 (1988).
[2] M.P.Soriaga, Prog. Surf. Sci. 39, 325 (1992).
[3] S.Trasatti, K.Wandel (Eds.), Surface Science and Electrochemistry, reprinted from Surf. Sci. 335 (1995), Elsevier, 1995.
[4] F.Lu, G.N.Salaita, H.Baltruschat, A.T.Hubbard, J. Electroanal. Chem. 222, 305 (1987).
[5] B.C.Schardt, S.-L.Yau, F.Rinaldi, Science 243, 981 (1989).
[6] S.-L.Yau, C.M.Vitus, B.C.Schardt, J. Am. Chem. Soc. 112, 3677 (1990).
[7] R.Vogel, I.Kamphausen, H.Baltruschat, Ber. Bunsenges. Phys. Chem.96, 525 (1992).
[8] N.Shinotsuka, K.Sashikata, K.Itaya, Surf. Sci. 335, 75 (1995).
[9] M.Hourani, M.Wasberg, C.Rhee, A.Wieckowski, Croat. Chem. Acta, 63, 373 (1990).
[10] L.-J.Wan, S.-L.Yau, G.M. Swain, K.Itaya, J. Electroanal. Chem. 381, 105 (1995).
[11] M.P.Soriaga, J.A.Schimpf, A.Carrasquillo, Jr., J.B.Abreu, W.Temesghen, R.J.Barriga, J.-J.Jeng, K. Sashikata, K.Itaya, Surf. Sci..335, 273 (1995).
[12] B.M.Ocko, G.M.Watson, J.Wang, J. Phys. Chem. 98, 897 (1994).
[13] T.Yamada, N.Batina, K.Itaya, J. Phys. Chem. 99, 8817 (1995).
[14] N.Batina, T.Yamada, K.Itaya, Langmuir 11, 4568 (1995).
[15] T.Yamada, K.Ogaki, S.Okubo, K.Itaya, Surf. Sci. 369, 321 (1996).
[16] M.Kunitake, N.Batina, K.Itaya, Langmuir 11, 2337 (1995).
[17] N.Batina, M.Kunitake, K.Itaya, J. Electroanal. Chem. 405, 245 (1996).
[18] S.Chiang, Scanning Tunneling Microscopy I, H.-J.Guntherodt, R. Wiesendanger (Eds.), Springer-Verlag, Berlin, 1992, pp. 181-205.
[19] S.-L. Yau, Y.-G.Kim, K.Itaya, in preparation.
[20] B.G. Bravo, S.L.Michelhaugh, M.P.Soriaga, I.Villegas, D. W. Suggs, J.L. Stickney, J. Phys. Chem. 95, 5245 (1991).
[21] R.L.McCarley, A.J. Bard, J. Phys. Chem. 95, 9618 (1991).
[22] W.Haiss, J.K.Sass, X. Gao, M.J.Weaver, Surf. Sci. Lett. 274, L593 (1992).
[23] X. Gao, M.J.Weaver, J. Am. Chem. Soc. 114, 8544 (1992).
[24] N.J.Tao, S.M.Lindsay, J. Phys. Chem. 96, 5213 (1992).
[25] G.N.Salaita, F.Lu, L.Laguren-Davidson, A.T.Hubbard, J. Electroanal. Chem. 229, 1 (1987).
[26] O.M.Magnussen, J.Hotlos, G.Beitel, D.M.Kolb, R.J. Behm, J. Vac. Scl. Technol. B9, 969 (1991).
[27] T.Hachiya, H.Honbo, K.Itaya, J. Electroanal. Chem. 315, 275 (1991).
[28] S.Manne, P.K.Hansma, J.Massie, V.B.Elings, A.A.Gewirth, Science, 251, 183 (1991).
[29] M.F.Toney, J.N.Howard, J.Richer, G.L.Borges, J.G.Gordon, O.R.Melroy, Phys. Rev.Lett. 75, 4472 (1995) and references cited therein.
[30] O.M.Magnussen, J.Hotlos, R.J.Behm, Faraday Discuss. 94, 329 (1992).

[31] G.J.Edens, X. Gao, M.J.Weaver, J. Electroanal. Chem. 375, 357 (1994).
[32] A.M.Funtikov, U.Linke, U.Stimming, R.Vogel, Surf. Sci. 324, L343 (1995).
[33] L.-J.Wan, S.-L.Yau, K.Itaya, J. Phys. Chem. 99, 9507 (1995).
[34] K.Sashikata, N.Furuya, K.Itaya, J. Electroanal. Chem. 316, 361 (1991).
[35] T.Abe, G.M.Swain, K.Sashikata, K.Itaya, J. Electroanal. Chem. 382, 73 (1995).
[36] S.Sugita, T.Abe, K.Itaya, J. Phys. Chem. 97, 8780 (1993).
[37] N.Kimizuka, K.Itaya, Faraday Discuss. 94, 117 (1992).
[38] A.T.Hubbard, J.L.Stickney, S.D.Rosasco, M.P.Soriaga, D.Song, J. Electroanal. Chem. 150, 165 (1983).
[39] J.Lipowski, P.N.Ross (Eds.), Adsorption of Molecules at Metal Electrodes, VCH, Weinheim, 1992.
[40] N.J.Tao, G.Cardenas, F.Cunha, Z. Shi, Langmuir, 11, 4445 (1995) and references cited there in.
[41] K.Itaya, N.Batina, M.Kunitake, K.Ogaki, Y.-G.Kim, L.-J. Wan, T. Yamada, Solid-Liquid Electrochemical Interfaces, ACS Symposium series 656, G.Jerkiewicz, M.P. Soriaga, K. Uosaki, A. Wieckowski (Eds.), 1996, pp. 171-188.

Electrochemical Nanotechnology
In-situ Local Probe Techniques at Electrochemical Interfaces
Edited by W. J. Lorenz and W. Plieth

The growth and the surface properties of polypyrrole on single crystal graphite electrodes as studied by in-situ electrochemical scanning probe microscopy

Chr. Froeck, A. Bartl, L. Dunsch

Contents

1	Introduction	150
2	Experimental	151
3	Results and discussion	152
4	Conclusions	156
5	References	157

Summary. The growth of polypyrrole (PPy) films on highly oriented pyrolytic graphite (HOPG) electrodes is investigated by in-situ electrochemical scanning tunneling microscopy (STM) and in-situ atomic force microscopy (AFM) both applied in modified electrochemical cells. The PPy film formation at electrodes is studied in aqueous solutions with and without phosphate buffer in the range of pH 5 and pH 7 and with toluene-4-sulfonic acid (tosylate) as supporting electrolyte. Polymer films produced at lower pH are much smoother than films produced in buffer-free solution, i.e., they show a lower surface roughness. At pH 7 no film deposition can be observed. All films are deposited under conditions of low current density where the first nucleation centers are formed at a close distance to steps on the HOPG surface. These nuclei are in the nanometer range. Their growth leads to islands of PPy with a surface area in the micrometer range during the polymerization. Entire PPy films deposited at the electrode were studied in blank electrolyte solutions with respect to their surface morphology. A dependence of the PPy surface roughness on the applied electrode potential was found caused by surface processes in the PPy film.

1 Introduction

Because of its high stability and its good electrical conductivity polypyrrole (PPy) can be used in many technical applications, e.g., in the field of microchips and microstructured electronic devices. Polypyrrole can also be used as a material in sensor technology. The interaction of different gases with the polymer structure can be detected by the paramagnetic resonance [1] or electrical conductivity measurements [2]. By producing PPy films, electrical conductivities up to 150 S/cm can be obtained. Electropolymerized PPy films differ in their molecular structure according to polymerization conditions such as the electrochemical parameters of the polymerization. At low current densities (l.c.d.) below 3 mA/cm^2 one-dimensional polypyrrole chain structures are mainly produced [3]. Higher current densities predominantly lead to two-dimensional molecular polymer structures. The electronic state of such PPy films produced with high current density (h.c.d.) has been investigated by several solid-state spectroscopic methods such as ultraviolet and X-ray photoelectron spectroscopy (UPS and XPS), as well as temperature-dependent electrical conductivity measurements [4 - 6].

In this paper we focus on electrochemically prepared PPy produced at low current densities. The growth and the dependence of the film morphology on electrode potential after deposition are of special interest. Due to the relatively high conductivity of the doped polypyrrole films they can be investigated by both atomic force microscopy (AFM) and scanning tunneling microscopy (STM) techniques. Li and Wang did ex-situ STM and lateral force microscopy (LFM) measurements [7] at intrinsic conducting polymers differing in some respects from the results of in-situ STM and AFM investigations presented here. They observed island structures of PPy films produced on different electrode surfaces. Naoi et al. have discussed a nodular surface PPy structure obtained at charge densities of 0.5 mC/cm^2 and ordered crystalline structures at charge densities of 0.2 mC/cm^2 [8]. Several other groups have reported on helical and superhelical PPy structures found by STM methods [9 - 12]. The advantage of in situ STM is that the initial stages of the formation of nucleation centers on the electrode surface can be studied in respect of their time and local distribution in the electrochemical environment with possible scan sizes of several nanometers up to 0.7 μm. To avoid pH-induced polypyrrole film deposition caused by self-protonation, pH buffers are applied. AFM was applied to check the validity of the STM results. In these AFM investigations even larger areas (up to 125 x 125 μm^2) can be scanned in-situ at the electrode surface.

Both methods were used in the electrochemical studies with the usual three-electrode

arrangement with HOPG as working electrode. Both the initial stages of the polymer and the influence of the electrode potential on the surface morphology of an entire PPy film were studied in-situ.

2 Experimental

The supporting electrolyte used in all electropolymerization techniques was toluene-4-sulfonic acid (tosylate) (0.1 - 0.2 M). Solutions were made with twice-distilled water. Pyrrole distilledunder vacuum and stored in a refrigerator has been used in concentrations in the range 0.04 - and 0.1 M. For slowing down the polymer formation rate by protonation, pH buffers were applied to the aqueous solutions. Phosphate buffer was used for the range pH 5 - 7. The NanoScope III (Digital Instruments, Santa Barbara, CA, USA) was used for the SPM studies. For electrochemical studies, electrochemical AFM and electrochemical STM equipment was applied. The scanning heads used allow atomic resolution and 0.7 x 0.7 μm^2 scan areas (for electrochemical STM and electrochemical AFM) and large-scale scanning of 0.5 x 0.5 μm^2 and 125 x 125 μm^2 for electrochemical AFM. Electrochemically etched Pt/Ir (80:20) tips with a wire diameter of 0.25 mm and a length of about 12 mm were prepared for a use in in situ electrochemical STM after insulating the tip in molten apiezon wax. To obtain an uncovered end of the tip just this very end (approx. 250 μm^2 surface area [13]) of the tunneling tip was exposed to an electrolyte solution. For electrochemical AFM, commercial Si_3N_4 cantilevers (gold-coated NanoProbes; Digital In-struments) were used. The working electrode (WE) was freshly cleaved HOPG (Advanced Ceramics, Cleveland, OH, USA). As counter electrode (CE) an oxide-free Pt wire (flame-reduced) was used for electrochemical AFM. For electrochemical STM a Pt ring electrode (treated in the same manner) arrangement was possible due to the cell geometry. An Ag/AgCl reference electrode (RE) was used for both electrochemical SPM methods. The potentiostat was driven by the NanoScope III electrochemical software, version 3.0. The data were processed with the same software. The polypyrrole films were produced both potentiostatically and potentiodynamically. For the potentiostatic mode a voltage ramp from the open cell potential (approx. 20 mV) to +500 mV was created. Potentiodynamic PPy formation was performed by cycling the electrode potential between -200 and +500 mV. The sweep rate was varied between 20 mV/s and 500 mV/s. After deposition, the PPy films were washed with distilled water and dried overnight in a desiccator. Afterwards the PPy electrodes were replaced in the electrochemical in-situ cells of the AFM and STM and studied in monomer-free tosylate solutions.

3 Results and Discussion

In the in-situ electrochemical STM and electrochemical AFM investigations the first steps of the cyclovoltammetric formation of PPy could be seen. The polymer formed nuclei at a definite distance from steps on the HOPG working electrode surface (Fig. 1). This can be interpreted as follows. Pyrrole monomers are oxidized at the most reactive centers on the WE surface such as steps and the defect sites of the single crystal surface. These oxidized pyrrole
molecules form oligomers which are desorbed from the electrode and react with unoxidized pyrrole molecules in the electrolyte solution. The oligomers so formed react with further monomers until they reach a critical size where they become insoluble in the electrolyte. They are precipitated on the WE surface as the nuclei for further polymerization processes. Due to a pH gradient from the highly reactive sites towards the planar electrode surface, the path length for becoming insoluble is nearly constant for each molecule. From this behavior the parallel orientation of the nuclei from steps of the nuclei on the HOPG surface can be understood. After the formation of the nucleation centers polypyrrole starts to grow at these centers and forms islands. In Fig. 2 the polymeric growth of such an island close to an HOPG step can be seen as a sequence of AFM images. The single crystal step is clearly seen in the upper left corner of the sequence. On the right side of the images the growth of the polymer island can be followed. The small knots on the right-hand side of the islands in Fig. 2 become larger with increasing time. Also, the height of the whole island increases during the polymerization process. With further cyclovoltammetric pyrrole oxidation the island increases in diameter and height. The step on the working electrode appears to be unchanged. The potentiostatic growth of PPy at different pH values shows a dependence on the velocity of growth. Without pH buffer, the PPy formation is dominated by rapid three-dimensional growth. The protons formed cause an additional chemical polymerization. The polymer islands formed expand very fast. This leads to rough surfaces because the growth of several separated nuclei causes extreme differences in height. These nuclei overlap very fast. By usage of phosphate buffers the growing velocity can be decreased. At a pH of 5, single polymer islands on the graphite surface can be detected by scanning probe microscopy. In comparison with potentiostatic polymerization the films are smoother those without a pH-buffer system. The growing velocity is decreased even further at a pH of 7. Neither electrochemical STM nor electrochemical AFM shows the formation of polypyrrole nuclei on the electrode surface with tosylate electrolyte in high- resolution or in large-scale investigations. The PPy films produced by potentiostatic and potentiodynamic methods were washed with distilled water and dried overnight. Afterwards they were replaced

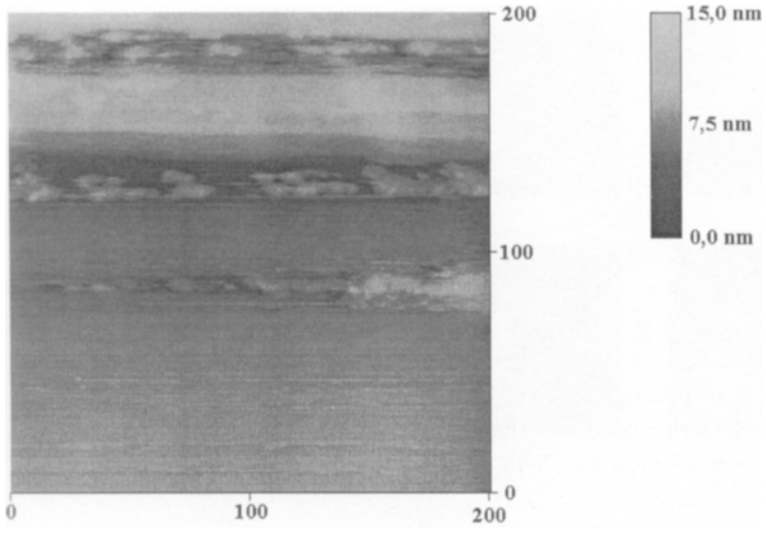

Fig. 1. PPy nuclei at a definite distance from HOPG steps at cyclovoltammetric conditions after 14 cycles (0-500 mV vs. Ag/AgCl at 500 mV/s) investigated by in-situ electrochemical STM.

again in the electrochemical SPM cells and tosylate electrolyte was added to the system without pyrrole monomers. The polymer film covered the working electrode. The surface morphology was investigated by in-situ electrochemical SPM at different potentials. It could be observed that not only does a potentiostatically produced fresh PPy film appear rougher than the potentiodynamically produced film, but this roughness also shows a dependence on the applied potential (Fig. 3). At more oxidizing potentials the polymer surface gets rougher until a saturation value is reached at the beginning of the overoxidation of the PPy film. This increasing roughness at increasing potentials is reversible to some extent. The behavior of the film inchanging its surface structure is interpreted as a gradient of the counter ions in the molecular tissue of the polymer. By oxidizing the PPy film, more counter ions diffuse into the film surface. These counter ions (tosylate) are diffusing into the polymer tissue to compensate the positive charge

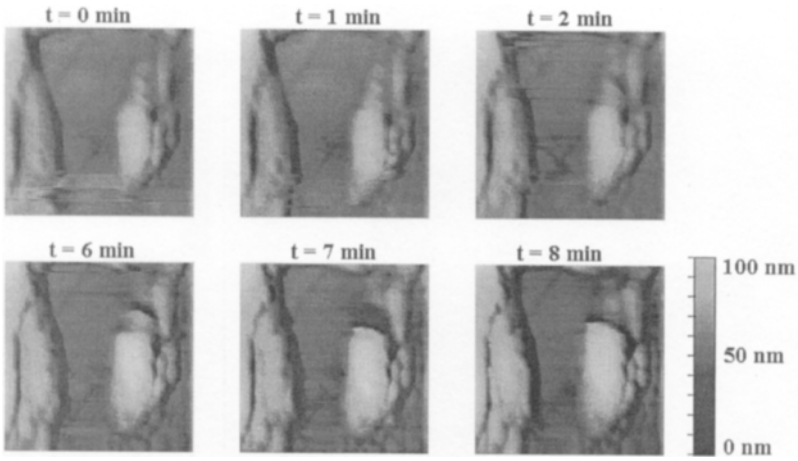

Fig. 2. Island growth of PPy at an HOPG step (scan size 606.3×606.3 nm², height 100 nm) investigated by in situ electrochemical AFM (-100 -350 mV vs. Ag/AgCl at 20 mV/s).

on the polymer chains. When the charge on the film surface is balanced, it becomes more and more difficult for the counter ions to diffuse into the film. For these reasons, the surface tensions differ from the tensions in the bulk polymer. This difference in the tensions leads to a further contraction which also causes an increase in the surface roughness.

A change in the surface roughness of potentiodynamically produced films is not observed (Fig. 4). From the equilibrium potential towards oxidizing potentials and also towards reducing potentials, no change of the films roughness can be observed. Moreover, films which were produced potentiostatically and which are more than one day old do not show any increase in the roughness from the applied potential. This, together with the higher roughness values for potentiostatically produced PPy films, leads in general to the conclusion that in fresh films the polymer chains are formed with a larger disorder than in potentiodynamically produced films. This disorder causes more unsaturated chain endings. After polymerization has finished it takes time to saturate these reactive centers in the polymer bulk. By applying an oxidizing potential

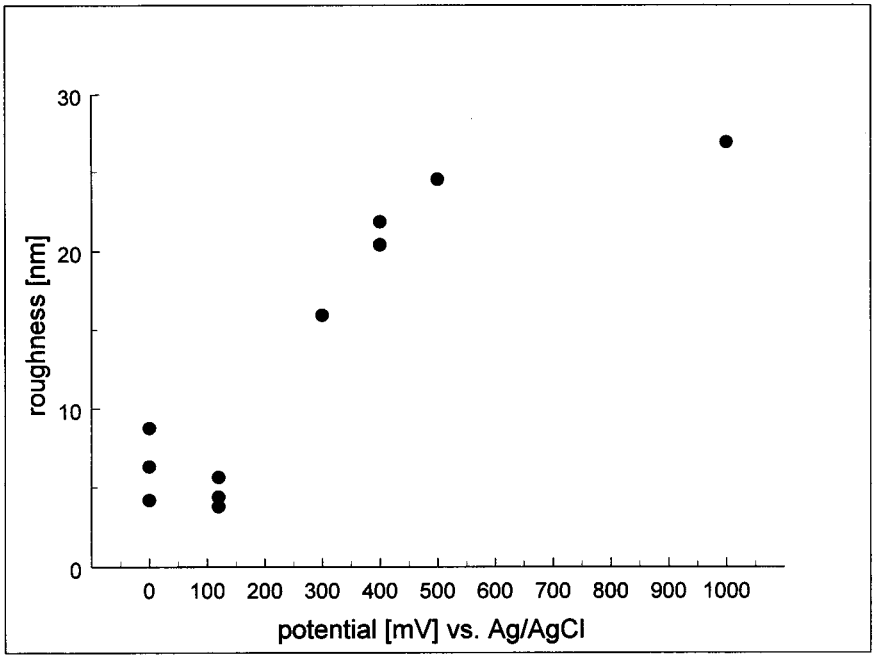

Fig. 3. Dependence of roughness a fresh potentiostatically polymerized PPy film from the applied potential.

these chain ends are oxidized. Potentiodynamically produced films are smoother, i.e., the polymer chains are of higher order. The higher order also leads to a polymer film of higher density than a potentiodynamically produced film. The surface structure appears to be more homogeneous and therefore the oxidizing potential has an even effect on the whole polymer film. Because of that, the local SPM investigation of a few square nanometers or micrometers shows no influence at all on the roughness values from an applied potential.

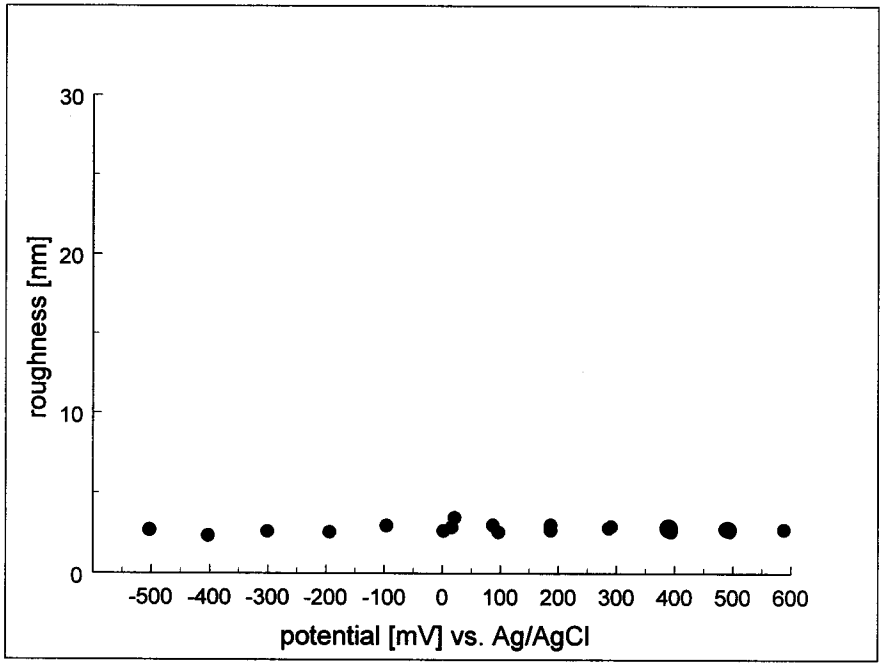

Fig. 4. Dependence of roughness of a fresh potentiodynamically polymerized Ppy film from the applied potential.

4 Conclusions

The growth of electrochemically produced PPy islands takes place at a distinct distance from the electrodes reactive sites due to a pH gradient from these sites towards the surface planes.

Potentiostatically produced PPy films are rougher than potentiodynamically produced films because of a faster growing process. Potentiostatically produced polymer films show a change in their surface roughness when they are electrochemically oxidized which is in contrast to potentiodynamically produced PPy caused by a counter ion

diffusion gradient. The use of pH buffers of pH 3 and higher leads to smoother PPy film surfaces because the proton induced chemical polymerizaion is negligible.

5 References

[1] A.Bartl, L.Dunsch, H.Naarmann, D.Schmeißer, W.Göbel, Synth. Met. 61, 167 (1993).
[2] F.Selampinar, L.Toppare, U.Akbulut, T.Yalcin, S.Süzer, Synth. Met. 68, 109 (1995).
[39 G.Paasch, D.Schmeißer, A.Bartl, H.Naarmann, L.Dunsch, W.Göpel, Synth. Met. 66, 135 (1994).
[4] D.Schmeißer, H.Naarmann, W.Göpel, Synth. Met. 59, 211 (1993).
[5] D.Schmeißer, W.Göpel, Ber. Bunsenges. Phys. Chem. 97, 372 (1993).
[6] D.Schmeißer, W.Göpel, A.Bartl, L.Dunsch, H.Naarmann, Synth. Met. submitted.
[7] J.Li, E.Wang, Synth. Met. 66, 67 (1994).
[8] K.Naoi, Y.Oura, Y.Okamotura, N.Oyama, Posterabstract No. 1945, 2654 (1993).
[9] R.Yang, K.M.Dalsin, D.F.Evans, L.Christensen, W.A.Hendrickson, J.Phys. Chem. 93, 511 (1989).
[10] R.Yang, D.F.Evans, L.Christensen, W.A.Hendrickson, J. Phys. Chem. 94, 6117 (1990).
[11] L.L.Madsen, K.Carneiro, B.N.Zaba, A.E.Underhill, M. van der Sluijs, Synth. Met. 41-43, 2931 (1991).
[12] L.Christensen, W.A.Hendrickson, R.Yang, D.F.Evans, Am. Chem. Soc., Polymer Prepr. 30, 100 (1989).
[13] C.E.Bach, R.J.Nichols, W.Beckmann, H.Meyer, A.Schulte, J.O.Besenhard, P.D.Jannakoudakis, J. Electrochem. Soc. 140, 1281 (1993).

Part IV

Electrochemical Nanotechnology
In-situ Local Probe Techniques at Electrochemical Interfaces
Edited by W. J. Lorenz and W. Plieth

Nucleation and growth at metal electrode surfaces

O. M. Magnussen, F. Möller, M. R. Vogt, R.J. Behm

Contents

1	Introduction	159
2	Structural transitions of the electrode surface	160
3	Phase transitions in adsorbate layers	162
4	Metal deposition	163
5	Dynamic metal deposition/dissolution equilibrium	166
6	Outlook and conclusions	167
7	References	168

Summary. Time-resolved, atomic-scale, in-situ STM studies of phase formation at metal electrode surfaces are described. Examples include structural phase transitions within the electrode surface layer and in anionic or metallic adsorbate layers as well as metal deposition and dissolution processes.

1 Introduction

The formation of two- and three-dimensional phases on electrode surfaces is a topic of central importance in interfacial electrochemistry. It is of relevance not only to fundamental problems, such as the formation of ionic and molecular adsorbate films, but also to areas of great technological interest, such as thin-film deposition, self-assembly of monolayers, and passivation. So far, phase formation in electrochemical systems has been studied predominantly by kinetic measurements using electrochemical or spectroscopic techniques. In order to understand and control these processes as well as the resulting interface structure better, however, improved

knowledge of the atomic-scale processes involved in the nucleation and growth at electrode surfaces and their dependence on electrolyte composition, electrode potential, and substrate structure is required.

Studies of mechanistic aspects of surface processes have benefited strongly from the advent of scanning tunneling microscopy (STM) and atomic force microscopy (AFM). By observing local changes in the atomic structure and the surface morphology the individual atomic processes could often be deduced in these experiments. From the rapidly increasing number of results obtained by these methods under well-defined conditions, in particular under ultrahigh vacuum (UHV), a detailed view on the microscopic aspects of phase transitions in adsorbed layers and of thin film growth is emerging [1]. In a similar way, in-situ STM and AFM studies are well suited to unravel phase formation processes in an electrochemical environment on an atomic scale. The electrochemical interface offers several advantages over surfaces in vacuum for the study of these phenomena. First, most processes can be performed under or close to thermodynamic equilibrium and secondly they can be easily controlled by the applied potential. Due to this control, in-situ electrochemical STM experiments are ideally suited for direct, time-resolved observations of growth processes, as will be shown below.

In this paper recent results of our in-situ STM studies on the structure of bare and adsorbate-covered electrode surfaces are summarized. In particular, we discuss transitions between different phases on these surfaces, which often proceed via nucleation and growth processes. This includes structural transitions in the electrode surface layer, phase transitions in adsorbate layers, electrodeposition processes, and dynamical fluctuations at the metal-electrolyte interface under equilibrium. We show that in-situ STM provides a valuable tool for time-resolved, atomic-scale studies of such processes. For experimental details and for in-depth discussions the reader is referred to the original literature.

2 Structural transitions of the electrode surface

It has been shown previously by ex-situ and spectroscopic techniques that after transfer into an electrochemical environment the reconstruction of Au single crystals, well known from UHV studies, is preserved at negative potentials but is lifted upon raising the potential above a critical limit [2, 3]. Furthermore, the transition between the reconstructed and unreconstructed surface is reversible, with the transition potential depending on the electrolyte composition. These results have been recently confirmed by in-situ STM [4 - 10]. Particularly well studied is the hexagonal reconstructed

Au(100) electrode surface [4, 5, 9, 10], where the "hex" ↔ (1x1) transition is strongly kinetically hindered, leading to a large hysteresis in the transition potentials.

The onset of this structural transition from the "hex" reconstructed to the unreconstructed (1x1) phase is illustrated in the STM images presented in Fig. 1 [9]. At potentials below the transition potential (Fig.1(a)) an atomically flat Au(100) terrace with several domains of the "hex" reconstruction is visible. The reconstructed domains consist of integer multiples of individual, row-like elements, which in this case are terminated at a step edge running horizontally. These domains are separated here by unreconstructed areas, which appear darker in the STM images. Raising the potential above the transition potential (Fig. 1(b)) a slow removal of the reconstruction sets in. This process starts in the direct vicinity of the step edge. In the transition from the higher-density reconstructed phase to the (1x1) phase surplus Au atoms are expelled

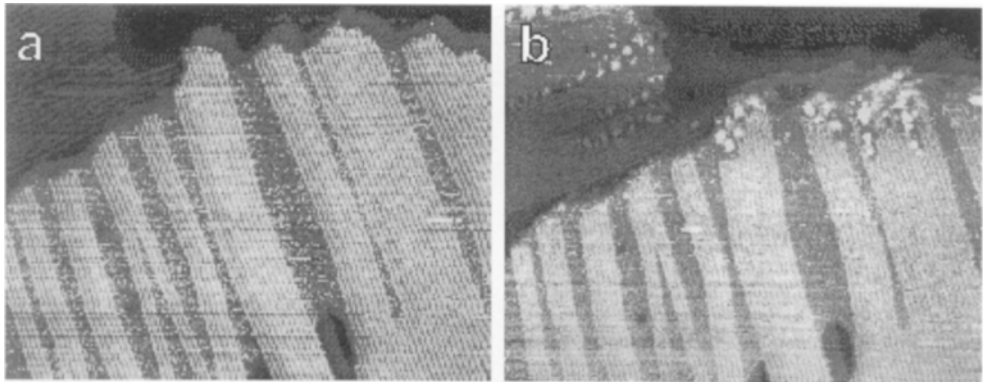

Fig. 1. Initial stages of the "hex" → (1x1) transition on Au(100) in 0.01 M H_2SO_4; (a) -0.15 V_{SCE} and (b) 0.3 V_{SCE} (1300 x 1060 Å^2) [9].

onto the surface, where they coalesce into small islands that are plainly visible in the STM experiments. With time, the unreconstructed areas grow along the reconstruction rows towards the center of the terrace. As evident from the unchanged appearance of the domain boundaries in the center of the terrace, the (1x1) areas do not grow perpendicular to the reconstruction rows (Fig. 1(b)). Hence, the lifting of the reconstruction, as well as the reverse process of the potential-induced growth of the "hex" reconstruction, proceed via heterogeneous nucleation at defects (e.g., steps) and subsequent quasi one-dimensional growth. This is in good agreement with the zero-order kinetics found in spectroscopic experiments [2]. The growth and removal of

individual quasi one-dimensional reconstruction elements is the microscopic mechanism of all transitions between the reconstructed and the unreconstructed phases on the three low-index Au surfaces [5, 7-10]. A similar growth behavior was observed in UHV studies for the removal of the structurally identical "hex" reconstruction of Pt(100) by CO adsorption [11, 12].

3 Phase transitions in adsorbate layers

It has been realized that the phase behavior on the liquid side of the interface is often much more complex than in the traditional view, where ions are supposed to be randomly adsorbed at the electrode surface.

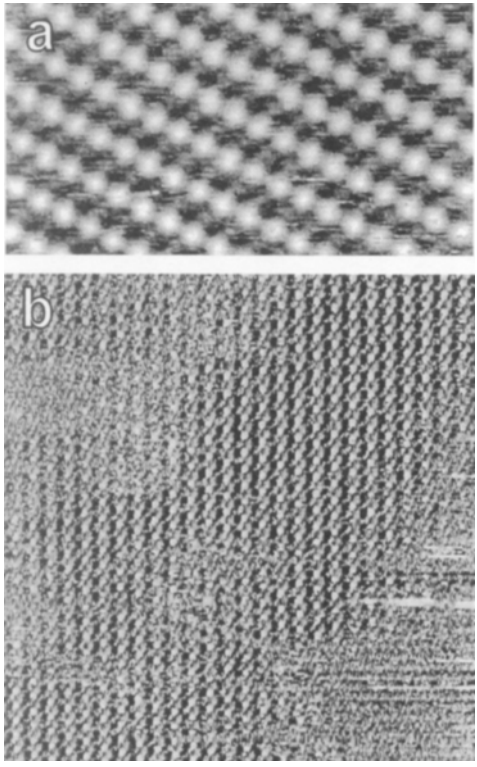

Fig. 2. Sulfate superstructure on Au(111) (a) at 0.85 V_{SCE} in 0.1 M H_2SO_4 (58 x 44 Å^2) and (b) at the transition potential 0.7 V_{SCE} in 1 M H_2SO_4 (185 x 205 Å^2) [13].

As an example, the ordered sulfate superstructure formed on Au(111) in sulfuric acid at potentials ≈0.5 V higher than the potential of zero charge is shown in Fig. 2(a) [13]. Although a $\begin{pmatrix} 2 & 1 \\ 1 & 2 \end{pmatrix}$ unit cell can be assigned to this structure, in agreement with the coverage of 0.2 monolayers found in radiotracer and coulometric experiments [14], the precise composition of this structure is still unknown. This structure is only observed above a critical potential; at lower potentials no ordered superstructure is observed.

The disorder-order transition is marked by a sharp peak with only minimal hysteresis in the corresponding cyclic voltammogram. This indicates that the transition is fast and requires only very small changes in the sulfate coverage. Time-resolved STM observations of the corresponding, fast nucleation and growth processes turned out to be impossible. However, by keeping the potential very close to the transition potential, coexistent disordered and ordered areas with highly mobile domain boundaries in between, are observed. An example is shown in Fig.2(b) with islands of the disordered phase predominantly in the upper left and lower right corner of the image. In these disordered areas the (1x1) lattice of the underlying Au(111) substrate is faintly visible. The observed two-phase regime either may indicate that the ordered sulfate adlayer forms by a nucleation and growth mechanism or may correspond to the critical fluctuations near a second-order phase transition. An unambiguous interpretation requires further detailed investigations of these phenomena.

4 Metal deposition

An important effect in the initial stages of electrochemical metal deposition is the formation of a metal monolayer at potentials positive relative to the Nernst potential, known as underpotential deposition (UPD). These metal adlayers often form ordered structures, which can strongly depend on the anion species in the electrolyte. The most prominent example of the latter is the UPD adlayer of Cu on Au(111) in sulfuric acid, where a ($\sqrt{3}$ x $\sqrt{3}$)R30° superstructure is observed [10, 15-19]. According to recent X-ray scattering results [20], a 1/3 monolayer of sulfate is embedded in a honeycomb of a 2/3 monolayer of Cu in this structure. In the presence of strongly co-adsorbing anions, such as chloride, other superstructures are observed, signaling a structure-decisive influence of the respective anions on the Cu UPD behavior [17, 21]. Similar effects were found also on the other low-index Au surfaces [22, 23]. The formation of the ordered phases in the UPD range is usually too fast to be observed directly in STM experiments. Only by using very low metal concentrations in the electrolyte can the metal monolayer be grown under diffusion control on a time scale compatible with the STM measurements. As an example, the growth of the ($\sqrt{3}$ x$\sqrt{3}$)R30° superstructure on

Au(111) is shown in two successively recorded STM images obtained in sulfuric acid containing 10^{-6} M $CuSO_4$ (Fig. 3) [10]. In the lower half of the images formation of a highly defective ($\sqrt{3}$ x $\sqrt{3}$)R30° island is observed. Such islands coexist with areas where no atomic structures are discernible. Most likely, the Au(111) substrate in these featureless areas is covered by a dilute adlayer of mobile Cu atoms. The observation of an island growth mechanism is in good agreement with electrochemical measurements of the kinetics of adlayer phase formation [24] and indicates clearly that the gross lateral interactions between the adsorbed anions and the Cu atoms in the ($\sqrt{3}$ x $\sqrt{3}$)R30° structure are attractive.

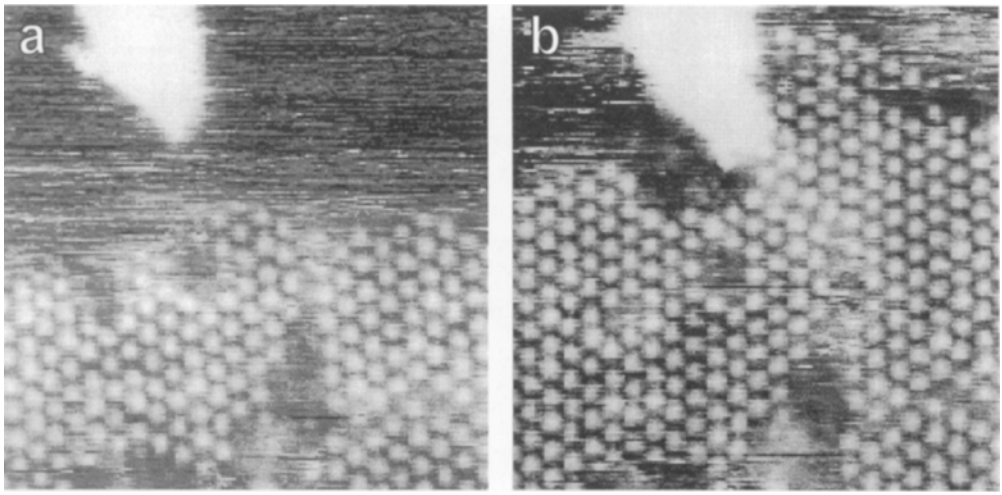

Fig. 3. Formation of the ($\sqrt{3}$ x $\sqrt{3}$)R30° superstructure on Au(111) in 0.01 M H_2SO_4 + 10^{-6} M $CuSO_4$ at 0.13 V_{SCE} (100 x 90 Å^2) [10].

Comparative studies in an electrochemical environment and under UHV conditions gain detailed information on the mechanistic role on anions and solvent molecules. This is demonstrated for nucleation and growth of thin epitaxial Ni films on Au(111). In contrast to Cu, no UPD or anion effects were found for Ni on Au [25]. In addition, due to the negative deposition potential of Ni the Au(111) electrode can be kept in a potential regime in which the surface exhibits the "herringbone" reconstruction, well known from UHV studies [26]. In Fig. 4(a), recorded in a modified Watts electrolyte [25], the zigzag pattern of the "herringbone" reconstruction is clearly visible on the electrode surface.

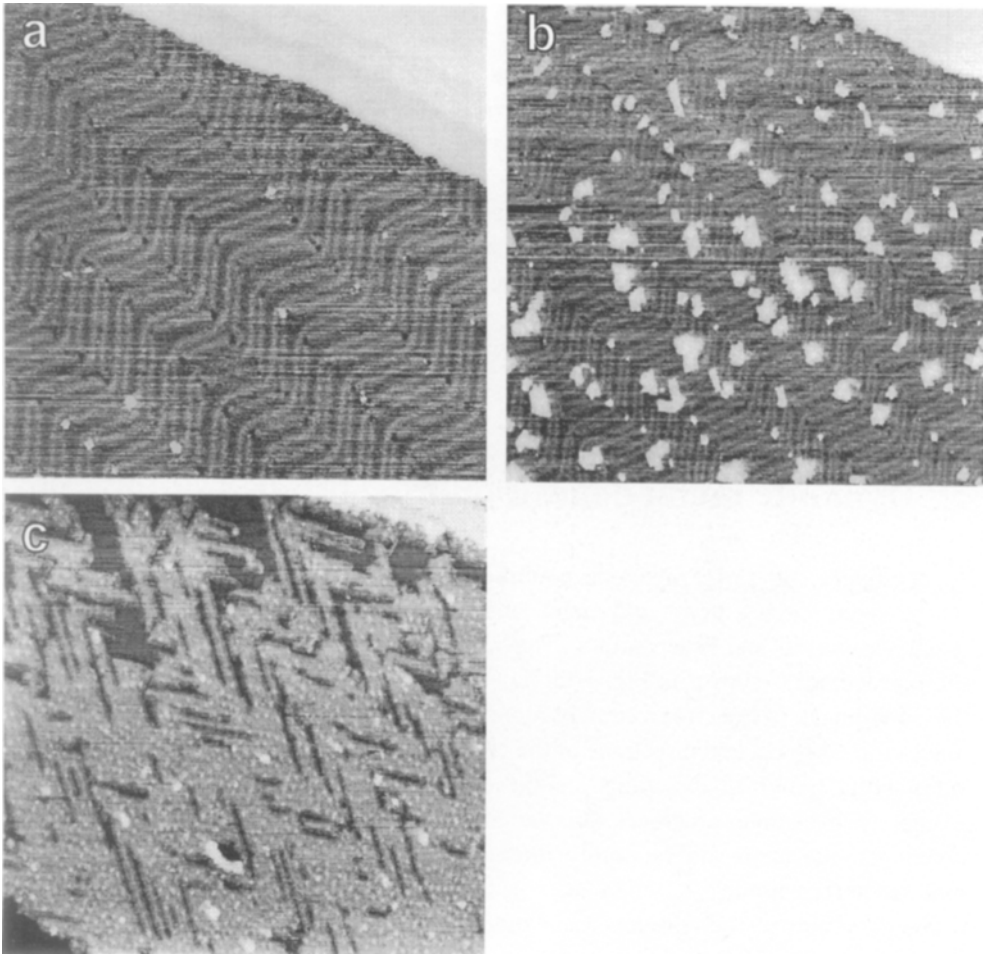

Fig. Deposition of Ni on Au(111) in modified Watts electrolyte (with 10^{-3} M $NiSO_4$) at (a) -0.64 V_{SCE} (1100 x 1100 $Å^2$), (b) -0.64 V_{SCE} (1500 x 1500 $Å^2$), and (c) -0.68 V_{SCE} (1500 x 1500 $Å^2$) [25].

At low overpotentials nucleation of the Ni deposit starts at the "elbows" of the reconstruction (Fig. 4(b)), followed by anisotropic growth of monolayer islands perpendicular to the double rows of the reconstruction (Fig. 4(c)). For multilayer coverages a layer-by-layer growth of the Ni thin film was observed up to thicknesses of six layers. Under UHV conditions, this system exhibits a similar nucleation behavior but the subsequent growth proceeds isotropically and in a more three-dimensional fashion [27]. Both in UHV and in the electrochemical environment the nucleation of islands is preceded by the formation of depressions at the elbows. This indicates that Au surface atoms at these sites are replaced by Ni atoms, which subsequently act as centers for adlayer island nucleation [28]. This demonstrates far-reaching mechanistic similarities for deposition at the metal-vacuum and the metal-electrolyte interface, even in complex cases.

5 Dynamic metal deposition/dissolution equilibrium

At reactive electrodes a dynamic equilibrium is established at the Nernst potential, where metal surface atoms and metal ions in solution are continuously exchanged by local dissolution and redeposition. The morphological rearrangement resulting from these processes is shown in Fig. 5 for Cu(100) electrodes in HCl [29]. In the center of the STM image in Fig. 5(a) a straight monoatomic step is visible, which runs parallel to one of the close-packed directions of the c(2x2) superstructure formed by adsorbed Cl. steps along preferred directions are the direct result of a rearrangement of surface atoms by exchange processes. In the absence of a Cl adlayer, at very negative potentials, the steps are randomly oriented and appear frizzy, indicative of highly mobile Cu step atoms.

The dynamics of the rearrangement processes on the Cl-covered Cu(100) surface is illustrated in Fig. 5(b). In this image the upper terrace grows during the 90 s recording time by ten c(2x2) rows. The addition of each row proceeds by rapid growth along the step edge. Due to the fast growth, STM experiments merely probe when a growing row crosses the scanned area but cannot resolve the individual atomic processes. Apart from the dynamic effects caused by the growing rows, the step edges always appear straight in the STM images. This indicates that the creation of energetically unfavorable kink sites is largely avoided. The reverse process of local Cu dissolution proceeds in a completely analogous way by removal of atoms from kink sites.

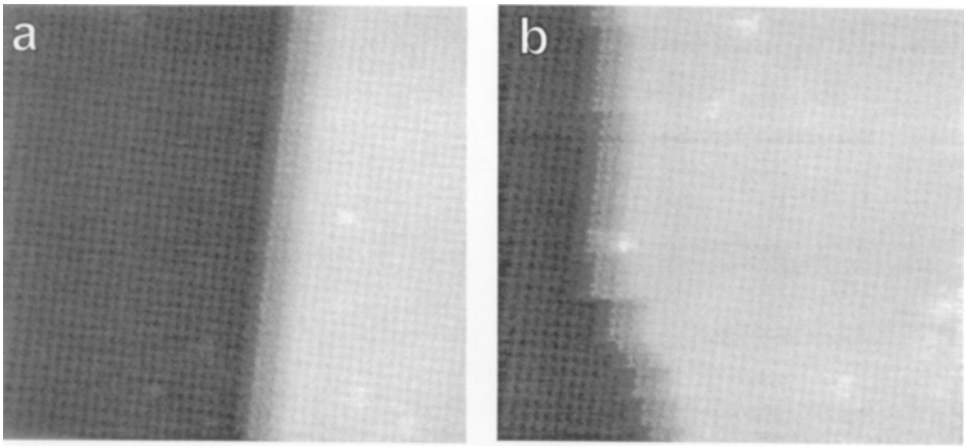

Fig. 5. Local Cu deposition on Cu(100) in 10^{-3} M HCl at -0.073 V_{SCE} (140 x 140 $Å^2$) [29].

6 Outlook and conclusions

As demonstrated above, atomic-scale, in-situ STM studies are an excellent method for the analysis of the microscopic processes involved in the nucleation and growth of two- and three-dimensional phases at the metal-electrolyte interface. By controlling the growth rate via potential and diffusion, time-resolved STM observations are feasible for a wide range of processes. In the future, studies of anionic and organic adsorbates, for which an extensive body of thermodynamic and kinetic data exists, will gain importance but also studies of metal deposition in the under- and overpotential regime will continue to attract considerable interest. In addition, more work on reactive surfaces, such as Pt, Cu, and transition-metal electrodes, is expected to emerge. Progress here is closely correlated with progress in the preparation of clean, atomically flat metal surfaces required for high-resolution STM experiments. These experiments in well-defined systems will lead to a better understanding of the atomic processes,

which form the microscopic basis of the complex but technically important problems in applied electrochemistry, corrosion science, and electrocatalysis.

Acknowledgment. We gratefully acknowledge the contributions of J. Hotlos, J. Hageböck, J. Kintrup, and C.M. Schilz, who contributed to individual topics presented in this work.

7 References

[1] C. Günther, S. Günther, E. Kopatzki, R.Q. Hwang, J. Schröder, J. Vrijmoeth, R.J. Behm, Ber. Bunsenges. Phys. Chem. 97, 522 (1993).
[2] J. Schneider, D.M. Kolb, Surf. Sci. 193, 579 (1988).
[3] D.M. Kolb, in: Frontiers in Electrochemistry, Vol. 2. Structure of Electrified Interfaced, J. Lipkowski, R.N. Ross (Eds.),VCH, New York, 1993, p. 65.
[4] X. Gao, A. Hamelin, M.J. Weaver, Phys. Rev. Lett. 67, 618 (1991).
[5] X. Gao, G.J. Edens, A. Hamelin, M.J. Weaver, Surf. Sci. 296, 333 (1993).
[6] X. Gao, A. Hamelin, M.J. Weaver, Phys. Rev. *B* 44, 10983 (1991).
[7] N.J. Tao, S.M. Lindsay, Surf. Sci. 274, L546 (1992).
[8] O.M. Magnussen, J. Wiechers, R.J. Behm, Surf. Sci. 289, 139 (1993).
[9] O.M. Magnussen, J. Hotlos, R.J. Behm, N. Batina, D.M. Kolb, Surf. Sci. 296, 310 (1993).
[10] O.M. Magnussen, Ph.D. Thesis, University of Ulm (1993).
[11] E. Ritter, R.J. Behm, G.O. Pötschke, J. Wintterlin, Surf. Sci. 181, 403 (1987).
[12] A. Borg, A.-M. Hilmen, E. Bergene, Surf. Sci. 306, 10 (1994).
[13] O.M. Magnussen, J. Hageböck, J. Hotlos, R.J. Behm, Faraday Discuss. 94, 329 (1992).
[14] Z. Shi, J. Lipkowski, M. Gamboa, P. Zelenay, A. Wieckowski, J. Electroanal. Chem. (1993).
[15] M.S. Zei, G. Qiao, G. Lehmpfuhl, D.M. Kolb, Ber. Bunsenges. Phys. Chem. 91, 349 (1987).
[16] O.M. Magnussen, J. Hotlos, R.J. Nichols, D.M. Kolb, R.J. Behm, Phys. Rev. Lett. 64, 2929 (1990).
[17] O.M. Magnussen, J. Hotlos, G. Beitel, D.M. Kolb, R.J. Behm, J. Vac. Sci. Technol. B 9, 969 (1991).
[18] T. Hachiya, J. Honbo, K. Itaya, J. Electroanal. Chem. 315, 275 (1991).
[19] S. Manne, P.K. Hansma, J. Massie, V.B. Elings, A.A. Gewirth, Science 251, 133 (1991).
[20] M.F. Toney, J.N. Howard, J. Richer, G.L. Borges, J.G. Gordon, O.R. Melroy, Phys. Rev. Lett. 75, 4472 (1995).
[21] J. Hotlos, O.M. Magnussen, R.J. Behm, Surf. Sci. 335, 129 (1995).
[22] F. Möller, O.M. Magnussen, R.J. Behm, Phys. Rev. B 51, 2484 (1995).

[23] F. Möller, O.M. Magnussen, R.J. Behm, Electrochim. Acta 40, 1259 (1995).
[24] M. Hölzle, U. Retter, D.M. Kolb, J. Electroanal. Chem. 371, 101 (1994).
[25] F. Möller, O.M. Magnussen, R.J. Behm, Phys. Rev. Lett. 77, 3165 (1996); *ibid* 77, 5249 (1996); Phys. Rev. B, in press (1997).
[26] J.V. Barth, H. Brune, G. Ertl, R.J. Behm, Phys. Rev. B 42, 9307 (1990).
[27] D.D. Chambliss, R.J. Wilson, S. Chiang, Phys. Rev. Lett. 66, 1721 (1991).
[28] J.A. Meyer, I.D. Baikie, E. Kopatzki, R.J. Behm, Surf. Sci. 365, L647 (1996).
[29] M.R. Vogt, F.A. Möller, C.M. Schilz, O.M. Magnussen, R.J. Behm, Surf. Sci.. 367 (1996); M.R. Vogt, A. Lachenwitzer, O.M. Magnussen, R.J. Behm, Surf. Sci., in press (1997).

Electrochemical Nanotechnology
In-situ Local Probe Techniques at Electrochemical Interfaces
Edited by W. J. Lorenz and W. Plieth

STM Study of Electrodeposition of Strained-Layer Metallic Superlattices

T. P. Moffat

Contents

1	Introduction		172
2	Experimental details		173
3	Results and discussion		174
	3.1	Substrate preparation and structural characterization	174
	3.2	Reductive desorption of chloride adlattice	177
	3.3	In-situ observation of growth dynamics on Cu(100)	180
	3.4	Heteroepitaxial Deposition on Cu(100)	182
4	Conclusions		183
5	References		184

Summary. An STM study has been initiated to investigate the various processes associated with electrodeposition of Cu-Ni multilayers on Cu(100). The substrates were prepared by electropolishing in phosphoric acid followed by immersion in 10 mmol/l HCl. A $(\sqrt{2} \times \sqrt{2})R45^{\circ}$ adlattice of oxidatively adsorbed chlorine is formed under these conditions. The adlayer stabilizes the surface steps in the <100> direction which corresponds to the close packed direction of the chloride adlattice. In dilute (millimolar) solutions of cuprous ion, reduction occurs under mass transport control with the electrocrystallization reaction proceeding by step flow in the <100> direction. At more negative potentials chloride is partially desorbed. Coincidentally, the highly kinked metal steps become frizzy and move towards adopting the close-packed <110> orientation of the metal lattice. Preliminary experiments on heteroepitaxial nickel deposition reveal regions where electrocrystallization on Cu(100) occurs via step flow in the <110> direction.

1 Introduction

Over the last ten years a large effort has been focused on the synthesis and characterization of compositionally modulated alloys [1]. These materials offer several enhanced properties, ranging from hardness to enormous magnetoresistance. Metallic superlattices of Cu-Ni the most studied system due largely to the fact that Cu and Ni have the same face-centered cubic (fcc) crystal structure and similar lattice parameters, with ~2.6 % misfit. Furthermore, copper and nickel represent two of the most common electroplated coatings. Consequently, we have undertaken a study of the growth and properties of electrodeposited Cu-Ni multilayers as a function of the modulation orientation. Control of the modulation orientation may be pursued by taking advantage of the epitaxial constraint imposed by single-crystal or highly textured substrates. In fact, single-crystal Cu-Ni multilayers have been successfully grown on Cu(100) (2) as shown in Fig. 1, where X-ray scattering from (200) planes of the multilayer and the substrate is apparent.

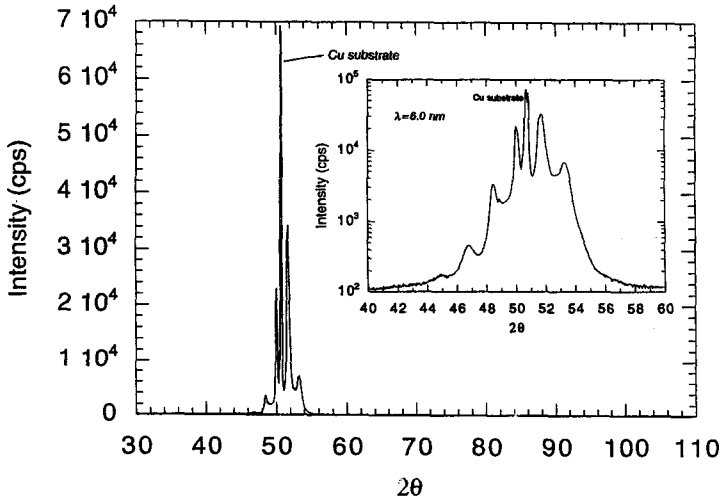

Fig. 1. X-ray diffraction from a Cu-Ni strained-layer superlattice grown on Cu(100). The inset figure shows an expanded version of the (200) scattering envelope with the intensity shown on a logarithmic scale to reveal higher-order satellites. The multilayer was 2.4 μm thick.

This demonstrates that the compositional modulation is oriented exclusively in the <100> direction while the superlattice lines reflect the periodicity and quality of the multilayer. The materials are typically grown from a nickel-based electrolyte containing ~10 mmol/l copper ions. The copper layer is deposited under diffusion-limited conditions while the nickel layer is grown under charge transfer control [2]. A programmed coulometer is used to switch the potentiostat between the appropriate potentials thereby building the multilayer. To obtain more insight into the relevant electrocrystallization reactions an in-situ STM study has been initiated. In this report our findings for copper and nickel deposition on Cu(100) are presented.

2 Experimental Details

Single-crystal squares 3-4 mm thick were cut from a 2.5 cm-diameter Cu(100) cylindrical ingot which had been aligned by Laue X-ray diffraction. The crystals were mechanically polished to a 0.1 μm diamond finish followed by electropolishing in 85 vol% phosphoric acid [3]. After extensive rinsing with water the substrate was transferred to the STM electrochemical cell and immersed in 10 mmol/l HCl. A Digital Instruments Nanoscope III STM was used for these experiments. The electrochemical cell incorporated an Ag/AgCl or immersed copper wire "quasi" reference electrode, a platinum counter electrode and an insulated tungsten tunneling probe. The tungsten probes were prepared by etching a W wire to form a sharp tip in 1 mol/l KOH. The etching parameters were 30 V a.c. (Variac) versus a carbon rod followed by a 15 second etch at 8-10 V a.c. The probes were then coated with polyethylene, which in the most favorable cases results in a background Faradaic current of less than 10 pA. Homoepitaxial deposition of copper was examined in a dilute, nominally ~1 mmol/l, cuprous chloride electrolyte while the preliminary investigation of nickel deposition was performed using a concentrated electrolyte of 1.5 mol/l $Ni(SO_3NH_2)_2$ (Fluka), 0.5 mol/l H_3BO_3, with a pH of 3.5.

3 Results and Discussion

3.1 Substrate Preparation and Structural Characterization

Immediately prior to multilayer deposition, the Cu substrates were typically immersed in 10 mmol/l HCl for 5-30 min. The solution was open to the atmosphere (i.e., oxygen),

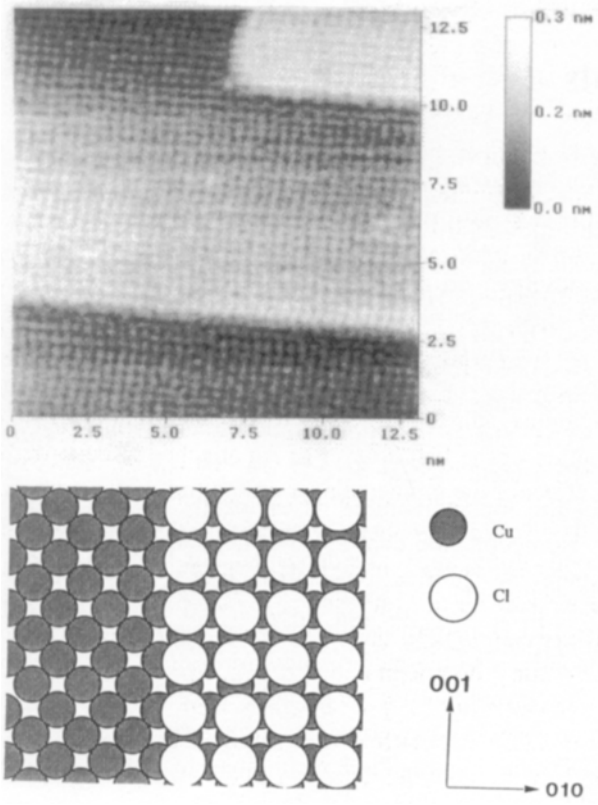

Fig. 2. A 13 nm x 13 nm STM image of a ($\sqrt{2}$ x $\sqrt{2}$)R45° chlorine adlattice on Cu(100) at -0.169 V vs. Cu/Cu^+ in 10 mmol/l HCl with E_{tip} = 0.120 V, I_t =9.0 nA, and a frame time of 32 s. A schematic of the proposed chloride adlayer structure is also shown.

which results in etching of the surface [4, 5] and the formation of large (100) terraces on the miscut Cu(100). For short pretreatment times this results in a root mean square (rms) surface roughness on the order of ~1.4 nm over a 100 μm^2 area. The terraces are completely covered by a ($\sqrt{2}$ x $\sqrt{2}$)R45° Cl adlattice as determined by low-energy electron diffraction (LEED) and in-situ STM [6, 7, 8]. As shown in Fig. 2, a high-resolution constant-current STM image obtained at -0.25 V vs. Cu/Cu^+ reveals a series of terraces bounded by <100> oriented steps. The <100> step orientation is in sharp contrast to the close-packed <110> orientation associated with clean copper surfaces in ultrahigh-vacuum (UHV) systems [9]. The <100> step edge corresponds to the close packed direction of the chlorine adlattice.

Similar observations of the influence of a ($\sqrt{2}$ x $\sqrt{2}$)R45° oxygen adlayer on the step structure of Ni(100) were recently reported [10]. In the present case, the chloride adlattice has a dominant influence on the binding energy of an adatom to a step as well the activation energy for migration along a step edge and thereby controls the evolution of the step morphology on Cu(100). Interestingly, the importance of enhanced step edge mobility relative to terrace mobility has been previously noted for Cu atoms on clean Cu(100) in UHV [11]. This results in kink-saturated <100> metal steps beneath the adlattice. The monatomic step height of ~0.18 nm corresponds to copper (a_0 = 0.361). The ($\sqrt{2}$ x $\sqrt{2}$)R45° Cl adlattice allows the coexistence of two possible domains within a terrace. Unambiguous imaging of such domain boundaries with atomic resolution proved difficult, however; numerous mesoscopic images were obtained of the migration of individual line defects across the (100) terraces as shown in Fig. 3. On this scale the domain boundaries generally tend to be aligned in the <110> which corresponds to the kink-saturated directions for the chlorine adlattice. The chemical potential driving the process may be related to the differing registry between ($\sqrt{2}$ x $\sqrt{2}$)R45° Cl adlayers on two neighboring terraces leading to chlorine-rich and -poor step edges. The different energetics of these steps may also account for the tendency of the small island to adopt a rectangular shape. This argument is analogous to that used for the rectangular growth habit of nickel islands that form during homoepitaxial growth on Ni(100) which is covered with a ($\sqrt{2}$ x $\sqrt{2}$)R45° oxygen adlattice [10]. In a similar vein, the movement of the domain boundary in the Cl ($\sqrt{2}$ x $\sqrt{2}$)R45° adlattice were somewhat hindered at steps due, presumably, to the phase shift of the adlattice between neighboring terraces. The domain boundaries were most often noted for substrates which had first been exposed to 10 mmol/l $HClO_4$ prior to immersion in 10 mmol/l HCl.

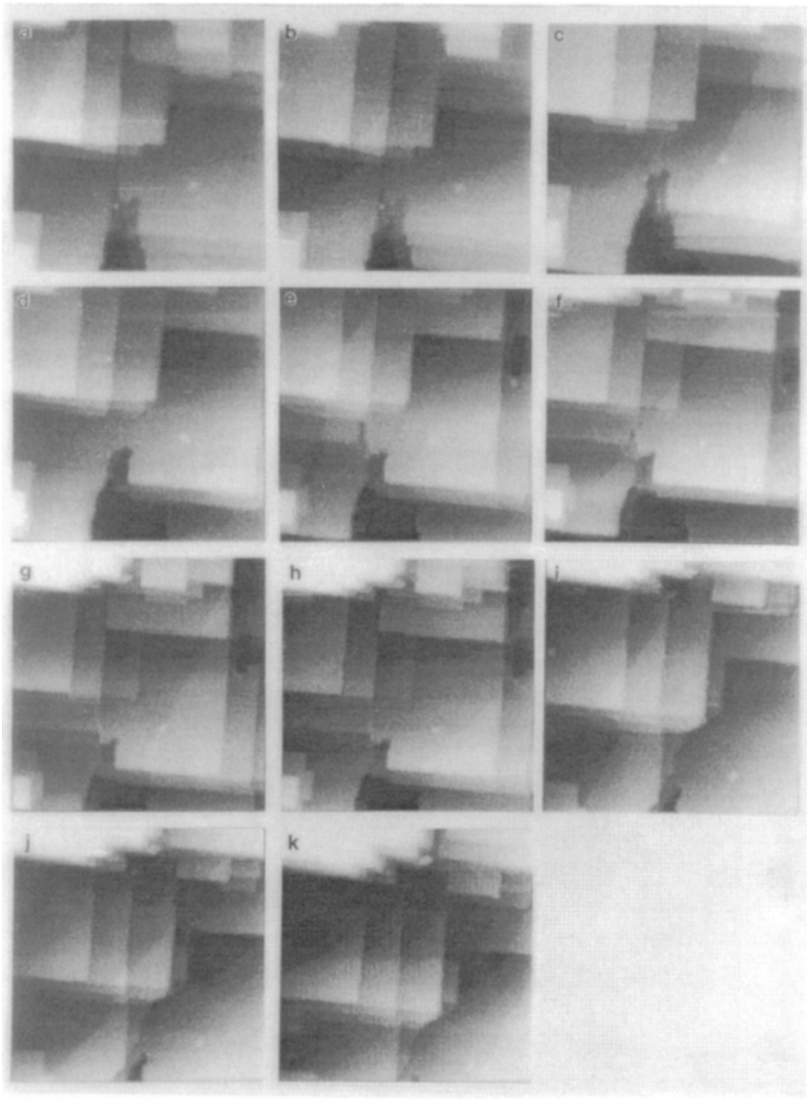

Fig. 3. A sequence of 75 nm x 75 nm images revealing the movement of a domain boundary in the chlorine adlattice across the Cu(100) surface at -0.250 V vs. Cu/Cu^{+} with E_{tip}= 0.056 V, I_t= 9 nA, and a frame time of 35 s.

In contrast to halide media, immersion in 10 mmol/l sulfuric or perchloric acid results in an ill-defined surface step structure and obtaining reliable atomically resolved images of Cu(100) proved difficult. The recent observations [12] of the influence of chloride on the kinetic anisotropy of copper deposition compared to the isotropic nature of deposition from sulfate solution may be, at least partially, related to oxidative halide adsorption. As noted above, compared to perchlorate and sulfate solutions, adsorbed chloride leads to a distinct anisotropy in the step morphology of the evolving Cu(100) surface. The impact of halide adsorption on the electrochemical processing of copper is further highlighted by its ubiquitous presence as an additive in most commercial copper electroplating baths [13]. In addition, the recent observation of the formation of well-ordered organic monolayers on gold which are mediated by an adsorbed iodine layer should stimulate much interest in the study of organic copper plating additives in the presence of chloride [14].

3.2 Reductive Desorption of Chlorine Adlattice

The oxidatively adsorbed adlayer of chlorine may be partially reduced to chloride at negative potentials, as shown by LEED and atomic emission spectroscopy (AES) studies [6]. The voltammetric signature associated with this process on Cu(111) was recently reported [15]. Desorption begins at potentials more positive than that associated with heteroepitaxial nickel deposition and the structural ramifications of this reaction are of some importance to the growth of multilayered materials. Consequently, the evolution of this reaction on Cu(100) was examined in 10 mmol/l HCl. A series of topographic images were collected while the potential was repeatedly stepped between -0.250 V and -0.650 V. As shown in Fig. 4, rapid movement of the surface steps along with the development of significant curvature is apparent immediately upon setting the potential to -0.650 V. Specifically, the steps migrate away from the <100> orientation and are somewhat frizzy.

Numerous attempts were made to obtain atomically resolved images of the terraces without success. The experiment was performed using both a constant imaging bias as well as a fixed tip potential with no apparent effect on the images obtained. This sequence of images demonstrates that partial disruption and/or desorption of the chloride adlattice at negative potentials leads to rapid movement and rearrangement of the highly kinked <100> metal steps. In UHV, surface steps on clean Cu(100) are aligned in the close-packed <110> direction [9]; thus, in the first approximation, the surface steps should relax towards this orientation upon desorption of chlorine. The frizziness of the steps may be

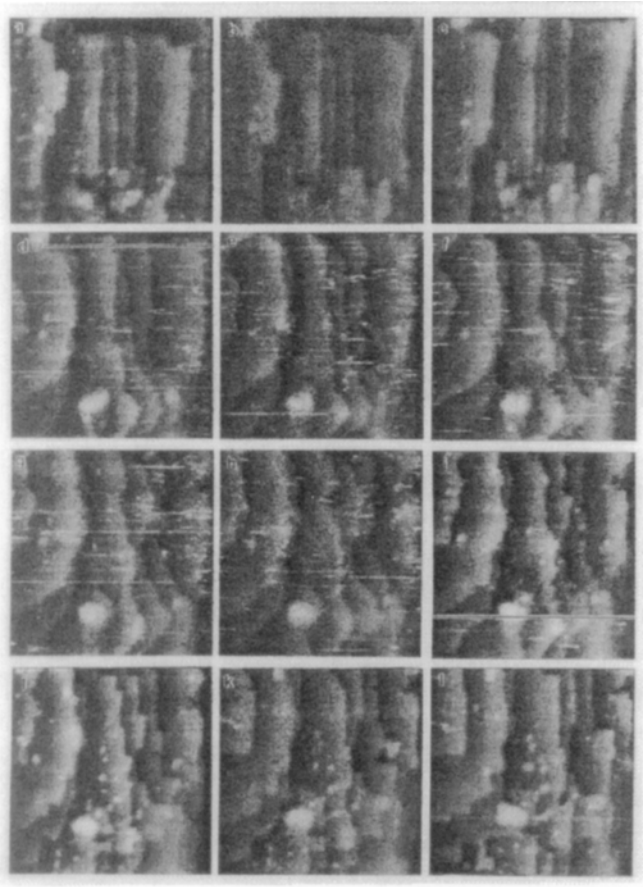

Fig. 4. A continous sequence of 50 nm x 50 nm images revealing the effects of stepping the potential between -0.25 and -0.65 V vs. Cu/Cu^+ in 10 mmol/l HCl with E_{tip} = 0.050 V, I_t = 9 nA and frame time of ~22 s The black horizontal line in images (d), (i), (p) and (t) correspond to the instant when the potential was stepped between the two values. A ($\sqrt{2}$ x $\sqrt{2}$)R45° chlorine adlattice is stable at -0.25 V whereas the adlattice is reductively disrupted at -0.65 V. For images (a) - (d) E =-0.25 V, (d) -(i) E=-0.65 V, (i) - (p) E=-0.25 V, (p) - (t) E=-0.65 V and (t) - (x) E=-0.25 V. The rapid movement and development of step curvature in images (d) - (i) and (p) - (t) corresponds to the reductive disruption and desorption of the chloride adlattice. The images, which take ~18 s to collect were obtained over a period of 8 min this reveals the remarkable effects of surface rearrangement associated with the adsorption/desorption process.

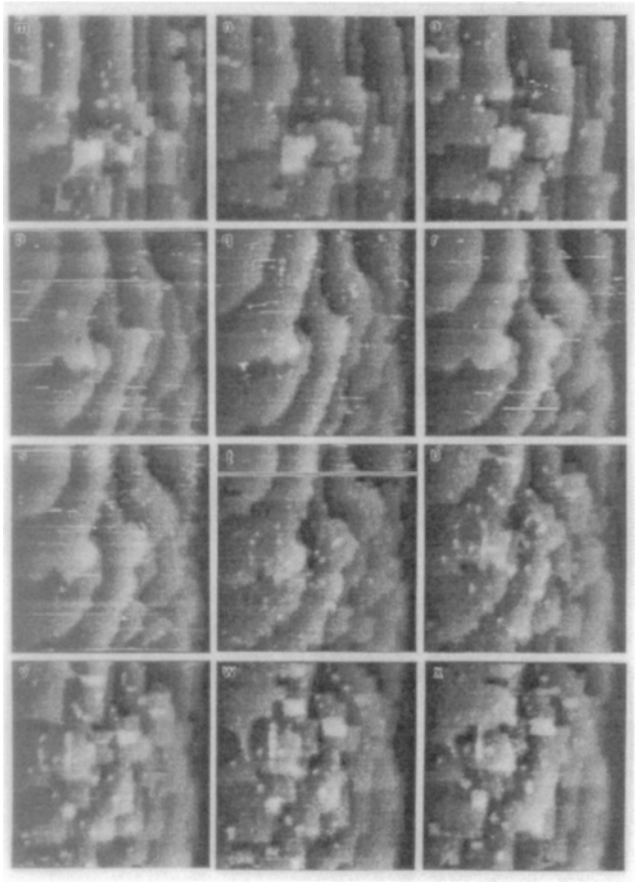

Fig. 4. A continous sequence of 50 nm x 50 nm images revealing the effects of stepping the potential between -0.25 and -0.65 V vs. Cu/Cu^+ in 10 mmol/l HCl with E_{tip} = 0.050 V, I_t = 9 nA and frame time of ~22 s The black horizontal line in images (d), (i), (p) and (t) correspond to the instant when the potential was stepped between the two values. A ($\sqrt{2}$ x $\sqrt{2}$)R45° chlorine adlattice is stable at -0.25 V whereas the adlattice is reductively disrupted at -0.65 V. For images (a) - (d) E =-0.25 V, (d) -(i) E=-0.65 V, (i) - (p) E=-0.25 V, (p) - (t) E=-0.65 V and (t) - (x) E=-0.25 V. The rapid movement and development of step curvature in images (d) - (i) and (p) - (t) corresponds to the reductive disruption and desorption of the chloride adlattice. The images, which take ~18 s to collect were obtained over a period of 8 min this reveals the remarkable effects of surface rearrangement associated with the adsorption/desorption process.

ascribed to the rapid movement of kinks and the curvature may correspond to higher activity of copper adatoms on the terraces. This explanation is congruent with the observation of thermally induced frizzy steps on Cu(100) in UHV [9]. When the potential is stepped back to -0.250 V an ordered chlorine adlattice is rapidly re-formed and the surface steps quickly move to adopt the anticipated <100> orientation. High-resolution images confirmed the ($\sqrt{2}$ x $\sqrt{2}$)R45° chlorine adlattice structure. Simultaneously, the nucleation of small islands on the terraces occurs, presumably due to a quenching of the elevated adatom density associated with the increased step curvature at negative potentials. The sequences of images in Fig. 4(i) - (o), and (t) - (x), reveal the reordering and coarsening of step structure.

An additional experiment was performed to investigate the role of chloride in the kinetics of the reordering and coarsening process. The ($\sqrt{2}$ x $\sqrt{2}$)R45° chlorine adlayer was initially formed at -0.250 V and allowed to coarsen for at least one hour. The chloride solution was then replaced with 10 mmol/l H_2SO_4 and the potential was stepped to -0.650 V. The surface steps became disordered with the reductive desorption of chlorine. However, when the potential was stepped back to -0.250 V the surface took a much longer time to reorder compared to the experiments performed in 10mmol/l HCl. This reflects the sharply diminished chloride concentration in the electrolyte. Nevertheless, the ordering process evolves, albeit more slowly, due to residual chloride present as contamination from the exchange of electrolytes.

3.3 In-situ Observation of Growth Dynamics on Cu(100)

In a general sense, STM may be used for dynamic studies whereby the long unresolved issue of the influence of adsorbates on the microstructural evolution of electrodeposited films may be addressed. In this vein a variety of notable reports of copper deposition on gold have been described [16]. Our initial studies focus on homoepitaxial growth on Cu(100) under conditions relevant to our multilayer synthesis program. During multilayer growth copper reduction occurs under diffusion control and this raises the possibility of developing morphological instabilities. However, the fact that laminar multilayers have been successfully grown [1, 2] suggests that there is a significant degree of surface or step mobility associated with the electrocrystallization reactions such that compact surface structures are formed [2].

This argument is supported by our STM observations. Immersion of Cu(100) in 10 mmol/l HCl followed by polarization at -0.250 V vs. Cu/Cu^+ results in the formation of a stable chlorine adlattice as described previously. In the presence of a dilute cuprous

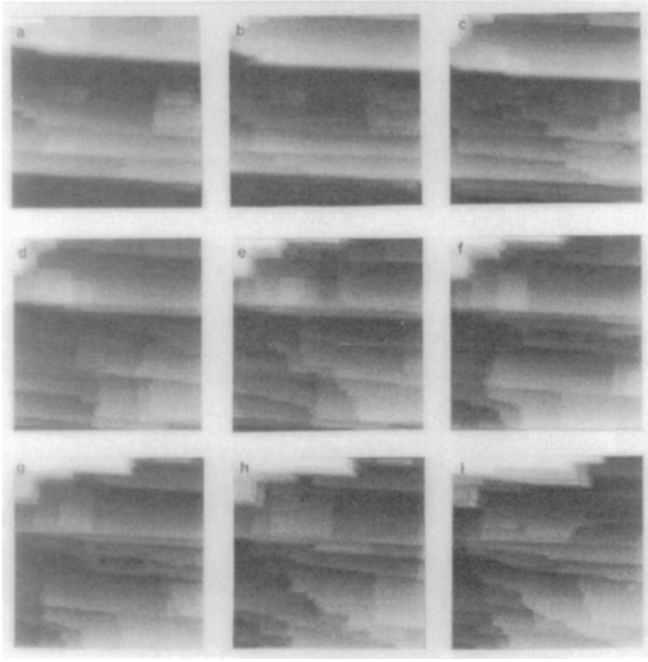

Fig. 5. A series of 125 nm x 125 nm STM images of step flow associated with Cu^+ deposition on Cu(100) at -0.25 V vs. SCE, with E_{tip} = 0.010 V , I_t = 15 nA and a frame time of ~19 s for images collected over a period of 3 min; scanning (a) down 0-18.7s, (b) up 18.9s-37.6s, (c) up 55.6-74.3s, (d) down 74.4-93.2s, (e) up 93.25-112s, (f) down 112.1-130.8s, (g) up 130.7-149.7s, (h) down 149.7-168.5s, (i) up 168.5-187.3s.

chloride solution, nominally 1 mmol/l Cu^+ in 10 mmol/l HCl, metal reduction proceeds under diffusion control at -0.250 V. Growth is generally observed to occur by step

propagation in the <100> direction with the energetics associated with the chlorine adlattice dominating the evolution of step morphology as shown in Fig. 5. The electrocrystallization reaction develops according to a combination of two competing mechanistic paths. In the first instance, reduction of the cuprous chloride complex may be at catalyzed the kink-saturated <100> steps. This is consistent with the marked difference reported for the exchange current for silver deposition at step edges versus the adatom state [17]. The distinct <100> step orientation results from subsequent energy minimization which is facilitated by the rapid transport of reduced atoms along step edges.

An alternative scenario for step-mediated growth would entail the capture of adatoms from a two-dimensional (2D) gas on neighboring terraces. In this model the terrace adatoms which form the 2D gas are presumed to be sufficiently mobile so as not to be imaged by the STM [18]. Similarly, in this instance the adatom density relative to the mean diffusion length must be such that adatoms are trapped by the steps as opposed to nucleating as islands on the large terraces. This second model follows from a direct analogy with physical vapor deposition [19] and thus ignores the possible influence of the higher-coordination step edges on the inner-sphere reduction reaction. Nonetheless, at least two possible homogeneous island nucleation events are visible in Fig. 5(a) and (i).

Further experimentation under controlled conditions of saturation and crystal miscut will enable us to address the growth mechanism more accurately. As noted earlier, it is encouraging that several theoretical works already exist for describing homoepitaxy of Cu on Cu(100) from the vapor phase [11].

3.4 Heteroepitaxial Deposition on Cu(100)

A preliminary experiment was performed to investigate the possibility of examining nickel deposition on Cu(100). In this experiment a concentrated nickel electrolyte, 1.5 mol/l $Ni(SO_3NH_2)_2$ with 0.5 mol/l H_3BO_3, was used which corresponds directly to that utilized for multilayer deposition. The potential of the Cu(100) electrode was swept in the negative direction until a significant cathodic current, ~0.1 mA/cm^2, was observed at approx.. -0.658 V. The potential was held at this value while the surface was imaged continuously as nickel was deposited. Numerous imaging instabilities were encountered; however, as shown in Fig. 6, nickel grows epitaxially via step flow with propagation of <110> oriented steps. Further work is in progress.

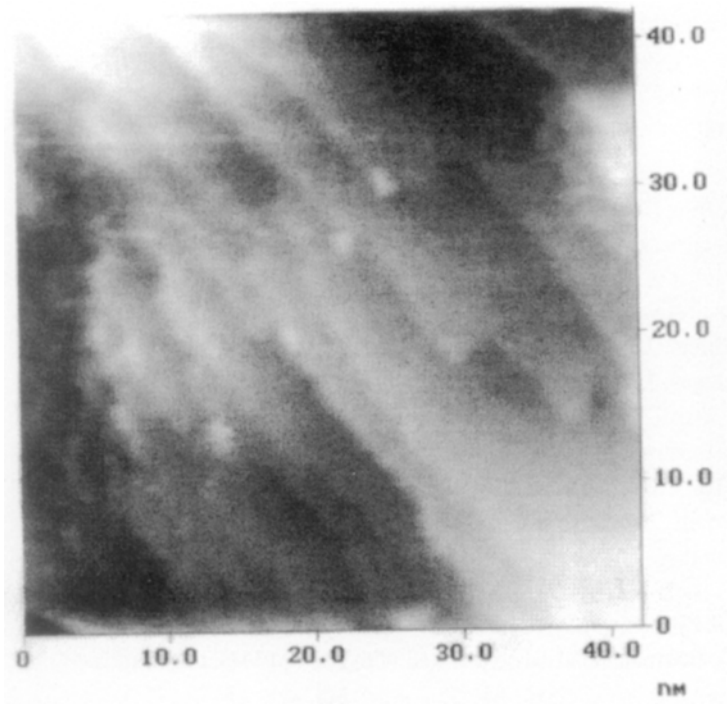

Fig. 6. A 42 nm x 42 nm image of nickel deposited on Cu(100) at -0.658 V vs. Cu/Cu^+, with E_{tip}= 0.051 V, I_t = 16 nA and frame time of 31 s. Note the surface steps are oriented in the close-packed <110> direction.

4 Conclusions

An in-situ STM study has been initiated to investigate the various processes associated with electrodeposition of Cu-(Ni, Co, Fe) multilayers. This paper gives an example of the remarkable utility of STM for imaging the structure and dynamics associated with electrodeposition processes. Specifically, the significant role of anion adsorption in homoepitaxial deposition on Cu(100) has been demonstrated.

Acknowledgments. The author gratefully acknowledges the support of Gery Stafford, Bob Shull and the NIST Nanostructural Initiative Program.

5 References

[1] C.A. Ross, Annu. Rev. Mater. Sci. 24, 159 (1994).
[2] T.P. Moffat, J. Electrochem. Soc. 142, 3767 (1995).
[3] R. Vidal, A.C. West, J. Electrochem. Soc. 142, 2682 (1995); idem, ibid. 142, 2689 (1995).
[4] U. Bertocci, J. Electrochem. Soc.113, 604 (1966).
[5] I.Villegas, C.B. Ehlers, J.L. Stickney, J. Electrochem. Soc. 137, 3143 (1990).
[6] C.B. Ehlers, I Villegas, J.L. Stickney, J. Electroanal. Chem. 284, 403 (1990).
[7] D. W. Suggs, A.J. Bard, J. Phys. Chem. 99, 8349 (1995).
[8] T.P. Moffat, in: Nanostructured Materials in Electrochemistry, P. Searson, J. Meyer (Eds.), PV 95-8, The Electrochemical Society, Inc., Pennington, NJ, 1995, pp. 225 - 237.
[9] M. Poensgen, J.F. Wolf, J. Frohn, M. Giesen, H. Ibach, Surf. Sci. 274, 430 (1992).
[10] E. Kopatzki, S. Gunther, W. Nichtl-Pecher, R.J. Behm, Surf. Sci. 284, 154 (1993).
[11] M. Breeman, G.T. Barkema, M.H. Langelaar, D.O. Boerma, Thin Solid Films, submitted; M. Breeman, D.O. Boerma, Surf. Sci. 287/288, 881 (1993); G.T. Barkema, O. Biham, M. Breeman, D.O. Boerma, G. Vidali, Surf. Sci. 306, L569 (1994); C-L. Liu, Surf. Sci. 316, 294 (1994); H. Durr, J.F. Wendelken, J-K. Zuo, Surf. Sci. 328, L527 (1995).
[12] D. Barkey, F. Oberholtzer, and Q. Wu, Phys. Rev. Lett., 75, 16, 2980 (1995)
[13] S. Yoon, M. Schwartz and K. Nobe, Plating and Surface Finishing, p65, December (1994).
[14] M. Kunitake, N. Batina, K. Itaya, 188th Meeting of the Electrochemical Society, Inc., Chicago, IL, (1995, Abstract No. 907); N. Batina, M. Kunitake, K. Itaya, ibid. Abstract No. 908.
[15] G.M. Brisard, E. Zenati, H.A. Gasteiger, N.M. Markovic, P.N. Ross, Langmuir, 11, 2221 (1995).
[16] M.H. Holzle, V. Zwing, D.M. Kolb, Electrochim. Acta 40, 1237 (1995); N. Batina, D.M. Kolb, R.J. Nichols, Langmuir 8, 2572 (1992).
[17] J.D. Porter, T.O. Robinson, J. Phys. Chem. 97, 6696 (1993).
[18] C. Gunther, S. Gunther, E. Kopatzki, R.Q. Hwang, J. Schroder, J. Vrijmoeth, R.J. Behm, Ber. Bunsenges. Phys. Chem. 97, 522 (1993).
[19] Electronic Thin Film Science, K.-N. Tu, J.W. Meyer, L.C. Feldman, Macmillan, New York, 1992.

Part V

Electrochemical Nanotechnology
In-situ Local Probe Techniques at Electrochemical Interfaces
Edited by W. J. Lorenz and W. Plieth

STM Studies of Thin Anodic Oxide Layers

Philippe Marcus, Vincent Maurice

Contents

1	Introduction	185
2	STM Data on the Passivation of Non-noble Metals and Alloys	186
3	Discussion	194
4	Conclusion and Outlook	196
5	References	196

Summary. Scanning tunneling microscopy (STM) provides new possibilities to explore the link between the structure and the properties of thin oxide overlayers (passive films) formed electrochemically on well-defined metal surfaces. Passive oxide films protect many metals and alloys against corrosion. A better understanding of the growth mechanisms, the stability, and the degradation of passive films requires precise structural data. Recently, new results on the atomic structure of passive films have been obtained by STM. The important questions of crystallinity, epitaxy and the nature of defects have been addressed. Data on the structure of passive films on Ni, Cr, Fe, Al, and Fe-Cr alloys are reviewed with emphasis on atomically resolved structures. The perspectives of future developments are discussed.

1 Introduction

Data on the chemistry and structure of thin oxide layers (passive films) produced by anodic polarization of metallic electrodes are necessary to understand and predict the properties of these films, in particular their corrosion resistance. There are now many available data on the chemical composition of passive films formed on metals and alloys. Surface chemical analysis techniques have been, and still are, very useful to obtain such data. In sharp contrast, there is a lack of data on the structure of passive films. This is in part due to the difficulty of any structural analysis of very thin films on

substrates that are often rough, using for example reflection high-energy electron diffraction (RHEED) and grazing-incidence X-ray diffraction. The advent of near-field microscopies (STM (scanning tunneling microscopy) and AFM (atomic force microscopy)) has opened up new prospects in this field. Direct imaging of the structure with atomic resolution can now be performed in both ex-situ (UHV or air) and in-situ conditions.

The objective of this paper is to review the published data on ex-situ and in-situ STM of passivation of metals (Ni, Cr, Fe, Al) and alloys (Fe-Cr), with special emphasis on atomically resolved structures, and to discuss, on the basis of the reviewed data, the questions of crystalline versus amorphous character of passive films, the nature of the defects, the relation of the structure to the available chemical information, and the implications of the structural features in the stability and the breakdown of passive films.

2 STM data on the passivation of non-noble metals and alloys

Lev et al. [1] were the first authors to investigate the possibility of in-situ STM imaging of transitions induced by the electrochemical potential at non-noble metal surfaces. They studied nickel in sulfuric acid. At the rest potential and in the active region, the images were reproducible. Current versus tip-surface distance (*I-d*) curves showed the exponential decrease characteristic of the tunneling mechanism. When the potential was stepped in the passive region, erratic images were recorded under the same tunneling conditions. The *I-d* response was asymmetric and spread over large distances, which is not typical of tunneling. This effect was attributed to mechanical fractures of the tip with the passive layer. Surface deposition of a nickel sulfate film resulting from the extensive dissolution produced by the potential step may also have been responsible for the failure to record STM images of the passive film in this experiment.

Bhardwaj et al. [2] studied by in-situ real-time STM imaging the passivation of polycrystalline iron in borate buffer. They proceeded by alternating oxidation steps at increasing anodic potentials and reduction steps at cathodic potential. After reduction of the natural oxide at the cathodic potential, relatively flat surfaces were produced supposedly corresponding to the metal substrate. Upon oxidation at anodic potential, rougher surfaces were at first produced, with patches or clusters of nanometer dimensions. These patches were observed in the first image after the oxidation step,

indicating instantaneous formation on the time scale of the data acquisition. Upon continuous imaging at the same oxidation potential, the surface was observed to smoothen. This was attributed to the completion of the passive layer by a fusing effect of the patches. When the potential was stepped back at the reduction value, surface roughening was first observed followed by smoothening within minutes of polarization. These topographic changes were attributed to the reduction of the passive film. The vertical dimensions of the patches produced at first by oxidation were found to increase from about 1 to about 4 nm when the anodic oxidation potential was increased. This suggested an increasing thickness of the passive film after completion for increasing values of the oxidation potential. This was supported by the increasing time periods necessary to reduce completely the passive film at cathodic potential. This study suggests that the growth process of the passive film by patches or islands fusing together is related to a nucleation, growth, and coalescence mechanism. The same authors performed a similar study on polycrystalline Al in sodium hydroxide [3]. They also observed that reduction of the oxide formed at anodic potentials reproduced the original substrate surface, and that when the potential is increased in the positive direction an oxide begins to grow nonuniformly as small humps or patches of nanometer dimensions, which later fuse together after longer elapsed times or at more positive potentials. As in the case of iron, it is suggested that the formation of the passive film occurs via a nucleation, growth, and coalescence mechanism.

Ex-situ STM imaging has been applied in our group to the investigation of the passive films formed on Ni, Cr and Fe-22Cr in aqueous sulfuric acid solutions [4-8]. The study on Ni [4] was the first investigation of passive films with achievement of both lateral and vertical atomic resolution. In our surface science-oriented approach to passivation and corrosion, well-defined surfaces of single crystals are used. For Ni [4, 5], the (111) orientation was selected as a previous investigation had demonstrated the crystallinity of the passive film formed on this surface [9]. Much care was given to surface pretreaments. The samples were electrochemically polished and annealed at high temperature in a flow of pure hydrogen for several hours. These pretreaments were necessary to produce large atomic terraces of the substrate (of the order of tenths of micrometers). The passive films were produced in 0.05 M H_2SO_4 by potential steps from the corrosion potential value to three different values in the passive region (+550, +650 and +750 mV/RHE). STM analyses were performed in air, in which conditions the passive films were stable.

Modifications of the passivated Ni surfaces with respect to the nonpassivated one were recorded on two different lateral scales. On a mesoscopic scale of hundreds of nanometers, islands were observed. Their size was found to decrease and their density was found to increase with increasing passivation potential. Their shape varied from trigonal contours with ledges oriented along the main crystallographic directions of the

substrate, to hexagonal contours still with ledges oriented along the main crystallographic directions, and finally to nonsymmetrical contours with nonoriented ledges after passivation at +550, +650 and +750 mV/RHE, respectively.

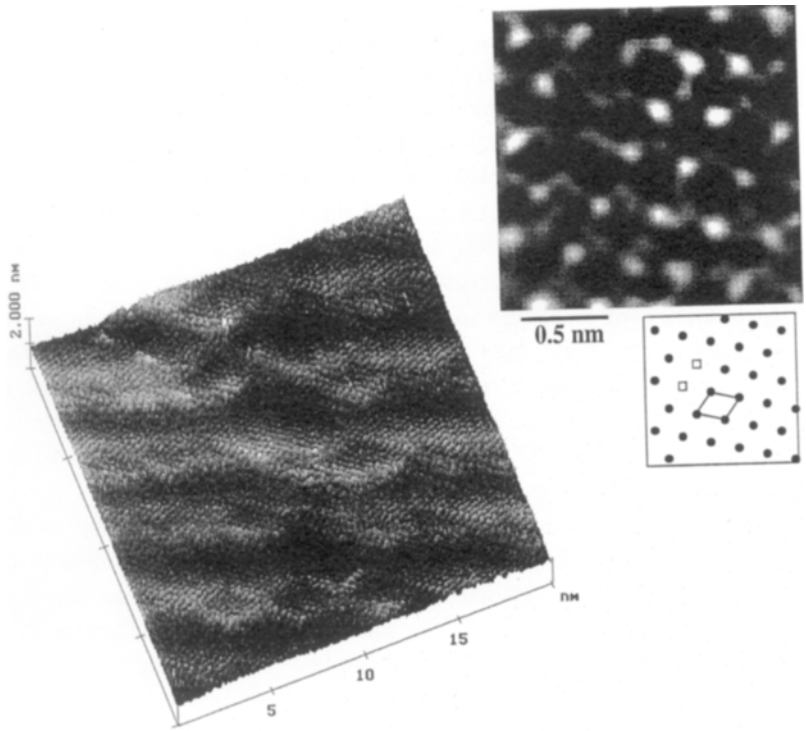

Fig. 1. STM images of the passive film formed on Ni(111) in 0.05M H_2SO_4 at +750 mV/RHE. The left image shows the stepped crystalline lattice corresponding to NiO. The right image shows the lattice recorded on some terraces consistent with NiO(111). The unit cell and two point defects are marked.

These variations have been assigned to competition, during the passivation treament, between metal dissolution and formation of the passive film. The roughening effect due to dissolution increases with potential and produces a higher density of islands with less oriented ledges. On these submicroscopic islands, a stepped crystalline lattice was imaged on the atomic scale. A typical image is shown in Fig. 1. The lattice

parameters measured on the terraces of the stepped lattice correspond to the lattice parameters of the (111) orientation of NiO, the inner component of the passive film. These lattice parameters and the step density were found to be independent of the passivation potential. The density and height of the steps correspond to an average tilt of 8(±5)° between the surface of the film and the (111) orientation of the terraces. The resulting epitaxy relationships with the substrate are: NiO(433)//Ni(111) with NiO[0-11]//Ni[0-11] and NiO(765)//Ni(111) with NiO[1-21]//Ni[1-21]. The tilt is thought to result from a relaxation of the strained epitaxy due to a mismatch of 16% between the lattice parameters of the oxide film and those of the metal substrate and/or from a relaxation of the polar NiO(111) terraces. A possible atomic model of the interface between a 10 nm thick NiO(111) layer tilted by 8° and the Ni(111) substrate is shown in Fig. 2. It illustrates different chemical terminations of the oxide film and possible

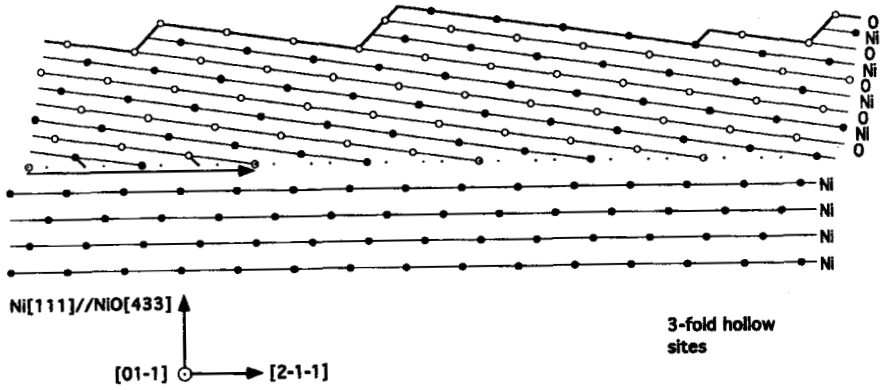

Fig. 2. Section profile along [2-1-1] of the interface between the thin oxide film and the metal substrate constructed from bulk parameters in the case of the NiO(433) // Ni(111) with NiO[0-11] // Ni[0-11] epitaxy (8.02° tilt between the (111) planes of the oxide and those of the substrate). The atomic planes and nodes are indicated. Different terminations of the oxide film are illustrated. The vector of the coincidence cell along [2-1-1] is $4\sqrt{3}$ times that of the substrate. Possible atomic displacements at the interface towards the nearest three-fold sites of the substrate are indicated.

atomic displacements (marked by arrows) at the interface towards the nearest threefold hollow sites of the substrate. The presence of terraces and steps at the surface of the passive film may also reflect a preferential dissolution at steps in the passive state. In

addition to steps and kinks at the surface of the passive film, other crystalline defects such as point defects possibly related to vacancies have been imaged. One example is also shown in Fig. 1. The presence of crystalline defects at the surface of the passive film may play a key role in the resistance to breakdown. The bottoms of steps and kinks correspond to sites of reduced thickness of the passive film where the barrier property of the film is expected to be diminished. These defects may also constitute sites of preferential adsorption of aggressive ions such as chloride ions. The hydroxide layer present in the outer part of the film, which is about one monolayer thick [10-13], could not be observed in a distinct manner in the STM images. The possible role of the hydroxyl groups in the tunneling mechanism is discussed below.

The crystalline nature of the passive film formed on Ni has been confirmed by in-situ STM for a different crystallographic orientation of the electrode and in a different electrolyte: Ni(100) in 1M NaOH [14]. At low potential (-0.7 to -0.5 V/NHE), oxidation resulted in the formation of a well-ordered rhombic structure resistant to reduction and assigned to the irreversible formation of the $Ni/Ni(OH)_2$ interface. At increasing potential, a distortion of this rhombic structure was first observed, followed at higher potential (>0.18 V/NHE) by a quasi-hexagonal structure with a nearest-neighbor spacing consistent with either β-$Ni(OH)_2$(0001) or NiO(111). These results suggest that independently of the substrate orientation (Ni(100) or Ni(111)), the crystalline passive film is NiO (111) oriented and terminated by a β-$Ni(OH)_2$(0001) hydroxide layer in (1x1) epitaxy on the oxide layer.

For the study of chromium passivation performed in our group [6], (110) oriented single crystal surfaces were used. Pretreaments by electrochemical polishing and annealing at high temperature in hydrogen revealed, as for Ni, atomic terraces of lateral dimensions of the order of tenths of micrometers. Passivation was performed in 0.5 M H_2SO_4 by potential steps from the corrosion potential to three different potentials in the passive region (+300, +500 and +700 mV/RHE). Different time periods of polarization were investigated (20 min, 2 and 22 h). The STM measurements were combined with X-ray photoelectron spectroscopy (XPS) analysis. The XPS analysis (in UHV) showed that the passive film contains trivalent chromic species only. The oxide inner part of the film varies from dispersed three dimensional (3D) islands to a complete layer about 0.9 nm thick. The thickness of the hydroxide outer layer varies from about 0.6 to about 1.3 nm. Composition and thickness were found to be stable upon exposure to air. STM measurements in air showed that unlike Ni, the surface is quite homogeneous on the submicroscopic scale after passivation. This is due to the quasi-absence of dissolution during the passivation treatment. On Cr, the surface topography is heterogeneous only

on a nanoscopic scale. It is characterized by disordered protrusions of 1 - 4 nm lateral dimensions which induce vertical variations of 0.4 - 0.8 nm amplitude. A typical image is shown in Fig. 3. This topography is independent of the passivation conditions. On the atomic scale, small areas of limited lateral extension are detected.

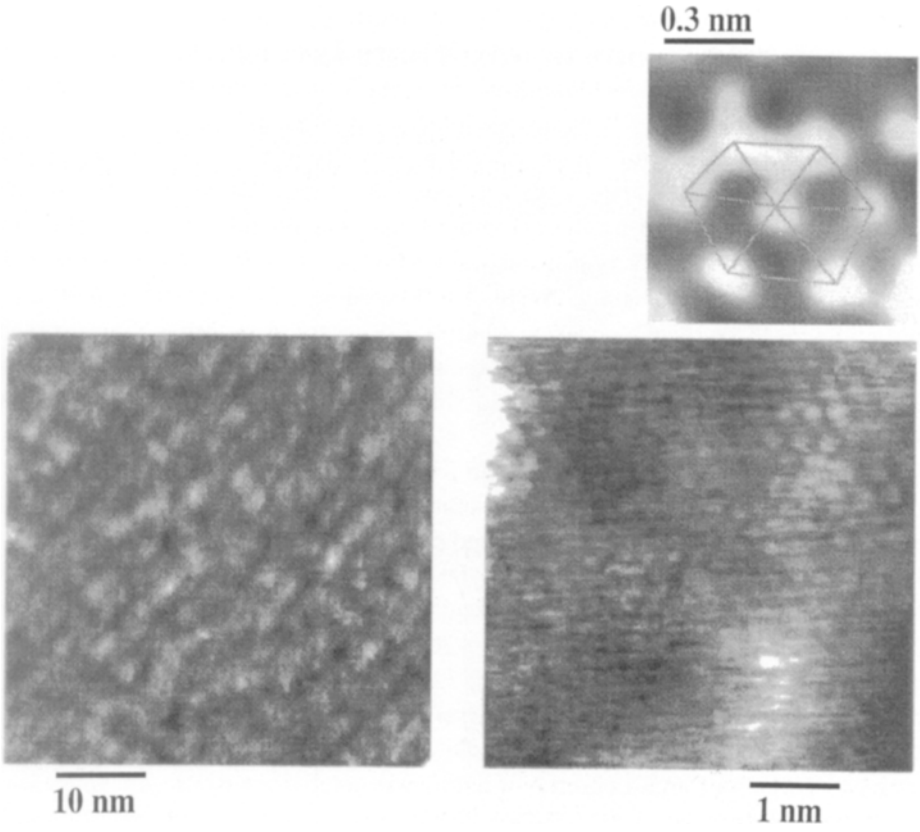

Fig. 3. STM images of the passive film formed on Cr(110) in 0.5M H_2SO_4 at +500 mV/RHE. The left image shows the disordered protrusions of nanoscopic dimensions. The right images show a small ordered domain assigned to a nanocrystal of oxide (α-Cr_2O_3(0001)) at two different magnifications.

This is also shown in Fig. 3. These areas are characteristic of small ordered domains assigned to nanocrystals of oxide emerging at or near the film surface. The quasi-hexagonal arrangement and the nearest neighbor distances of the corrugations are consistent with the arrangement of the O^{2-} ligands in the basal plane of the oxide (α-Cr_2O_3(0001)). Larger ordered domains are observed by STM when more oxide is formed in the inner part of the film, according to XPS measurements. These ordered domains are surrounded by areas where no structural periodicity is evident which are assigned to the hydroxide outer part of the film. No crystalline defects are detected at the boundaries of the ordered domains. In terms of resistance to breakdown, the topography variations of the hydroxide outer part also induce sites of reduced thickness of the passive film where the barrier property of the film is expected to be diminished. However, crystalline defects are not evident in these sites, probably because they are cemented by the amorphous structure of the hydroxide. Therefore, they are expected to offer higher resistance to film breakdown. In addition, the amorphous structure of the hydroxide is expected to minimize the variations of coordination of the surface atoms at crystalline defects and therefore to induce a higher chemical passivity at these sites. Hence, the nanocrystalline structure of the oxide and the role of cement played by the hydroxide would be responsible for the higher passivity of the film formed on Cr.

Moffat et al. [15] also reported an ex-situ STM investigation of Cr(110) passivated in 1M H_2SO_4. Their images confirmed the presence of ordered domains consistent with the structure of α-Cr_2O_3 oriented (0001) and parallel to Cr(110).

The structure of the passive film on a Fe-22Cr alloy [7, 8] was investigated with (110) oriented single crystal surfaces. The passivation was performed in 0.5 M H_2SO_4 at potential values of +300, +500 and +700 mV/RHE. Different time periods of polarization were investigated (20 min, 2, 22 and 63 h). The XPS analysis (in UHV) showed that the passive film is well described by a bilayer model with a mixed trivalent oxide inner layer enriched in Cr_2O_3 (from 88 to 95% and 0.7 to 1.4 nm thick with increased aging) and a chromium hydroxide outer layer whose thickness varies from a 1 nm-thick 3D layer to 2D islands with increased aging. Upon exposure to air, only the films aged for 22 and 63 h do not show a significant evolution of the (much thinner) hydroxide outer layer. STM measurements in air showed that the terrace topography of the substrate surface is maintained after passivation. Similar protrusions (up to 10 nm across) to those recorded on Cr(110) are observed on the alloy. However, in the case of the alloy, a fusing process has been observed as a function of aging under polarization. This process is attributed to the coalescence of islands of the passive film occurring during film growth and aging (in a similar way to that observed on Fe [2] but on a much longer time scale). On the atomic scale, the passive film has been found to be noncrystalline after polarization for 2 h at +500 mV/RHE. Aging under polarization

favors a crystallization process evidenced by the presence of epitaxial crystalline areas consistent with the structure of α-Cr_2O_3. This is illustrated in Fig. 4. Similarly to Cr(110), the basal plane (0001) of Cr_2O_3 is found to be parallel to the (110) plane of the substrate. Deviations from a quasi-hexagonal arrangement of the corrugations are measured. This is possibly due to the presence of OH groups, as discussed below. On

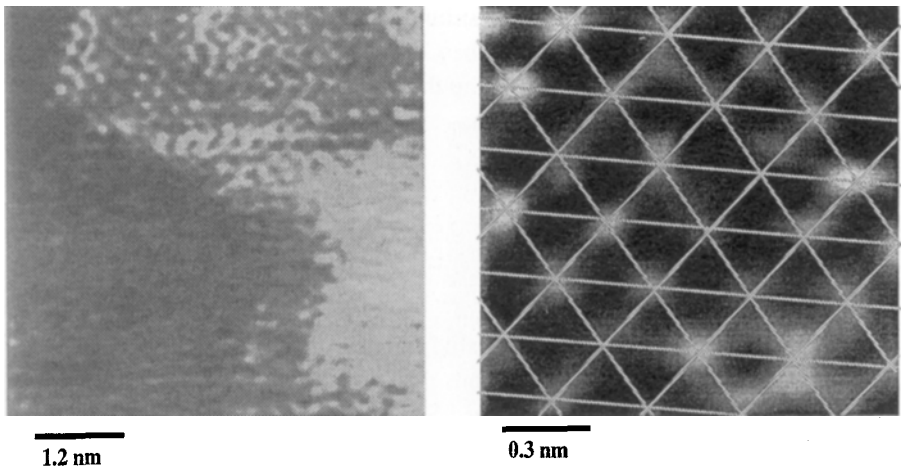

Fig. 4. STM images of the passive film formed on Fe-22Cr(110) in 0.5M H_2SO_4 at +500 mV/RHE and aged 63 h under polarization. The left image shows a crystalline area with (possibly) the emergence of a screw dislocation. The right image shows an ordered area at higher magnification. The quasi-hexagonal lattice is consistent with the basal plane of chromium oxide: α-Cr_2O_3(0001). Deviations from a perfect periodicity of the corrugations are observed in these crystalline areas.

the alloy, three different azimuthal orientations of the oxide islands have been found. However, the crystallization is not complete in these conditions and the topography of the passive film is intermediate between that recorded on passivated Ni(111) (complete crystallization with large crystals) and that recorded on passivated Cr(110) (nanocrystals cemented by noncrystalline areas). It shows the presence of both crystalline defects and noncrystalline areas.

Ryan et al. [16, 17] studied ex-situ and in-situ microcrystalline Fe-Cr surfaces prepared by sputter deposition and passivated at a low potential in the passive region where mostly Cr is expected to participate in film formation. The noncrystalline character of the passive film formed on Fe-Cr alloys has been confirmed in-situ after

1h of passivation [17]. In this study, it was observed that after 1 h of passivation the amount of disorder increased sharply for a Cr content of the alloy between 14.7 and 16.5%. The effect of aging was tested only in ex-situ conditions and it was observed that it favors the (re)crystallization of the passive film for 18 and 21% Cr content [15]. The structural order observed in the passive film was consistent with the (0001) orientation of α-Cr_2O_3. In the case of pure Fe sputter-deposited thin films polarized at high anodic potentials in borate buffer solution, the same group reported long-range crystalline order in both ex-situ and in-situ conditions of examination [18].

It appears from these studies that both the Cr content of the alloy and the conditions of aging of the film are critical factors ruling the crystallization of the passive film.

3 Discussion

A major requirement for the interpretation of high-resolution images acquired by STM is a precise knowledge of the chemistry of the object investigated. For example, the interpretation of the data recorded in the study of the passive films formed on Ni and Cr [4-6] would have been difficult without the knowledge of the distribution of the different phases within the passive films. Such chemical information can only be obtained in ex-situ conditions using surface analytical techniques (e.g., XPS). To correlate this chemical information with the structural information deduced from STM is a major objective of ex-situ STM investigations of passive films on various substrates. This approach must be considered as the first step of a more complete structural investigation which should include both ex-situ and in-situ measurements. Besides, one advantage of ex-situ investigations is to stop dynamic processes taking place in-situ and this favors high-resolution imaging. However, the drawback is that the electrode must be removed from solution, which may cause modifications of the surface species. The extent of the modifications due to removal of the electrode depends on the stability of the anodic layer upon exposure to atmospheric pressure of air or inert gas, and/or exposure to reduced pressure (from vacuum to UHV) and therefore this stability should be tested in the conditions of the ex-situ investigation. A critical evaluation of the differences related to the conditions of the STM measurements is necessary. The similarities between ex-situ and in-situ studies reported both on Ni [4, 5, 14] and Cr [6, 15] show the relevance of this combined approach.

In addition to the precise knowledge of the chemistry of the passive film, another requirement is necessary if the crystallinity of the passive films is investigated: it is to work with well-defined substrate surfaces. The criterion of a well-defined surface is the observation of atomic terraces. This is obtained with single-crystal surfaces. The use of

such surfaces allows us to study passive films formed on metal substrate planes of the desired crystallographic orientation and to minimize and control the possible influence of the substrate defects on the defects of the passive film.

On both Ni and Cr substrates, the passive film is made of an inner oxide layer at the metal interface and of a hydroxide layer in the outer part of the film. On Ni [10-13], the thickness of the oxide inner part is about 0.4 - 1.2 nm and that of the hydroxide outer part is at most that of one monolayer (about 0.6 nm). No distinct evidence of the hydroxide layer has been found in the STM images of the passive film on Ni. This can be explained if one considers two possible tunneling mechanisms. The first possible mechanism involves tunneling from the oxide layer to the tip (or vice versa) through the hydroxide layer. In this case the oxide layer is imaged but the hydroxide layer is not. The integrity of the hydroxide layer during STM measurements depends on the width of the tunneling gap. If it is smaller than 0.6 nm, the hydroxide layer may be damaged by the scanning tip. The second possible mechanism involves direct electron transfer from the metal substrate to the surface hydroxyl groups and tunneling from these groups to the tip (or vice versa). In this case, the hydroxide layer can be imaged. The recorded images suggest then that the monolayer-thick hydroxide layer is in epitaxy on the crystalline NiO host lattice with a (1x1) relationship, and thus the structure of the hydroxide monolayer duplicates the structure of the NiO host lattice. The point defects visible in Fig. 1 could then correspond to OH vacancies (-OH on Ni^{2+} or -H on O^{2-}). On Cr [6], the nonordered areas measured by STM have been assigned to this hydroxide layer on the basis of data recorded on passive films containing only dispersed islands of oxide in the inner part whereas the ordered areas were assigned to oxide nanocrystals. It cannot be excluded that OH groups are present in (1x1) epitaxy above the ordered domains assigned to α-Cr_2O_3, hence suggesting that a mechanism involving tunneling from (or at) OH groups could also exist for oxide areas on Cr. A similar situation can be postulated for Fe-Cr alloys. The presence of these OH groups could possibly explain the measured deviations (see Fig. 4) from the perfect hexagonal arrangement of the basal plane of α-Cr_2O_3.

STM offers the possibility of performing local spectroscopic measurements (I vs. V curves). These measurements can be performed in-situ and ex-situ. Ex-situ UHV conditions are however more appropriate to ensure the nonconductivity of the tunneling barrier between surface and tip. Such measurements on passive films formed on Ni and Cr should provide valuable information on the conductivity of the films. This is a promising perspective for the local characterization with high resolution of the electronic properties of passive films. On the subject of the relation between chemistry at the atomic scale and atomic structure, the STM results on the passive film formed on Ni also show promising perspectives for further characterization: accurate bias-dependent measurements of the terraces of the NiO oxide should provide

information on their chemical termination (cation or anion). Also, such measurements should allow us to characterize the nature of point defects such as those shown in Fig. 1 (i.e., cation or anion vacancy).

4 Conclusion and outlook

This review of STM studies of thin anodic oxide (passive) films formed on metals and alloys shows that important results have been obtained by direct imaging of the surface structure, providing direct evidence on (for example). the crystallinity of passive films and the nature of defects. The fully crystalline character of the film on Ni has been demonstrated by STM. The nature of defects (steps, kinks, vacancies, points of reduced thickness) has been elucidated. This is important for a better understanding of the breakdown of passive films. The unique protectiveness of the film on Cr may be related to the observed structure with oxide nanocrystals cemented by a noncrystalline hydroxide. Many more results are expected to be produced, in the future, on the atomic structure of passive films, including the local interactions of impurities and anions with passive films and especially with surface defects, the local conductivity of passive films derived from *I-V* curves at specific sites, and chemical features derived from spectroscopic imaging. All these data should drastically improve our understanding of the relation between structure and properties of passive films.

5 References

[1] O. Lev, F.-R. Fan, A.J. Bard, J. Electrochem. Soc. 135, 783 (1988).
[2] R.C. Bhardwaj, A. Gonzalez-Martin, J.O'M. Bockris, J. Electroanal. Chem. 307, 195 (1991).
[3] R..C. Bhardwaj, A. Gonzalez-Martin, J. O' M. Bockris, J. Electrochem. Soc. 138, 1901 (1991).
[4] V. Maurice, H. Talah, P. Marcus, Surf. Sci. 284, L431 (1993).
[5] V. Maurice, H. Talah, P. Marcus, Surf. Sci. 304, 98 (1994).
[6] V. Maurice, W. Yang, P. Marcus, J. Electrochem. Soc., 141, 3016 (1994).
[7] V. Maurice, W. Yang, P. Marcus, Proc. of the H. H. Uhlig Memorial Symposium - Corrosion Science: From Theory to Practice, F.B. Mansfeld, R.M. Latanision, A.I. Asphanani, H. Bohni (Eds.), The Electrochemical Society Proceedings Series PV 94-26, Miami Beach, Florida, 1994.
[8] V. Maurice, W. Yang, P. Marcus, J. Electrochem. Soc. 143, 1182 (1996).

[9] J. Oudar, P. Marcus, Appl. Surf. Sci. 3, 48 (1979).
[10] P. Marcus, J. Oudar, I. Olefjord, J. Microsc. Spectrosc. Electron. 4, 63 (1979).
[11] B.P. Lochel, H.-H. Strehblow, J. Electrochem. Soc. 131, 713 (1984).
[12] F. T. Wagner, T. E. Moylan, J. Electrochem. Soc. 136, 2498 (1989).
[13] D.F. Mitchell, G.I. Sproule, M.J. Graham, Appl. Surf. Sci. 21, 199 (1985).
[14] S.-L. Yau, F.-R.F. Fan, T.P. Moffat, A.J. Bard, J. Phys. Chem. 98, 5493 (1994).
[15] T.P. Moffat, F.-R. F. Fan, S.-L. Yau, A. J. Bard, Proc. H. H. Uhlig Memorial Symposium - Corrosion Science: From Theory to Practice, F.B. Mansfeld, R.M. Latanision, A.I. Asphanani, H. Bohni (Eds.), The Electrochemical Society Proceedings Series PV 94-26, Miami Beach, Florida, 1994.
[16] M.P. Ryan, R.C. Newman, G.E. Thompson, Philos. Mag. 70, 241 (1994).
[17] M.P. Ryan, R.C. Newman, G.E. Thompson, J. Electrochem. Soc. 141, L164 (1994).
[18] M.P. Ryan, R.C. Newman, G.E. Thompson, J. Electrochem. Soc. 142, L177 (1995).

Electrochemical Nanotechnology
In-situ Local Probe Techniques at Electrochemical Interfaces
Edited by W. J. Lorenz and W. Plieth

Local Probing of Electrochemical Interfaces in Corrosion Research

A. Schreyer, T. Suter, L. Eng, H. Böhni

Contents

1	Introduction		200
	1.1	Passivity and local breakdown	200
	1.2	Principle of microelectrochemical measurements	201
	1.3	Investigation of local tunneling barrier heights	202
2	Experimental		202
	2.1	Material and sample preparations	202
	2.2	SPM equipment	203
	2.3	Microelectrochemical equipment	204
3	Results		205
	3.1	Passivation (STM measurements)	205
	3.2	Inclusions	207
4	Conclusions		211
5	Outlook		212
6	References		213

Summary. The corrosion resistance of stainless steel is mainly caused by heterogeneities. Inclusions especially play a key role as potential initiation sites. Since most of the electrochemical techniques provide only average data integrating over a relatively large surface area (square millimeters to square centimeters) they are inadequate for studying localized corrosion processes. Use of in-situ scanning probe microscopy (SPM, e.g., scanning tunneling micrsocopy (STM), atomic force microscopy (AFM)) and tip-sample distance modulation spectroscopy in conjunction with microelectrochemical techniques with a current detection limit of ≤10 fA enables investigations in the nano- and micrometer range.

1 Introduction

1.1 Passivity and local breakdown

Figure 1 shows a current-potential plot of DIN 1.4301 stainless steel in 0.01 M sulfuric acid and of iron in a boron buffer solution (at pH 8.4). As seen, the current density resulting from corrosion attacks drops by several orders of magnitude for a certain potential value (E = -550 mV and E = -300 mV respectively).

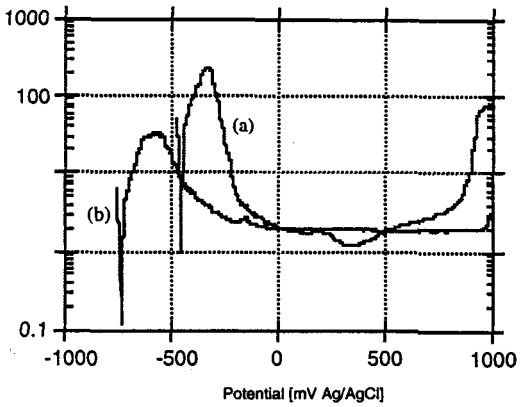

Fig. 1. Current density vs. potential plots of (a) iron in a boron buffer solution and (b) DIN 1.4301 stainless steel in 0.01 M sulfuric acid. A clear drop in the current density is observed at the passivation potential.

This is explained by the formation of an oxide layer, the so-called passive layer, which forms on the metallic surface. However, the exact composition of this passive layer is not known and descriptions in the literature are very contradictory. Photoelectrochemical measurements [1] lead to the following model describing the formation of a passive layer on stainless steel and iron.

The oxide layer on iron in a boron buffer solution mainly consists of Fe_2O_3. Fe^{2+} ions in the film act as misfits. They disturb bondings within the film and lead to dangling, bonds. These misfits strongly influence the electronic behavior of the semiconducting passive layer.

The oxide layer on stainless steels in 0.01 M sulfuric acid mainly consists of Cr_2O_3. Depending on the concentration of alloying elements in the bulk material, the layer shows a varying concentration of Fe and, sometimes, Mo. Again Fe^{2+} ions act as misfits and influence the electronic behavior of the semiconducting passive layer.

Yet the corrosion resistance of these metallic materials is usually limited by the occurrence of localized corrosion processes such as pitting and crevice corrosion. Due to the manufacturing process, every kind of steel possesses a certain amount of inclusions such as manganese sulfide or chromium carbide. These inclusions may drastically influence the electrochemical behavior of highly alloyed stainless steels, especially having an influence, on pitting the behavior [2-5]. This is the reason why it is necessary to obtain accurate knowledge on the shape, size distribution, and electrochemical behavior of these inclusions. Furthermore it is from this basis that further investigations of local processes on and at the interface of inclusion may be started. In order to understand the mechanisms of initiation and propagation of localized corrosion, the processes should also be studied in the micro- and nanometer ranges.

1.2 Principle of microelectrochemical measurements

A new electrochemical technique with a current detection limit of $\leq$10 fA enables investigations in the micrometer range [6].

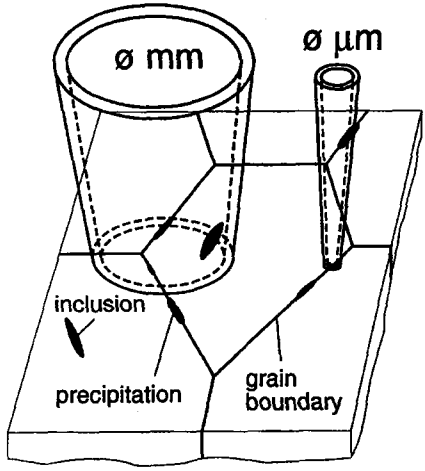

Fig. 2. Schematic of microeiectrochemical measurements on inhomogeneous substrates using various capillary sizes.

The use of an electrochemical microcell allows to reduce the size of the exposed surface area (Fig. 2).
Small-area measurements have two great advantages:

(1) The electrochemical background noise is considerably reduced. Therefore.processes and can be detected which otherwise would not be seen within the noise spectrum [7, 8].

(2) The reduction of the sample area enables the study of single heterogeneities.

1.3 Investigation of local tunneling barrier heights

In one of the first publications on STM, Binnig and Rohrer discussed the possibility of recording the local tunneling barrier height V by a modulation experiment [9]. Their result can be summarized with the following equation:

$$\Phi = \frac{\left(\frac{d \ln I_t}{ds}\right)^2}{I_0^2 \cdot A^2} \tag{1}$$

where A $\approx$ 1.0251 eV^{-1}. $Å^{-1}$, I_0 represents the initial current and s the tip-sample distance.

By modulating the distances between tip and sample surface and recording the varying tunneling current I_t it is possible to deduce the local barrier height by Eq. (1). Changing the chemical composition of either the substrate or the tip leads to different local barrier heights. Differences in the chemical composition of the substrate therefore result in various barrier potentials.

2 Experimental

2.1 Material and sample preparation

Different types of stainless steel as well as pure iron were investigated in different solutions. Table 1 lists the various compositions of these metals.

2.1.1 Sample preparation for SPM measurements

All samples were mechanically polished witha 0.25 mm diamond spray, then ultrasonically cleaned in ethanol. Prior to both STM and AFM measurements all substrates were cathodically pre-polarized at $E \approx 100$ mV vs. Ag/AgCI/NaCI (1 M).

2.1.2 Sample preparation for microelectrochemical measurements

The samples were mechanically ground with SiC emery paper up to 4000-grit and finally polished with 1 μm diamond paste. They were rinsed with distilled water and ultrasonically cleaned in ethanol. Prior to microelectrochemical measurements all substrates were cathodically prepolarized at -500 mV vs. SCE (saturated calomel electrode)

Table 1. Chemical composition [wt%] of materials examined

DIN	AISI	Fe	C	Cr	Ni	Mo	Mn	S
1.4301	304	(a)	0.034	18.12	8.53	-	1.55	0.001
1.4301	304	(a)	0.045	18.10	8.70	0.06	1.30	0.003
1.4301	304	(a)	0.040	18.4	8.62	0.40	1.86	0.017
1.4301	3.04	(a)	0.042	18.2	9.10	-	1.05	0.022
1.4305	303	(a)	0.069	17.6	8.70	0.30	1.81	0.360
1.4529	-	(a)	0.012	20.8	24.9	6.42	0.82	0.002
Fe	-	99.99	-	<2ppm	<5ppm	-	1ppm	10ppm

(a) Bal, balance.

2.2 SPM equipment

The STM/AFM unit (Unversial SPC 400 SPM, Park Scifentific Instruments) consisted of an electronic unit which provided both the scan control for scanning the tip over the surface and an electronic feedback loop maintaining a constant working distance between tip sample. Additionally a four-electrode bi-potentiostat that was connected to the control unit was capable of setting the potentials of both tip and substrate

independently. This system allowed minimization of the electrochemical current flowing through the tip and hence could reduce the overall noise superposed on the tunneling current.

All AFM and STM topographic images were obtained in the mode of constant interaction. The distance modulation measurements were recorded by modulating the z-position of the piezo with a sinusoidal signal having an amplitude and frequency of 1 - 5 Å and 1.5 kHz respectively.

2.3 Microelectrochemical equipment

For all microelectrochemical experiments a metallurgical microscope was used. The sample was mounted on the microscope stage and the electrochemiqal microcell was fixed at the revolving nosepiece like an ordinary objective. This set-up enabled selection of an interesting area before the measurement and allowed a visible control of the investigated area after the measurement. The electrochemical microcell basically consisted of a glass microelectrode with the tip grounded (tip diameter = 2-1000 µm). As a seal a layer of silicone rubber is used for the front end. Such microcells lasted for about 50-100 experiments (Fig. 3).

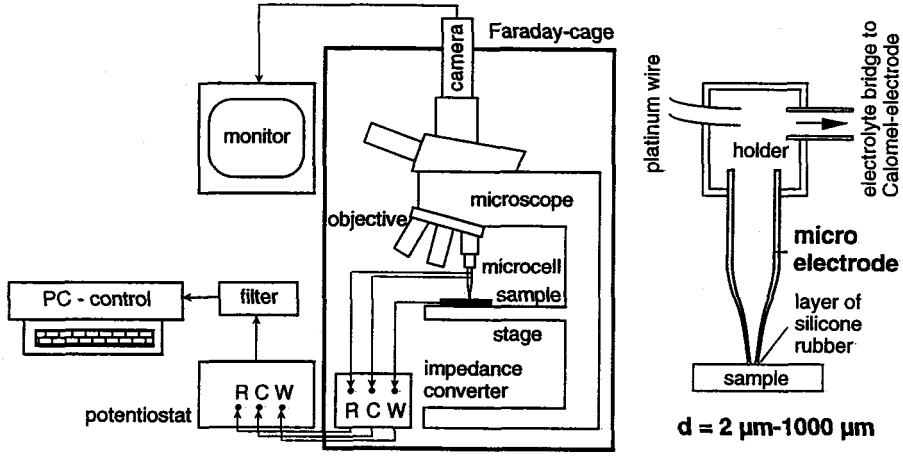

Fig. 3. Experimental set-up and electrochemical microcell.

In order to perform electrochemical measurements in the micrometer range, with currents ranging from 10^{-12} to 10^{-15} a several precautions were necessary. Besides good

shielding to suppress electromagnetic interferences, a specially modified battery-operated high-resolution potentiostat (Jaissle 1002T-NC-3) was used. Additionally,the remaining noise of the measured output signal had to be reduced further by a home-made filter. This technique, which a current resolution of $\leq$10 fA, enabled the detection of processes in the micrometer range [7, 8].

3 Results

3.1 Passivation (STM measurements)

The averaged tunneling barrier height measured on the oxide-free iron surface approaches $\Phi \approx 0.4$ eV, but with the values in the range $0.05 < V < 1.1$ eV (Fig. 4, E = -750 mV). This is in good agreement with the published results for a gold surface immersed in perchloric acid [10]. Compared to measurements in vacuum this result is substantially lower, which can be explained by electronic interactions of water molecules with the metal surface [11, 12]. The formation of an oxide layer leads to a decreased tunneling barrier (Fig. 4). Already the very thin, so-called pre-passive layer at E = -600 mV lowers the barrier height by a factor of 10. Nevertheless the measured values recorded at such a potential scatter widely and can be attributed to both the low thickness and the inhomogeneity of the pre-passive film. When the film grows thicker and becomes more structured the barrier height is further lowered by another order of magnitude.

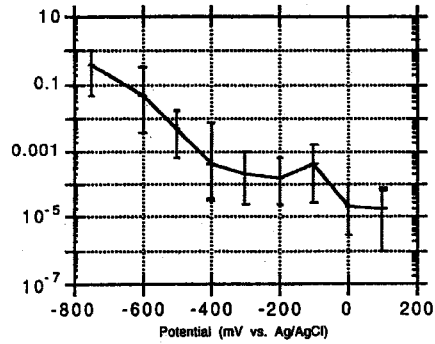

Fig. 4. Mean tunneling barrier height vs. substrate potential on iron in a boron buffer solution. The formation of an oxide layer leads to lower tunneling barrier height.

This lowering may be explained by induction of localized electronic states with their energy levels lying within the tunneling barrier. They therefore act as resonating states for indirect tunneling processes. A comparison with photoelectrochemical results [1, 13] leads to the hypothesis that it is the Fe^{2+} ion which induces such localized states, since it disturbs the physical structure of the oxide layer, leading to dangling bonds.

The same tendency of the oxide layer to lower the tunneling barrier height can be seen for stainless steel. As seen in Fig. 5, the formation of a passive film on DIN-1.4301 also leads to a decrease of the measured tunneling barrier height. Two regions with different tunneling barrier height values can be distinguished. The pre-passive layer, which is not strictly chemically bound to the surface, is formed at potentials in the range -300 mV < E < -200 mV. At potentials higher than E = -200 mV the film becomes more structured and chemically bound to the surface. The influence of Fe^{2+} misfits is enhanced and diminishes the tunneling barrier by another order of magnitude.

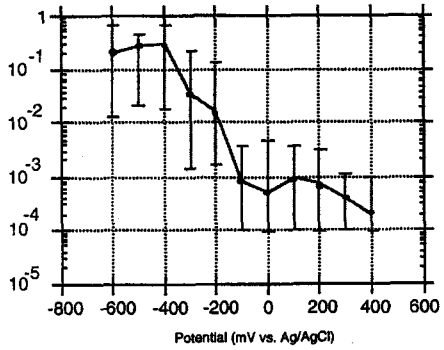

Fig. 5. Mean tunneling barrier height vs. substrate potential on DIN 1.4301 in 0.01 M sulfuric acid. The formation of an oxide layer leads to lower tunneling barrier height.

In Fig. 6 both the measurements on DIN 1.4301 and on DIN 1.4529 immersed in 0.01 M H_2SO_4 at E = 0 mV are shown. It is obvious that the tunneling barrier on the more highly alloyed DIN 1.4529 is substantially higher than for DIN 1.4301 stainless steel. This is due to the fact that the passive layer on the less alloyed steel contains more Fe^{2+} ions and therefore introduces more localized states which lower the tunneling barrier. In case of the more highly alloyed steel the presence of Mo ions in the passive film may replace the Fe^{2+} and, due to their multivalent nature will not lead to electronic misfits.

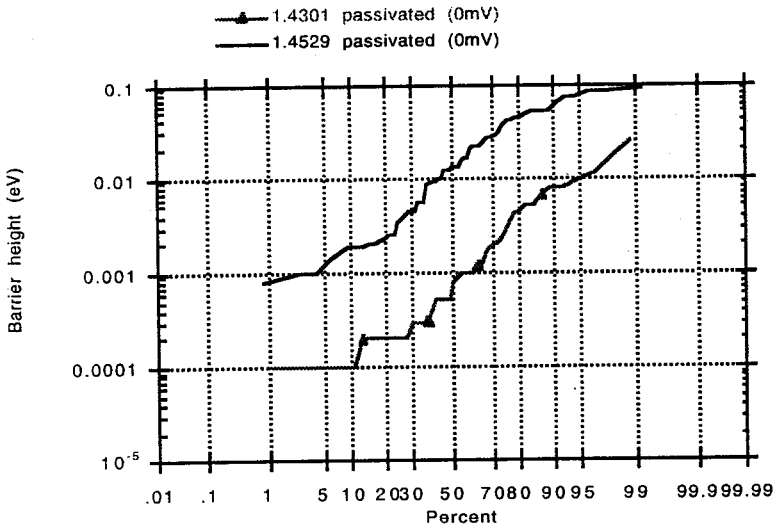

Fig. 6. Measured tunneling barrier height on DIN 1.4301 and 1.4529 in 0.01 M sulfuric acid at $E = 0$ mV, covered by an oxide film.

3.2 Inclusions

3.2.1 SPM measurements

Figure 7 presents both an STM and a d*I*/d*s* picture of DIN 1.4301 obtained in 0.01 M H_2SO_4 at a potential where no passive layer is formed on the surface. The spectroscopic image clearly shows four inclusions (dark spots), which are not seen in the pure topographic image (left).

It is also possible to detect inclusions by d*F*/d*s* using AFM, as shown in Fig. 8. The smallest inclusion found by spectroscopic STM and AFM investigations measured approximately 5 nm in diameter, as shown in Fig. 9.

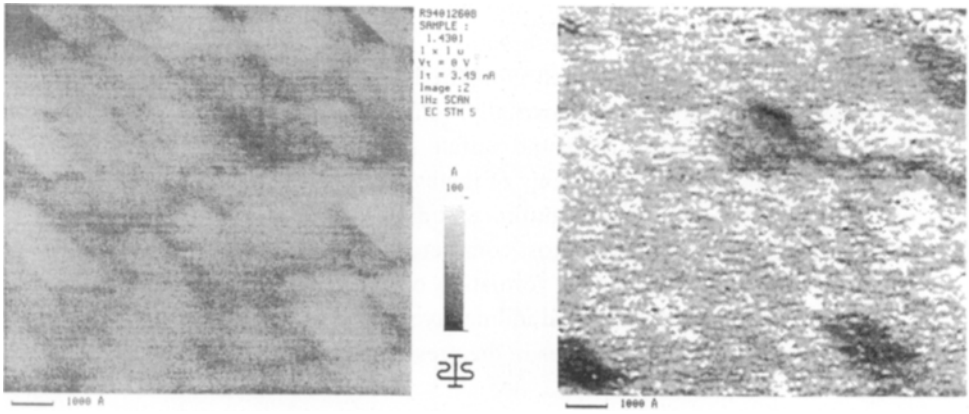

Fig. 7. STM (left) and d*I*/d*s* picture (right) of DIN 1.4301 in 0.01 M H_2SO_4 at E = 600 mV. Some inclusions are visible in the spectroscopic image (black bar corresponds to 1000 Å).

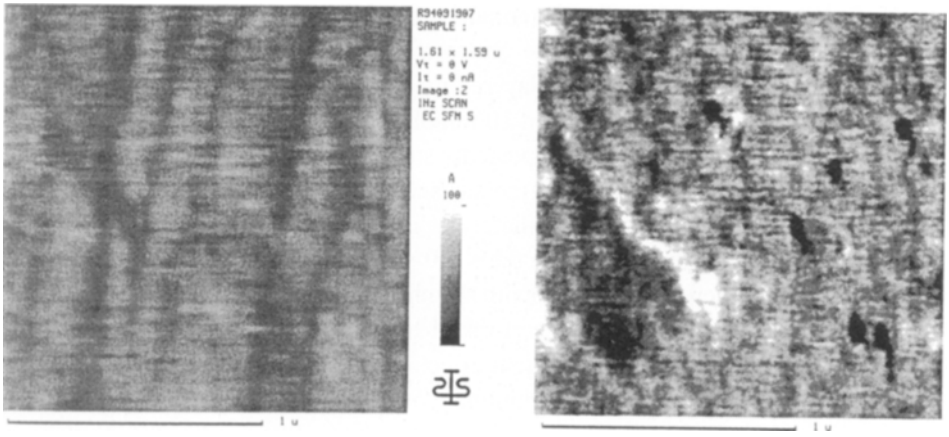

Fig. 8. AFM (left) and d*F*/d*s* (right) pictures of DIN 1.4301 in 0.01 M H_2SO_4 at 0 E = -600 mV. Some inclusions are visible in the spectroscic image (black bar corresponds to 1 μm).

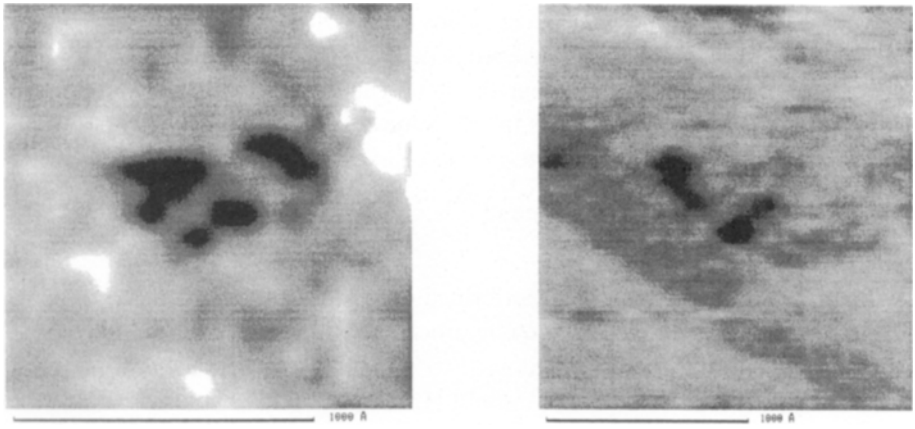

Fig. 9. Smallest detectable inclusions by STM (left) and AFM (right) (black bar corresponds to 1000 Å).

3.2.2 Microelectrochemical measurements

With microelectrochemical experiments the dissolution of single inclusions of stainless steels has been studied.

Measurements showed that, even in the chloride-free Na_2SO_4 solution, MnS inclusions are dissolved [7]. Since the inclusions are dissolved rather slowly and no stable pitting occurs, the dissolution processes can be assigned to single inclusions quite well. Measurements at sites with inclusions are shown in Fig. 10. Two local potentiodynamic polarization curves of the steel DIN 1.4301 (0.017% S) were measured. In the case of an active 10 µm x 5 µm inclusion, the electrochemical current shows an abrupt increase over a limited potential range (shaded areas). To avoid the dissolution of an inactive 3 µm x 3µm inclusion in the transpassive range, the measurement was stopped at 1000 mV. Subsequent optical microscopy studies of the same area revealed that the inclusion had been dissolved during the experiment. The SEM pictures indicate the nearly complete dissolution of the oval, active inclusion (Fig. 10, top left), whereas the inactive inclusion of a rounded shape (Fig. 10, bottom) did not dissolve at all.

In the presence of chlorides an even larger number of transients could be observed, indicating that additional nucleation sites were activated. Measurements in solutions

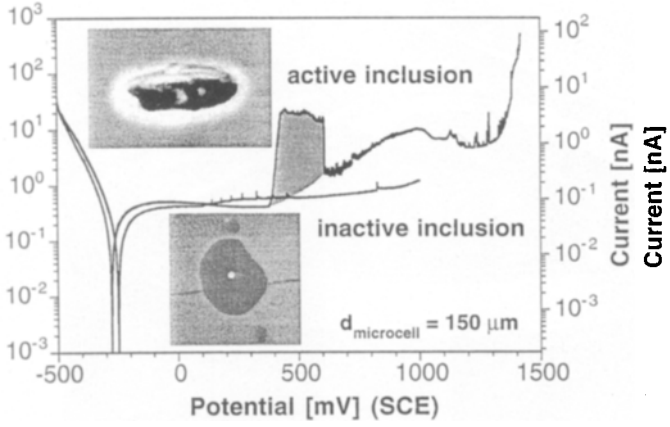

Fig. 10. Local potentiodynamic polarization curves of DIN 1.4301 stainless steel (0.017% S) at an active (10 µm x 3 µm) MnS inclusion and an inactive (5 µm x 5µm) MnS inclusion: 1 M Na_2SO_4, $dV/dt = 0.2$ mV/s.

with and without chlorides showed that only in presence of chlorides could a limiting pit growth potential be observed, above which stable pit growth takes place. Obviously chlorides are necessary to stabilize pit growth.

Local potentiodynamic polarization curves of the steel DIN 1.4301 (0.003% S) in a 1 M NaCl solution showed that the pitting potential does not have a constant value. With the usual large-area technique a value of about 300 mV is obtained. Diminishing the exposed surface to an area of 50 µm in diameter leads to an increase of the pitting potential to about 1200 mV (Fig. 11(a)). The pitting potential is usually considered to be independent of the area. There exist specific values for a particular combination of material and electrolyte. However, this work shows that the pitting potential also is an area-dependent value.

Figure 11(b))shows the polarization curves of three DIN 1.4301 stainless steel with different sulfur contents. All samples were 250 µm in diameter. The pitting potential of the purest steels was about 790 mV. An increase of the sulfur content to 0.017% S and 0.36% S decreased the pitting potential to 380 mV and 170 mV respectively. The low resistance against pitting of the DIN 1.4305 steel in comparison with the DIN 14301 steel was also proved by the examination of fastening elements in the Mont Blanc alpine road tunnel [14]. Small-area experiments showed the same effect as a reduction of the sulfur content. In both cases the number of sulfide inclusions was decreased.

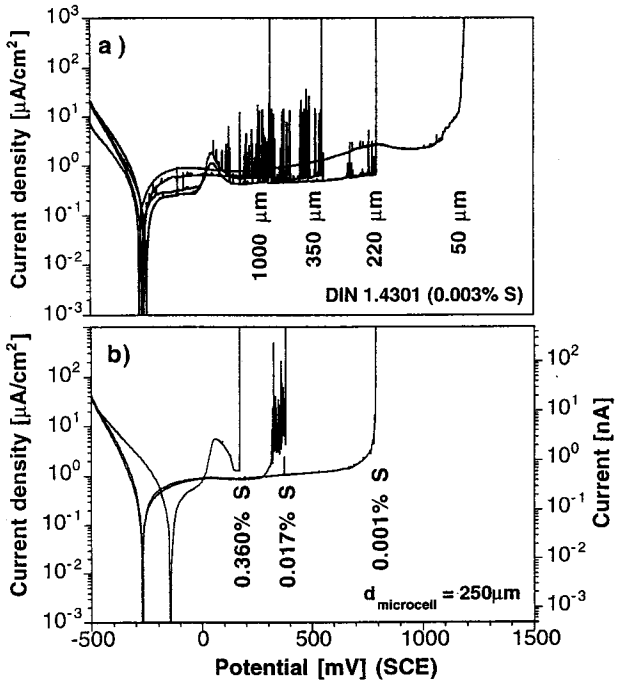

Fig. 11. Local potentiodynamic polarization curves in 1 M NACI, dV/dt = 0.2 mV/s. The diameter of the microcell (a) and the sulfur content (b) are varied.

4 Conclusions

(1) Tunneling on passivated metal surfaces with small tunneling voltages (U_t<500mV) is only possible when localized electronic states within the passive layer exist. They act as resonance centers for indirect tunneling processes. Therefore, the topographic images of such surfaces represent the interface metal/oxide and not the passive layer itself.

(2) The passive layer on DIN 1.4301 has significantly more localized states than the one on DIN 1.45429. This fits well with the higher amount of iron in the film.

(3) Ionic inclusions in the bulk material can be detected down to a size of 5 nm in diameter using dI/ds and dF/ds spectroscopy.

(4) A new microelectrochemical technique with a current detection limit of $\leq$ 10 fA and the use of an electrochemical microcell allow reduction of the exposed surface area. Such microelectrochemical measurements have several advantages:
- By reducing the sample area, the electrochemical current noise is strongly reduced. Therefore processes can be detected which in large-scale experiments would be hidden by the noise.
- Different aspects of pitting corrosion can be studied by varying the diameter of the microcell.
- The easy positioning of the microcell at different locations enables several measurements on the same sample.

5 Outlook

There is a new project with the aim of developing a method which combines the advantages of microelectrochemistry and of SPM. It should be possible to perform microelectrochemical measurements and SPM investigations at the same local points on a sample. This technique will allow observations of corrosion attacks and their surroundings before and after exposure to corrosive conditions.
A experiment will include several cycles and one cycle will consist of three steps:

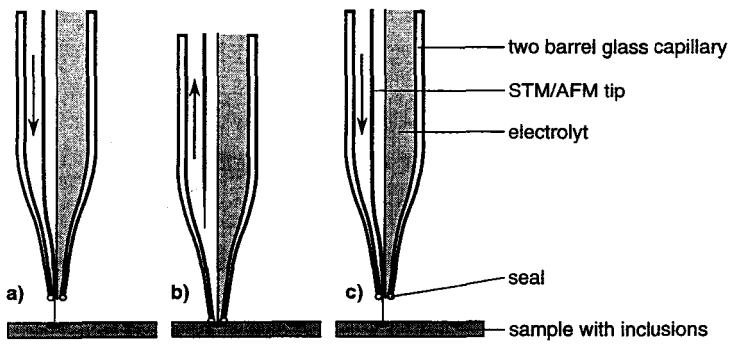

Fig. 12. Combination of microelectrochemistry and STM/AFM.

(l) STM/AFM measurement before electrochemical measurement (Fig.12(a)).
(2) Electrochemical measurement at the same spot with the STM/AFM tip being withdrawn (Fig. 12(b)).
(3) STM/AFM measurement after electrochemical measurement (Fig. 12(c)).

Acknowledgment. The authors thank the Schweizerische Nationalfond for financial support of the present work.

6 References

[1] P. Schmuki, M. Büchler, H. Böhni, R. Müller, L. J. Gauckler, J. Electrochem.Soc. 142, 3336 (1995).
[2] G. Wranglen, Corros. Sci. 14, 331 (1974).
[3] G.S. Eklund, J. Electrochem Soc. 121, 467 (1974).
[4] Z. Szlarska-Smialowska, Pitting Corrosion of Metals, NACE, Houston, TX, 1986.
[5] R. Ke, C. Alkire, J. Electrochem. Soc. 139, 1573 (1992).
[6] R.M. Rynders, C-H. Paik, R. Ke, R.C. Alkire, J.Electrochem. Soc. 141, 1439 (1994).
[7] T. Suter, T. Peter, H. Böhni, Proc. EMCR V, Lisboa, Material Science Forum 192-194, 25 (1995).
[8] H. Böhni, T. Suter, A. Schreyer, Electrochim. Acta 40, 1361 (1995).
[9] G. Binnig, H. Rohrer, Helv. Phys. Acta 55, 726 (1982).
[10] M. Binggeli, D. Carnal, R. Nyffenegger, H. Siegenthaler, R. Christoph, H. Rohrer, J. Vac. Sci. Technol.B9, 1985 (1991).
[11] W. Schmickler in: Nanoscale Probes of the Solid/Liquid Interface, A. A. Gewirth, H. Siegenthaler (Eds.), NATO ASI Series No. 288, 1995, p. 5.
[12] W. Schmickler, D. Henderson, J. Electroanal. Chem. 290, 283 (1990).
[13] P. Schmuki, H. Böhni, J. Electrochem. Soc. 139, 1908 (1992) and J. Electrochem. Soc. 141, 362 (1994).
[14] H. Haselmair, R. Morach, H. Böhni, Corrosion 50, 160 (1994).

Electrochemical Nanotechnology
In-situ Local Probe Techniques at Electrochemical Interfaces
Edited by W. J. Lorenz and W. Plieth

Morphology and Nucleation of Ni-TiO_2 LIGA layers

M. Strobel, U. Schmidt, K. Bade, J. Halbritter

Contents

1	Introduction	216
2	Experimental	216
	2.1 Preparation of samples	216
	2.2 ARXPS and STM/DTS measurements	217
3	Results	221
4	Discussion	222
5	Conclusions	224
6	References	224

Summary. The quality of an Ni LIGA layer and its adhesion to TiO_{2-x} depend crucially on interface morphology and chemistry. The unique combination of ARXPS (angle-resolved photoelectron spectroscopy), STM (scanning tunneling microscopy) and DTS (distance tunneling spectroscopy) yield new insights in morphology and stoichiometry on the porous TiO_{2-x} plating ground, on the $TiO_{2-x}(OH)_yNiO_zNi$ interface, and on the Ni-nucleation and growth. Besides TiO_{2-x} pore dimensions, we identified carbon hillocks with retarded Ni coverage, and the adhesion-promoting interface oxide $TiO_{2-x}(OH)_yNiO_z$, and we measured, for the first time, in-situ and ex-situ STM nucleation and growth of Ni.

1 Introduction

In all deposition and growth processes the initial interface is crucial for adhesion, nucleation, composition and, finally, the actual growth of the three-dimensional bulk. In the past, we studied interfaces and nucleation, e.g., in oxidation or sputter deposition In all these cases, the bonding or epitaxy was determined by covalently bonded interface compounds, identified in composition and morphology by angle resolved photolelectron spectroscopy (ARXPS). Here, we present results on the electro-deposition of Ni onto semiconducting TiO_{2-x}, as used in the LIGA process [3].

This paper is structured as follows: in Section 2.1 the preparation of TiO_{2-x} is outlined, together with the electro deposition process, with a short account of ARXPS results [4]. We found as wetting interface layer $TiO_{2-x}(OH)_yNiO_z$ at a thickness of 1-2 nm and carbon residues showing a retarded Ni coverage. Section 3 gives the results of scanning tunnel microscopy (STM). For the first time, the distance tunnel spectroscopy (DTS) has been applied successfully to differentiate between metallic and semiconducting surfaces. The surface morphology has been studied ex-situ in air and in-situ under potential control in the sulfamate electrolyte. This section includes initial electroplating in-situ electrochemical STM results. The results are discussed in Section 4, and conclusions in Section 5.

2 Experimental

2.1 Preparation of samples

The layer system $Si/Ti/TiO_{2-x}$ was used as an electrode for the cathodic deposition of nickel. The Si/Ti substrate was supplied by HL-Planar, Dortmund, Germany. It was fabricated by sputtering 3 μm Ti onto a silicon wafer. By a wet chemical oxidation of the Ti layer with H_2O_2/NaOH, a porous oxide layer is formed with an approximate thickness of 40 nm which conducts sufficiently to act as the plating base commonly used in the LIGA process. As outlined in detail in [5], the electrochemical deposition of nickel was carried out in a sulfamate bath under potentiostatic control -0.715 V vs. SHE. During deposition, an Hg/Hg_2SO_4/0.5 M Na_2SO_4 reference electrode was used. The potentials reported in this paper are given with repects to the standard hydrogen electrode (SHE). Recording of current transient and potential control was done with a potentiostat (EG&G Model 273A). The amount of deposited nickel was determined by

the charge obtained by integrating the current transient. The electrolyte composition was the typical one used for the electroforming step in the LIGA process: nickel as sulfamate (78 g/1), boric acid (40 g/l), and surfactants. The temperature maintained during deposition was 52°C and the pH was adjusted to 3.6.

2.2 ARXPS and STM/DTS measurements

The interface chemistry up to a depth of about 5 - 10 nm of Ni-TiO_{2-x} nucleation layers was obtained by ARXPS measurements and is summarized in Fig. 1 [4]. Scanning tunneling microscopy (STM) is commonly used for imaging the morphology and atomic structure of solid-state surfaces in contact with ultrahigh vacuum (UHV), gases, or liquids (Fig. 2) [6].

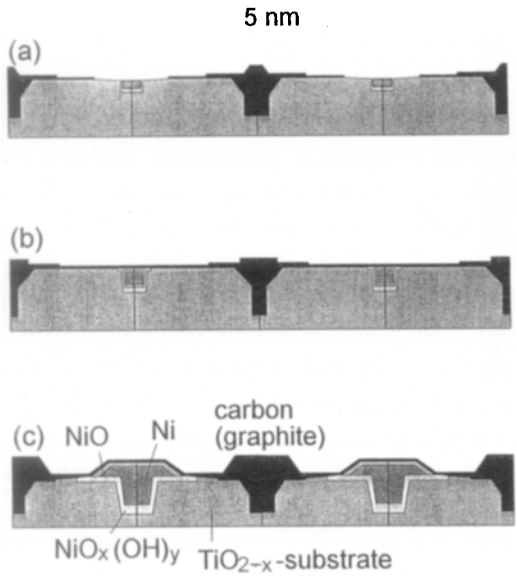

Fig. 1. Models of Ni/TiO_{2-x} films with (a) 0.07, (b) 0.12, and (c) 0.72 mg/cm^2 Ni. Those models should be regarded as an average over the whole measurement area. The slow change of XPS intensity decrease at small photo electron take-off angle yields a lateral periodicity length of 40 nm [4].

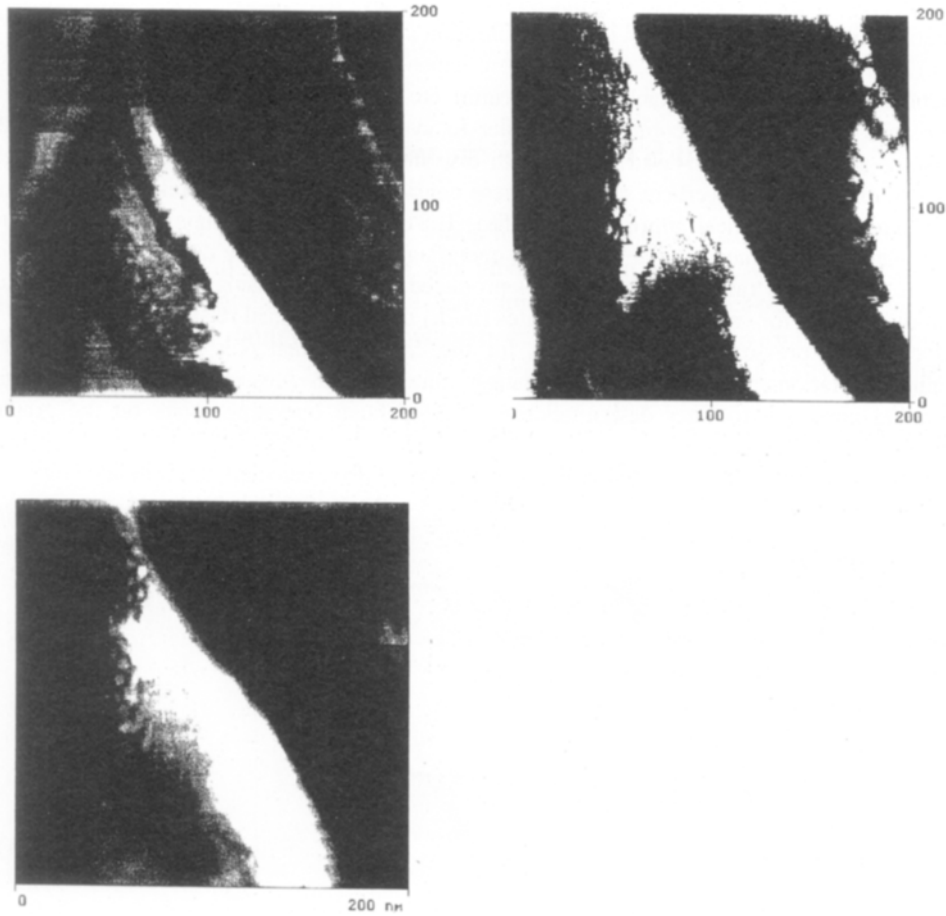

Fig 2. (a) First Ni nuclei after a current pulse of 600 mV for 20 s (CCM) 200 nm/200 nm scans show a maximal height variation of 25 nm; (b -c) STM images taken while Ni nuclei were growing. Clearly, one can see the growth while enhancing the electroplating voltage. The CCM height variation is still 25 nm on a 200 nm/200 nm scan.

The STM imaging resolution is mainly determined by the tunneling mechanism, which may be identified by distance tunneling spectroscopy (DTS). DTS is characterized by measuring the tunneling current, I_t, as a function of the tip-substrate distance, d, at constant tunnel voltage E_t. For ex-situ measurements E_t is the applied

bias between tip and sample. In in-situ experiments E_t is given by the difference between the potential of the tip, E_{tip}, and the substrate, E, controlled relative to the electrolyte. Traditionally, the I_t (E_t,d) dependencies are expressed as Eqs. (1) and (2),

$$I_t(d) = a \cdot \mathbf{exp}[-2\kappa d] \tag{1}$$

$$\kappa(E_t) = \frac{2\pi}{h}\left[2m_e V_{eff}(E_t)\right]^{1/2} \tag{2}$$

where a is related to the density of states of tip and substrate, depending weakly on d only. The inverse decay length 2κ is a function of the tunneling voltage E_t and $V_{eff}(E_t)$ denotes the effective tunnel barrier height, which decreases linearly with the voltage across the tunnel gap according to $V = \Phi_0 - x/d \cdot e\,E_t$. Here, Φ_0 is given for a vacuum by the work function Φ_{vac} or by the conduction band of the dielectric causing the tunnel gap. The approximation (Φ_0=Φ_{vac}) holds only for the case of a clean metal/vacuum/metal tunnel junction. For in-situ STM, we have to expect adsorbates, especially water adlayers on the surface of both tip and substrate. The dipole resonances in such oriented water molecules or localized states in defective oxides lead to intermediate-state tunneling and, consequently, smaller effective tunnel distances $d_{eff} = d/(N_i+1)$. Assuming a uniform density of localized states, the following distance dependencies result [7]:

$$I_t(d) = d^{N_i-1}\,\mathbf{exp}\left[-2\kappa d/(N_i+1)\right] \tag{3}$$

or

$$V_{eff} = \Phi_0/(N_i+1)^2 \tag{4}$$

As one can see, the effective tunnel barrier height decreases with increasing number of intermediate states n and so depends on the oxide or adsorbate coating (Fig.3).

The ex-situ (in air) and in-situ (in Ni sulfamate solution) STM measurements were performed using a Nanoscope Ill (Digital Instruments). In ex-situ experiments the tunneling bias is held constant, whereas in in-situ STM measurements the tip and

substrate potentials, E_{tip} and E, are independently controlled by an external bipotentiostat [8]. The experiments were performed with uninsulated and apiezon-insulated Pt-Ir tips (Digital Instruments), respectively. A superficially oxidized Au wire was used as quasi reference electrode and a Pt wire as counter electrode. The Ni sulfamate solution is the same as used for electroplating our samples (Section 2.1), but was diluted by a factor three with suprapure water and used at 300 K to keep the deposition at a slow, observable rate. Before the STM cell was filled, the solution was deaerated by nitrogen bubbling (Fig. 2, [8]).

The effective barrier height V_{eff} was determined from the slope of the $\ln(I_t)$ measurements as a function of d at a constant E_t of 0.5 V. The $I_t(d)$ data were acquired while approaching the tip to a minimum distance, d_0, determined by the setpoint current. The DTS covered a typical range Δd of about 2 nm. Withdrawal and approach of the tip were carried out slowly with a rate of approximately 10^{-6} cm/s (Fig. 5).

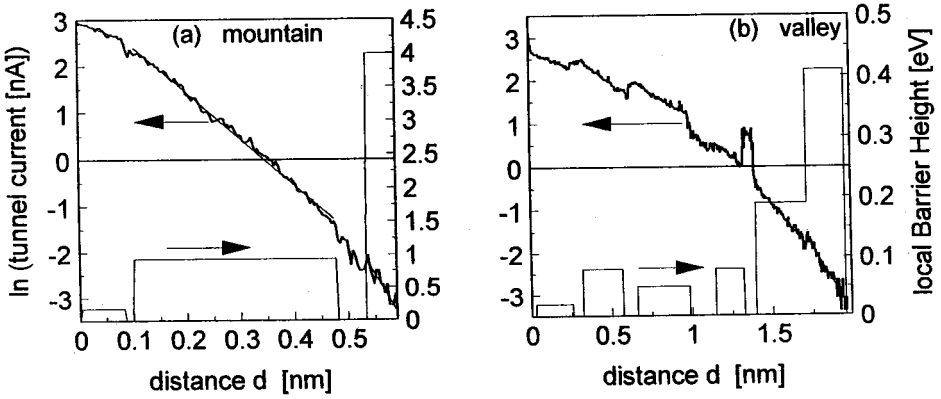

Fig. 3. $I(d)$ plots of TiO_{2-x} substrate in Ni sulfamate solution. Measurement on the mountains shows a higher effective barrier height (a) than in holes (b). See (Fig 2(a)).

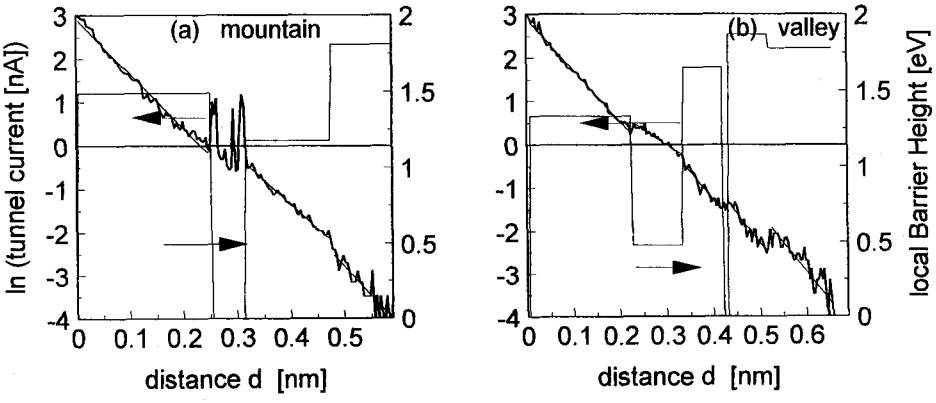

Fig. 4. *I(d)* plots on Ni seeds directly after electroplating in the sulfamate solution, i.e., $E = 0$ (Fig. 2). The effective barrier height V_{eff} does not show any increase with distance d. Its value ranges from 1 to 2 eV.

3 Results

Typical in-situ STM images are shown in Fig. 2. As expected from XPS measurements, one sees a fissured landscape, making DTS in both valleys and mountain desirable. In the meantime, X-ray photoelectron spectroscopy (XPS) results indicate the existence of different materials on mountains (carbon) and in valleys (TiO_{2-x}), see Fig. 1. As a local spectroscopy method, DTS makes it possible to obtain information about the local chemical nature of the substrate. Figure 3 shows typical InI(d) on both (a) mountains and (b) valleys. The expected linear dependence of InI vs. d is followed only for small parts of the plots, indicating a variation in the number of intermediate states active in the tunneling process. The effective tunneling barrier height V_{eff} on mountains increases as tip-substrate distances increase from 0.2 to 4 eV and in valleys from 0.05 to 0.4 eV (Fig. 3).

In order to obtain more detailed information on Ni electroplating, surface morphology changes during Ni electrodeposition were studied by in-situ STM. After large potential pulses of 200 mV had been applied in the scanned TiO_{2-x} region, only slight changes in surface morphology could be observed in Fig. 2(a) not changing much by additional potential pulses. Again, a fissured landscape is observed (Fig. 2(c)).

By increasing the substrate potential range from 0 to 200 mV in steps of 10 mV, the nucleation and growth of small Ni islands, mainly in valleys (Fig. 2) then over thewhole surface, could be imaged. Because the Ni elctrodeposition on TiO_{2-x} is irreversible, DTS on Ni deposits was possible under the same conditions, like DTS measurements on TiO_{2-x} substrates. The InI(d) curves taken on freshly deposited Ni

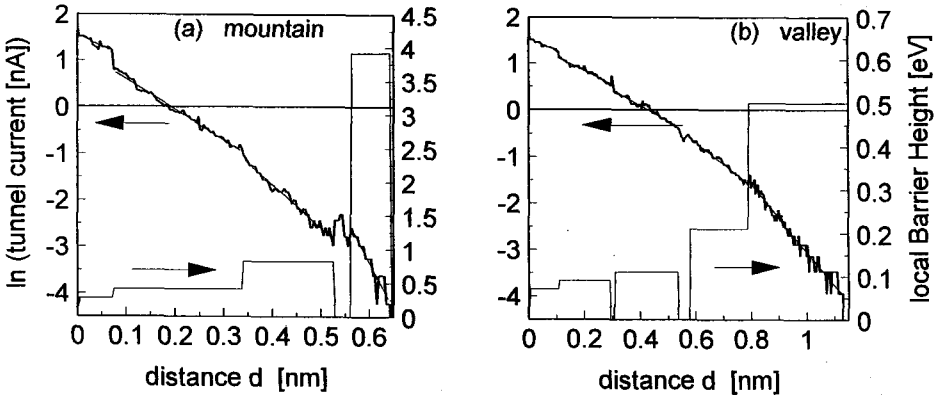

Fig.5. *I(d)* plots on Si/Ti/TiO_{2-x}/Ni layer measured in air. Compared to measurements in electrolytic solution (Fig. 4), the effective barrier heights was increased. Measurement on a mountain (a) and in a deep valley (b).

nuclei (Fig. 4) do not show any slope increase with increasing distance d. The measured tunneling barrier height ranges between 1 and 2 eV. The result can be compared with ex-situ DTS measurements in Fig. 3. In a distance range between 0 and 0.5 nm the DTS curves show a slow increase of barrier heights from 0.4 to 0.8 eV on mountains, and of 0.07 to 0.11 eV in valleys.

4 Discussion

In Section 2.1 the substrates used and their preparation have been summarized: porous $TiO_{2-x}(OH)_y/H_2O$ coating the Si wafer, probably with an excess of H_2O_2 due the oxidation process of the sputtered Ti layer. In Section 3 it was described how ARXPS and STM/DTS confirmed the TiO_{2-x} roughness on a nanometer scale but revealed a

stoichiometric inhomogeneity, as well. The carbon mountains may be sputter residue because in Ti sputtering a C sublayer is used for easy removal from the Si wafer [4]. According to Section 3 or [4], the electrodeposition of Ni starts in the pores yielding the $NiO_x(OH)_y$ interface compound with $TiO_{2-x}(OH)_y$ in a thickness range from 0.8 to 2.5 nm. This thick interface oxide-hydroxide is an indication of good wettability and good adhesion of Ni on TiO_{2-x}.. This Ni-interface oxide-hydroxide is much thicker than the natural oxidecoating Ni in a thickness of 0.2 nm shown in Fig. 1. At up about 1 mg/cm^2 Ni deposition on carbon, no Ni was found by ARXPS; this leads to the conclusion that carbon inhibits the Ni nucleation, which worsens the adhesion between substrate and Ni overlayer.

Because Fig. 1 gives only a spatial average of the Ni deposition process on TiO_{2-x}, local detection methods such as STM and DTS were used to identify the surface topography and the corresponding stoichiometry on a nanometer scale. Our STM morphology in Fig. 2 confirms our averaged ARXPS results and shows actual mountains and pores with a height difference of 25 nm on a $(200\ nm)^2$ size scale. The potential-controlled Ni deposition in the electrochemical STM cell starts in pores (valleys), forming small nuclei which lead to a more compact Ni deposit shown in Fig. 2. The filling of the pores by such spherical nuclei are a consequence of the large overpotential and the wetting interface $TiO_{2-x}(OH)_zNiO_y$.

DTS measurements shown in Figs. 3 - 5 were made with the constant tunnel voltage $E_t = E_{tip} - E = 0.5$ V. In all cases step-like decays occurred indicative of changing intermediate states. Measurements on the TiO_{2-x} substrate (Fig. 4) in sulfamate solution showed on the mountains a tunnel barrier height (V_{eff} terminating at 4 eV, and in the pores lower V_{eff} values starting with 0.02 - 0.1 eV. Such low V_{eff} values are typical for semiconductors with varying intermediate states in parallel [7]. This is quite typical for TiO_{2-x} or $NiO_x(OH)_y$ with O vacancies acting as such states. When the tip leaves TiO_{2-x} for $\Delta d > 1$ nm, $V_{eff} \approx 0.4$ eV is reached; this is typical for distinct H_2O-OH interface. Similar V_{eff} values are observed for TiO_{2-x}-Ni-$NiO_x(OH)_y$ surfaces in Fig. 4 in the Ni-covered pores. Thus the tunneling terminates in the intermediate states of the $NiO_x(OH)_y$ layer related to the rest potential due to handling. Directly after Ni deposition in the sulfamate,.bath, i.e., at $E = 0$, such an oxide hydroxide layer does not exist on Ni, which is then covered by a polarized OH-H_2O layer only, the compact part of the electrochemical double layer [7]. Such interfaces show $V_{eff} \cong 1$ eV by one to two intermediate states. The mountains in Fig. 2 show $V_{eff} > 0.4$ eV increasing to 4 eV under all conditions, indicative of a hydrophobic carbon with its double layer having up to 1 mg/cm^2 Ni coverage.

5 Conclusions

The electrodeposition of Ni on semiconductive TiO_{2-x} layers is used succesfully in LIGA technology. In this process different Ni structures of high aspect ratio in the micron range are obtained. However, the adhesion, nucleation, and growth processes of Ni are yet well understood. The aim of this paper has been to present initial results. A combination of ARXPS measurements, which gave integral stoichiometric information, with local, ex-situ and in-situ STM imaging and DTS analysis has been carrried out for the frst time in the nanometer range. Ni-TiO_{2-x} interface compounds, Ni nucleation and growth have given a new insight into the crucial processes defining the quality of Ni-LIGA structures.

6 References

[1.] A. Darlinski, J. Halbritter, J. Vac. Sci. Technol. A5, 1235 (1987).

[2] H.J. Hedbabny, A. Darlinski, J. Halbritter, Mater. Lett. 5, 337(1987); 0. Karstens, J.W. Schultze, W. Bacher, R. Ruprecht, Metalloberfläche 48, 148 (1994).

[3] W. Bacher, W. Menz, J. Mohr, IEEE Ind. Elec. 42, 431 (1995).

[4] M. Strobel, XPS- und STM-Untersuchungen der Morphologie uno Keimbildung von Ni-TiO_2-Liga' Schichten, Diploma. Thesis, University of Karlsruhe, 1996.

[5] A. Michaelis, J.W. Schultze, A. Thies, W. Bacher, R. Ruprecht, Dechema Monograph.Vol. 125, VCH, Weinheim, 1992, p. 459.

[6] G. Binnig, R. Rohrer, Ch. Gerber, E. Weibel, Phys. Rev. Lett. 49, 57 (1982); W.J.Güntherodt, R. Wiesendanger (Eds.), Scanning Tunnel Microscopy I, II, III, Springer Verlag Berlin, 1991 - 1995.

[7] J. Halbritter, G. Repphun, S. Vinzelberg, G. Staikov, W.J. Lorenz, Electrochem. Acta 40, 1385 (1995); G. Repphun, J. Halbritter, J. Vac. Sci. Technol. A 13, 1693 (1995).

[8] U. Schmidt, Elektrochemische in-situ STM-Untersuchungen der Adsorption und Eektrokristallisation von Blei auf realen und quasi-perfekten Silbereinkristalloberflächen, PhD thesis, University of Karlsruhe, 1994.

Electrochemical Nanotechnology
In-situ Local Probe Techniques at Electrochemical Interfaces
Edited by W. J. Lorenz and W. Plieth

SPM Investigations on Oxide-covered Titanium Surfaces: Problems and Possibilities

C. Kobusch, J. W. Schultze

Contents

1	Introduction		226
	1.1	Methods	226
	1.2	Role of the sample preparation and measurements conditions	228
	1.3	Aspects of nanotechnology	228
2	Experimental		229
3	Results		229
	3.1	AFM of fine-grain titanium	229
	3.2	STM of fine-grain titanium	231
	3.3	AFM/STM of TiN	232
	3.4	Tunneling spectroscopy of TiO_2/TiN	233
4	Discussion		237
5	References		238

Summary. A survey of SPM (Scanning Probe Microscopy) methods on oxide-covered surfaces is given, regarding the role of preparation, examination techniques and conditions. STM and AFM measurements were carried out on oxide-covered titanium and TiN. Fine-grain titanium with lateral dimensions of 10-30 μm exhibited, after careful polishing, height differences of only a few nanometers at the grain boundaries. AFM pictures showed small substructures on these grains with xy dimensions of 20-50 nm and a z-range of 1-5 nm. The polishing process is discussed as a function of the (hkl) orientation of the grains. Stable STM pictures could not be recorded if the oxide films were prepared electrochemically in sulfuric acid. The modification of these oxide films with hydrogen, water, or nitrogen implantation is discussed. On nitrogen-implanted surfaces stable STM conditions were achieved. The reason for this behavior could be found in the voltage tunneling spectra: TiN exhibited a much better conductivity than normal TiO_2.

1 Introduction

1.1 Methods

SXM (STM/AFM/spectroscopy) methods are powerful tools for the investigation of surfaces in the nano- and micrometer range. The topography, mechanical properties (stiffness [1], lateral forces [2]) and electronic properties (conductivity, band structure, barrier height) can be investigated. Titanium substrates are used for corrosion protection as well as for medical implants. SXM investigations on these surfaces have already been performed [3-9], but the substrates were often not well defined or modified and the analytical techniques were only partially completed. Table 1 shows the possible methods applied to titanium surfaces so far. Most of these investigations have been performed either with one or two methods only, or without variation of the sample preparation. Some aspects of SXM (especially STM) investigations cannot be found in the pictures, but only in the associated text: several authors report that stable STM conditions could not be achieved under certain circumstances. However, an interpretation was not yet given. A combined STM/AFM-investigation on the same sample position has not yet been published for titanium surfaces. A combination of STM/AFM with other methods (light microscope, infrared light, SEM) has been demonstrated partially, but not systematically.

These investigations have shown that the resulting SXM data depend highly on

- the tip material used;
- the voltage applied in STM;
- the analyzing conditions (vacuum, dry nitrogen, wet air);
- the analyzing techniques (initial conditions, prepulsed or linear spectra, scan rate);
- the preparation / modification of the surface;
- the orientation of the investigated grains;
- the thickness of the oxide.

An understanding of these surfaces can only be achieved if all SXM methods are applied together to a well-defined substrate, dependending on all the parameters mentioned above. In addition to these difficulties, some more problems should be mentioned. The absolute z-position of the tip is usually unknown. On metallic surfaces one can safely assume that

the tip is not in contact with the surface, but on semiconducting or even insulating oxide surfaces, the tip can be in contact with the surface or it may even penetrate into the oxide. This will result in bad STM conditions. Another problem is the xy position in the micrometer range. If an experiment is conducted on one xy position, then (after retracting the tip) it is very difficult to find the same position again, which is important for microstructured surfaces.

Table 1. Survey of SPM[(a)] investigations on titanium surfaces.

Titanium	STM	Spectroscopy	AFM	LFM	dF/ds
Polished	Jobin [7] Olin [8]	Jobin [7]	Jobin [7]		
Thermal oxide	Olin [8] Rohrer [18]				
Anodized, wet	Brown [3]		Brown [3]		
Anodized, dry	Kobusch [17]	Kobusch [17]	Kobusch [17]	Kobusch [17]	Kobusch [17]
Heated in H_2	Fan [22]	Sakamaki [9] Fan [22]			
Sputter-deposited	Sugimura [6]				
Nitrogen-implanted	Kobusch [17]	Kobusch [17]	Kobusch [17]	Kobusch [17]	Kobusch [17]
Locally modified	Sugimura [10]				
Orientation-dependent	Kobusch [19]	Kobusch [19]	Kobusch [19]	Kobusch [19]	Kobusch [19]
Thickness-dependent		Kobusch [20]			

[(a)] SPM, any of the methods tabulated; STM, scanning tunneling microscopy; AFM, atomic force microscopy; LFM, lateral force microscopy; dF/ds, stiffness.

1.2 Role of the sample preparation and measurement conditions

Table 1 shows that many authors have conducted experiments on even more different surfaces. Most authors refer to TiO_2 surfaces, but the sample was either electrochemically polished covered with natural oxide, or was covered with thermal or anodically grown oxide. The tunnel current arises due to defects in the oxides. Some authors increase the conductivity with annealing, heating in hydrogen, water adsorption or nitrogen implantation. These modified surface films can no longer be described as TiO_2. The chemical and physical state of this „reduced oxide" is unclear. The measurements were carried out in vacuum, dry nitrogen or with water films due to wet air or electrolyte. Since the tunnel current arises from the outermost layer of the surface, the chemical state of this layer determines the STM picture. In vacuum or dry nitrogen the surface will be dehydrated, in wet air or in electrolyte the surface will be hydrated or covered with a water film. For AFM and LFM this water film will be important as well, since lateral forces will be induced by the motion of the tip over the surface (changing the entire picture). In AFM the force curve will be changed due to water films (not necessarily changing the picture at the applied force, but resulting in different pictures at different forces and a hysteresis between forward and backward scans).

1.3 Aspects of nanotechnology

There are three possible ways of structuring surfaces: (1) positive (deposition), (2) negative (etching or mechanical removal) and (3) modification (implantation). An example of (1) is given by Sugimura et al. [10, 11]: Structures with xy dimensions of 20-50 nm and z dimensions of 1-5 nm could be generated by applying high positive bias voltages (STM-experiments in wet air) on silicon and titanium. Standard STM pictures could be obtained by using negative voltages on highly n-doped silicon and on hydrogen-saturated titanium dioxide. When the voltage was changed to highly positive values (+5-8V), then the surface was modified. This modification was monitored by changing back to a negative bias or by AFM. If the STM tip was moved over the surface during the period of positive bias, then a modification trace was left on the surface. These modifications

were discussed as anodically grown oxide. The wet air leaves a thin water film on the substrate. This water is used for the oxidation of the surface during the application of a high electric positive field. Laser-induced oxide growth on titanium and silicon was first observed by Schultze and coworkers [12-14]. In addition, Ag traces could be measured with laser-light in $AgNO_3$/MeOH solution [15]. These structures have *z* dimensions of only 10-100 nm. In this paper, we demonstrate the investigation of thin, well defined, anodically grown TiO_2 films with SPM techniques. In addition, we discuss aspects (2) and (3): removal of TiO_2 by STM, and modification by nitrogen implantation.

2 Experimental

Fine-grain titanium from Goodfellow (99.6%) was used. Titanium rods (5 mm radius) were ground and then electropolished according to [16]. Thin TiO_2 films were achieved by anodic oxidation in 0.5 m sulfuric acid according to [12]. TiN layers were preparad by ion implantation (3 keV, implanted dose 2 x 10^{17} N_2^+/cm^2 into the fine-grain titanium surfaces. Sputter-Ti surfaces were 3 μm Ti sputtered on a silicon wafer (without grains and grain boundaries). Oxide films on these surfaces were prepared by the same technique as described above. STM and contact-mode AFM investigations were performed on a Topometrix TMX 2000 Discoverer in ambient air or in a nitrogen atmosphere. Spectroscopy measurements were recorded on a modified NanoScope I STM (described in more detail in [20]). All spectra were recorded while the STM was in a black box without light, since light has a significant influence on the tunnel current on semiconducting surfaces [21]. AFM tips were standard tips with a radius of 50nm (Si_3N_4 with a spring constant of 0.032 N/m). STM tips were prepared electrochemically (Au in 3 M KCN solution and W in 2 M NaOH with 100 Hz sine and 2-5 V_{pp}).

3. Results

3.1 AFM of fine grain titanium

AFM pictures of a titanium surface are shown in Fig. 1. Grains with lateral dimensions of 10-30 mm can be clearly distinguished, while the surface of a single grain ist flat with a

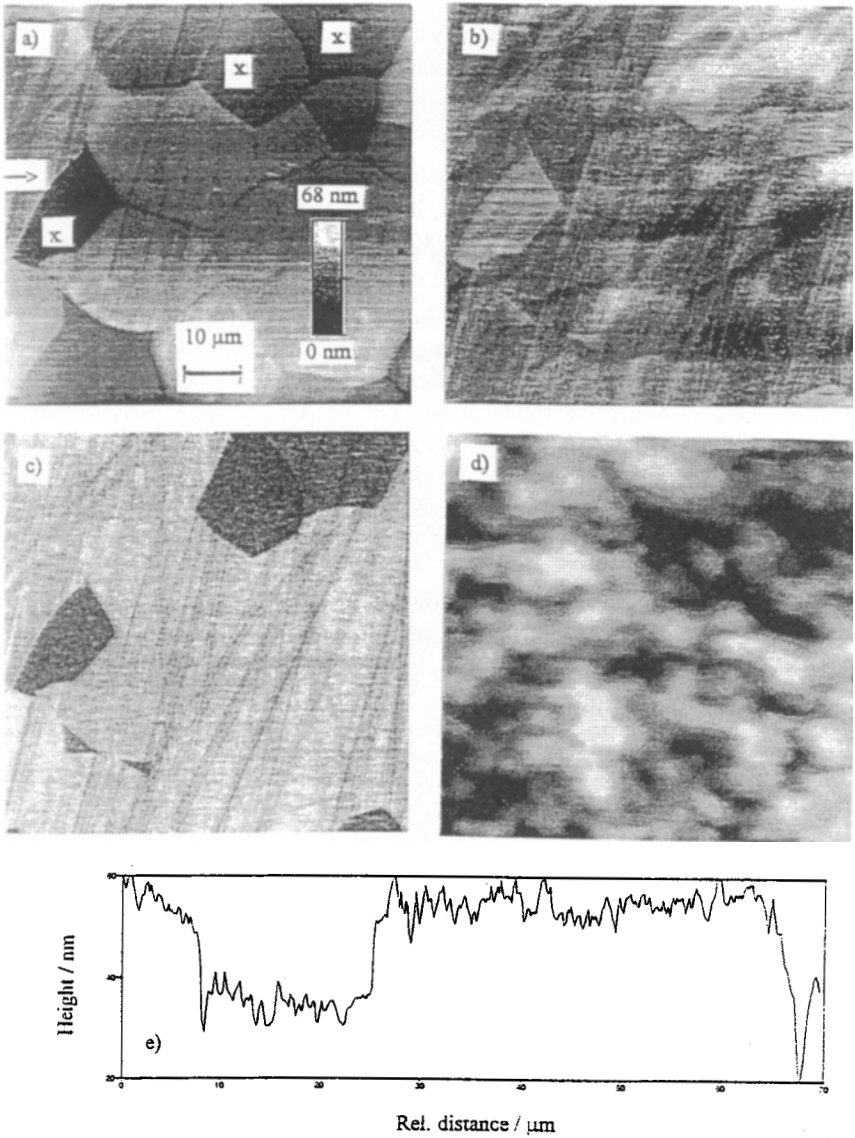

Fig. 1. (a) AFM-picture of a fine grain titanium surface covered with 20 nm TiO_2 (anodized up to 10 V), xy range: 70 µm, z_{max} = 68 nm; (b) LFM picture, same position; (c) dF/ds picture, same position; (d) AFM-picture of the same surface, zoom on a grain, xy range 586 nm, z_{max} = 5 nm; (e) line profile (as indicated by the arrow in (a).

roughness of only 1-3 nm. Quantitative data can be obtained from the line profile in Fig. 1(e): the height differences between these grains are 5-20 nm. The grain boundaries have lateral dimensions of 100-200 nm therefore the dz/dx-gradient ranges from 5-10%. In Fig.1(b) and (c) the corresponding (simultaneously recorded) LFM (lateral force) and dF/ds (stiffness) pictures are shown, respectively. The lateral forces are higher on the marked grains (with different crystal orientation, described in more detail in [17]), and meanwhile the relative stiffness is lower on these grains. This indicates that oxide films on grains with different orientation (within the grains a crystal structure is assumed) have significantly different mechanical properties. These two additional pieces of mechanical information are a fascinating new aspect in surface analysis. In [17] it is documented, that the electronic properties vary as well with the orientation. Figure 1(d) shows a zoom on one of the grains: Small structures can be seen with xy dimensions of 20-50 nm and heights of 1-5 nm. These structures were found on all titanium dioxide surfaces. Even on a Ti single crystal these substructures could be detected (after electrochemical polishing and anodizing with 20 nm oxide).

3.2 STM of fine-grain titanium

In order to probe the electronic conductivity, STM experiments were performed on these surfaces. A result is shown in Fig. 2. It is not possible to get a clear picture of the surface, the grain and the grain boundaries. The feedback system regulates the piezos to maintain a setpoint of 1nA (resulting in scratch-lines all over the picture, where the hard W tip is moved into the softer TiO_2 this is indicated by the unreal z range, which is 10 times higher than in the AFM pictures). It does not matter whether the bias is -5 V or +5 V, or even larger. Smaller values than 2 V (positive and negative) results in totally instable conditions (the piezos are extended to their maximum towards the surface, indicating that it is impossible to get a current of 1 nA or -1 nA, respectively). If the bias is -3 V (-1 nA setpoint), then pictures can be recorded. However, no clear structures can be seen and the pictures are irreproducible. Some regions in these pictures seem to be reproducible, and obviously in these areas the feedback system can maintain the current setpoint. This indicates that the electronic conductivity of anodically grown TiO_2 films is not sufficient for STM experiments if they are performed in dry nitrogen. However, some grains have a larger number of defect states (over which the current arises), resulting in poor, but possible, STM conditions. If the experiments were performed directly after the oxide film

Fig.2. Example of an irreproducible STM picture of fine-grain titanium covered with 20nm TiO_2, xy range: 75 µm, -3 V bias, -1 nA setpoint, z_{max} = 643 nm, scan rate 100 µm/s, W tip, normal air. Horizontal white or black lines between homogeneous areas indicate feedback irregularities.

was prepared electrochemically (without drying the surface in nitrogen), then it was possible to get pictures in some areas (not all), with the same structures as seen in the AFM picture (Fig. 1(d)). It was not possible to make large scans on these surfaces without tip crashes.

3.3 AFM/STM of TiN

Since most experiments in the literature were performed on highly doped oxide surfaces, we implanted nitrogen into these TiO_2 films. The resulting surface is almost metallized, similarly to TiN. AFM pictures (Fig. 3(a)) show the same structure as unimplanted surfaces (the z range is higher due to a longer electropolishing time; some grains (depending on their crystal orientation and electronic properties) will be electropolished

more strongly than others. STM investigations on these surfaces were possible without difficut. Figure 3(b) shows a picture taken with -3 V and -1 nA setpoint. The bias could be varied up to -1 V (1 V respectively) and a stable tunneling condition was still achieved. The small substructures as seen in Fig. 1(d) were detected on these surfaces as well. In [17] we will demonstrate AFM and STM pictures of the same position on the TiN, which is important for an interpretation of STM effects on differently conducting grains.

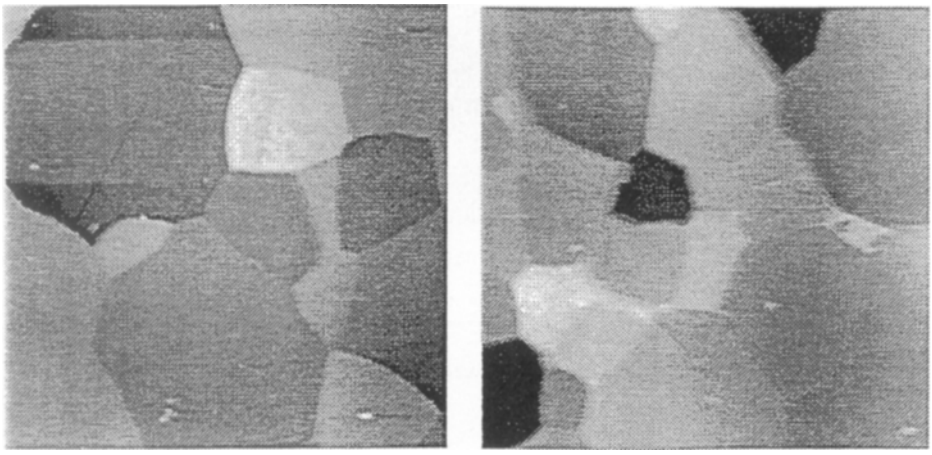

a) b)

Fig. 3. (a) AFM picture of nitrogen implanted TiO_2, xy range 75 μm, z_{max} = 558 nm; (b) STM picture of the same surface, xy range 75 μm, z_{max} = 393 nm, -3V bias, -1 nA setpoint, W tip.

3.4 Tunneling spectroscopy of TiO_2/TiN

An investigation on tunneling spectroscopy on titanium has already been presented in [20]. In addition, a systematic investigation was performed [17], which included the comparison between TiO_2 and TiN films on titanium. Figure 4 shows the voltage tunneling spectra of

the two surfaces (with the same substrate as in Fig. 3). It is obvious that TiN has a higher conductivity at all voltages than TiO_2 meanwhile the band gap is only apparent and cannot be correlated with the surface band gap. The apparent resistances (in branches) are several hundreds of megaohm, increasing to several gigaohms in the „band gap". The higher conductivity is the reason why STM pictures on implanted surfaces are possible in contrast to normal, anodically grown TiO_2, recorded in a dry nitrogen atmosphere. In contrast to the expected behavior we have found a dependency on the oxide thickness, the initial parameters, prepolarization, scan direction, scan rate, scan form, tip material and environmental conditions. Since the apparent band gap depends significantly on the oxide thickness, we have concluded (a) that it cannot be related to the surface band gap and (b) that the tip penetrates into the oxide and the mechanism is not a normal vacuum-type tunnel mechanism. Figure 5 shows some of these dependencies. Figure 5(a) is a comparison of voltage tunneling spectra on 5,15, or 40 nm oxide-covered titanium. The thicker the oxide, the higher the bias voltage needed to establish 1nA. If the initial bias was set to -1V, it was possible to obtain a stable tunneling current of -1nA only on the 5 nm oxide, but not on thicker oxides.

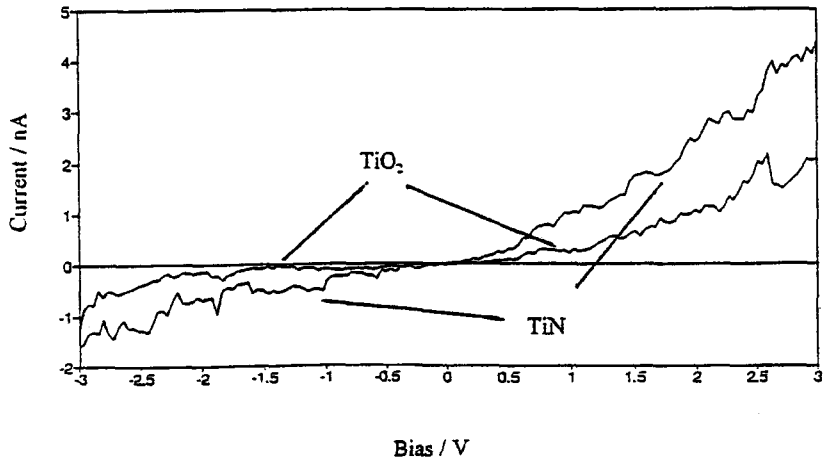

Fig.4. Voltage tunneling spectra on a 20nm TiO_2 film on titanium (a) and on a nitrogen-implanted region of the same sample. Initial conditions were -3 V (-1 nA setpoint), scan rate 3 V/s; W tip, samples were dried with nitrogen.

This is an additional evidence for the above mentioned partial penetration of the tip into the surface. Figure 5(b) shows distance tunneling spectra on a 5 nm oxide-covered titanium. The spectrum was started from the normal STM conditions (-1 V bias, -1 nA setpoint), and the tip was then retracted from the surface. According to the Gamov formula exponential behavior is expected. With a barrier of some electronvolts the tunnel current should decrease within 0.1-0.2 nm to 1/10 of the initial value. On these surfaces however, the tunnel current decreases to 1/10 of the initial (-1nA) value at more than 2 nm, validating the above theory of partial penetration. If the apparent barrier height is calculated according to the Gamov formula, a value of only some millielectronvolts is obtained. It is interesting to compare the spectra under dry nitrogen and wet air (I and II in Fig. 5(b)). The spectra were recorded directly after each other with identical parameters, except that between the recording of spectra the surface/tip system was flushed with a stream of dried nitrogen for 10 min. The wet air leaves a water film on the surface and the tip will be surrounded by this water film as well water due to capillary forces. Even while the tip is retracted for the distance spectrum, this water film will allow tunnel current to flow over a larger distance than without this film, resulting in a smaller dependency on the distance, as seen in Fig. 5(b).

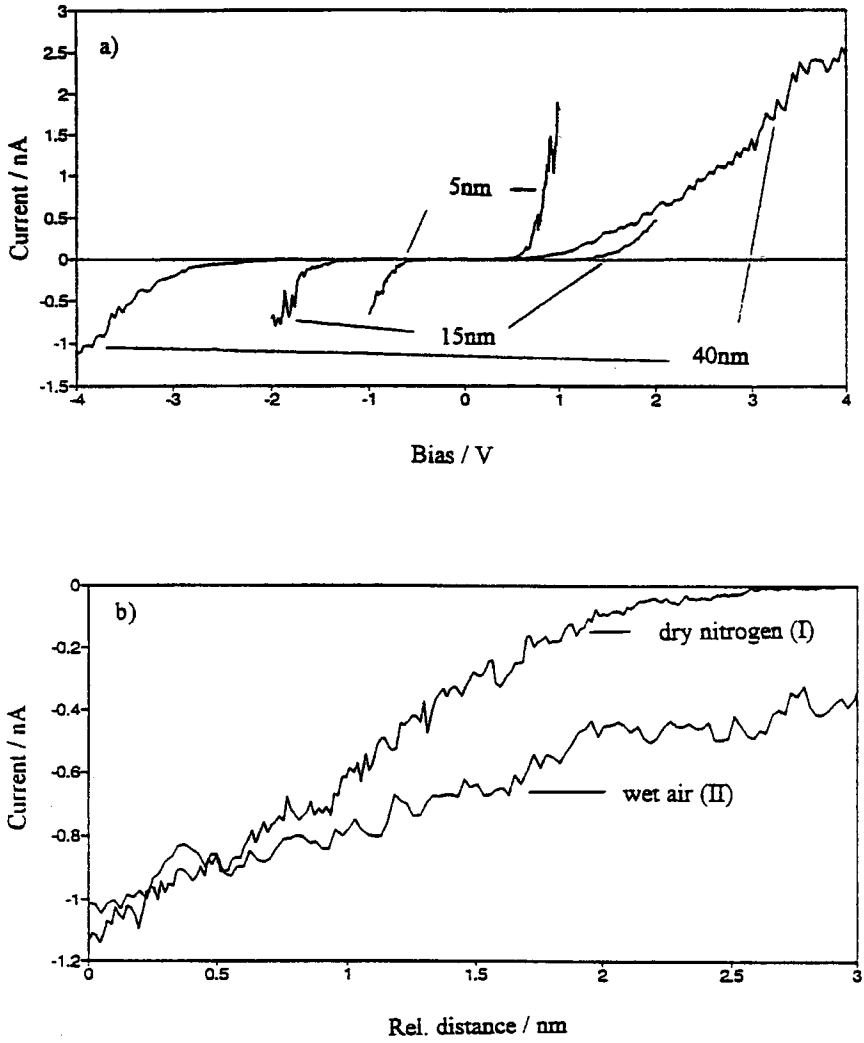

Fig. 5. A) Voltage tunneling spectra on 5/15/40 nm oxide covered Sputter-titanium recorded with Au-tip, under dry nitrogen atmosphere. B) Distance tunneling spectrum on an 5 nm oxide covered titanium, under dry nitrogen (I) and wet air (II), scan rate 3 nm/s, bias -1 V.

4 Discussion

The titanium surfaces were investigated to gain insight into mechanical and electronic properties. With AFM and related methods it was possible to identify grains (and their orientation in correlation to optical data) and grain boundaries. The surface could be prepared in such a way that the single grains had a flat surface with substructures of only some nanometers. The height differences between the grains were located at the grain boundaries with dz/dx gradients of only 5-10%, if the surface was carefully electropolished. However, if the titanium was strongly electropolished the grain boundaries showed height differences of several hundreds of nanometers and gradients of more than 50%. Thin anodically prepared TiO_2 films have a typical roughness (in the z-direction) of 1-3 nm and substructure in the xy-dimension of 20-50 nm. Other investigations in the literature have found the same substructures [3, 8, 10] on similar surfaces. Only Rohrer et al. [18] have found atomic resolution on a reduced single crystal of TiO_2, with special preparation. Since most surfaces were prepared in a different way, it is difficult to compare these results. The chemical and physical properties of modified TiO_2 surface films (either by reducing in hydrogen or implating nitrogen) are not well defined. It is necessary to apply all the possible analytical tools in order to obtain a full picture of these surfaces. That includes all SPM methods, but also XPS, Auger, classical electrochemistry, photoelectrochemistry, or ellipsometry. In this paper we have demonstrated the SPM part of these investigations. The grains exhibited different mechanical properties (as seen in the dF/ds and LFM pictures). Comparisons with experiments in the light microscope, microelectrochemistry, and microellipsometry [12, 13, 19] have shown that grains with different orientation (either on a single crystal with defined orientation or on fine-grain titanium with approximate orientation of the individual grains) have different mechanical, electronic, and electrochemical properties. The SPM data add a new dimension to these experiments due to the increased resolution and mechanical and electronic data of individual grains. It is impossible to determine surface properties in the nanometer range (xy- and z-dimension) with any of the other methods mentioned. The tunnel spectra have shown that the tip is in contact with the surface, resulting in a more or less symmetrical spectrum in the anodic as well as in cathodic range. However, it is also possible to record spectra with n-type semiconducting behavior (as would be expected for anodically prepared TiO_2 films), if the bias is changed to higher values [17]. For these experiments the initial tip-sample distance was increased, resulting in less or no penetration of the tip into the oxide. All tunnel spectra were

recorded at one position, without movement of the tip in the xy-directions during any of the measurements. However, STM experiments (as seen in Fig. 2) require this movement, resulting in bad or unstable conditions. If the tip is not moved, then the feedback system has time to drive the tip gently into the surface to get a tunnel current. But while it is moving over the surface this is not possible and the tip crashes (damaging the tip and the surface, resulting in irreproducible conditions). We have shown here that with all SXM techniques it is possible to obtain data even on these surfaces. In addition to information on the topography, we achieved a correlation between grain orientation, mechanical, electronic and electrochemical properties.

Acknowledgments. We thank the Fonds des Verbandes der Chemischen Industrie for the grant for C. Kobusch and the Ministerium für Wissenschaft und Forschung (NRW) for the financial support of this work.

5 References

[1] M. Radmacher, R.W. Tillmann, M. Fritz, H.E. Gaub, Science 257, 1900 (1992).
[2] J.L. Wilbur, H.A. Biebuyck, J.C. MacDonald, G.M. Whitesides, Langmuir 11, 825 (1995).
[3] G.M. Brown, T. Thundat,D.P. Allison,R. Warmack, J. Vac. Sci. Technol. A10, 3001 (1992).
[4] S.E. Gilbert, J.H. Kennedy, J. Electrochem. Soc. 2386 (1988).
[5] S.E. Gilbert, J.H. Kennedy, Surf. Sci. Lett. 225, L1 (1990).
[6] H. Sugimura, N. Kitamura, H. Masuhara, Jpn. J. Appl. Phys. 31, L1506 (1992).
[7] M. Jobin, M. Taborelli,R. Emch,F. Zenhausern, P. Descouts, Ultamicroscopy 42-44, 637 (1992).
[8] H. Olin,B.-O. Aronsson,B. Kaemo,J. Lausmaa,M. Rodahl, Ultramicroscopy 42-44, 567 (1992).
[9] K. Sakamaki, K. Itoh, A. Fujishima, Y. Goshi, J. Vac. Sci. Technol. A8, 614 (1990).
[10] H. Sugimura, T. Uchida, N. Kitamura, H. Masuhara, Appl. Phys. Lett. 63, 1288 (1993).
[11] H. Sugimura, N. Nakagiri, Jpn. J. Appl. Phys. 34, 3406 (1995).

[12] S. Kudelka, A. Michaelis, J. W. Schultze, Ber. Bunsenges. Phys. Chem. 99, 1020 (1995).
[13] S. Kudelka, A. Michaelis, J. W. Schultze, Electrochim. Acta 41 (1996) in press
[14] J. W. Schultze, K. Bade, A. Michaelis, Ber. Bunsenges. Phys. Chem. 95, 1349 (1991).
[15] O. Karstens, Dissertation, Universität Düsseldorf 1995.
[16] Lj. D. Arsov, Electrochim. Acta 30, 1645 (1985)
[17] C. Kobusch, Thesis, Heinrich-Heine-Universität Düsseldorf 1996.
[18] G.S. Rohrer, V.E. Henrich, D.A. Bonnell Sci. Rep. 250, 1239 (1990).
[19] C. Kobusch, O. Voigt, J.W. Schultze, in preparation.
[20] C. Kobusch, J.W. Schultze Electrochim. Acta 40, 1395 (1995).
[21] D.A. Bonnel, G.S. Rohrer, J. Vac. Sci. Technol. B9, 551 (1991).
[22] F.-Ren F. Fan, A.J. Bard, J. Phys. Chem. 94, 3761 (1990).

Part VI

Electrochemical Nanotechnology
In-situ Local Probe Techniques at Electrochemical Interfaces
Edited by W. J. Lorenz and W. Plieth

Electrochemical surface processing of semiconductors at the atomic level

P. Allongue, C. Henry de Villeneuve

Contents

1	Introduction	241
2	Silicon surfaces	243
	2.1 Etching mechanism and surface structure	243
	2.2 Preparation of ideally flat surfaces	246
3	Sulfide passivation of GaAs surfaces	248
4	Formation of molecular monolayers	249
5	Conclusions	250
6	References	251

Summary. Electrochemical processing of semiconductors is gaining interest for future applications because new technologies will require a control of the surface structure and chemistry on the atomic level. Real-time in-situ STM imaging in the electrolytic environment makes it possible not only to observe surfaces with a high resolution but also to characterize the chemistry and the dynamics of processes. Si etching and GaAs passivation as well as molecular grafting have been studied in this way in our group.

1 Introduction

A high-tech industry such as microelectronics currently uses wet chemical etching of semiconductors although manufacturing ultra large scale integrated (ULSI) circuits requires great attention to the compositional and structural homogeneity of surfaces. This example illustrates the possibilities offered by surface electrochemistry for a

control of surfaces down to the atomic scale. Multiple examples could be given. In all these fields a better understanding and control of interfacial processes has recently been gained with in-situ local probe techniques which may yield access to the composition and structure of surfaces as well as the dynamics of processes.

Preparing ordered semiconductor surfaces by a wet chemical treatment is a challenging problem because one cannot use surface self diffusion of atoms to rearrange the surface as is usually done upon annealing in ultrahigh vacuum (UHV). In the case of silicon, an oxide is first grown at elevated temperature (ca 1050 °C) in dry oxygen such that the interface Si/SiO_2 is as flat as possible on the atomic scale (Fig. 1(a)). The second step is *selective* stripping of the oxide in HF to obtain a surface in a state close to the fingerprint of the Si/SiO_2 interface (Fig. 1(b)).

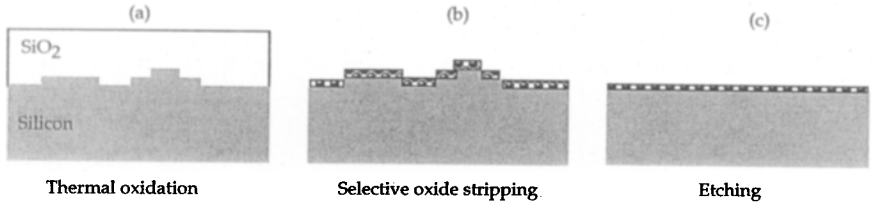

Fig. 1. Schematic preparation to obtain an ideal Si. (a) Oxide formation, (b) *selective* oxide stripping in HF. The surface is H-terminated with a structure which is close to the fingerprint of the Si/SiO_2 interface, (c) after subsequent chemical etching.

The last step is surface anisotropic etching to remove the remaining adatoms and islands and leave terraces atomically flat (Fig. 1(c)). This technique of preparation is specific to Si and is made possible by the high quality of the Si/SiO_2 interface and the extreme selectivity of SiO_2 to Si etching in HF (Si is almost not etched in acidic HF). With other materials like compound semiconductors procedures are generally different.

During the last couple of years we have been using in-situ STM/AFM to investigate semiconductor surface etching as well as molecular grafting on these materials. Metal deposition is a younger topic and is not considered further in this contribution.

Imaging semiconductor surfaces in liquids raises several kinds of difficulties which have been recently reviewed [1, 2]. In the case of STM, n-type samples must for instance be cathodically polarized since the contact of a semiconductor with a liquid is a diode and proper tunneling requires the diode be forward-biased so as to reach a sufficient density of electrons at the surface. In the case of AFM, the laser detection

may cause uncontrolled photoeffects under reverse bias, such as photocorrosion with n-type substrates. The friction of the tip may also enhance surface reactions locally. Despite these limitations, in-situ STM/AFM imaging semiconductors under potential control, has the great advantage that this minimizes interactions between the tip and the substrate by comparison with imaging at ambient conditions. Unless the atmosphere is sufficiently controlled, ambient conditions STM generally leads to some uncontrolled electrochemical reactions in the layer of contamination, a phenomenon which can however be utilized in nanolithography applications [3, 4].

2 Silicon surfaces

2.1 Etching mechanism and surface structure

Hydrogenated silicon surfaces, simply prepared by dipping in HF, are the prototype of ideally passivated semiconductor surfaces [5]. They are electronically inert with the lowest recombination velocity ever reported [6] and are chemically resistant to air oxidation [5]. The pH of HF or NH_4F solutions has a great influence on the microstructure of etched surfaces [7-9]. The images in Fig. 2 are typical large-scale views of n-Si(111) surfaces taken in 1 M NH_4F solutions of pH 4 and 8 [9]. Atomic resolution in fluoride solutions has been reported by others [10, 11]. As described in Section 1 the silicon substrate was cathodically biased for imaging.

By showing that flat terraces appear at elevated pH Fig. 2 illustrates the pH dependence of the etching mechanism [9, 12]. There are indeed two routes, one electrochemical and the other chemical (no free-charge carrier exchanged). At pH 4 the first route dominates and the surface is rough because the process is isotropic. As the pH increases, the rate of the chemical reaction increases leaving (111) terraces atomically flat because the process is highly anisotropic for steric reasons [9]. At alkaline pH, etching is even more anisotropic with (111) planes which etch more than 100 times slower than (110) and (100) planes [13]. This unique property has long been used for micromachining Si wafers. Most of our STM work was performed in these solutions where the dynamics of the process has been analyzed in great detail.

Figure 3 is a high-resolution image of a Si(111) in NaOH. It shows that the surface has a great chemical homogeneity and that the STM may have some chemical sensitivity. With the exception of a few ≡Si-OH [14] visible (white spots), which represent only 0.1 % of atomic sites, the surface is indeed (1x1) H-Si(111). That ≡Si-OH appear as protrusions surrounded by a dark ring comes from an increased local density of states and a three-dimension (3D) potential distribution induced by the large

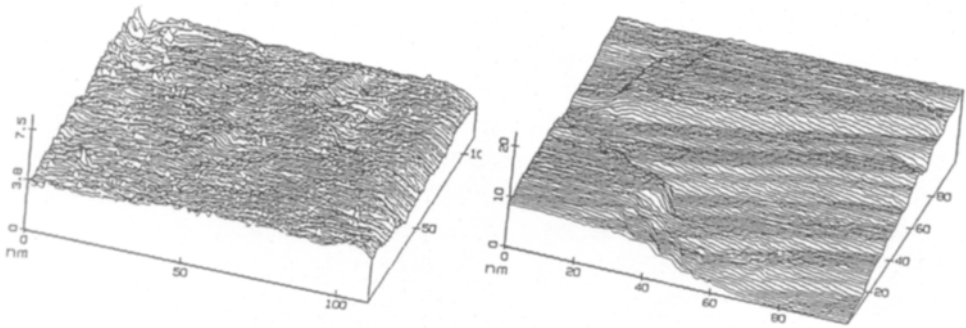

Fig. 2. 1000x1000 $Å^2$ images of n-Si(111) surfaces in ammonium fluoride solutions of pH 4 (a) and 8 (b). After [9].

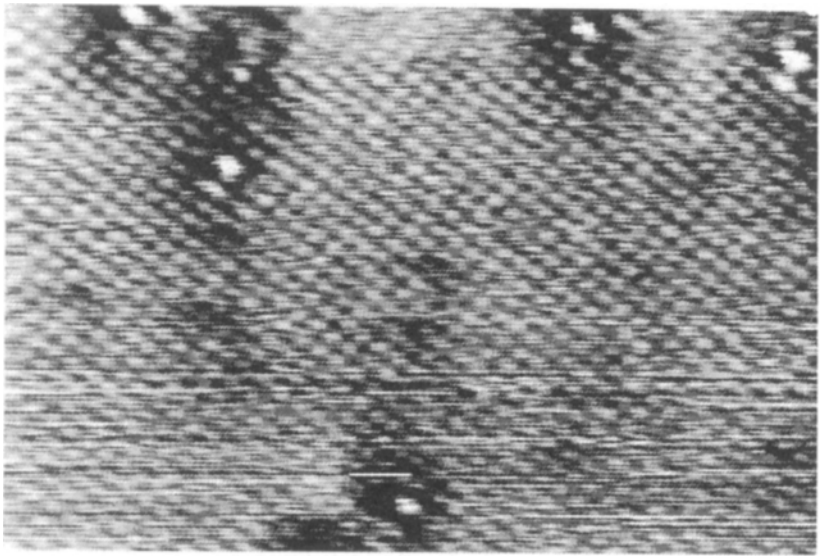

Fig. 3. 103x 70 $Å^2$ STM image showing the surface of n-Si(111) in NaOH. The surface is (1x1)-H-terminated except for a few ≡Si-OH groups (after [14]).

electronegativity difference between Si and the OH group. The H-termination, though energetically less favorable when comparing the energies of Si-H and Si-O bonds, may be explained in terms of kinetics.

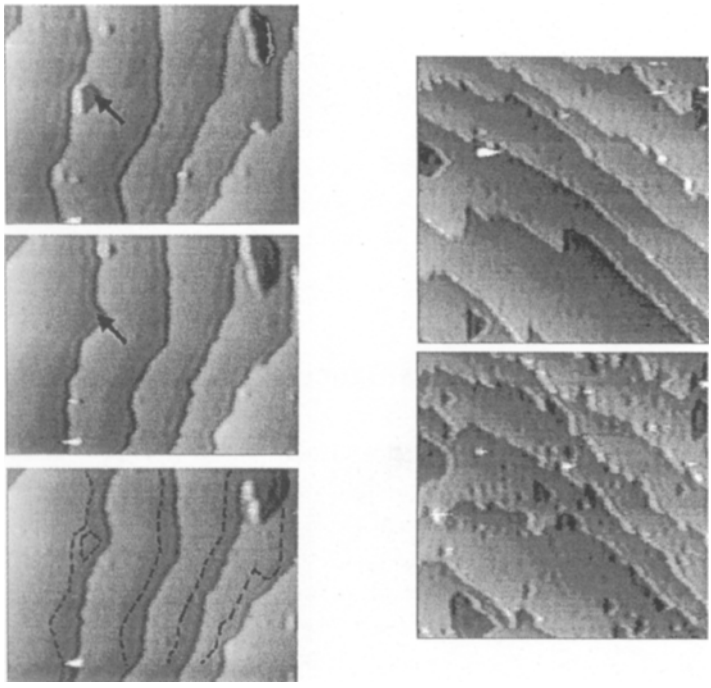

Fig. 4. Time sequences of STM images showing Si(111) etching in NaOH. (a): Cathodic bias (90s between images; frames are 1260x970 Å^2). (b): At the rest potential for 3 s using a special procedure is used (frames are 1400x1400 Å^2) (after [12]).

The substitution Si-H → Si-OH, which is the very initial step of the dissolution, is indeed rate-determining in NH_4F at all pH values [9] as well as in NaOH. The H-termination has been proved by in-situ FTIR [15, 16].

The generation mechanism and the stability of Si-OH surface groups both depend on the surface site [9]. At step edges, hydroxyl groups may easily bind chemically on step di- and monohydrides, forming =Si-HOH or ≡Si-OH entities which are rapidly removed by chemical breaking of the Si-Si back bonds. This leads to the lateral migration of atomic steps observed at cathodic bias (Fig. 4a). Vertical ≡Si-OH group formation stems by contrast exclusively from the electrochemical process and therefore occurs only at potentials close to and positive of the rest bias. Vertical Si-OH groups are also more stable than step ≡Si-OH and not every group leads to the initiation of an

etch pit. According to a simulation (Monte-Carlo method) it can indeed be inferred that the formation of a nano cluster of suboxide is necessary prior to the nucleation of an etch pit [17]. The triangular etch pits observed in Fig. 4(b) have been created at the rest bias but imaged at cathodic bias, using a special procedure [12].

The time sequences presented in Fig. 4 have been used to measure the local etch rates, i.e. on a 0.01 μm^2 scale. Etch rates thus derived are 0.2 and 8 $Å/min^{-1}$, respectively, in sequences (a) and (b) of Fig. 4, values which are surprisingly in very good agreement with macroscopic determinations, performed on a mm^2 scale, that is on a surface area 10^8 times larger [12]. More recently we have been able to determine the reaction rates on the atomic scale from the direct comparison of in-situ STM sequences and Monte-Carlo simulations.

2.2 Preparation of ideally flat Si surfaces

Ideally flat (111) surfaces do not exist in practice. There are always steps and pits according to the angle of crystal miscut. One possible way to obtain surfaces with an ordered staircase structure consists in using vicinal (111) surfaces with a miscut angle of a few degrees in the proper direction so as to make the lateral flow of steps faster than the nucleation and growth processes of etch pits on terraces (Fig. 5(a)). The rate of dissolution is indeed ~1 s^{-1} on step dihydrides and 10^{-2} s^{-1} on step monohydrides, and ranges between 10^{-3} and 10^{-4} s^{-1} on vertical terrace monohydrides [17]. Using additives is another possibility which is less dependent on crystal orientation. Amount traces of Triton [formula : $C(CH_3)_3CH_2(CH_3)_2$-C_6H_4 -(OCH_2CH_2)nOH)] added to NaOH tends for instance to flatten the silicon surface on a large scale [18]. Figure 6 illustrates this effect. Unlike in pure NaOH, it is remarkable that the initial spacing between steps is preserved at the end of the series. With Si(100) flatter surfaces may be also obtained, with no formation of pyramids as usually observed after anisotropic etching in NH_4F.

Observations may be interpreted in terms of the formation of a monomolecular membrane floating on top of the surface as Fig. 5(b) sketches. The benzene rings favor indeed stacking of molecules on the atomically flat portions of the surface in a sort of self assembly, with the hydrophobic alkyl heads of the molecule in contact with the H-terminated surface (though Van der Waals interactions) while the hydrophilic tails -$(OCH_2CH_2)_n$OH point towards the solution. The sequence shows that any atomic size

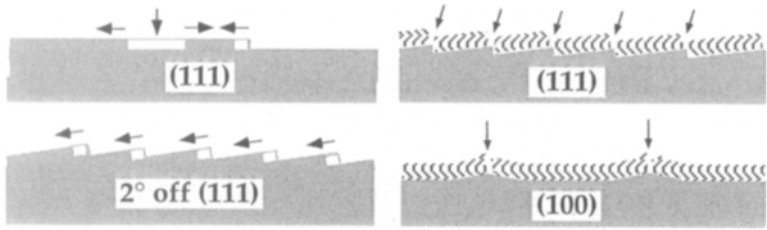

Fig. 5. Schematic technique to prepare ideal Si(111) surfaces. (a) Use of the crystal miscut; (b) Use of Triton as additive.

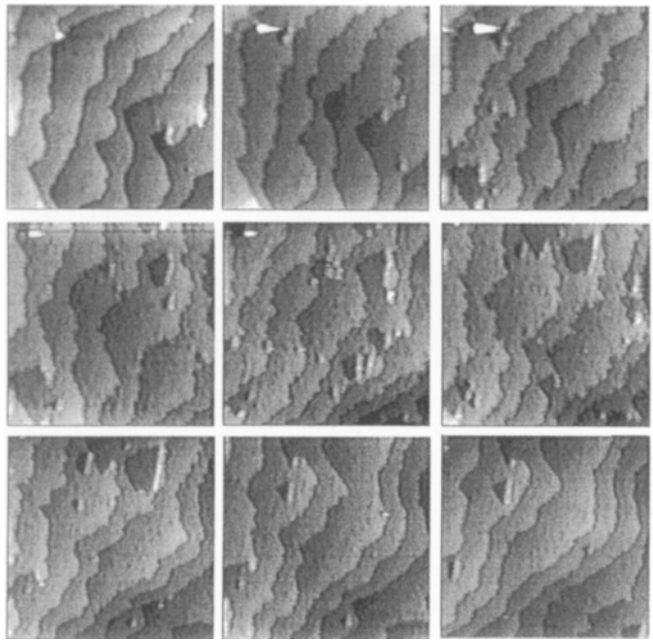

Fig. 6. Time sequence (45 s/image) taken on n-Si(111) tilted by 0.7° in Triton/NaOH. Chemical etching is promoted between images 2-6. In other images the surface is cathodically protected. Frames are 1400x1400 $Å^2$ (after [18]).

defects beaks this order and results in faster local etching in a self-repairing action which smoothens the surface on a larger scale. That the molecules do not bind chemically on the surface is of great interest for applications.

3 Sulfide passivation of GaAs surfaces

Unlike silicon, results with III-V compounds are much less spectacular and conclusive. There is not a simple procedure (Fig. 1) to obtain a flat surface. In addition, reaching a monolayer protection seems unlikely and has not been achieved to our knowledge. The anisotropy of etching is also much less important. One reason is that the surface is composed of two elements having different chemical reactivities.

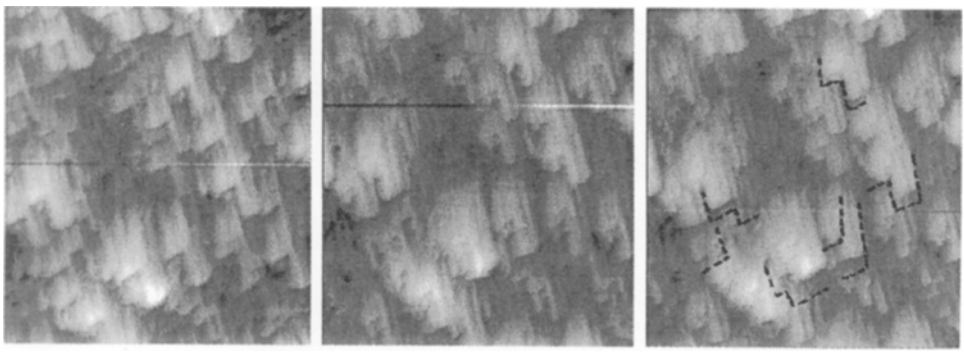

Fig. 7. STM images showing GaAs etching in Na_2S (1 min/image). The dotted lines in (c) mark the initial position of some steps. Frames are 3000x3200 $Å^2$. (unpublished images).

The sulfuration of III-V surfaces from the liquid phase remains to date one of the best passivation techniques. This builds several monolayer-thick protective layers [19] which explains why STM data are very sparse for that system [1]. In ambient conditions the layer degrades under the tip [20]. In liquids, tunneling is also difficult. In Fig. 7 the GaAs(100) surface (MBE layer) has however been imaged with the resolution of atomic steps in a dilute Na_2S solution of pH 14 [21]. The anisotropic shape of terraces results from a selective etching on the shorter edges of terraces as the images shows. The dotted lines in image 7c mark the initial position of some steps (as observed in image 7a) to illustrate the anisotropy of the dissolution The vertical etch rate is ~5 Å/h. The step height, equivalent to several times the height of double atomic

layers, further suggests that the surface is terminated with only one kind of atom bound to the top layer. The most probable termination is a Ga topmost layer bound to sulfur species, since large-scale AFM imaging and electrical studies indicate that Ga(111) planes are etch stop planes. Atomic resolution showing a (1x1) structure has been obtained in UHV after annealing at 200°C [22].

4 Formation of molecular monolayers

Molecular grafting on semiconductors is thought to be of great importance in the near future to functionalize surface and/or passivate them (e.g. application to sensors and thin dielectric layers). The process is however generally referred to as reaction of molecules with the oxide layer on top of the material [23]. Direct grafting should offer other opportunities because the organic layer would be in electrical contact with the material. This last possibility, which has been explored by very few groups, raises some difficulties and fundamental questions since, unless one operates in the UHV, the semiconductor surface is initially covered with foreign ligands covalently attached. These must be substituted by the molecules of interest.

A chemical process including a pretreatment to terminate the surface highly electronegative species (e.g., Cl, S, or organic radicals) as precursors may be used [24]. Electrochemistry is however an alternative way of modification. Anodic grafting of $-OCH_3$ on porous Si has for instance been demonstrated from anhydrous methanol to stabilize the surface [25]. The coverage is nevertheless incomplete. In a mixture of NaOH and containing isopropanol, anodic molecular binding has also been observed by STM [14].

The above approaches present the disadvantage that the surface may chemically oxidize or dissolves (case of anodic grafting) leading to incomplete coverage. More dramatic, the surface may loose its ideal structure. To overcome these questions, we have recently developed a new approach, based on the cathodic reduction of suitable organic molecules (substituted diazonium salts) so as to generate radicals that react with the H-terminated surface [26]. XPS and FTIR reveal that ≡Si-phenyl bonds are formed, and Fig. 8 shows that the organic adlayer is close-packed with a (2x1) structure. Different substituents on the phenyl ring could be successfully used, which opens up to a simple route to functionalize Si surfaces.

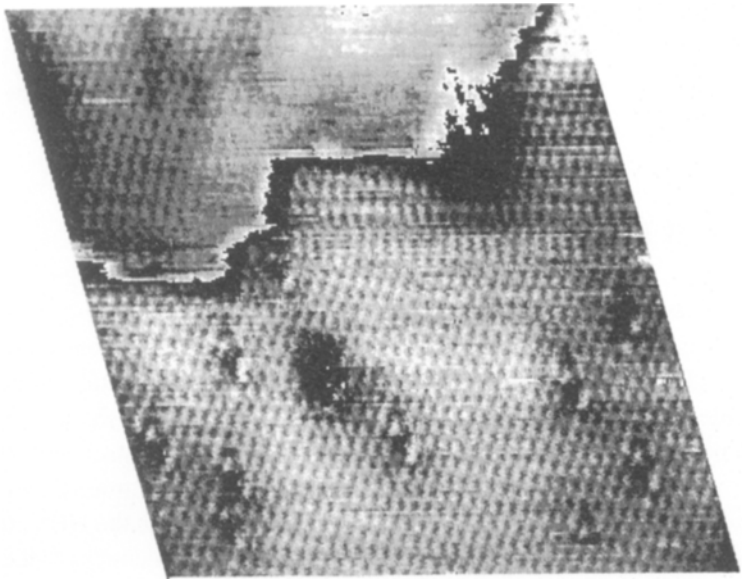

Fig. 8. 160x180 Å^2 STM image of Si(111) covered by a monolayer of bromophenyl. The step is a bilayer high. (Unpublished image).

5 Conclusions

Investigations of semiconductor surfaces by STM/AFM have yielded new insights into the preparation of flat surfaces by chemical etching. Among future applications of flat Si(111) surfaces, nanostructure formation, such as tip-induced nanodeposits and nanomachining, are probably most relevant, technological challenges. In this respect the electrolytic environment offer interesting opportunities which need being investigated.

Acknowledgments. P.A. dedicates this contribution to Professor H. Gerischer, with whom he started his STM work on silicon as Alexander von Humboldt fellow. We also thank V. Kieling, J. Kasparian, and A. Ankoudinov for their contributions to the results presented.

6 References

[1] P. Allongue, in: Advances in Electrochemical Science and Engineering, Vol. 4, H. Gerischer, C.W. Tobias (Eds.), VCH, Weinheim, Chap. 1, pp. 1-66.

[2] P. Allongue, in: Nanoscale Probes of the Solid/Liquid Interface, A.A. Gewirth, H. Siegenthaler (Eds.), Kluwer Academic Publishers, NATO ASI Series E, Vol. 288 pp.45-68, 1995.

[3] J.A. Dagata, J. Schneir, H.H. Harary, J. Benett, W. Tseng, J. Vac. Sci. Technol. B9, 1384 (1991); N. Barniol, F. Perez-Murano, X. Aymerich, Appl. Phys. Lett. 61, 462 (1992).

[4] E.S. Snow, P.M. Campbell, Appl. Phys. Lett. 64, 1932 (1994).

[5] For a book review, see G.S. Higashi, Y.J. Chabal, in: Handbook of Semiconductor Wafer Cleaning Technology, W. Kern (Ed.), Noyes Publications, Park Ridge, 1993.

[6] E. Yablanovitch, D.L. Allara, C.C. Chang, T.Gmitter, T.B. Bright, Phys. Rev. Lett. 57, 249 (1986).

[7] P. Jakob, Y.J. Chabal, J. Chem. Phys. 95, 2897 (1991).

[8] H.E. Hessel, A. Feltz, U. Memmert, R.J. Behm, Chem. Phys. Lett. 186, 275 (1991).

[9] P. Allongue V. Kieling, H.Gerischer, Electrochim. Acta 40, 1353 (1995); H. Gerischer, P. Allongue, V. Costa Kieling, Ber. Bunsenges. Phys. Chem. 97, 753-757 (1993).

[10] S. Lin Yau, F.F. Fan, A. J. Bard, J. Electrochem. Soc. 139, 2825 (1992).

[11] Sueh-Lin, K. Kaji, K. Itaya et al. Appl. Phys. Lett. 77, 766 (1995).

[12] P. Allongue, V. Kieling, H. Gerischer, J. Electrochem. Soc. 140, 1009 and 1018 (1993); P. Allongue, H. Brune, H. Gerischer, Surf. Sci. 275, 414 (1992).

[13] D.L. Kendall, Appl. Phys. Lett. 26, 195 (1975) idem, Annu. Rev. Mater Sci. 9, 373 (1979).

[14] P. Allongue, Phys . Rev. Lett. 66, 1986 (1996).

[15] A. Venkateswara Rao, F. Ozanam, J.-N. Chazalviel, J. Electrochem. Soc. 138, 153 (1991).

[16] J. Rappich, H.J. Lewerenz, H. Gerischer, J. Electrochem. Soc. 141, L187 (1994).

[17] P. Allongue, J. Kasparian, Microsc., Microstruct. Microanal. 5, 257 (1994); J. Kasparian, P. Allongue, Surf. Sci. (1997) in press.

[18] P. Allongue, V. Kieling, H. Gerischer, J. Phys. Chem. 99, 9472 (1995); P. Allongue, V. Bertagna, V. Costa-Kieling, H. Gerischer, J. Vac. Sci. Technol. B12, 1539 (1994).

[19] C.J. Sandroff, M.S. Hegde, C. C. Chang, J. Vac. Sci. Technol. B7, 841 (1989).

[20] J.A. Dagata, W. Tseng, J. Bennett, J. Schneir, H. H. Harary, Appl. Phys. Lett. 59, 3288 (1991); J.A. Dagata, W. Tseng, J. Bennett, J. Schneir, H.H. Harary, Ultramicroscopy 42-44, 1288 (1992).

[21] P. Allongue, C. Henry de Villeneuve, A. Ankoudinov, unpublished.

[22] N. Yokoi, H. Andoh and M. Takai, Appl. Phys. Lett. 64, 2578 (1994).

[23] A. Ulman, An Introduction to Ultrathin Organic Films from Langmuir-Blodgett to Self-assembly, Academic Press, Boston, 1991.

[24] M.R. Lindford, C.E.D. Chidsey, J. Am. Chem. Soc. 115, 12632 (1993); M.R. Lindford, P. Fenter, P. Eisenberger , C. E. D. Chidsey, bid. 117, 3145(1995).

[25] M. Warntjes, C. Veillard, F. Ozanam, J.N. Chazalviel, J. Electrochem. Soc., submitted

[26] C. Henry de Villeneuve, J. Pinson, P. Allongue, J. Phys. Chem. 101, 2415 (1997); P. Allongue, C. Henry de Villeneuve, J. Pinson, F. Ozanam, J.N. Chazalviel, Mat. Res. Soc. Proc., Symposium Electrochemical Synthesis and Modification of Materials, Boston, 1996.

Electrochemical Nanotechnology
In-situ Local Probe Techniques at Electrochemical Interfaces
Edited by W. J. Lorenz and W. Plieth

In-situ Electrochemical AFM Study of Semiconductor Electrodes in Electrolyte Solutions

K. Uosaki, M. Koinuma

Contents

1	Introduction		253
2	Experimental		254
3	Results		255
	3.1	Electrochemical reaction of p-InSe electrodes	255
	3.2	Atomically resolved structure of GaAs(100) surfaces in electrolyte solutions	257
	3.3	Electrodeposition of Cu on GaAs(100) surfaces	259
	3.4	AFM tip-induced modification of GaAs(100) surface structure	262
4	Conclusion		263
5	References		264

Summary. Atomically resolved surface structures were observed at the van der Waals face of InSe and the (100) face of p- and n-GaAs electrodes in electrolyte solutions under potential control by electrochemical atomic force microscope (AFM). The surface structure change of these electrodes during electrochemical reactions was followed.

1 Introduction

Control and observation of electrochemical and photoelectrochemical reactions at semiconductor electrodes are very important in establishing the electrochemical/photoelectrochemical etching processes and stable photoelectrochemical cells

reactions, in-situ information of morphological and electronic structures of semiconductor electrode surfaces with atomic resolution is essential. Although techniques such as electron microscopy and optical microscopy have been applied to examine the morphology of the surface of solid substrates, electron microscopy can be used only for ex-situ examination and optical microscopy has poor resolution [3, 4].

Scanning tunneling microscope (STM) has now become a popular tool for imaging electrode surface in-situ with atomic resolution and has been proved to be a very useful aid to understanding the fundamentals of electrode processes [5]. This technique has, however, some limitations. Because STM uses tunneling current as a probe, only the surface of conducting materials can be imaged. Thus, STM measurement of semiconductor electrodes is not possible under reverse bias because of the existence of a space charge layer [6,7]. On the other hand, AFM measurement can be carried out over a wide potential region as it is not affected by the sample conductivity. Furthermore, electrochemical processes on the tip which may cause serious problems in the STM measurements in electrolyte solutions can be avoided in the AFM measurements.

In this work, we employed electrochemical AFM to investigate the surface structure of InSe and GaAs single-crystalline electrodes as these semiconductors have attractive properties described below but very limited information is available on the surface structure in electrolyte solution on a nanometer scale.

InSe is a III-VI layered compound semiconductor which has interesting properties, including strong conductivity anisotropy [8, 9]. Because of high photosensivity with an optimum energy gap for solar energy conversion (1.3 eV) [10] and the expected high electrochemical stability of the van der Waals face [11], InSe has been considered as a good candidate for photoelectrodes. The importance of surface conditions with respect to photoelectrochemical properties of this electrode has been demonstrated by using a laser spot scanning microscope with micron resolution [12, 13].

GaAs is one of the most attractive semiconductor materials to be used in various electronic devices and in dry/wet solar cells [14-16].

2 Experimental

AFM images were obtained using a NanoScope II or E (Digital Instruments, CA) operating in the constant force repulsive mode. Microfabricated Si_3N_4 cantilevers 100 μm long with a spring constant of 0.58 N/m were used throughout. Typical force during imaging was less than 1 nN. Calibrations of the piezo scanner for the x and y planes were carried out by imaging mica and a single-crystal Au(111) face in Milli-Q water.

p-InSe single crystals grown by the Bridgman-Stockbarger method and GaAs(100) single crystals were donated by Dr. Chevy [15] and by the Mitsubishi Chemical Corporation, respectively. A clean surface of InSe was obtained by removing some layers using adhesive tape, and GaAs substrates were cleaned in hot acetone and in ethanol and rinsed with Milli-Q water (Millipore Co.) before each experiment. Ohmic contacts were made by using an In-Zn alloy for p-type and In for n-type substrates.

A glass fluid cell of 0.2 ml volume (Digital Instruments) was used for the electrochemical AFM measurements. The counter electrode and reference electrode were a Pt wire and an Ag/AgCl electrode, respectively. The area of exposed electrode in contact with the solution was about 0.32 cm^2. The electrolyte solutions for electrochemical AFM measurements were prepared by using reagent-grade chemicals (Wako Pure Chemicals) and Milli-Q water. The solution was deaerated by passing purified N_2 gas for at least 20 min prior to the experiment.

3 Results

3.1 Electrochemical reaction of p-InSe electrodes

Surface structure changes of p-InSe were monitored by AFM with atomic resolution when the potential was scanned from negative (-1.0 V) to positive (+0.2 V) and back again at a rate of 15 mV/s. Figure 1 shows the AFM images obtained sequentially when the potential was cycled [16]. All images shown in Fig. 1 were obtained while the tip was scanned from the left to the right. It took 11 s to capture one image and therefore the potential differs by 165 mV between the top and the bottom of each image. In relatively negative potential region (less than -0.5 V), the atomic arrangement was clearly resolved (Fig. 1(a)). The image is essentially the same as those obtained in air [17] and in water [16] and is in good agreement with the structure expected from the crystallographic structure. This result suggests that the surface is stable under these conditions. When the potential became more positive than -0.5 V, the atomic image became less clear (Fig. 1(b)). The more positive the potential was, the larger was the non-atomically resolved area (Fig. 1(c) and (d)). The atomic image was completely lost at potentials more positive than 0 V (Fig. 1(d)). The atomic image was partly recovered when the potential was scanned back to a potential more negative than -0.7 V (Fig. 1(e)) and was completely recovered if the potential was kept at -0.8 V for 1 min (Fig. 1(f)).

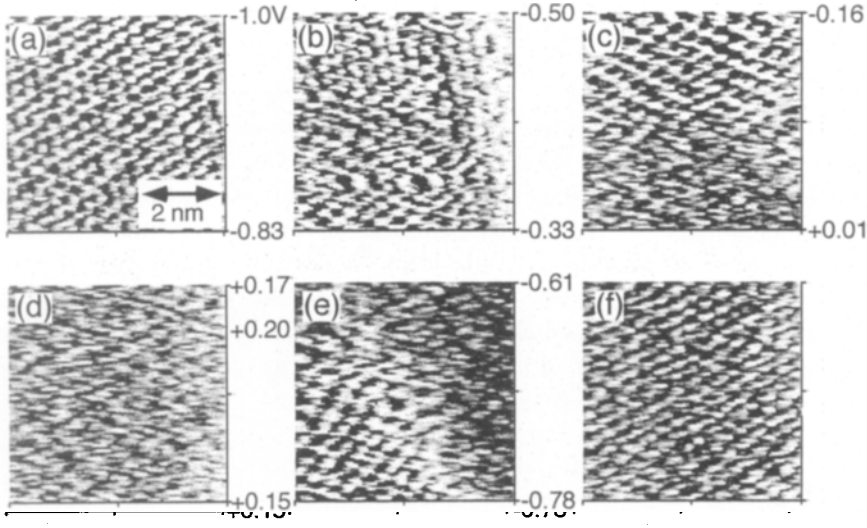

Fig. 1. (a) - (e) Sequentially obtained AFM images of p-InSe in 10 mM Na_2SO_4 while the potential was scanned. Potential regions where images were taken are shown in the figure. (f) The image was taken after the potential was kept for 1 min at -0.8 V.

It is known that the anodic process at InSe is [18] :

$$InSe + H_2O \rightarrow Se + InOH^{2+} + H^+ + 3e^- \quad (1)$$

Since $InOH^{2+}$ is soluble but Se is insoluble in the solution, Se is left on the InSe surface and forms an amorphous layer upon oxidation. This should explain why the atomic image was lost at positive potentials. The deposited Se is removed reductively in cathodic potential region by [19]:

$$Se + H^+ + 2e^- \rightarrow HSe^- \quad (2)$$

when the Se layer is not too thick, and the atomically ordered van der Waals face appears again.

3.2 Atomically resolved structure of GaAs(100) surfaces in electrolyte solutions

Since a GaAs surface is covered with native oxide, atomic arrangement is not observed in air. When an electrode was immersed in electrolyte solution and a cathodic potential was applied, the oxide layer seemed to be reduced electrochemically as atomic arrangement was observed at the p-GaAs electrode, as shown in Fig. 2 [20]. The top view (Fig. 2(a)) and the Fourier spectrum (Fig. 2(b)) show that the atomic structure is of nearly four-fold symmetry with a nearest neighbor distance of about 0.42 ± 0.04 nm. This result shows that the surface has a GaAs(100)-(1xl) structure [21]. This is in contrast with the fact that a GaAs(100) surface forms a reconstructed structure such as

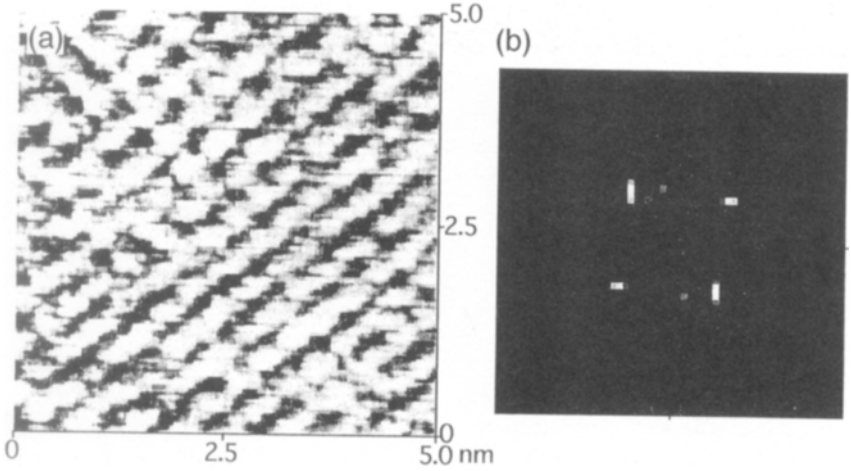

Fig. 2. (a) An atomically resolved AFM image of the p-GaAs electrode surface in 10 mM HCl obtained at 0 V vs. Ag/AgCl. (b) Two-dimensional Fourier spectrum of the image.

c(2 x 8), (2 x 4), and c(4 x 4) in UHVconditions because of the existence of the dangling bond in (1 x l) structures. In HCl solution, the atomic images are clearer near the open circuit potential than in more cathodic potential regions. XPS shows that the Ga/As ratio is higher and the Cl peak is stronger for samples which were removed from the cell after a positive potential was applied than at samples without anodic treatment

Thus, we speculate that the topmost atoms are Ga-terminated with Cl and the (1 x 1) structure is stabilized by the Cl termination.

In H_2SO_4 solution, however, atomic images were obtained more clearly at the potentials close to that of H_2 evolution than at the potentials near the open-circuit potential [22]. Figure 3 shows a cyclic voltammogram and atomically resolved AFM images at the various potential regions of p-GaAs in H_2SO_4 solution. As the electrode potential became closer to the open-circuit potential, the atomic arrangement became less clear. This result suggests that the SO_4^{2-} ion does not stabilize the dangling bonds on the GaAs(100) surface. In the cathodic potential region where the atomically ordered structure was observed, the GaAs(100)-(1 x 1) structure seems to be stabilized as a result of termination with H^+ ions.

The atomically ordered surface structure of (100)-(1 x 1) was observed also at n-type GaAs(100) electrodes.

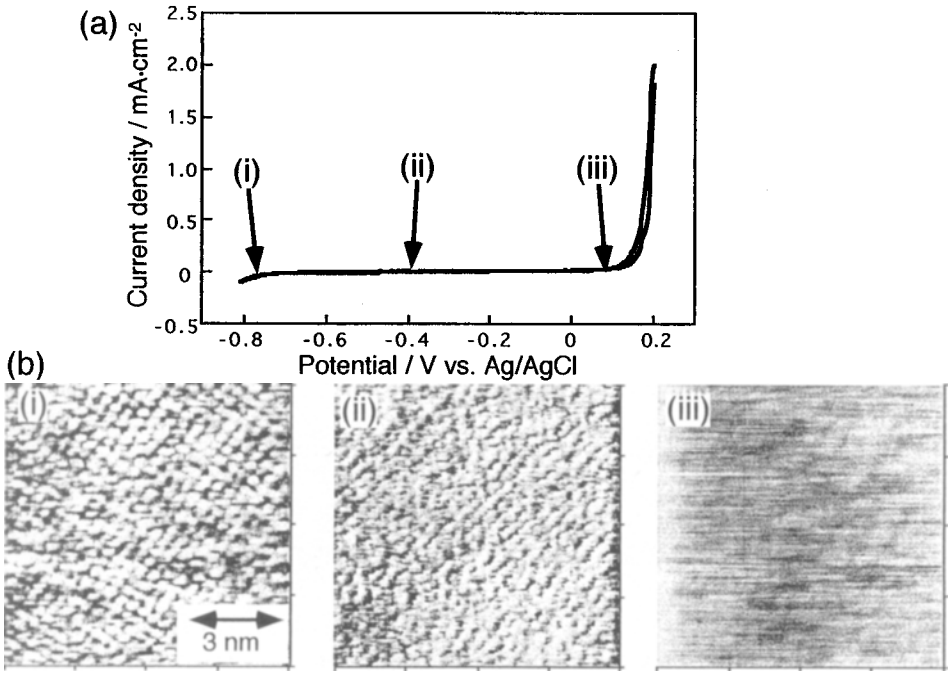

Fig. 3. (a) Cyclic voltammogram of p-GaAs(100) in 10 mM H_2SO_4. (b) AFM images of potential regions where images were taken as shown in (a).

3.3 Electrodeposition of Cu on GaAs(100) surfaces

Figure 4 shows the cyclic vottammogram of p-GaAs in 9 mM HCl + 1 mM $CuCl_2$ solution. Cu deposition took place at potentials more negative than -0.1 V and anodic stripping peaks were observed at +0.01 V and +0.09 V. How the electrodeposition of Cu proceeded was strongly dependent on the structure of the substrate [23]. Typical examples are shown in Figs. 5 and 6. Figure 5 shows a series of AFM images taken (a) before and (b) - (f) during bulk deposition of Cu on a relatively flat surface of p-GaAs(1 00) in 9 mM HCl + 1 mM $CuCl_2$ solution. The potential was stepped from +0.1 V to -0.15 V at the time indicated by a thick arrow in Fig. 5(b). Figure 5(b) clearly shows that immediately after the potential had been stepped to -0. 15 V, a large number of small grains were generated with spacings of several tens of nanometer. These initial deposits of Cu on the surface acted as effective nucleation centers and the initial

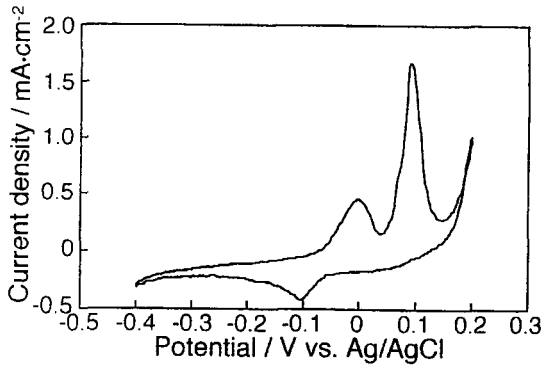

Fig. 4. Cyclic voltammogram of p-GaAs(100) in 9 mM HCl + 1 mM $CuCl_2$.

growth of these grains seemed to be three-dimensional. AFM images were captured continuously at -0. 15 V and are shown in Fig. 5(c) - (e). As time progressed the grains of Cu overlapped with each other and finally truncated pyramidal structures of relatively uniform size were formed (Fig. 5(e)). The potential was pulsed back to +0.1 V, as indicated by a thick arrow in Fig. 5(f). Upon stepping the potential back to +0.1 V, Cu deposits were removed immediately within the time domain of AFM measurement and the surface was returned to a state similar to that before Cu deposition (Fig. 5(f)).

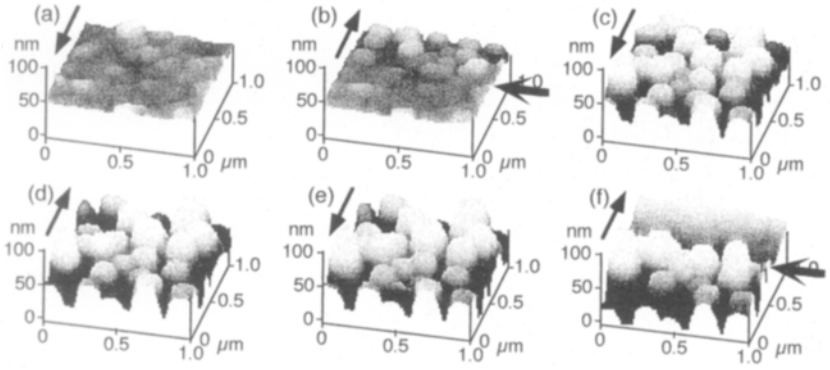

Fig. 5. Sequentially obtained AFM images of p-GaAs in the relatively flat region in 9 mM HCl + 1 mM $CuCl_2$ solution (a) at +0.1 V vs. Ag/AgCl, (b) while the potential was pulsed to -0. 15 V, (c)-(e) at -0. 15 V, and (f) when the potential was taken back to the initial potential (+0.1 V). The time after the application of -0.15 V at the beginning of imaging was (c) 4 s, (d) 12 s, (e) 20 s, and (f) 74 s. Thick arrows indicate the onset of deposition and stripping. Arrows beside the figure indicate the scan direction of the tip.

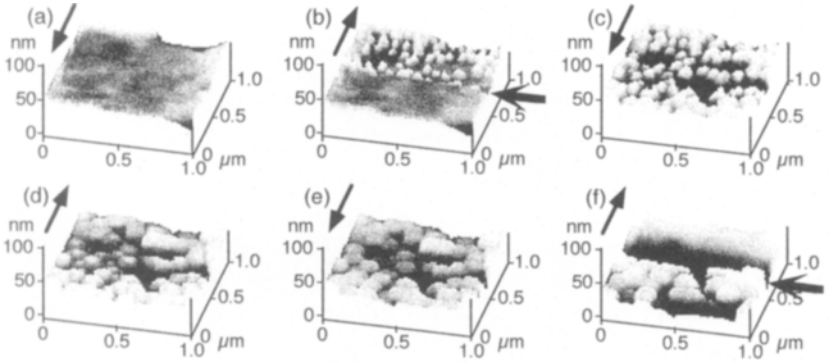

Fig. 6. Sequentially obtained AFM images of a p-GaAs surface with preformed truncated pyramidal structures in 9 mM HCl + 1 mM $CuCl_2$ solution (a) at +0.1 V vs. Ag/AgCl, (b) while the potential was pulsed to -0. 15 V, (c)-(e) at -0. 15 V, and (f) when the potential was taken back to the initial potential (+0.1 V). The time after the application of -0. 15 V at the beginning of imaging was (c) 36 s, (d) 116 s, (e) 196 s, and (f) 204 s. Thick arrows indicate the onset of deposition and stripping. Arrows beside the figure indicate the scan direction of the tip.

When potentials more positive than 0 V were applied to the GaAs electrode in HCl solution, truncated pyramidal structures were formed on the substrate surface as a result of the anodic dissolution of GaAs. Actually, it was hard to obtain an atomically flat surface over a wide range if the electrode was kept in the anodic potential region where no Cu deposition took place. The surface shown in Fig. 5(a) was one of the flattest surfaces observed. To examine the effect of the surface structure on Cu deposition, we also monitored the deposition process of Cu on the surface with the preformed truncated pyramids of relatively uniform size as shown in Fig. 6(a). Totally different time sequences were observed for the electrodeposition of Cu on this surface, as shown in Fig. 6(b) - (e). As soon as the potential had been stepped to the bulk deposition region (-0.15 V), Cu electrochemical deposition occurred along the preformed structure (Fig. 6(b)). Grains observed in Fig. 5 were not seen in this image. The truncated pyramids grew with the progress of deposition, mainly in the height direction.

Figure 7(a) shows AFM images of a Cu deposited surface in 1 mM $CuSO_4$ + 10 mM H_2SO_4 solution. Many Cu islands with relatively uniform size were located on the GaAs surface. High-resolution AFM images on the top of a Cu island and the portion between Cu islands are shown in Fig. 7(b) and (c), respectively [221. Figure 7(b) shows that topmost atoms have a hexagonal structure with a nearest-neighbor distance of 0.26 ± 0.04 nm, which is almost equal to the known lattice constant (0.256 nm) of

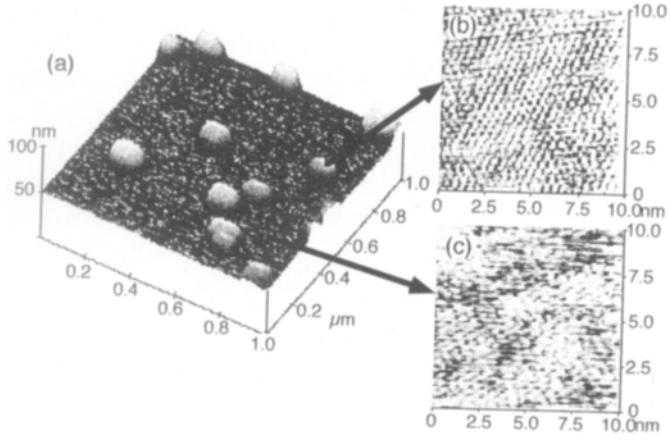

Fig. 7. (a) An AFM image (1 μm x 1 μm) of the surface of Cu islands formed on the p-GaAs(100) surface. Atomically resolved AFM images of (b) the top of a Cu deposit and (c) the portion between the Cu deposits in 1 mM $CuSO_4$ + 10 mM H_2SO_4 solution at -0.2 V vs. Ag/AgCl.

bulk Cu in the (111) basal plane. Thus, Cu deposits seemed to have a closed-packed structure. On the other hand, the atomic arrangement of a square lattice with atomic distance of about 0.4 nm corresponding to the underlying GaAs(100)-(1 x 1) structure was observed in the region between the deposited Cu. The atomic rows of the Cu(111) structure on the top of Cu islands were different from each Cu deposit. These results suggest that bulk Cu deposition on the GaAs surface proceeded without any strong influence of the orientation of the underlying GaAs(100) surface.

3.4 AFM tip-induced modification of GaAs(100) surface structure

The GaAs(100) surface can be modified by an AFM tip if it is scanned with relatively large force (10 nN) in 10 mM H_2SO_4 solution at various electrode potentials [24]. Figure 8 shows a typical AFM image of a p-GaAs(100) surface at an open-circuit potential after the tip was scanned at an open-circuit potential (1 μm x 1 μm) for 30 min in only the x-direction of 500 nm with a scan rate of 25 lines/s. It is clear that there is a wedge in the central part of the image where the tip was initially scanned with a strong force. Figure 9 shows the relation between the electrode potential and the depth of the fabricated wedge. The more positive the potential, the larger the anodic current and the deeper the depth of the wedge structure. However, when the electrode potential became more positive than +0.075 V, the wedge structure was not clearly observed because the dissolution process on the p-GaAs surface proceeded violently and large hill-and-valley structures were formed everywhere on the surface. On the other hand, if the potential was kept in the cathodic range, surface modification did not occur. These results suggest that the formation of wedge structures on the surface requires both the scanning of the tip and the flow of anodic current, i.e., the modification is the result of tip-induced electrochemical etching. The wedge structure was formed even at the open-circuit potential (Fig. 8), because a small anodic current corresponding to GaAs dissolution flowed to compensate the cathodic photocurrent which was generated by laser light used for sensing the deflection of the cantilever.

When Cu was electrochemically deposited onto the GaAs surface part of which was modified by the AFM tip, Cu was deposited selectively on the scratched portion. This result may lead to a novel technique for the submicron fabrication.

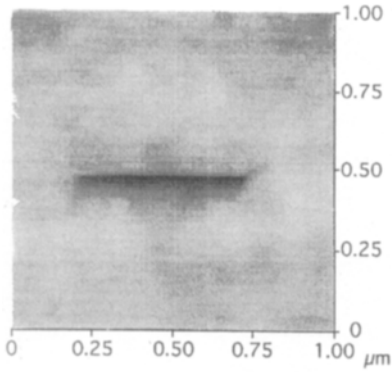

Fig. 8. AFM image (1000 x 1000 nm^2) of a p-GaAs surface in 10 mM H_2SO_4 at the open-circuit potential after only the x-direction had been scanned for 30 min with stronger a force (10 nN).

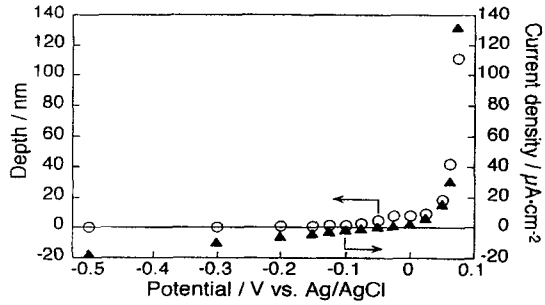

Fig. 9. The mean depth and the steady current as a function of the electrode potential for a p-GaAs electrode in 10 mM H_2SO_4 solution.

4 Conclusion

We have demonstrated here that clean and atomically ordered surfaces of compound semiconductors can be prepared in electrolyte solutions if the surface is properly

treated. This fact should lead to the new development of semiconductor electrochemistry. The discovery of tip-induced etching and selective deposition of Cu on the modified portion should open the way to novel fabrication techniques.

Acknowledgement. We are grateful to Dr. Chevy of Université Pierre et Marie Curie-Paris VI and Mr. H. Fujita of Mitsubishi Chemical Corporation for providing us with InSe and GaAs single crystals, respectively. This work was partially supported by Grant-in-Aids for Scientific Research (04555191) and for Priority Area Research (0545202, 0645202, 0745202, 06239204, 07239024) from the Ministry of Education, Science, Sports and Culture, Japan and by the Kato Science Foundation. M.K. acknowledges the Japan Society for the Promotion of Science for the JSPS Research Fellowships for Young Scientists.

5 References

[1] S.R. Morrison (Ed.), Electrochemistry at Semiconductor and Oxidized Electrodes Plenum Press, New York, 1980.
[2] H. Gerischer, J. Electroanal. Chem. 58, 263 (1975).
[3] A. Damjanovoic, T.H.V. Setty, J. O'M. Bockris, J. Electrochem. Soc. 113, 429 (1966).
[4] M.H.J. Hottenhuis, A.L.M. van den Berg, J. P. van den Eerden, Electrochim. Acta 33, 1519 (1988).
[5] For example, A.A. Gewirth, H. Siegenthaler (Ed.), Nanoscale Probes of the Solid/Liquid Interface, Kluwer Academic Publishers, Dordrecht, 1995.
[6] K. Uosaki, M. Koinuma, Faraday Discuss. 94, 361 (1992).
[7] K. Uosaki, S. Ye, N. Sekine. Bull. Chem. Soc. Jpn. 69, 275 (1996).
[8] J. Camassel, P. Merle, H. Mathieu, A. Chevy, Phys. Rev. B 17, 4718 (1978).
[9] V.N. Katerinchuk, Z. D. Kavalyuk, I. V. Mintyanskii, Sov. Phys. Solid State 25, 94 (1983).
[10] N. Piccioli, R. Le Toullec, F. Bertrand, J. C. Chervin, J. Physique 42, 1129 (1981).
[11] S.M. Atakishiev, G.A. Aknundov, Phys. Stat. Sol. 32, K33 (1969).
[12] P. Carisson, B. Holrnstr6m, K. Uosaki, H. Kita, Appi. Phys. Lett. 53, 965 (1988).
[13] S. Eriksson, P. Carlsson, B. Holmstr6m, K. Uosaki, J. Appl. Phys. 69, 2324 (1991).
[14] K.W. Frese, Jr., M.J. Madou, S.R. Morrison, J. Electrochem. Soc. 128, 1527 (1981).
[15] P. Allongue, H. Cachet, Electrochim. Acta. 33, 9 (1988).
[16] K. Uosaki, Y. Shigematsu, S. Kaneko, H. Kita, J. Phys. Chem. 93, 6521 (1989).
[17] A. Chevy, A. Kuhn, M. S. Martin, J. Crystal Growth 38, 118 (1977).

[18] K. Uosaki, M. Koinuma, J. Electroanal. Chem. 357, 301 (1993).
[19] K. Uosaki, M. Koinuma, Appl. Phys. Lett. 74, 1675 (1993).
[20] V.V. Losev, A.1. Molodov, Encyclopedia of Electrochemistry of the Elements, Vol. VI, A.J. Bard (Ed.), Marcel Dekker, New York, 1975, p. 2.
[21] S.I. Zhdrarov, Encyclopedia of Electrocliemistry of the Elements, Vol. IV, A. J. Bard (Ed.), Marcel Dekker, New York, 1975, p. 352.
[22] M. Koinuma, K. Uosaki, Surf. Sci. Lett. 311, L737 (1994).
[23] J.S. Blakemore, J. Appl. Phys. 53, R123 (1982).
[24] M. Koinuma, K. Uosaki, J. Electroanal. Chem. 409, 45 (1996).
[25] M. Koinuma, K. Uosaki, Electrochem. Acta 40, 1345 (1995).
[26] M. Koinuma, K. Uosaki, Surf. Sci. 358, 565 (1996).

Part VII

Electrochemical Nanotechnology
In-situ Local Probe Techniques at Electrochemical Interfaces
Edited by W. J. Lorenz and W. Plieth

In-situ STM and electrochemical UHV technique: Complementary, Noncompeting Techniques

M.P. Soriaga, K. Itaya, J.L. Stickney

Contents

1	Introduction	268
2	Experimental	268
3	Results and discussion	269
	3.1 Adsorbate-catalyzed dissolution: Pd(111)-($\sqrt{3}$ x $\sqrt{3}$)R30°-I	269
	3.2 Electrochemical atomic layer epitaxy: Se on Au(100)	272
4	Outlook	275
5	References	275

Summary. The development of in-situ scanning tunneling microscopy (STM) has opened new avenues of research in electrochemical surface science. By itself, this nanometer-scale structural tool cannot be regarded as a panacea for the many problems that confront researchers in the interfacial sciences. However, when employed in tandem with other surface-sensitive analytical methods, even exceedingly complex processes can be investigated. Two cases are presented here that showcase the power of in-situ STM coupled with combined electrochemical UHV techniques.

1 Introduction

The invention of the scanning tunneling microscope (STM) [1], and the developmental work [2] that ensued to adapt the technique in the study of the electrode-electrolyte interface under reaction conditions, have provided significant advances in the area of

electrochemical surface science. While such advances may tempt a few to regard the combination of STM and electrochemical STM as the panacea to the myriad problems in interfacial electrochemical science, it need only be stated that the utter complexity of heterogeneous processes cannot be unraveled by just one technique. The true strength of electrochemical STM lies in its integration with other surfacesensitive analytical methods such as those that permit the determination of other critical interfacial parameters such as composition and electronic structure; one such approach is the combination of electrochemical STM with tandem electrochemical UHV technique [3].

In this paper, two studies are presented to showcase the power of UHV-electrochemical STM. The first illustration involves the dissolution of Pd that occurs only when a monolayer of iodine was present on the surface [4]. The structural features of the halogen-metal interface that accompany the adsorbate-catalyzed corrosion were first explored with low-energy electron diffraction (LEED); initial- and final-state structures were readily determined. However, questions such as the mechanism for dissolution required an in-situ technique for answers; it was in this regard that electrochemical STM work was pursued [5].

The second example involves the surface chemistry of the compound semiconductor CdSe synthesized epitaxially on Au(100) by underpotential deposition (UPD). By analogy with the gas-phase epitaxial deposition procedure, this UPD-based method has been dubbed electrochemical atomic layer epitaxy (ECALE) [6]. Unique information on the interfacial structure of the first adlayer of Se electrodeposited was revealed by STM experiments.

2 Experimental

The experimental procedures unique to the electrochemical UHV technique [4, 6] and electrochemical STM [5] investigations have been described in detail elsewhere. electrochemical UHV technique work with Pd employed a commercially oriented and metallographically polished, 99.9999%-pure Pd(lll) single-crystal electrode; electrochemical STM studies were done with Pd(lll) single-crystal surfaces prepared by the Clavilier method, originally developed for Pt(lll) surfaces [7]. For the ECALE work, an oriented and polished Au single-crystal electrode was employed. Commercial instruments were used in the electrochemical UHV technique (Perkin-Elmer, Eden Prairie, MN) and electrochemical STM (Digital Instruments, Santa Barbara, CA) investigations.

3 Results and Discussion

3.1 Adsorbate-catalyzed dissolution: Pd(lll)-($\sqrt{3}$ x $\sqrt{3}$)R30°-I

Figure 1 shows the current-potential curve for a clean and an iodine-coated Pd(lll) facet, formed on a single-crystal bead, in halide-free 0.05 M H_2SO_4. The exceedingly large anodic peak at about 1.2 V represents the $Pd^{o}_{(s)}$-to-$Pd^{2+}_{(aq)}$ anodic stripping that occurs only when interfacial iodine is present [4, 5].

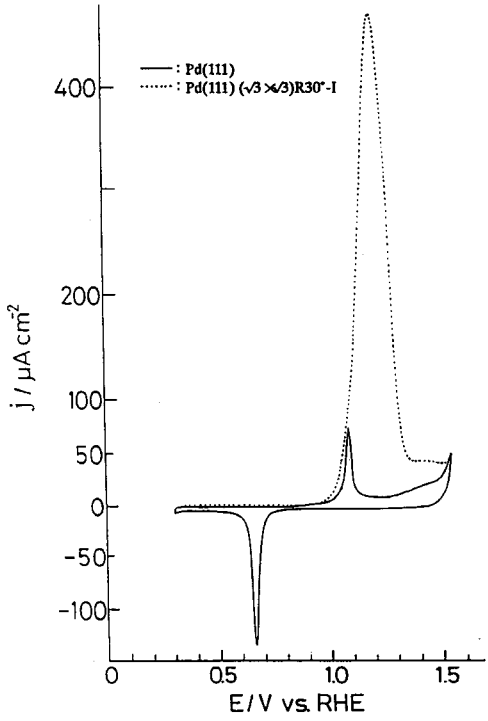

Fig. 1. Current density vs. potential curves in the surface-oxidation region in 0.05 M H_2SO_4 for a Pd(lll) facet on a single-crystal bead, clean (solid curve) and I-coated (broken curve). Potential sweep rate, r = 10 mV s-1.

It is important to mention that, if the potential is held just below 1.2 V, the current, as expected from a material-limited dissolution process, does not decay but remains constant.

Figure 2 shows photographs of LEED patterns for Pd(lll)-($\sqrt{3}$ x $\sqrt{3}$)R30°-I prior to and after removal of about 30 monolayers of Pd surface atoms. In this experiment, the potential was held close to but not past the anodic dissolution peak; that is, the dissolution was carried out at a fairly high rate. The LEED data clearly show that the post corrosion I-coated Pd surfaces remained as well-ordered as they were prior to the dissolution reaction. A layer-by-layer dissolution process is thus suggested. The LEED results, however, do not provide information on whether the corrosion transpires at steps or via place-exchange between the I and Pd atoms. For such information, in-situ STM experiments were invoked.

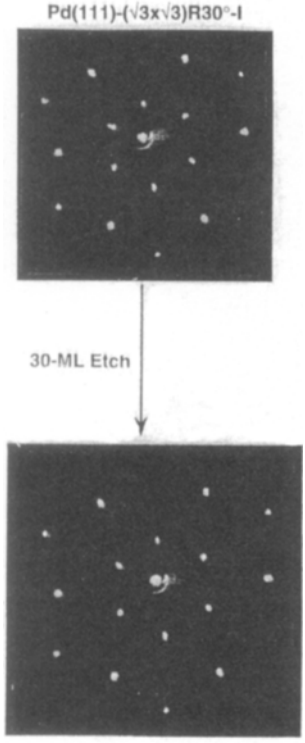

Fig. 2. Low-energy electron diffraction (LEED) patterns for Pd(111)-($\sqrt{3}$x$\sqrt{3}$)R30°-I adlattices before and after anodic dissolution of approx. 30 monolayers of Pd surface atoms. Beam energy = 60 eV; beam current = 2μA.

Figure 3 shows typical electrochemical STM images of Pd(111)-($\sqrt{3}$x$\sqrt{3}$)R30°-I before and after the I-catalyzed dissolution; provides evidence for the well-ordered Pd(111)-($\sqrt{3}$x$\sqrt{3}$)R30°-I structure at the terrace was obtained in a separate electrochemical STM requiment. In this experiment, a scratch on the surface was

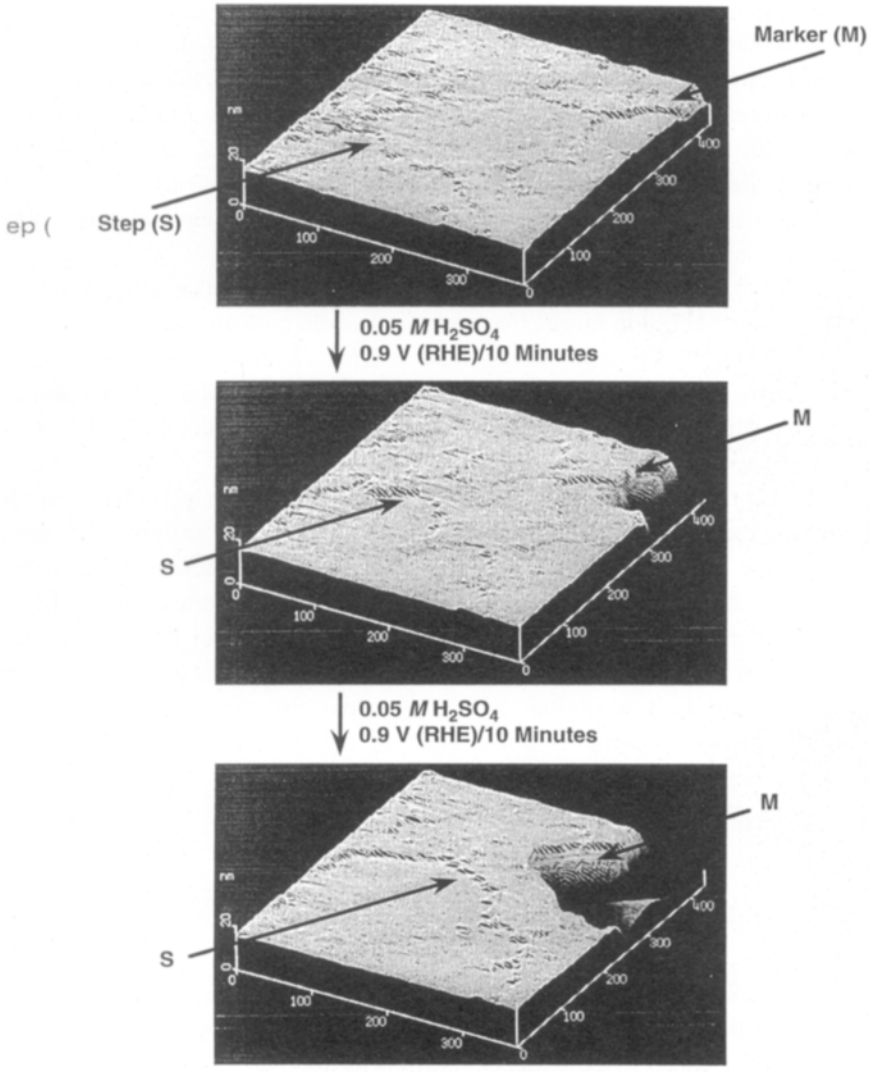

Fig. 3. In-situ scanning tunneling microscope images of a Pd(111)-($\sqrt{3}$x$\sqrt{3}$)R30°-I facet on a single-crystal bead at various stages of adsorbate-catalyzed dissolution. M, marker; S, step.

a marker (M) to ensure that the STM scans are always done at the same area of the corroded surface. The top photograph was obtained prior to dissolution; the step, monatomic and diatomic in height, that was monitored during the dissolution process is marked S. The middle photograph was taken after 10 min of mild oxidative dissolution at 0.9 V, a potential at the foot of the anodic stripping peak. In this image, it can be seen that: (i) the step has moved towards the marker, and (ii) an enlarged smooth terrace has been formed. The bottom image was obtained after another 10 minutes of additional dissolution. It is more evident here that not only has the step progressed further towards the marker but also that the area of the atomically smooth terrace has become much larger. The formation of wide-area smooth terraces is in agreement with the sharp LEED patterns shown in Fig. 2 after dissolution of multilayers of Pd surface atoms. The STM images in Fig. 3 clearly demonstrate: (i) layer-by-layer dissolution, and (ii) selective corrosion at the steps, at least under the present conditions of mild dissolution.

It is difficult to obtain reliable electrochemical STM information at high dissolution rates; hence, the dissolution mechanism near the anodic peak has not been determined. As noted earlier, LEED experiments were carried out near the anodic peak; the possibility exists that place-exchange between the iodine and Pd interfacial atoms may transpire at such high dissolution rates, yet result in an ordered final state upon emersion.

The STM result that dissolution of Pd atoms occurs selectively at step (disordered) sites provided the impetus for an additional study which demonstrated that the $I_{(ads)}$-catalyzed anodic dissolution process is able to regenerate an ordered Pd(111) surface from one that had been subjected to extensive Ar^+-ion bombardment [8]. This particular reordering reaction is unique because it occurs (i) in the absence of bulk corrosive reagent, and (ii) only if a chemisorbed layer of iodine is present. This process may be viewed similarly to digital etching [9] under electrochemical conditions [10] except that (a) bulk material is not needed to replenish the adsorbed iodine that activates the surface, and (b) the dissolution process does not cease even after the atomically smooth surface has been regenerated.

3.2 Electrochemical Atomic Layer Epitaxy: Se on Au(100)

In the formation of the compound semiconductor CdSe on Au(100) by ECALE [6] the chalcogenide is the choice for the first atomic layer due to its increased stability after loss of potential control. If Cd is deposited first, it undergoes partial but spontaneous oxidation by residual oxygen gas; in the presence of an Se adlayer, no such Cd oxidation occurs as it is now stabilized by compound formation with Se.

On Au(100), Se is cathodically deposited, from a $HSeO_3^-$ solution in, different atomic layer structures depending upon the duration and potential of electrodeposition. The structures formed were: Au(100)-p(2x2)-Se at a coverage Θ ($\equiv$ Se atoms/Au atoms) of 0.2, Au(100)-(2 x $\sqrt{10}$)-Se at Θ = 0.3, Au(100)-c(2 x 2)-Se at Θ = 0.5, and Au(100)-(3 x $\sqrt{10}$)Se at Θ = 0.9 [61. The LEED patterns for the Au(100)-c(2 x 2)-Se and Au(100)-(2x$\sqrt{10}$)-Se and adlattices are shown in Figs. 4(A) and 4(B), respectively.

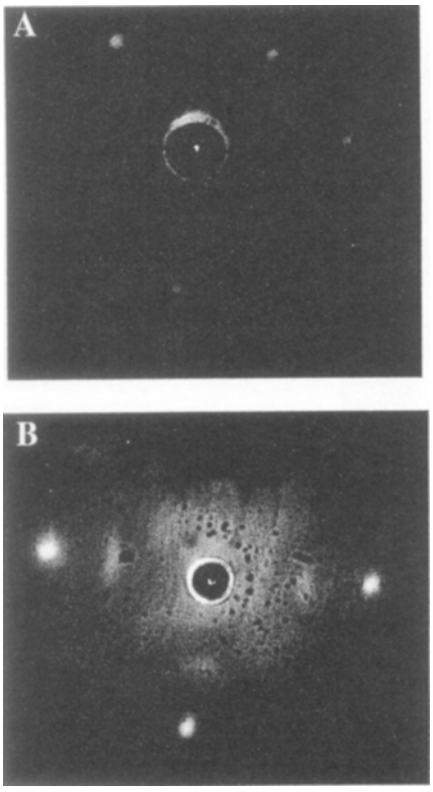

Fig. 4. Low-energy electron diffraction (LEED) patterns. Top, Au(100)-c(2 x 2)-Se at Θ = 0.5; bottom, Au(100)-(3 x $\sqrt{10}$)-Se at Θ = 0.9. Beam energy = 62 eV; beam current = 2 μA.

Although the two-dimensional adlayer symmetries can quite readily be deduced from the LEED patterns, no information can be obtained on the chemical nature of the

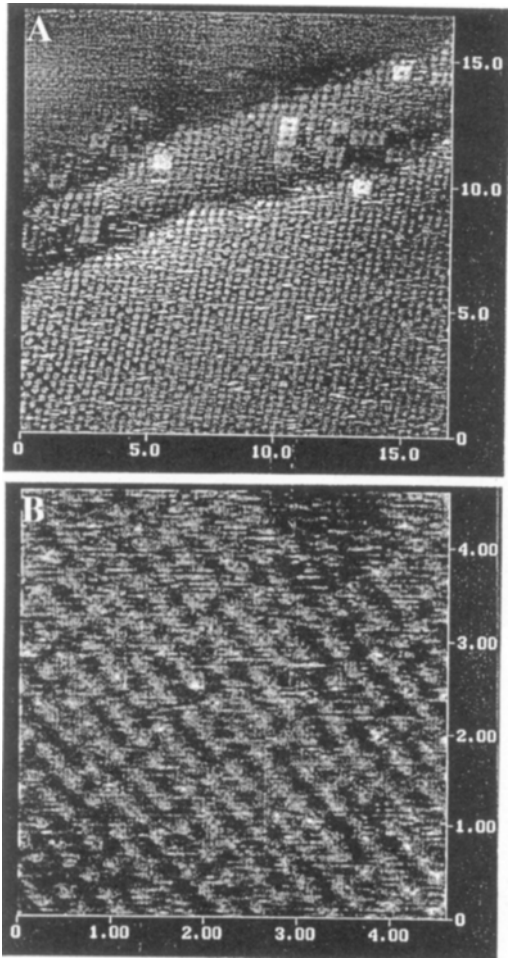

Fig. 5. Scanning tunneling microscope images. Top, Au(100)-c(2x2)-Se at 0 = 0.5; bottom, Au(100)-(3 x $\sqrt{10}$)-Se at $\Theta = 0.9$.

adlayer unless dynamical LEED simulations are performed [11]. The inclusion of STM in the arsenal of surface structural tools often negates the requirement of such LEED simulations. This is clearly illustrated in Figs. 5(A) and 5(B) which, respectively, show the evolution of Se_8 rings as the coverage is increased from just above 0.5 to 0.9. Coincident with the development of the Se_8 rings was the formation on the surface of pits, a random occurrence that can be revealed only by STM experiments. Quantitative

analysis of the STM images suggested that the pits (i) were monatomic in depth and, (ii) contained the same Se_8 ring structure at the bottom. The coverage of the pits accounts for about 10% of the total surface area at high Se coverages. Pit formation is discussed in greater detail elsewhere [6].

4 Outlook

Among the many advantages of STM, two are most prominent in the cases described here: (i) its adaptability for measurements under reaction conditions, and (ii) its ability to resolve localized nanometer-scale structural features. Based upon these two advantages alone, it is not difficult to comprehend why STM has already become a pillar among the many powerful techniques employed in surface science. On the other hand, its inability to probe surface energetics, composition, and electronic structure will always require additional surface spectroscopic techniques if a more complete understanding of complex heterogeneous processes is desired. A strategy that combines in-situ STM with electrochemical UHV technique may be compelling since it bridges the gaps inherent in the separate techniques.

Acknowledments. MPS wishes to acknowledge the National Science Foundation and the Robert A. Welch Foundation. KI thanks the Ministry of Education, Science, and Culture, Japan and the ERATO-Itaya Electrochemiscopy Project, JRDC. JLS acknowledges the support of the National Science Foundation and the Office of Naval Research.

5 References

[1] (a) G. Binnig, H. Rohrer, C. Cerber, E. Weibel, Phys. Rev. Lett. 50, 120 (1983); (b)G. Binnig, H. Rohrer, Surf. Sci. 157, L373 (1985).

[2] (a) M.M. Dvek, M.J. Heben, N.S. Lewis, R.M. Penner, C.F. Quate, in: Electrochemical Surface Science, M.P. Soriaga (Ed.), American Chemical Society, Washington, DC 1988; (b) A.J. Bard, H.D. Abruña, C.E. Chidsey, L.R. Faulkner, S. Feldberg, K. Itaya, 0. Melroy, R.W. Murray, M.D. Porter, M.P. Soriaga, H.S. White, J. Phys. Chem. 97, 7147 (1993); (c) K. Itaya, in: The Handbook of Surface Imaging and Visualization, A. T. Hubbard (Ed.) CRC Press, Boca Raton, FL 1995.

[3] M. P. Soriaga, Prog. Surf. Sci. 39, 525 (1992).

[4] (a) J R. McBride, M.P. Soriaga, J. Electroanal. Chem. 303, 255 (1989); (b) J.R. McBride, J.A. Schimpf, M.P. Soriaga, J. Am. Chem. Soc. 114, 10950 (1992).

[5] M.P. Soriaga, J.A. Schimpf, J.B. Abreu, A. Carrasquillo, W. Temesghen, R. J. Barriga, J.-J. Jeng, K. Sashikata, K. Itaya, Surf. Sci. 335, 273 (1995).
[6] H.M. Baoming, T.E. Lister, J.L. Stickney, in: The Handbook of Surface Imaging and Visualization, A.T. Hubbard (Ed.), CRC Press, Boca Raton, FL, 1995.
[7] J. Clavilier, J. Electroanal. Chem. 107, 211 (1980).
[8] (a) J.B. Abreu, R.J. Barriga, W. Temesghen, J.A. Schimpf, M.P. Soriaga, J.Electroanal.Chem. 381, 239 (1995); (b) J.A. Schimpf, A. Carrasquillo, M.P. Soriaga, Electrochim. Acta. 40, 1203 (1995).
[9] (a) T.Meguro, M. Hamagaki, S. Modaressi, T. Hara, Y. Aoyagi, M. Ishii, Y. Yamamoto, Appl. Phys. Lett. 56, 1552 (1990); (b) P.A. Maki, D.J. Ehrlich, Appl. Phys. Lett. 55, 91 (1989).
[10] Q.P. Lei, J.L. Stickney, Mat. Res. Soc. Symp. Proc. 237, 336 (1992).
[11] G.A. Somorjai, Surfaces: Chemistry in Two Dimensions, Cornell UniversityPress, Ithaca, NY, 1981.

Electrochemical Nanotechnology
In-situ Local Probe Techniques at Electrochemical Interfaces
Edited by W. J. Lorenz and W. Plieth

Growth morphology and molecular orientation of additives in electrocrystallization studied by surface-enhanced Raman spectroscopy

B. Reents, W. Plieth

Contents

1	Introduction		277
2	Experimental		278
3	Results		279
4	Discussion		285
	4.1	General properties of Raman spectra of silver cyanide complexes	285
	4.2	Development of the CN^- SER signal with time	286
	4.3	Splitting of the CN^- stretch vibration	288
5	Conclusions		288
6	References		289

Summary. Surface-enhanced Raman spectrsocopy (SERS) can be used as an in-situ method for monitoring the development of surface morphology, nucleus formation, and crystal growth. The correlation between the true surface area and the Raman intensity was investigated. The splitting of the CN stretch vibration is interpreted as a representation of a surface cluster distribution.

1 Introduction

In order to obtain information about the process of crystal formation and growth, a variety of in-situ and ex-situ methods, such as chronoamperometry, impedance

spectroscopy, reflectance electron microscopy (REM), or transmission electron microscopy (TEM), has been used. A great step forward was the application of in-situ scanning tunneling microscopy, STM, to observe the surface during the growth process (see other chapters in this book). Recently we pointed out the possibility of using surface-enhanced Raman spectroscopy (SERS) as a sensitive tool for in-situ monitoring of electrochemical deposition.

One can follow the electrodeposition of SER-active metals by the development of vibrational bands of the surface-active components. Using chronocoulometry and semiempirical theories of nucleation it is possible to determine the kinetic parameters of nucleation and to compare this information about micro- and submicrostructures of a growing surface layer with the Raman intensities. This comparison shows that the SERS intensity is related to the surface structure. The method has been further developed for in-situ monitoring of electrocrystallization, mainly of silver [1].

Using the double-pulse method for the electrodeposition process [2], the kwon SERS signal of adsorbed cyanide ions at 2110 cm^{-1} showed a splitting into different bands; first results were reported in [3]. A tentative explanation was given by the assumption of formation of different sizes of clusters with different SER frequencies of the adsorbed ions.

In this report we show in more detail correlation between the intensity of the Raman signal and the developing surface morphology. We show SER spectra of adsorbted cyanide ions during the electrocrystallization and crystal growth in comparison with in-situ capacity measurements representing the „true area" of a growing surface. Furthermore, we present more results of the observed splitting of the CN^- band on an Ag surface and discuss in greater detail the explanation of this splitting. The purpose of this contribution to the monograph is to give an example of the way in which other methods such as surface-enhanced Raman spectroscopy might complement the results of STM in studying the electrocrystallization process. In-situ surface-enhanced Raman spectroscopy was chosen because it adds the power of vibrational spectrscopy to the geometrical results of STM.

2 Experimental

The measurements were performed with an usual setup for surface-enhanced Raman spectroscopy: The Raman spectra were measured with a Spex 1406 spectrometer, the samples were illuminated with a Spectroscopy Instruments argon ion laser (λ = 514 nm, 30 mW) and the spectra were detected by a Princeton Instruments optical multichannel analyzer under computer control. All experiments were performed in an electrochemical cell containing an inert platinum working electrode mechanically

polished with diamond paste down to 0.25 μm, a counter electrode of platinum and a saturated calomel reference electrode. A standard silver cyanide bath was used with the concentrations represented in Table 1.

Tabl. 1: Electrolytes and concentrations.

Electrolyte	c [mol l^{-1}]		
	KCN	$AgNO_3$	KNO_3
I	0.027	0.001	0.36
II	0.027	0.002	0.36
III	0.027	0.003	0.36

The electrolyte consisted of p.a. chemicals and was deaerated by a nitrogen stream, the temperature being kept at approximately 23°C. Electrochemical results could be stored digitally by using a galvanostat/potentiostat (HEKA Electronics) under computer control, connected by an IEEE interface to a personal computer. The capacity measurements were performed with an impedance workstation (Zahner). All potentials are quoted against the saturated calomel electrode (SCE).

3 Results

The classical procedure for the activation of an electrode surface is to obtain a surface roughness by cycles of oxydation and reduction. This type of activation is easy to apply but does not give an opportunity to produce well-defined surfaces, whereas deposition of an SERS-active metal on an inert electrode offers the possibility of achieving the enhancement effect as well as controlling the surface structure. Some potential programs useful for the activation of the electrode surface are depicted in Fig. 1.

For the standard silver cyanide bath we obtained the activation by switching the potential from 0 V to a potential, in general -800 mV, where reduction of silver occured. After a couple of seconds an SER signal was observed, increasing in intensity within the following minutes. In general a braod maximum was obtained at a wavenumber of 2110 cm^{-1} (see Fig. 2). It was shown that the development of the Raman signal is connected with the development of the morphology of the surface, mainly depending on the initial state represented by the number of active sites and nuclei formed [1].

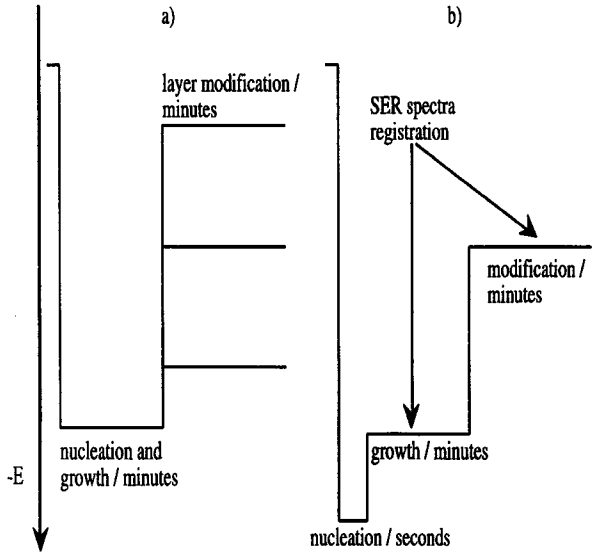

Fig. 1. Potential pulse programs used for SERS activation of the electrode by SER-active metal deposition on platinum.

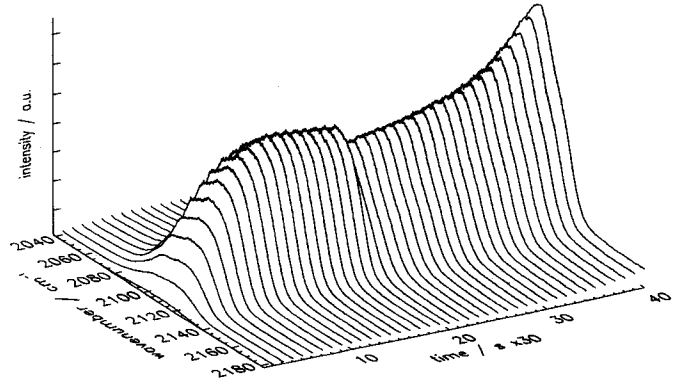

Fig. 2. Development of the SER signal of the CN stretch vibration during silver deposition on platinum, electrolyte III.

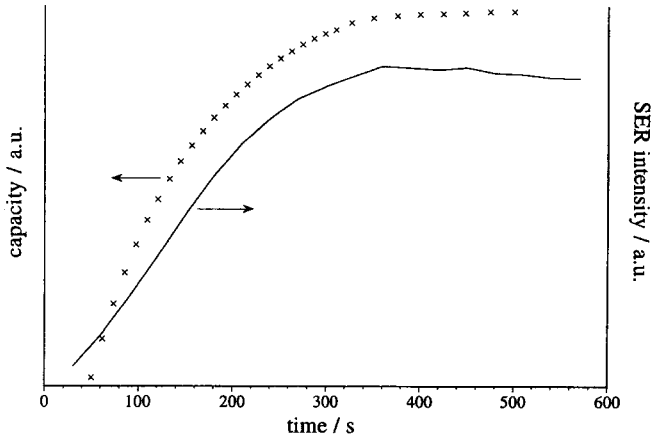

Fig. 3. Development of the double-layer capacity and the SER intensity of adsorbed cyanide ions during silver deposition on platinum, electrolyte III, E = 800 mV_{SCE}.

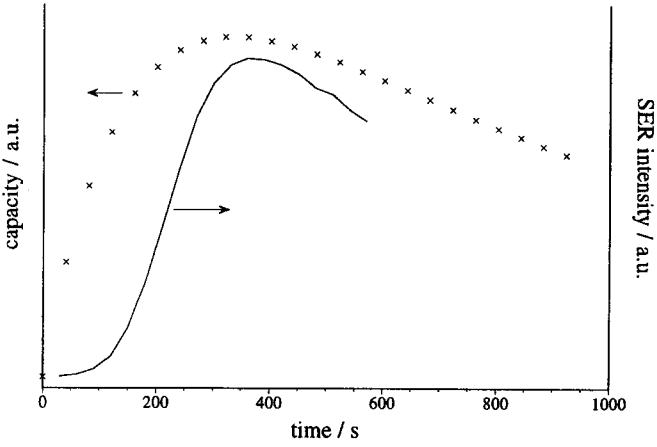

Fig. 4. Development of the double-layer capacity and the SER intensity of adsorbed cyanide ions during silver deposition on platinum, electrolyte II, E = 800 mV_{SCE}.

A comparison of the development of the SER intensity with the changes of the true surface area, represented by the double-layer capacity, is shown in Figs. 3 and 4. The two examples measured under similar conditions demonstrate the scattering of the general shape of Raman-time and capacitance-time plots. The good correlation in the shape of the curves found in the experiments leads to the assumption of a proportionality relation between the SER intensity and the „true area" of the surface.

Using the potential program described in Fig. 1(b) results in a splitting of the CN^--stretch vibration of the broad cyanide peak into a large number of single peaks, shown in Fig. 5.

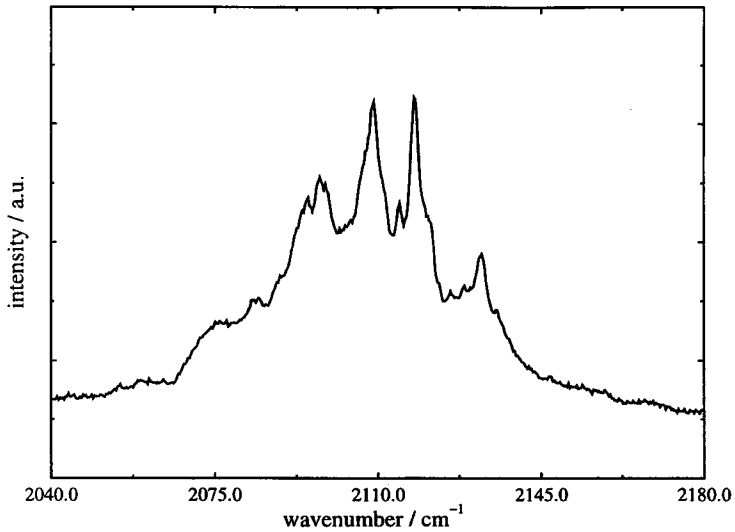

Fig. 5. SER spectrum of the CN^- stretch vibration after silver deposition on platinum obtained by applying the potential pulse programming of Fig. 1(b) electrolyte I.

This splitting of the SER signal depends mainly on the pretreatment of the inert platinum electrode and on the type of activation. The optimal conditions to observe the splitting are not yet completely known but, for all cases, a single nucleation pulse in the higher cathodic regions for a short time followed by a potential where only deposition takes place is a useful procedure. The splitting was detected not only at the beginning of the film formation but could be observed during the whole time of growth; see Fig. 6. in order to elucidate the conditions for the observed splitting we varied both the

nucleation time t_N and concentration of the silver ions c_{Ag}^{+}; two examples are shown in Figs. 7 and 8.

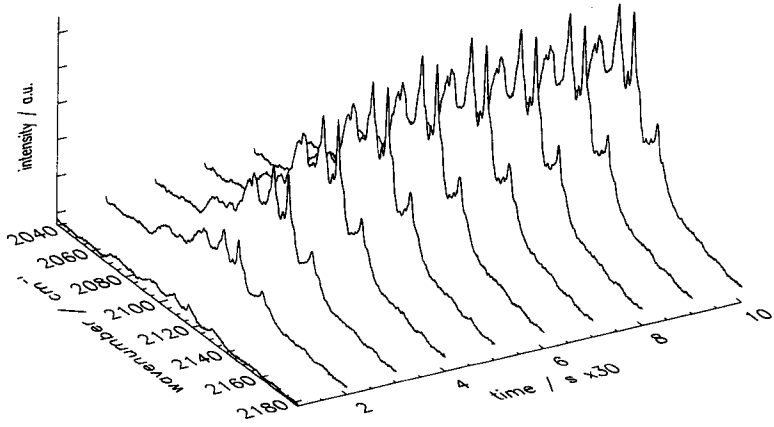

Fig. 6. SER spectra of the CN^- stretch vibration during silver deposition on platinum obtained by applying the potential pulse programming of Fig. 1(b), electrolyte I.

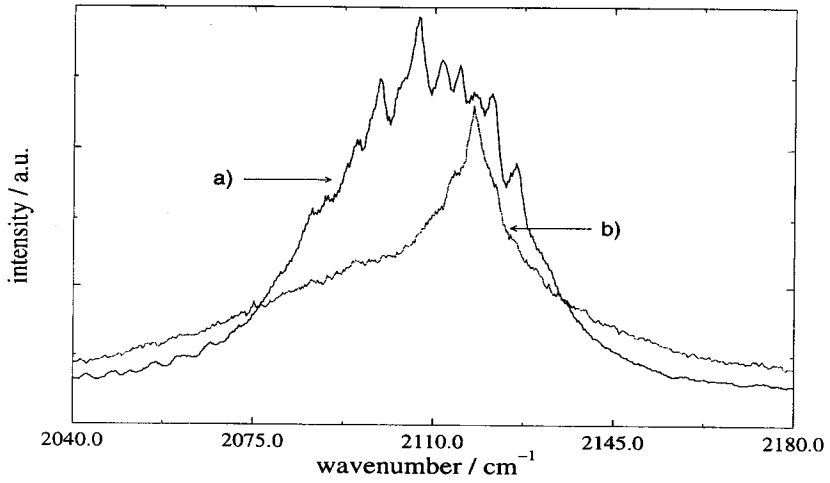

Fig. 7. SER spectra of the CN^- stretch vibration for different durations t_N of the nucleation pulse (electrolyte II): (a) $t_N = 3$ s; (b) $t_N = 7$ s.

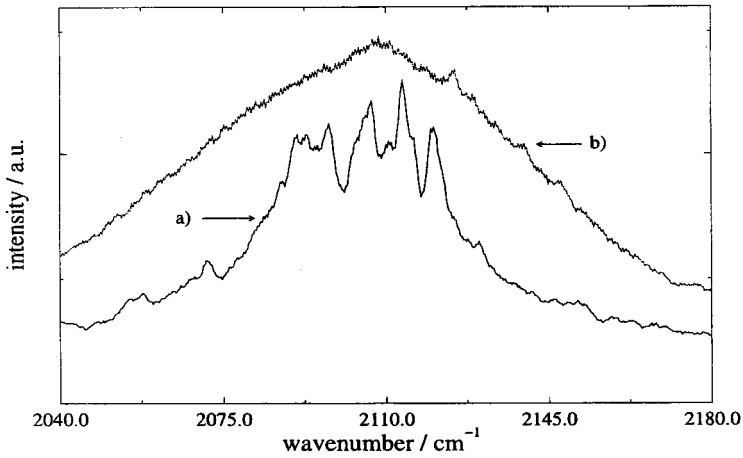

Fig. 8. SER spectra of the CN^- stretch vibration for different silver concentrations (t_N = 3 s): (a) electrolyte I; (b) electrolyte III.

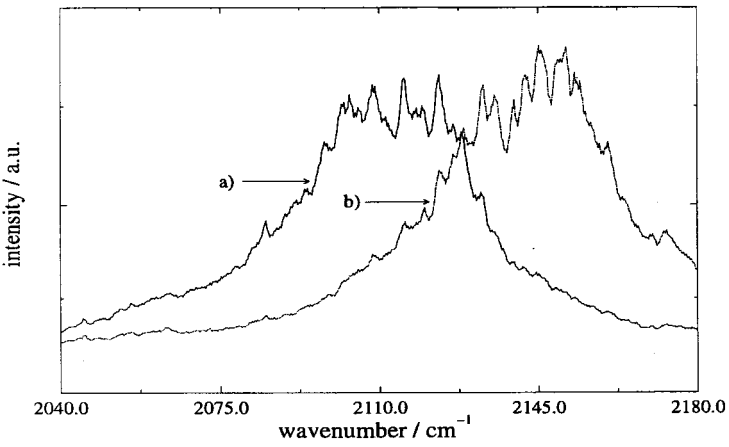

Fig. 9. SER spectra measured at (a) -700 mV and (b) 0 mV: shift from 2110 cm^{-1}; t_N = 1 s, electrolyte III.

Another example of this unusual behavior is shown in Fig. 9. The splitting could be conserved during the shift of the broad CN^{-1} signal from 2110 cm^{-1} to 2145 cm^{-1} evoked by a potential shift from -700 mV to 0 mV.

4 Discussion

4.1 General properties of Raman spectra of silver cyanide complexes

The chemistry of the silver cyanide bath is determined by a variety of silver cyanide complexes existing in the solution. The following equilibria for 25°C, are known in the literature [4, 5]:

$$Ag^+ + CN^- \leftrightarrow Ag(CN) \qquad K = 1.23 \times 10^{15}\ l^2\ mol^{-2}$$
$$Ag^+ + 2\,CN^- \leftrightarrow Ag(CN)_2^- \qquad K = 5.0 \times 10^{20}\ l^2\ mol^{-2}$$
$$Ag(CN)_2^- + CN^- \leftrightarrow Ag(CN)_3^{2-} \qquad K = 7.0\ l\ mol^{-1}$$
$$Ag(CN)_3^{2-} + CN^- \leftrightarrow Ag(CN)_4^{3-} \qquad K = 1.7\ l\ mol^{-1}$$

From these complexes Ag(CN) exists as a white precipitate which dissolves into one of the soluble complexes in the presence of an excess of cyanide. All these complexes are supposed to exist on the surface. The formation potentials of the complexes are the following [4]:

$$Ag(CN) + e^- \rightarrow Ag + CN^- \qquad E_{0(SCE)} = -0.266\ V$$
$$Ag(CN)_2^- + e^- \rightarrow Ag + 2\,CN^- \qquad E_{0(SCE)} = -0.56\ V$$
$$Ag(CN)_3^{2-} + e^- \rightarrow Ag + 3\,CN^- \qquad E_{0(SCE)} = -0.75\ V$$

In principle it is possible to identify the complexes from their Raman spectra, as the cyanide group shows a characteristic vibrational band shifting to higher wavenumbers with increasing number of ligends. The following wavenumbers are knwon [6]:

$$\nu_{AgCN} = 2167\ cm^{-1} \qquad \nu_{Ag(CN)_3^{2-}} = 2111\ cm^{-1}$$
$$\nu_{Ag(CN)_2^-} = 2143\ cm^{-1} \qquad \nu_{Ag(CN)_4^{3-}} = 2097\ cm^{-1}$$

From the Raman spectra obtained it is assumed in the literatur [7] that under the conditions described for the silver deposition, $Ag(CN)_3^{2-}$ is the predominant complex at a potential of -800 mV_{SCE} on the surface, and $Ag(CN)_2^-$ at a potential greater than -250 mV_{SCE}.

4.2 Development of the CN^- SER signal with time

According to the theory of Raman enhancement by small metal particles, the Raman intensity of the CN^- stretch vibration is determined by the size und number of particles (nuclei) and by the surface coverage by CN^- ions on these particles. The results observed by SERS as depicted in Fig. 2 reflect the development of the crystalline structure of the silver layer on the metal surface: the adsorption of CN^- ions is approximately constant for a given area. The change in the SER intensity could be explained by a change in the true area of the surface. Taking the double-layer capacity as a scale for the true area, the results shown in Figs. 3 and 4 admit the conclusion that the development of the signal intensity mainly depends on the development of the surface area during the deposition [1, 8]. Otherwise, the Raman enhancement is connected with a special microstrucure of the surface. One can conclude from the results of Fig. 3 that this microstructure must be established before the growth process starts. The result of Fig. 4 is that the development of the microstructure and the increase of the „true" surface area might not be simultaneous in this experiment. Both examples are shown in order to demonstrate the complex nature of electrocrystallization.

4.3 Splitting of the CN^- stretch vibration

An explanation might be related to the formation of surface clusters of different sizes, e.g., Ag_n with n = 4,5,6...etc. In [3] we pointed out the influence of different cluster sizes on the stretch vibration, discussing the influence of an increasing weight of the Ag_n particles.

We considered the influence of the mass on the Ag_nC group using the normal-coordinate analysis. The results of these calculations indicated that an Ag mass increase from n = 1 to n = 4 only caused a shift of the CN^- stretching of about 2 cm^{-1}. The computed wavenumber shifts for n to n + 1 decreased drastically for n > 4. Therefore this simple explanation obviously failed.

Furthermore we discussed the possibility that the observed splitting of the CN^- vibrations resulted from differences in the density of charge in respect to a variety of silver cyanide complexes. In an early paper Otto et al. [7] explained the trend

ν_{CN^-}	<	$\nu_{Ag(CN)_4^{3-}}$	<	$\nu_{Ag(CN)_3^{2-}}$	<	$\nu_{Ag(CN)_2^-}$	<	$\nu_{Ag(CN)}$
2080 cm^{-1}		2097 cm^{-1}		2111 cm^{-1}		2143 cm^{-1}		2167 cm^{-1}

by changes in the bonding between silver and the ligands. In analogy to that paper we tentatively suggested the following explanation for the observed splitting of the SER signal: assuming that an increase of n in the $Ag_n(CN)_3^{2-}$ clusters effects a change in the density of charge, and moreover that this change influences the bonding between silver and the ligands, we suggested that with increasing mass of silver the average bond order between silver and the CN^- ions via the 5σ orbital increases. Thus the ligand stretch vibration should appear at higher frequencies, since the 5σ orbital is a bonding orbital between silver and the ligands but antibonding with respect to the intraligand bonding [3].

The earlier attempt to explain the splitting did not take into account the results shown in Fig. 9, i.e., the jump of spectral structure with the potential from peaks around ν = 2111 cm^{-1} (-700 mV_{SCE}) to ν = 2143 cm^{-1} (0 mV_{SCE}). This behavior is more reminiscent of an adsorption of the complex $Ag(CN)_3^{2-}$ (ν = 2111 cm^{-1}) changing with the potential to the complex $Ag(CN)_2^-$ (ν = 2143 cm^{-1}). That means we have to discuss the adsorption of $Ag_{ad}(CN)_x^{1-x}$ complexes on clusters of different size (Ag_n - $Ag_{ad}(CN)_x^{1-x}$). The splitting of the CN^- Raman signal must then be correlated with a change of the charge on the complexed Ag_{ad} atom with the size of the cluster Ag_n to which the Ag_{ad} atom is bound. The partial charge of the Ag_{ad} atom could be estimated from the width of the splitting:

For -700 mV_{SCE} 2080 - 2140 cm^{-1}

For 0 mV_{SCE} 2110 - 2175 cm^{-1}

by comparing the frequencies with the values for the complex ions in solution. This is carried out in the next section.

If one assumes a linear change of the frequency of the CN^- strech vibration with the value of the partial charge per CN^- ion, we obtain Fig. 10. The frequencies of AgCN and free CN^- were excluded because the frequency of AgCN was measured in the solid state and that of CN^- lacks the influence of Ag. As indicated in Fig. 10, one gets a $\delta+$ for the Ag_{ad} atom per CN^- ligand of 0.16 - 0.47 at the potential -700 mV_{SCE} and 0.32 - 0.68 at 0 mV_{SCE}. Then the variation of the average of the (positive) charge on the Ag_{ad}

atom is obtained by multiplying the δ+ value for -700 mV_{SCE} by the factor 3 and that for 0 mV_{SCE} by the factor 2. This gives $Ag_{ad}^{0.48}$ - $Ag_{ad}^{1.41}$ at -700 mV_{SCE} respectively

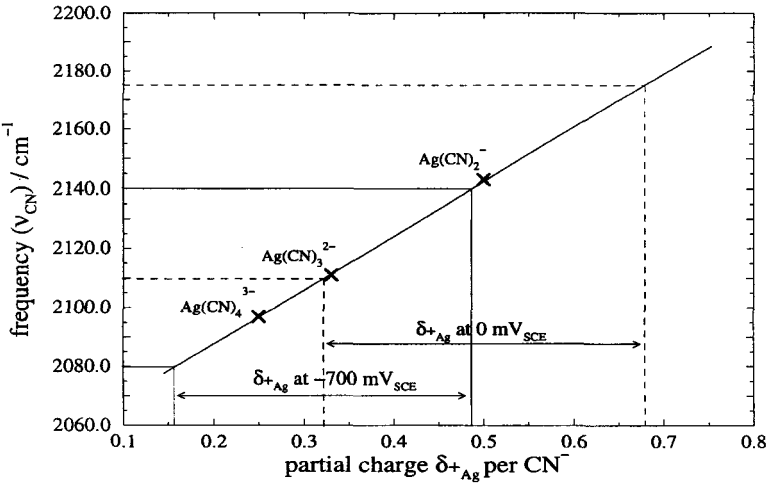

Fig. 10. Relation between the frequency of the CN^- stretch vibration in the different $Ag(CN)_x^{1-x}$ complexes and the partial (positive) charge per CN^- ligand; ν_{AgCN} and ν_{CN^-} were excluded.

$Ag_{ad}^{0.64}$ - $Ag_{ad}^{1.36}$ at 0 mV_{SCE} depending on the size of the cluster Ag_n to which the Ag_{ad} atom is bound. This variation of the positive charge on the Ag_{ad} atom would be an explanation for the appearance of the observed splitting of the C≡N stretch vibration.

5 Conclusions

The experiments described in this paper demonstrate the possibility of using SERS as a sensitive tool for in-situ monitoring and investigation of the electrocrystallization process of the active metals in parallel with other methods of investigation. The Raman signal can be followed to obtain information about the development of the real surface area and about the long-term stability of the growth conditions and the surface concentration of the molecular group followed by the SER signal. With a variation in the conditions for nucleus formation, more detailed results can be obtained reaching a molecular level in the analysis of metal-film formation. It is of special importance that

the Raman method gives valuable complementary information if compared to methods giving geometric information, such as STM or X-ray diffraction. Therefore this method in combination with the new in-situ methods will reveal more details of the picture of the electrocrystallization process then microscopy alone.

Acknowledments. We appreciate the financial support of the Deutsche Forschungsgemeinschaft.

6 References

[1] G. Lacconi, B. Reents, W. Plieth, J. Electroanal. Chem. 325, 207-217 (1992).
[2] M Milchev, E. Vassileva, V. Kertov, J. Electroanal. Chem. 107, 323 (1980).
[3] B. Reents, G. Lacconi, W. Plieth, J. Electroanal. Chem. 376, 185-188 (1994).
[4] W. Plieth, B. Roy, H. Bruckner, Ber. Bunsenges. Phys. Chem. 85, 499 (19981).
[5] M Fleischmann, G. Sundholm, Z.Q. Tian, Electrochim. Acta 31, 907-916 (1986).
[6] J. Billmann, G. Kovacs, A. Otto, Surf. Sci. 92, 153-173 (1980).
[7] A. Otto, J. Billmann, J. Eickmaus, U. Ertürk, C. Pettenkofer, Surf. Sci. 138, 319-338 (19984).
[8] W. Plieth, Electrochim. Acta 37, 2115-2121 (1992).

Electrochemical Nanotechnology
In-situ Local Probe Techniques at Electrochemical Interfaces
Edited by W. J. Lorenz and W. Plieth

Instrumental Design and Prospects for NMR-Electrochemistry

James B. Day, Jianjun Wu, Eric Oldfield, Andrzej Wieckowski

Contents

1	Introduction		292
2	Instrumentation		293
	2.1	The electrochemical NMR cell	293
	2.2	The mini-cell	294
	2.3	The NMR probes	295
	2.4	The NMR spectrometer	297
3	Experimental results		298
4	Conclusions		299
5	Future research		300
6	References		300

Summary. We describe the design, construction, and operation of two types of nuclear magnetic resonance (NMR) sample probes for use in electrocatalysis/surface NMR studies. The first is an electrochemical NMR cell, which permits observation of NMR signals of surface-adsorbed species under external potential control. This cell also permits conventional voltammograms to be recorded from the actual NMR sample. The second or mini-cell has a long, thin sample region and better sensitivity than the electrochemical NMR cell, but is not capable of voltammetry. Spectra have been obtained for ^{13}CO, $^{13}CN^-$ and $C^{15}N^-$ adsorbed on polycrystalline platinum black, as a function of applied potential, demonstrating the feasibility of multinuclear NMR studies at electrified interfaces.

1 Introduction

The use of spectroscopic techniques to investigate the structures of and reactions at the solid-liquid interface in electrochemical systems is an area of rapid progress [1]. However, because many conventional surface techniques are difficult to apply in these systems directly, there is a growing need to develop new approaches to structure determination, especially in systems of potential technological importance such as fuel cells. Nuclear magnetic resonance (NMR) spectroscopy, which has a long history in solid-gas interfacial studies, is one technique which can, in principle, give substantial amounts of information about the solid-liquid interface, and previously some preliminary results were reported [2, 3], showing feasibility.

The strengths of NMR lie in the detailed types of information which can be derived. These include structural and motional information with regard to the adsorbate being studied, e.g., what is the adsorbate [4]? Is there any motion such as diffusion or internal motion? Furthermore, in the case of adsorbates on metals, information regarding the electronic environment can also be obtained from the Korringa relation [5], which in suitable situations can be related to densities of states at the Fermi level. Thus, the use of NMR to study adsorbates at the electrochemical solid-liquid interface represents a logical and systematic progression in the investigation of adsorbates on heterogeneous catalysts. The study of CO, adsorbed from the gas phase (solid/gas interface), on supported catalysts has received considerable attention previously [6, 7] and the methodologies in this area, at least from the NMR perspective, should be directly transferable to the solid-liquid interface. To illustrate this, such information has already been determined for electrochemically prepared *sealed* samples [8], where from T_1 data it has been determined that the type of adsorbate derived from the electrodecomposition of methanol on polycrystalline (PC) platinum occupies a single adsorption site, regardless of the decomposition potential or surface coverage.

In this paper, we present recent work on the development of the electrochemical NMR cells for the study of electrode adsorbates as a function of applied potential. A number of novel design features permit the routine and reliable detection of adsorbed species, such as ^{13}CO (ex MeOH) and CN^- on fuel cell grade platinum black. Much higher sensitivity than previously reported is possible with our new instrumentation, which permits the recording of NMR frequency shifts as a function of applied potential. Although previous work from this laboratory demonstrated the feasibility of these techniques, it was limited in results and applicability in that the previous designs could only *maintain* the potential of the adsorbate during the NMR measurements, and sample preparation was accomplished in a separate cell suitable for the rigors of cyclic

voltammetry. This restricted application to adsorbates which could withstand being transferred from a preparation cell into the electrochemical NMR cell. The older versions of the electrochemical NMR cell also suffered from poor sensitivity and required $>10^5$ transients for modest signal-to-noise ratio spectra. Finally, the old designs suffered from joints and Teflon stoppers that were positioned below the electrolyte level and often leaked, thus placing time constraints on spectral measurements, preventing the lengthy and elaborate NMR experiments required for detailed structure/dynamics characterization from being performed. The new cells permit routine operation as a function of applied potential, and form the basis for an even higher-field (600 MHz, 14) system under construction.

2 Instrumentation

2.1 The electrochemical NMR cell

Our recent improvements in instrumentation are centered around the new electrochemical NMR cell (Fig. 1).

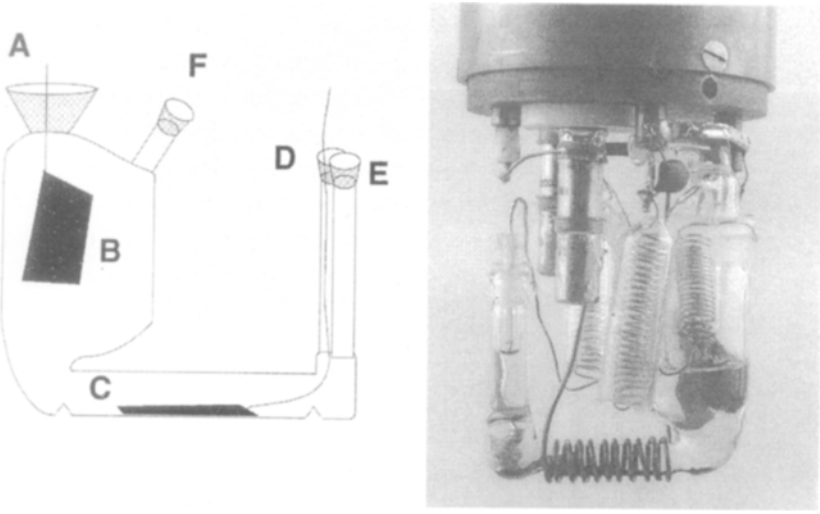

Fig. 1. (A) Diagram of electrochemical NMR cell: A, the counter electrode, encased in a 14/20 male joint. B, Upper electrolyte reservoir; C, Sample chamber for Pt black; D, working electrode lead connected to Pt gauze in sample chamber; E, vacuum/waste Luer connection; F, Reference electrode Luer connection. (B) The assembled electrochemical NMR probehead.

This cell has been designed to allow for sample preparation and signal acquisition to occur without interruption of circuit continuity, since it is now possible to prepare samples within the probe, then immediately begin NMR measurements. The large electrolyte reservoir, which houses the counter and reference electrodes, provides ample electrolyte for complex and lengthy measurements to be made, without solvent evaporation. The location of the PC platinum black powder is within the long sample region of the electrochemical NMR cell (Fig. 1(A)). The sample cell is wrapped with a copper wire (NMR coil) which serves for both excitation and signal acquisition (Fig. 1(B)). The electrochemical NMR cell incorporates the ability to exchange the electrolyte without removing the probe containing the electrochemical NMR cell from the magnet. When directly connected to a potentiostat, use of the electrochemical NMR cell requires electronic filtering of the electrochemical leads entering the probehead, in order to eliminate environmental radio-frequency (RF) pickup which would otherwise be introduced (see Section 2.3).

2.2 The mini-cell.

The second type of cell we have used for our studies of species adsorbed onto platinum black is the mini-cell (Fig. 2) [9].

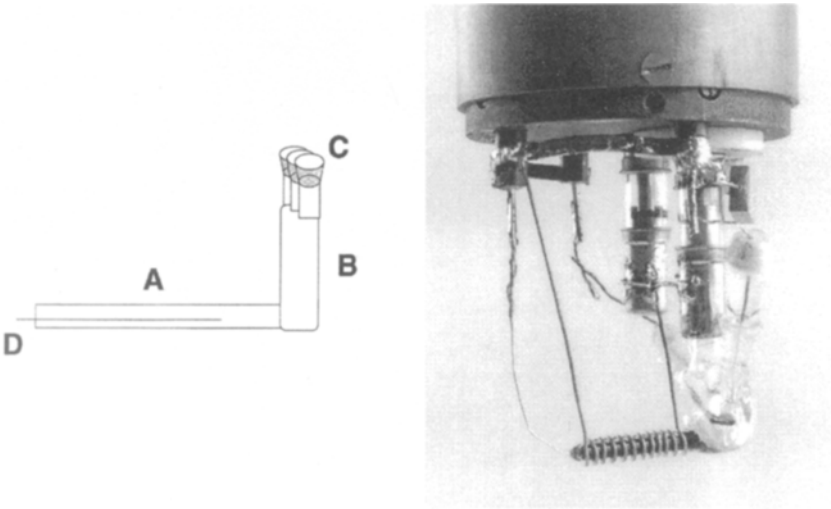

Fig. 2. A. Diagram of the mini-cell. A, Sample chamber; B, electrolyte reservoir; C, ports for counter and reference electrodes; D, platinum wire for contact with the platinum black sample. (B) Mini-cell probehead set for ^{15}N NMR data acquisition.

The mini-cell has higher sensitivity over the electrochemical NMR cell due to an enhanced filling of the RF coil. The tradeoff is that the mini-cell cannot be used directly in sample preparation, since it is difficult to obtain a voltammogram with this configuration. This limits its use to adsorbates that can withstand transfer from a more conventional „powder" electrochemical cell. The mini-cell has been used with and without electrochemical-lead filtering during signal averaging. We found that it was unnecessary to use RF filters for ^{13}C NMR signal acquisition from enriched sodium cyanide ($^{13}CN^-$) adsorbed onto PC platinum black, but for less-sensitive nuclei such as nitrogen-containing adsorbates ($C^{15}N^-$), RF filtering is essential. Clearly, more complex features such as skin depth, RF penetration and sample granularity also affect sensitivity, the main point being that, even in a „harsh" environment, external RF pickup can be greatly reduced even with electrodes being in direct contact with the NMR sample during data acquisition.

2.3 The NMR probes

Both the electrochemical NMR cell and the mini-cell require a custom-built probe (Fig. 3) in order to be loaded into the NMR spectrometer. The probe is designed for an 8.45 (360 MHz) wide bore (89 mm) superconducting magnet, and is loaded into the top of the magnet with the center of the sample positioned at the magnetic center. The electrochemical leads are connected to 0.141-inch diameter semi-rigid coaxial cable, which is part of the probe, by BNC connectors. The semi- rigid coax runs the length of the probe and enters into the probehead where the electrochemical NMR cell/mini-cell is located. LC low-pass filters are installed at this point (Figs. 1(B) and 4). These filters serve the dual purpose of (i) minimizing the introduction of environmental noise, which can be transmitted through the electrochemical leads, and (ii) also acting as RF chokes in the reverse direction, preventing the leakage of high-power excitation pulses out into the potentiostat. The optimal arrangement of the LC circuit is determined experimentally, and can be done on a benchtop with an oscilloscope and a frequency sweeper. Care must be taken to insure that the filter's inductor is not self-resonant at the Larmor frequency of the nuclei under investigation, or tuning problems arise due to multiple resonances in the probes'LC circuit. In the case of ^{13}C NMR at 8.45 T, the inductors are tuned to resonate at around 150 MHz. This prevents multiple tuning resonances at 90 MHz, yet provides sufficient impedance to block the RF power from shunting out of the electrochemical leads.

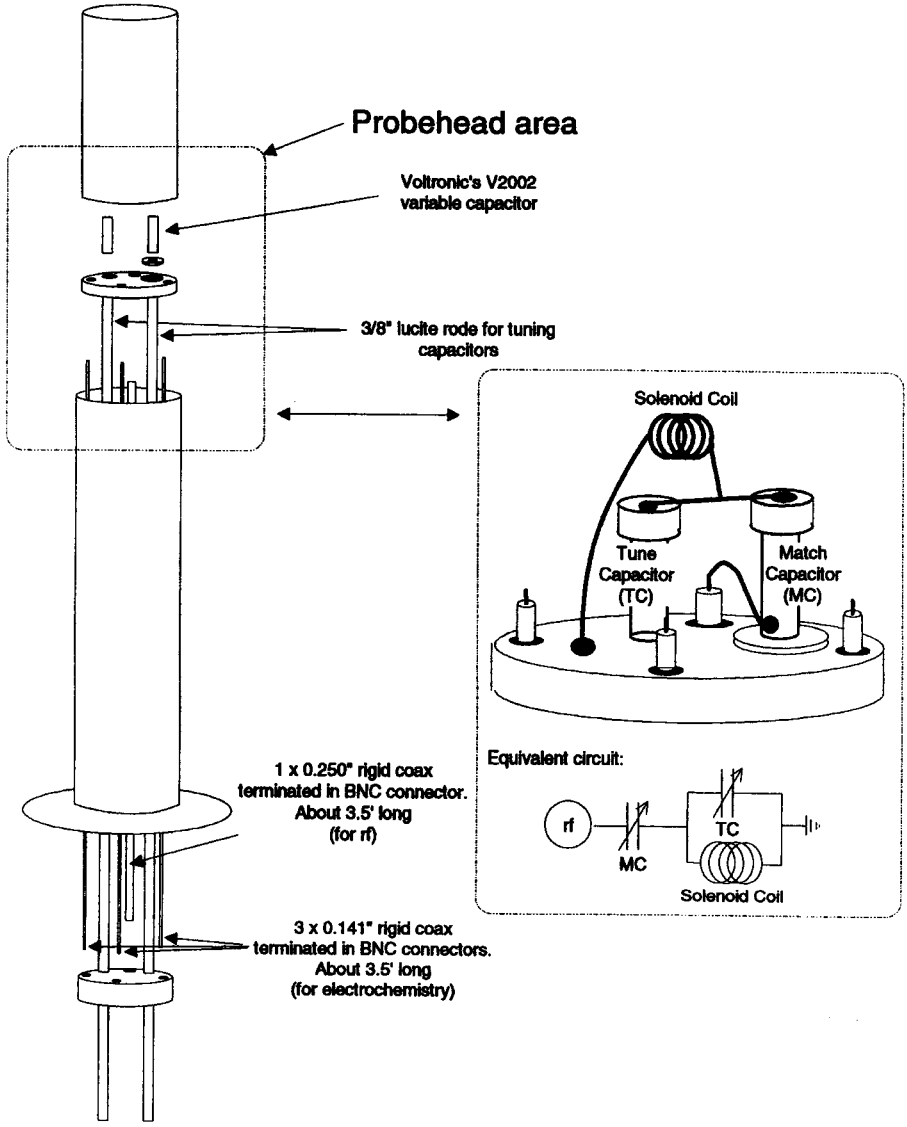

Fig. 3. Schematics of the electrochemical NMR probe and circuitry. The probes' casing and cap are made of brass. All the internal pieces are made of copper.

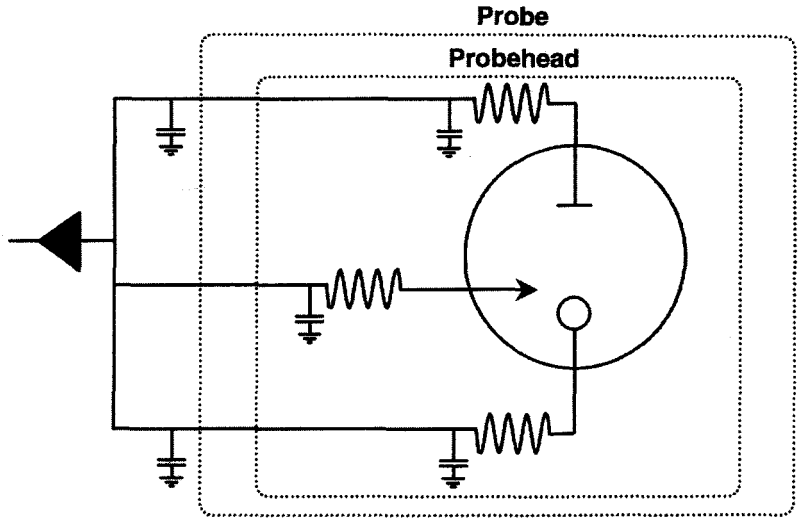

Fig. 4. Schematic of the low-pass filters used to enhance signal-to-noise ratio and prevent excitation power from shunting out the electrochemical leads. Table 1 lists the configuration of the tuning elements

2.4 The NMR Spectrometer.

The techniques and equipment necessary for solid-liquid interface surface adsorbate NMR signal acquisition are those typically used in solid-state NMR at the solid-gas interface. The frequency domain linewidths of typical ^{13}C or ^{15}N signals (^{13}CO, ^{13}CN, $C^{15}N$) on platinum at 8.45 signal are between ~20 and 30 kHz (full width at half maximum), requiring fast digitization for faithful reproduction of the rapidly decaying signal in the time domain (~1 - 5 μs dwell times). At present, we are using the following equipment: for digitization, a Nicolet Explorer IIIA fast digitizer; for pulse control and data acquisition and transformation, a Nicolet 1280 computer system. The magnet is a wide-bore (89 mm) Oxford superconducting magnet. The 90° pulse width used for ^{13}CO/Pt (electrochemical NMR cell) is ~10 μs, for ^{13}C of cyanide (mini-cell) it was 3.5 μs and 7.5 μs for ^{15}N of cyanide (mini-cell). Signal acquisition is accomplished by applying a Hahn spin-echo sequence followed by a signal acquisition period: [2-τ_0-π-τ_1-acquire] - where $\tau_1 < \tau_0$ so that acquisition begins before the echo

maximum. Typical values for τ_0 are in the range of 25 - 40 μs. The precise echo maximum is located prior to Fourier transformation.

The fact that the echo decays very rapidly in the time domain leads to a problem common in solid-state NMR work: the appearance of a „pulse feedthrong". This artifact results from the recovery of the receiver circuits and a ringdown of the transmitter and probe circuits after the high-power excitation pulses. To reduce this problem a pulse sequence used to eliminate „ringdown" in quadrupolar echo NMR was employed [10]. In this sequence, the phase of the $\pi/2$ and the π pulses of the Hahn-echo sequence are varied in such a way that the artifacts add destructively and are essentially eliminated.

Table 1. Configuration of filter elements

	^{13}CO (90 MHz)				$C^{15}N$ (36 MHz)			
	Probehead		Probe Input		Probehead		Probe Input	
Electrode	L [μH]	C [pF]	L [μH]	C [pF]	L [μH]	C [pF]	L [μH]	C [pF]
Working	1.1	680	-	-	8.0	680	-	300
Reference	1.1	680	-	-	11	-	-	-
Counter	1.1	680	-	-	3.5	680	-	330

3 Experimental results

A typical spectrum of ^{13}CO derived from the decomposition of ^{13}C-enriched methanol on PC platinum black is shown in Fig. 5(A). Fig. 5(B) shows the first electrochemical cycle after methanol decomposition, followed by rinsing, without circuit interruption. The voltammogram is used to determine surface coverage from the $CO \rightarrow CO_2$ oxidation peak at around 400 mV (versus a Ag/AgCl reference electrode, in 1.0 M NaCl). Typical mini-cell NMR spectra for ^{13}C- and ^{15}N-labeled CN^- on Pt black are shown in Fig. 6.

Using the electrochemical NMR cell, the potential dependence of the frequency shift for CO and CN on platinum black is currently being investigated. Data such as these will then be used as a basis for modeling how chemical shifts and electronic structure may be influenced by an applied electric field.

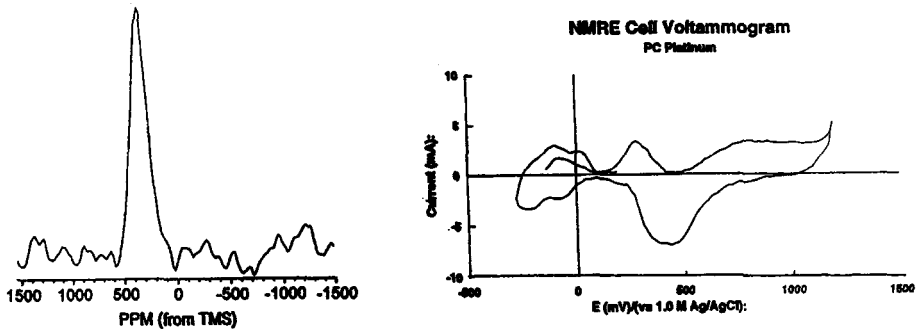

Fig. 5. (A) A typical ^{13}CO-Pt black spectrum with a 0.0 V applied potential at 8.45, 13200 transients, S/N ratio = 14.0:1. (B) CV after NMR measurements, taken at 0.1 mV/s (see text).

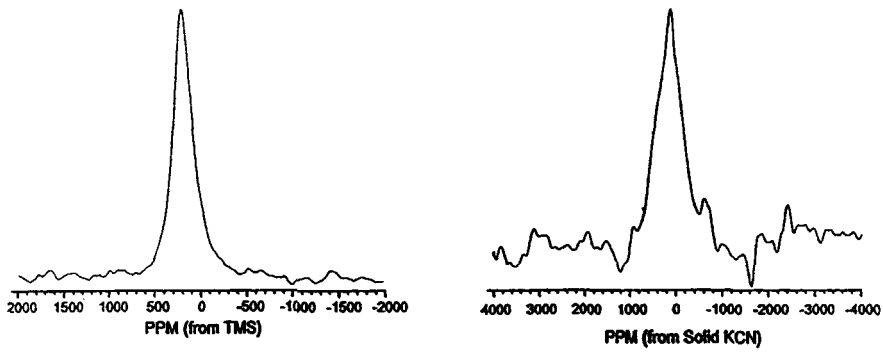

Fig. 6. (A) A spectrum of ^{13}CN-Pt black in the mini-cell, 3000 transients, S/N ratio = 36.2:1. (B) A spectrum of C^{15}N-Pt black in the mini-cell, 20000 transients, S/N = 9.4:1.

4 Conclusions

The results we have presented above show that quite high-sensitivity ^{13}C and ^{15}N NMR spectra of species adsorbed at a solid-liquid interface can now be obtained. The ability

to prepare samples, record cyclic voltammograms, and obtain surface NMR spectra under potential control opens up new avenues for NMR at the solid-liquid interface in general, and at electrified interfaces in particular. The signal-to-noise ratios obtained at 8.45 enable initial studies of T_1 and T_2, and as we note below, will be greatly facilitated in the future via higher-field operation.

5 Future Research

Studies using the present electrochemical NMR cell designs are practical for many types of adsorbates containing magnetically active nuclei such as ^{1}H, ^{2}H, ^{13}C, ^{15}N, ^{17}O, ^{103}Rh, ^{195}Pt, etc. Plans are under way in this laboratory for studies of the static and dynamic structure of CO on binary and ternary alloys (e.g., ruthenium/platinum/tin) in methanol for fuel-cell applications. Such alloys display enhanced resistance to CO poisoning, and the nature of this resistance is appropriate for NMR investigation. For example, Pt-CO bonding information such as Pt-C connectivities, CO orientation and clustering, are accessible by T_1, T_2, isotope dilution, and related techniques. In fact, essentially all of the techniques used in the past 20 years to study the solid-gas interface should now be applicable to NMR-electrochemistry, with the added bonus of potential control.

Work in this area is, of course, not limited to using Pt black as the electrocatalyst. Virtually any electroactive catalyst, such as gold, rhodium, or palladium, which can be prepared with a particle size small enough to provide the necessary surface area and RF penetration, can be investigated.

Acknowledgments. The authors acknowledge the Department of Defense under grant number DAAH04-95-0581, the Department of Energy under grant number DE-AC02-76ER01198, and the National Science Foundation under grant number CHE 94-11184.

7 References

[1] H. D. Abruña (Ed.), Electrochemical Interfaces - Modern Techniques for In-situ Interface Characterization, VCH, New York, 1991.

[2] P.J. Slezak, A. Wieckowski, J. Electroanal. Chem. 339, 401 (1992).

[3] P.J. Slezak, A. Wieckowski, J. Magn. Reson. 102, 166 (1993).

[4] W. Kolodziejski, J. Klinowski, in: *NMR Techniques in Catalysis,* Bell, A. T., Pines, A. (Eds.), Marcel Dekker, New York, New York, 1994, p 3.

[5] Korringa, J. Phys. 16, 601 (1950).
[6] J.P. Ansermet, C.P. Slichter, J.H. Sinfelt, Prog. NMR Spectrosc. 22, 401 (1990).
[7] T. M. Duncan, J. Phys. Chem. 16(1), 125 (1987).
[8] J.B. Day, P.-A. Vuissoz, E. Oldfield, A. Wieckowski, J.P. Ansermet, J. Am. Chem. Soc. 118, 13046 (1996).
[9] J. Wu, J.B. Day, K. Franaszczuk, B. Montez, E. Oldfield, A. Wieckowski, P.-A. Vuissoz, J.-Ph. Ansermet, Faraday Transactions 93, 1017 (1997).
[10] A.C. Kunwar, G.L. Turner, E. Oldfield, J. Magn. Reson. 69, 124 (1986).

Electrochemical Nanotechnology
In-situ Local Probe Techniques at Electrochemical Interfaces
Edited by W. J. Lorenz and W. Plieth

List of Contributors

Héctor D. Abruña
Department of Chemistry
Baker Laboratory
Cornell University
Ithaca
NY 14853-1301, USA

P. Allongue
Laboratoire de Physique des Liquides et
Electrochimie
CNRS-UPR 15
Université Pierre et Marie Curie
4 Place Jussieu
Tour 22
F-75005 Paris
France

Giovanni Aloisi
Dipartimento de Chimica
Università di Firenze
Via G. Capponi 9
I-50121 Firenze
Italy

E. Ammann
Department für Chemie und Biochemie
Universität Bern
Freiestrasse 3
CH-3012 Bern
Switzerland

Jens E. T. Andersen
Department of Chemistry
The Technical University of Denmark
Building No. 207
DK-2800 Lyngby
Denmark

A. J. Arvia
Instituto de Investigaciones Fisicoquímicas
Teóricas y Aplicadas (INIFTA)
Sucursal 4
Casilla de Correo 16
1900 La Plata
Argentina

K. Bade
IMF
Forschungszentrum Karlsruhe
Postfach 3640
D-76021 Karlsruhe
Germany

A. Bartl
Institut fürFestkörperforschung im IFW
Dresden e.V.
Abteilung Elektrochemie und Leitfähige
Polymere
Helmholtzstrasse 20
D-01069 Dresden
Germany

R. J. Behm
Abteilung Oberflächenchimie und Katalyse
Universität Ulm
D-89069 Ulm
Germany

H.Böhni
Institute of Materials Chemistry and Corrosion
Swiss Federal Institute of Technology
ETH Hönggerberg
CH-8093 Zürich
Switzerland

T. A. Brunt
Department of Chemistry
University Chemical Laboratory
University of Cambrige
Lensfield Road
Cambridge CB2 1EW
UK

M. Cavallini
Dipartimento de Chimica
Università di Firenze
Via G. Capponi 9
I-50121 Firenze
Italy

E. D. Chabala
Department of Chemistry
University Chemical Laboratory
University of Cambrige
Lensfield Road
Cambridge CB2 1EW
UK

James B. Day
Department of Chemistry
University of Illinois at Urbana Champaign
600 South Mathews Avenue
Urbana
IL 61801, USA

L. Dunsch
Institut für Festkörperforschung im IFW
Dresden e.V.
Abteilung Elektrochemie und Leitfähige
Polymere
Helmholtzstrasse 20
D-01069 Dresden
Germany

L. Eng
Institute of Physics
University of Basel
CH-4056 Basel
Switzerland

C. Froeck
Institüt für Festkörperforschung im IFW
Dresden e.V.
Abteilung Elektrochemie und Leifähige
Polymere
Helmholtzstrasse 20
D-01069 Dresden
Germany

Andrew A. Gewirth
Department of Chemistry
University of Illinois
600 South Mathews Avenue
Urbana
IL 61801, USA

Rolando Guidelli
Dipartimento de Chimica
Università di Firenze
Via G. Capponi 9
I-50121 Firenze
Italy

J. Halbritter
IMF I
Forschungszentrum Karlsruhe
Postfach 3640
D-76021 Karlsruhe
Germany

James E. Hudson
Department of Chemistry
Baker Laboratory
Cornell University
Ithaca
NY 14853-1301, USA

Kingo Itaya
Department of Applied Chemistry
Faculty of Engineering
Tohoku University
Sendai 980
Japan

C. Kobusch
AGEF e.V.-Institut
an der Universität Düsseldorf
Universitätsstrasse 1
D-40225 Düsseldorf
Germany

M. Koinuma
Physical Chemistry Laboratory
Division of Chemistry
Graduate School of Science
Hokkaido University
Sapporo 060
Japan

A. A. Kornyshev
Institut für Energieverfahrenstechnik
Forschungszentrum Jülich GmbH
D-52425 Jülich
Germany

W. J. Lorenz
Institute für Physikalische Chemie und
Elektrochemie
Universität Karlsruhe
D-76136 Karksruhe
Germany

O. M. Magnussen
Abteilung Oberflächenchemie und Katalyse
Universität Ulm
D-89069 Ulm
Germany

Philippe Marcus
Laboratoire de Physico-Chemie des Surfaces
CNRS (URA 425)
Université Paris VI
Ecole Nationale Supérieure de Chimie de Paris
11 rue Pierre et Marie Curie
F-75005 Paris
France

Vincent Maurice
Laboratoire de Physico-Chemie des Surfaces
CNRS (URA 425)
Université Paris VI
Ecole Nationale Supérieure de Chimie de Paris
11 rue Pierre et Marie Curie
F-75005 Paris
France

T. P. Moffat
Materials Science and Engineering Laboratory
National Institute of Standards and Technology
Gaithersburg
MD 20899, USA

F. Möller
Abteilung Oberflächenchemie und Katalyse
Universität Ulm
D-89069 Ulm
Germany

Per Møller
Institute of Manufacturing Engineering
The Technical University of Denmark
Building No. 425
DK-2800 Lyngby
Denmark

Brian K. Niece
Department of Chemistry
University of Illinois
600 South Mathews Avenue
Urbana
IL 61801, USA

P. I Oden
Abteilung für Chemie und Biochemie
Universität Bern
Freiestrasse 3
CH-3012 Bern
Switzerland

Eric Oldfield
Department of Chemistry
University of Illinois at Urbana Champaign
600 South Mathews Avenue
Urbana
IL 61801, USA

S. J. O'Shea
Engineering Department
University of Cambrige
Cambridge CB2 1PZ
UK

Waldfried Plieth
Institut für Physikalische Chemie und
Elektrochemie
Technische Universität Dresden
Mommsenstrasse 13
D-01062 Dresden
Germany

T. Rayment
Department of Chemistry
University Chemical Laboratory
University of Cambrige
Lensfield Road
Cambridge CB2 1EW
UK

Bert Reents
Institut für Physikalische Chemie und
Elektrochemie
Technische Universität Dresden
Mommsenstrasse 13
D-01062 Dresden, Germany

R. C. Salvarezza
Instituto de Investigaciones Fisicoquímicas
Teóricas y Aplicadas (INIFTA)
Sucursal 4
Casilla de Correo 16
1900 La Plata
Argentina

U. Schmidt
IPCE
Universität Karlsruhe
D-76182 Karlsruhe
Germany

A. Schreyer
Institute of Materials Chemistry and Corrosion
Swiss Federal Institute of Technology
ETH Hönggerberg
CH-8093 Zürich
Switzerland
(Present address:
Helbling Ingenieurunternehmung AG,
Hohlstrasse 610, CH-8048 Zürich, Switzerland)

J. W. Schultze
AGEF e.V.-Institut an der Heinrich-Heine-
Universität Düsseldorf
Universitätsstrasse 1
D-40225 Düsseldorf
Germany

H.Siegenthaler
Universität Bern
Abteilung für Chemie und Biochemie
Freiestrasse 3
CH-3012 Bern
Switzerland

Manuel P.Soriaga
Department of Chemistry
Texas A&M University
College Station
TX 77843, USA

G. Staikov
Institut für Physikalische Chemie und
Elektrochemie
Universität Karlsruhe
D-76136 Karlsruhe, Germany

John L. Stickney
Department of Chemistry
University of Georgia
Athens
GA 30602, USA

U. Stimming
Physik Department
der Technischen Universität München
Institut für Festkörperphysik und
Technische Physik E19
James-Franck-Straße 1
D-85748 Garching
Germany

M. Strobel
IEKP
Universität Karlsruhe
D-76182 Kalsruhe
Germany

M. Sumetskii
AT&T Bell Laboratories
Murray Hill
NJ 0794-0636, USA

T. Suter
Institute of Materials Chemistry and Corrosion
Swiss Federal Institute of Technology
ETH Hönggerberg
CH-8093 Zürich
Switzerland

Jens Ulstrup
Department of Chemistry
The Technical University of Denmark
Building No. 207
DK-2800 Lyngby
Denmark

K. Uosaki
Physical Chemistry Laboratory
Division of Chemistry
Graduate School of Science
Hokkaido University
Sapporo 060
Japan

Henry de Villeneuve
Laboratoire de Physique des Liquides et
Electrochimie
CNRS-UPR 15
Université Pierre et Marie Curie
4 Place Jussieu
Tour 22
F-75005 Paris
France

R.Vogel
Institut für Energieverfahrenstechnik
Forschungszentrum Jülich (KFA)
D-52425 Jülich
Germany

M. R. Vogt
Abteilung Oberflächenchemie und Katalyse
Universität Ulm
D-89069 Ulm
Germany

M. E. Welland
Engineering Department
University of Cambrige
Cambridge CB2 1PZ
UK

Andrzej Wieckowski
Department of Chemistry
University of Illinois at Urbana Champaign
600 South Mathews Avenue
Urbana
IL 61801, USA

Jianjun Wu
Department of Chemistry
University of Illinois at Urbana Champaign
600 South Mathews Avenue
Urbana
IL 61801, USA

List of Abbreviations

ac	alternating current
AES	atomic emission spectroscopy
AFM	atomic force microscopy
ARXPS	angle-resolved photoelectron spectroscopy
cd	current density
CE	counter electrode
dc	direct current
DTS	distance tunneling spectroscopy
ET	electron tunneling
EXAFS	extended X-ray absorption fine structure
fcc	face-centered cubic
GIXS	greating incidence X-ray spectroscopy
hcp	hexagonal close-packed
h,k,l	Miller indices of crystallographic surface orientation
HOPG	highly oriented pyrolytic graphite
LEED	low-energy electron diffraction
LFM	lateral force microscopy
LIGA	littographic galvanic deposition technique
MBE	molecular beam epitaxy
MW	molecular weight
NHE	normal hydrogen electrode
NMR	nuclear magnetic resonance
OPD	overpotential deposition
ORC	oxidation-reduction cycle
pzc	potential of zero charge
QCM	quartz crystal microbalance

RE	reference electrode
REM	reflectance electron microscopy
RF	radiofrequency
RHE	reference hydrogen electrode
RHEED	reflection high-energy electron diffraction
rms	root mean square
SCE	saturated calomel electrode
SECM	scanning electrochemical microscopy
SEM	scanning electron spectroscopy
SERS	surface-enhanced Raman spectroscopy
SFM	scanning force microscopy
SHE	standard hydrogen electrode
SNOM	scanning near-field optical microscopy
SPD	spectral power density
SPM	scanning probe microscopy
STM	scanning tunneling microscopy
SXS	surface X-ray scattering
TEM	transmission electron microscopy
UHV	ultra high vacuum
ULSI	ultra large scale integration
UPD	underpotential deposition
UPS	ultraviolet photoelectron spectroscopy
VTS	voltage tunneling spectroscopy
WE	working electrode
XPS	X-ray photoelectron spectroscopy

Electrochemical Nanotechnology
In-situ Local Probe Techniques at Electrochemical Interfaces
Edited by W. J. Lorenz and W. Plieth

Symbol list

Symbol	Name	Unit
a, a_0	lattice constant	m
b	radius of particle	m
C	capacitance	F
c_i	concentration of species i	mol dm^{-3}
D	diffusion coefficient	$m^2\ s^{-1}$
D_G	grain dimension	l
D_{FRAC}	local fractal dimension of the surface	l
D_{TOP}	topological dimension	l
D_S	surface diffusion coefficient	$m^2\ s^{-1}$
D_x, D_y	diffusion coefficients along x, y direction	$m^2\ s^{-1}$
d	surface distance, tip-sample distance, width of tunneling gap	m
d_{eff}	effective tunneling distance	m
d_S	column cross section	m^2
d_{STM}	avarage particle diameter measured with STM	m
d_{TEM}	avarage particle diameter measured with TEM	m
$d_{o,Me}$	interatomic distance of metal atoms	m
$d_{o,S}$	interatomic distance of substrate atoms	m
E	potential	V
E^o	standard electrode potential	V
$E_{me/Me^{z+}}$	Nernstian potential	V
E_F	Fermi energy	J
E_t	tunneling voltage	V
E_{tip}	tip potential	V
E	Young modulus	$N\ m^{-2}$
e	electron charge	C
F	Faraday constant	$C\ mol^{-1}$
F	force	N
h	height	m
h_S	average surface mean height	m
$<h>$	instantaneous surface mean height	m
h,k,l	Millers indices	l
$\hbar$	$h\ (2\pi)^{-1}$, with Plancks constant h	Js
I	current	A
I_o	initial current	A
$I(t)$	current-time dependence	A
$\bar{I}(t)$	average current	A
$i(t)$	random current-time dependence	A

Symbol	Name	Unit
I_t	tunneling current	A
I_{tip}	tip current	A
i	$\sqrt{-1}$	l
j	current density	A m^{-2}
K	equilibrium constant (dependent on the process)	l
$K(t)$	temporary current correlation function	A^2
k	Boltzmann constant	J K^{-1}
L	inductivity	H
l	length	m
l_S	length of surface profile	m
m_e	electron rest mass	kg
N	number of points	l
N_{crit}	number of atoms in critical cluster	l
N_{ad}	density of adatoms	m^{-2}
N_i	number of intermediate states	l
p	primitive unit cell vector	m
p_1,p_2,p_3	nonprimitive unit cell vectors	m
p	unit cell parameter	m
$p(r$	electron momentum	kg m s^{-1}
Q	parameter of bare gap	kg s^{-1}
q	coordinate of vibration	m
r	radius of curvature	m
r_j	point of adatom j on the surface	m
r_{tip}	tip radius	m
$S(\omega)$	current noise spectral density	A^2 Hz^{-1}
Δd	relative surface distance	m
T	temperature	K
T_1	spin-lattice relaxation time	s
T_2	spin-spin relaxation time	s
t	time	s
t	layer thickness	m
t_x	transition time	s
t_c^x, t_c^y	correlation times along coordinate x,y	s
$\hat{t}_c$	maximal correlation time	s
t_N	nucleation time	s
U	electrophoretic deposition potential	V

Symbol	Name	Unit
ΔU	electrophoretic pulse potential	V
$U_{(r-r_j)}$	potential of adatom j	V
u	lateral coordinate (x,y)	m
u, u_0, u_1	local coordinates	m
V	tunneling bias	V
V	local tunneling barrier height	eV
V_{eff}	effective tunneling barrier height	eV
$V(r)$	potential barrier	V
$V_o(r)$	bare potential (energy barrier)	
v	potential sweep rate	V s^{-1}
x	local coordinate	m
y	local coordinate	m
z	local coordinate	m
z	number of electrons	1
z	coarsening coefficient, $z = \alpha\, \beta^{-1}$	1
z_{max}	maximal change in z-direction	m
α	roughness exponent	1
β	growth exponent	1
γ	specific surface energy, surface tension	J m^{-2}
δ	partial charge	1
ε	surface strain	1
η	overpotential	V
η	stochastic noise, roughening term	1
θ	surface coverage	1
κ	inverse decay length	m^{-1}
λ	wavelength	m
λ	roughening term	1
μ	chemical potential	J mol^{-1}
$\tilde{\mu}$	electrochemical potential	J mol^{-1}
ν	Poisson ratio	1
ν	coefficient of surface tension, roughening term	1
ν_i	wavenumber of vibration i	cm^{-1}
σ	scattering cross section	m^2
σ_1, σ_2	surface stress	N V^{-1} m^{-1}
τ	relaxation time	s
ϕ	galvani potential	V
ψ	binding energy	eV

Symbol	Name	Unit
ω	angular frequency ($\omega = 2\,\pi f$)	Hz
$\omega(L,t)$	instantaneaus surface width	m
ω_{hM}	root mean square surface roughness	m
Θ	packing density	1
ϕ_o	work function of vacuum	eV
∇^2	Laplace operator	1

Subject Index

α-Cr_2O_3(0001) 191
α-dodecatungstosilicate
  on Ag(111) 121
β-$Ni(OH)_2$(0001) 190
α-$SiW_{12}O_{40}^{4-}$
  on Ag(111) 122
[Os(2,2'-bipyridine)$_2$(trimethylene-4,4'-bipyridine)Cl](PF$_6$)
  cyclic voltammograms 131
  STM image on Pt(111) 130
  STM image 131
[Os(2,2'-bipyridine)$_2$[4-(aminomethyl)pyridine]Cl](PF$_6$)
  STM image on Au(111) 127; 128
1,3-dicyclohexylcarbodiimide 127
$^{13}CN^-$ 291; 295; 299
^{13}CN-Pt black, NMR-spectrum 299
^{13}CO 291; 292; 297; 298; 299
^{13}CO-Pt black, NMR-spectrum 299
2-(N-morpholino)ethanesulfonic acid 36
2,3,5,6-tetrakis(2-pyridyl)pyrazine
  Ru complex 130
  STM image on HOPG 129
2D phase transition 104; 107
3-mercaptopropionic acid 127
4,4- bis (N-methylpyridinium)-p-phenylenedivinylene 144
4'-vinyl-2,2':6',2"-terpyridine
  Ru complex 130
  STM image on HOPG 129
5,10,15,20-tetrakis(N-methylpyridinium-4-yl)-21H,23H-porphine 140; 144; 146
activation 279
active sites 279
adatom density 182
adatom diffusion 47; 50
adatom lattice
  structures 116
adatom sites 52
adatoms 49
  diffusion coefficients 46
  additive 247
adenine
  Au(111) 107
adhesion force 133; 134
adsorbate formation 1; 2; 3; 5; 7; 8; 9; 11
adsorbate stability 1; 2; 11
adsorbate-substrate rearrangement 8
  AFM image 113; 117; 118; 119; 120
Ag 278
  on Au(111) 116
  in $KClO_4$ 108
  in NaF 106; 110
  on Au(111) 95
Ag underpotential deposition
  iodine adlayer 137; 139; 142; 143; 146
  Pt(111) on sulfuric acid 137; 139; 142; 143; 146
Ag UPD
  on HOPG(0001)/$HClO_4$ 22; 23
Ag(111) 103; 106
  in NaF + NaI 104; 105
  in NaF + Na_2S 106
  in NaOH + Na_2S 105
Ag(111)/$HClO_4$
  Pb UPD 19
  unreconstructed 15; 16; 20
Ag(CN) 285
Ag/Au(111)
Ag/Au(111)
  in $HClO_4$ 17
  sulfuric acid 94
Al 185; 186; 187; 196
alkylcyano-biphenyls 144
alloy electrodes 2
alloy formation 27
alloys
  compositionally modulated 172
angle-resolved photoelectron spectroscopy 215
anion
  asymmetric 186
  at defects 160; 161; 163; 164; 166; 167
anion co-adsorption 116
anion-anion interactions 95
anionic adsorbates 159; 163; 164; 167
anisotropic growth 166
argon ion laser 278
atomic cluster 45
atomic force microscopy 132; 149; 150; 151; 152; 154; 186; 199; 225; 226; 227; 228; 229; 230; 231; 232; 233; 237; 254
  atomic resolution 255
  catalytically active monolayers 113; 117
  combination with microelectrochemistry 212
  deposition of Cu 113; 117
  enhanced Cu deposition 113; 114; 115; 116; 117; 118; 119; 120
  ex-situ 57; 58; 61
  hydroxide adlattice on Cu 113; 117

in-situ 57; 58; 61; 253
molecular adsorbates on Au and Ag 113; 117
tip-induced modification 262
tip-sample interaction 113; 114; 115; 116; 117; 118; 119; 120
p-GaAs 257; 260
contact-mode 229
atomic layer epitaxy 268; 272
atomic resolution 102; 103
atomic terraces 187; 190; 194
atomic-scale 159; 160; 167
Au
columnar-structured 64; 65; 66
electrocapillary curve 87; 96
electrodeposits 57; 64; 66; 67; 69
polycrystalline flame-annealed 80; 81; 82; 82; 83
surface oxidation 31
Au(100)
CdSe 272; 268
"hex" - (1x1) transition 161
hexagonal reconstructed 161
Au(100)/$HClO_4$
Pb UPD 21
Au(111) 127; 128
in H_2SO_4 + NaCl 103
Au(111)/$HClO_4$
Ag UPD 17
Pb UPD 20
Au(111)/Se 273
average current 52
average surface morphology 80
azurin 28; 38
background noise 202
ballistic deposition model 59
bending beam method 89; 92
benztriazole 119; 120
biological adsorbates 27
bipotentiostat 28
bipotentiostatic control 14
Bi 88
adlattice 115; 116
UPD on Au(111) 115
Bockris-Mattson model 28
bromophenyl 250
bulk deposition 33
bulk nucleation 33
c(2x2) superstructure 166
$C^{15}N^-$ 291; 295; 299
$C^{15}N$-Pt black, NMR-spectrum 299
calibrations 254
cantilever 87; 90; 92
cantilever Si_3N_4 151
cantilever stress sensor
fast dynamic response 97
Si_3N_4 254
capacity measurments 279
carbon 215; 216; 221; 223
catalyst particles 77; 83; 85
catalytic activity 54
CdS 106
CdSe on Au(100) 272
epitaxially on Au(100) 268
chain structures 150
charge transfer control 173
chemical etching 241
chloride adlayer 174
chloride ions
adsorption 190
chlorine adlattice 177; 178; 180
chromate polishing 3
chromium carbide 201
Clavilier method 268
cluster
true shape 54
cluster sizes 286
CN^- - stretch vibration 277
dependance on experimental conditions 282
shift with potential 284
splitting 282; 286
CO adsorption 162
co-adsorbed sulphate
open (3x3) arrangement 95
co-adsorption of anions 88; 97
compressive stress 88; 94; 95; 96
conducting polymers 2
conductivity 150
constant interaction 204
continuous shrinking 81
copper clusters 75; 81; 82; 83; 84; 85
copper clusters 81
copper oxidase lactase 28
correlation function 48; 49; 52
correlation times 50
corrosion 27; 58; 63; 66; 69; 101; 102 199; 213
adsorbate-catalyzed 268
corrosion resistance 185
coumarin

Au(100)-(hex) 107
Au(111) 107
counter ions 153; 154
co-adsorbing 159; 163; 164; 167
Cr 185; 186; 187; 190; 191; 192; 193; 194; 195; 196
passivation 190
trivalent 190
Cr_2O_3 201
crevice corrosion 201
crystal growth 277
crystal miscut 247
Crystal Violet 139; 144
current
average 46
dependence on time 46
correlation function 46; 50
fluctuation spectra 53
fluctuations 46
noise 46
noise spectral density 47
Cu
deposition 259
deposition on polycrystalline Au 81
dissolution 82
electrodeposition, organic additives 30; 119
electrodissolution 30
gold alloy 34
island AFM image 261
on Au(111) 116
selective deposition 262
Cu Pt(111)
co-adsorbed sulfate anion 143
Cu surfaces 117; 119
Cu(100) substrate 182
Cu(110)
addition of Cl 117; 118; 119
in 0.1 M $HClO_4$ 117
initial stages of oxidation 117; 118; 119
Cu(111) 262
Cu underpotential deposition
on Au(111)/sulfuric acid 142
on Pt(111)/sulfuric acid 143
Cu/Au(111)
stress changes 88; 89
cuprous chloride complex 182
cyanide ions 278
cyclic voltammetry 33
cytochrom *c* on Au
STM image 39
cytochrome *c* 28; 38
cytosine
on Au(111) 107
decoration steps 5; 6; 7
defect density 78
defects 185; 186; 188; 190; 192; 193; 195; 196
diazonium salts 249
diffusion
anisotropic 52
isotropic 52; 53
diffusion, oxygen 53
length 182
diffusion-limited conditions 173
digital etching 138
dislocations 1; 2
disordered phase 163
disorder-order transition 163
dispersed catalyst 75
dissolution
adsorbate-catalyzed 269
anisotropy 248
distance modulation spectroscopy 199; 204; 207; 208; 212
distance tunneling spectra 235
distance tunneling spectroscopy 14; 215; 218
DNA 107
domain boundaries 175
domains
double rows 166
double-pulse method 278
dynamic line-scan 4
dynamic processes
visualization 84
dynamic scaling theory 57; 60; 61; 62; 63; 66; 67; 68; 69
dynamical fluctuations 160
dynamics 241
local 46
Edwards-Wilkinson 62
effective barrier height 220; 221; 222
effective medium theory 88
elastic tunneling 46
electrocapillary 87; 92; 96
electrocapillary curves
gold 89; 92; 93; 94
hysteresis 89; 92; 93; 94
platinum 89; 92; 93; 94
electrocapillary equation 89
electrocatalysis 54; 58
surface NMR studies 291

electrocatalysts 73; 74; 77
electrochemical atomic layer epitaxy 102; 106; 107
electrochemical force spectroscopy 125; 126; 132
electrochemical nanotechnology 73; 82
  analytical 13
  preparative aspects 13
electrochemical NMR cell 291; 292; 293; 294; 295; 297; 298; 300
electrochemical NMR probe 293; 296
electrochemical oxidation 78
electrochemical polishing 187
electrocompression 88; 138; 141
electrocrystallization 27; 277
electrodeposition 160; 278
electrodissolution 57; 67; 68; 69
electron momentum 48
electron transfer 40
electron tunnel routes 40
electron tunneling
  homogeneous 37
  interfacial 37
electron-adatom interaction 46
electronic devices 150
electroreduction of H_2O_2 116
epitaxial Ni film 164
epitaxy
  NiO(433) // Ni(111) 185; 189; 190; 195
  NiO[0-11] // Ni[0-11] 185; 189; 190; 195
etch pits 246
etch rates 246
etching mechanism
etching processes 253
EXAFS 88
Fe 185; 186; 187; 192; 193; 195; 200; 202; 205; 211
  borate buffer 186; 187
  boron buffer 205
  tunneling barrier height 205
$Fe(CN)_5$[4-(aminomethyl)pyridine]$^{-2}$ 127
  STM image on HOPG 128
Fe_2O_3 200
Fe-Cr 185; 186; 193
Fe-protoporphyrin IX 42
Fermi level control 14
first-order phase transformation 21
flame annealing 29
fluctuation-induced tunneling 37
Fourier spectrum
four-probe technique 14
fractal dimension 61
Frank-van der Merwe 17; 32; 59
frizzy steps 53; 177
fuel-cell, applications of NMR 300
GaAs 253
  native oxide 257
  passivation 241
  sulfide passivation 248
GaAs(100) 258
  electrodeposition of Cu 259
  tip-induced modification 262
GIXS 7
gold oxide 29
gold oxide layers 64
grain boundaries 2
grating structure 108
grazing-incidence X-ray diffraction 186
growth
  three-dimensional 57; 58; 59; 60; 61; 62; 63; 65; 66; 68; 69
  two-dimensional 57; 58; 59; 60; 61; 62; 63; 65; 66; 68; 69
growth dynamics 180
growth models 57; 59
herringbone reconstruction 164
heteroepitaxial deposition 82
hexagonal contours 188
highly oriented pyrolytic graphite 144; 149
  covalent immobilization 127
  defects 78; 79; 82; 83
  thermally oxidized 127; 128; 129; 130
  steps 153
  oxidation 78
homoepitaxial deposition 173
honeycomb structure 88
$HSeO_3^-$ 273
H-termination 245
hydroxide outer layer 190; 192
hysteresis 161; 163
image analysis 61
impedance measurements 53
inclusions 199; 201; 207
indirect tunneling processes 206; 211
induction period 81
inhomogeneous distribution 81
InSe (100) 253
in-situ FTIR 245
in-situ monitoring of electrocrystallization 278
in-situ scanning 27

in-situ STM
complementary use of LEED 138; 139; 141; 142; 143; 144; 146
large adsorbates 28
real time imaging 241
iodide 103; 104; 268
iodine adlayer 137; 138; 139; 140; 141; 142; 143; 144; 145; 146
adsorption of TMPyP 146
on Au(111) 137; 138; 139; 140; 142; 143; 146
centered rectangular phase 137; 138; 139; 140; 142; 143; 146
on Pd(111) 137; 138; 139; 140; 142; 143; 146
on Pt(111) 137; 138; 139; 140; 142; 143; 146
on Rh(111) 137; 138; 139; 140; 142; 143; 146
rotated hexagonal phase 137; 138; 139; 140; 142; 143; 146
iodine on Pd(111)
($\sqrt{3} \times \sqrt{3}$)R30°- structure 269
iodine overlayer
isolated atoms 103
partial charge transfer 103
iodine/CO replacement 138
IR studies 121; 122
island formation 33
island growth 59
islands 161; 163; 164; 166
isopropanol 249
$K_2[Fe(CN)_5$ [4-(aminomethyl)pyridine]]
STM image on HOPG 128
kinetic anisotropy 177
kinks 190; 196
Korringa relation 292
Langevin stochastic equation 60
lateral force 226; 227; 228; 231
lateral force microscopy 227
lateral growth 33
lattice structure 52
layer-by-layer dissolution 67; 270; 272
layer-by-layer growth 166
LEED 138; 139; 143; 146
LIGA layers 215
LIGA process 216
light
influence on the tunnel current 226; 229; 237
local molecular levels 40
local probe techniques
ex-situ 14
in-situ 14
UHV conditions 14
local pseudopotentials 40
local spectroscopic measurements 195
local structural information 74; 79
localized states 206; 211
low-energy electron diffraction 138; 175; 268; 270; 273
low-pass filters 295; 297
low-temperature fuel cell 74
manganese sulfide 201
mesoscopic scale 187
mesoscopic structure 73
metal clusters 73; 77
metal deposition 31; 159; 163; 166; 167
metal dissolution 31; 159; 166
metalloproteins 27; 37; 38
metastable systems 11
microcell 202; 204; 211; 212
microchips 150
microelectrochemical measurements 199; 201; 203; 209; 212
microelectrochemistry 237
microelectrode 204
microellipsometry 237
micromechanical sensor 87
micrometer technology 13
microstructural evolution 180
microstructure 286
mini-cell 291; 294; 295; 297; 298; 299
mismatch 189
MnS inclusions 209
model electrocatalyst 83
modification 74; 82; 84; 85
modulation orientation 172
molecular electronics 125
molecular grafting 241; 249
molecular reorientations 53
monoatomic island 4; 5; 6; 7; 8; 11
monoatomic pits 4; 5; 6; 8; 9; 11
monoatomic steps 4; 15; 19
monolayers 249
Monte-Carlo method 246
MoS_2 139; 144
motions of particles 46

multiphonon electron transfer 40
$N(C_4H_9)_4Br$ 79
$N(n\text{-}C_8H_{17})_4Br$ 77
nanoscale mechanical switch 134
nanostructure 83; 84
nanotechnology 13; 126; 134
Ni 185; 186; 187; 188; 189; 190; 193; 194; 195; 196
  electrochemical deposition 216; 217
  LIGA layers 215; 216; 217; 218; 219; 220; 221; 222; 223; 224
Ni nuclei
  distance tunneling spectroscopy 218
  STM image 218
Ni on Au(111) 165
Ni on TiO_{2-x}
  adhesion 223
  wettability 223
Ni thin film 166
Ni(100) 190
  homoepitaxial growth 175
  step structure 175
  sulfuric acid 186
NiO(111)
  point defects 188; 189; 190
  terraces 188; 189; 190
  unit cell 188; 189; 190
$Ni\text{-}TiO_2$ 215; 217; 224
$Ni\text{-}TiO_{2-x}$
  ARXPS 217
  STM/DTS 217
noise 40; 46
  low-frequency 50
noise spectral density 51
noise spectroscopy 46
non-contact mode 3
nonideal electrodes 1
nonperiodic features 2
nuclear magnetic resonance 291
nucleation 33; 159
nucleation centers 259
nuclei 279
O vacancies 223
  of Cu 81
OH vacancies 195
Ohmic contacts 255
oligomers 152
one-dimensional growth 161
optical multichannel analyzer 278
organic additives 33
organic adlayers 249
organic adsorbates 167
organic compounds 107
organic molecules, adsorption 137; 139; 143; 144; 146
orientational dynamics 54
oriented steps 175
osmium complex 127; 128
Otto configuration 110
overpotential deposition 13; 15; 17; 19; 20; 22; 24
oxidation-reduction cycle 108
oxide inner layer 192
oxide layers 185
oxydation
  cycle 279
oxygen adlayer 175
paramagnetic resonance 150
partial charge 88; 95; 96
passive film
  aging 186; 187; 192; 194; 196
  amorphous character 185; 186; 187; 194; 195; 196
  atomic structure 185; 186; 187; 194; 195; 196
  breakdown 185; 186; 187; 188; 189; 190; 191; 192; 193; 194; 195; 196
  chemical composition 185; 186; 187; 194; 195; 196
  coalescence 185; 186; 187; 188; 189; 190; 191; 192; 193; 194; 195; 196
  crystallinity, epitaxy 185; 186; 187; 194; 195; 196
  growth mechanisms 185; 186; 187; 194; 195; 196
  growth process 185; 186; 187; 188; 189; 190; 191; 192; 193; 194; 195; 196
  patches 185; 186; 187; 188; 189; 190; 191; 192; 193; 194; 195; 196
passive layer 2; 200; 201; 205; 206; 207; 211
Pb 88; 89
Pb adlayer
  hexagonally close-packed 7
  surface alloy 1; 2; 3; 4; 5; 7; 8; 9; 10; 11
Pb layer 19; 21
  compressed 2D hcp 20
Pb/Ag(100) c(2 x 2) domain 19
Pb/Ag(111)
  stepped Ag(111) 1; 2; 3; 4; 5; 7; 8; 9; 10; 11
Pb/Au(111) $HClO_4$ 17

PbS 106
Pd
  dissolution 268
Pd clusters
  surfactant-stabilized 77
Pd(111) 268
  LEED 138; 139
Pd(111)/iodine 269
perchloric acid 177
phase transitions 159; 160
phenoxide
  electrooxidation 121; 122
  on Au(111) in alkaline solution 121; 122
  STM image 121; 122
phosphate buffer 149; 151; 152
phosphoric acid 173
photocorrosion 243
photocurrents 108
photoeffects
  uncontrolled 243
photoelectrochemical cells 253
photoelectrochemical measurements 200
photoelectrochemical reactions 253
photoelectrochemical response
  local 101; 108; 109; 110
photoelectrochemistry 107; 110
photoelectron spectroscopy 150
photoemission
  tunneling-induced from the STM tip 109
pinholes 28
pits 274
pitting 201; 209; 210; 212
platinum black 291; 292; 294; 295; 298
point defects 188; 190; 195; 196
Poisson ratio 91; 92
polarization effects 40
poly(vinylferrocene) 133
polyatomic steps 2
  polycrystalline 29
polymer films
  neutral 129; 133; 134
  oxidized 129; 133; 134
polyoxometalates 121
polypyrrole 149; 150; 151; 152
  film morphology 149; 150; 151; 152; 153; 154; 155; 156; 157
  helical structures 149; 150; 151; 152; 153; 154; 155; 156; 157
  island structures 149; 150; 151; 152; 153; 154; 155; 156; 157
  modular surface 149; 150; 151; 152; 153; 154; 155; 156; 157
  nucleation centers 152
  overoxidation 149; 150; 151; 152; 153; 154; 155; 156; 157
  roughness 149; 150; 151; 152; 153; 154; 155; 156; 157
  superhelical 149; 150; 151; 152; 153; 154; 155; 156; 157
  surface morphology 149; 150; 151; 152; 154; 156
  surface roughness 149; 150; 151; 152; 154; 156
porphyrin 139
potential of zero charge 94
  Au(111) 94; 96
potential programs 279
pre-passive layer 205; 206
protoporphyrin IX 42
Pt
  columnar-structured 66
Pt cluster
  on HOPG 79; 83
Pt(111)
  iodine adlayer 137; 138; 139; 140; 142; 143; 144; 146
  modification by ruthenium 74; 75; 76
  nanometer-sized particles 74; 75; 76
  Ru-modified 74; 75; 76
  underpotential deposition of Ag 137; 138; 139; 140; 142; 143; 144; 146
  underpotential deposition of Cu 143
Pt/Ir tips 3; 220
pulse plating 37
  STM images of copper 36
purine 107
pyramidal structures
  AFM images 260
pyrimidine 107
pyrolytic graphite 28
quantum dots 40
Raman spectroscopy 277
random deposition model 59; 62
random diffusion 48
rapid growth 166
reactive surfaces 166; 167
reactivity 74; 75; 80; 83; 84; 85
real surfaces 63
real-space information 74
reconstruction 160; 161; 162; 164; 166

redox films 125; 126
reductive desorption 177
RHEED 186
resonance Raman spectroscopy
  excitation profile 41
resonance tunneling 40
resonant tunneling modes 126
Rh(111)
RNA 107
roughness 57; 66
RU complex
  STM image 129
Ru coverage 75
Ru/Pt(111) electrodes 75
scaling problem 80
scanning force microscopy 2, 3
scanning near-field optical microscope 110
scanning tunneling microscopy 2; 125; 126; 149; 150; 151; 152; 153; 185; 186; 187; 188; 190; 191; 192; 193; 194; 195; 196; 199; 202; 203; 204; 205; 207; 208; 209; 212; 213; 215; 225; 226; 227; 228; 229; 231; 232; 233; 234; 235; 238; 254
  analytical applications 74; 75; 77; 78; 79; 80; 82; 84; 85
  Au(100)-c(2 x 2)-Se 274
  catalytically active monolayers 113
  combination with microelectrochemistry 212
  deposition of Cu 113
  electrodeposition 171
  ex-situ 57; 58; 61; 64; 66; 67; 68; 69
  GaAs etching 248
  hydroxide adlattice on Cu 113
  in-situ 57; 58; 61; 64; 66; 67; 68; 69; 267
  molecular adsorbates on Au and Ag 113
  n-Si(111) 244; 245; 250
  strained-layer 171
  superlattices 171
scanning tunneling microscopy images
  copper crystallites 32
  figures machined 35
scattering cross-section 48
screw dislocations 16; 193
Se on Au(100)
  (3 x $\sqrt{10}$) structure 273
  c(2 x 2)-structure 273
  p(2x2)-Se 273
Se_8 rings 274
second-harmonic generation 108
second-order phase 163
selective deposition
  Cu 264
self-assembling
  iodine-modified electrodes 139; 144
self-assembly 121; 127; 130; 131
semiconductor 13; 15; 253; 254
  passivated 243
sensor technology 150
Se
  amorphous layer 256
SERS
  time dependence 286
Shuttleworth equation 93
Si(111)
  stepped 53
silver cyanide complexes 285
single crystal 149; 152
single-electron transfer processes 40
Si
  anisotropic etching 242
  ideally flat surfaces 246
  oxide formation 242
  selective oxide stripping 242
Si etching 241
Si(100) 22
Si/Ti/TiO_{2-x} 216; 222
signal-to-noise ratio 297; 300
Si-H bonds 244
Si-O bonds 244
Si-OH surface groups 245
Si-phenyl bonds 249
space charge layer 254
spectral power density 119
spectrometer 278
$SrTiO_3$ single-crystal 24
stainless steel 1.4301/sulfuric acid
  AFM image 208
  distance modulation spectroscopy 208
  lateral force microscopy 208
  local potentiodynamic polarization 200; 203; 206; 207; 208; 209; 210; 211
  MnS inclusions 200; 203; 206; 207; 208; 209; 210; 211
  STM image 208
  tunneling barrier height 200; 203; 206; 207; 208; 209; 210; 211
stainless steel 1.4529/sulfuric acid 203; 206; 207
step curvature 179
step edge 161; 166

step edge mobility 175
step orientation 182
step polarization 5; 6; 7
step-mediated growth 182
stepped terrace domains 4; 5; 6; 7; 8; 11
steps 186; 187; 189; 190; 196
stiffness 226; 227; 231
Stoney's equation 91
Stranski-Krastanov 17; 18; 33; 59
stress measurements 87
stress sensor
  schematic diagram 87; 89; 90; 94; 97
stress-voltage curve
  derivative 94; 97
structural characterization 75; 80; 84
structural transitions 160
structure and reactivity
  correlation 75; 80; 85
submicron fabrication 262
suboxide
  nano cluster 246
sulfamate electrolyte 216
sulfate adsorption 143
sulfate superstructure 162
sulfuration 248
superconductor 13; 15
supersaturation 14; 15
supramolecular organization 37
surface cluster distribution 277
surface defects 2; 15; 102; 103
surface diffusion 53
  anisotropic 50
surface diffusion model 68
surface dynamics 27
surface energy 93; 94
surface enhanced Raman spectroscopy 108; 277; 278
surface imperfections 33
surface mean height 60
surface mobility 36
surface modification 262
  surface morphology 1; 2; 3; 4; 5; 7; 8; 9; 10; 277
surface plasmons 108; 110
surface processing
  electrochemical 241
surface rearrangement 179
surface reconstruction 33
surface relaxation model 59
surface roughness 58; 60; 108; 109; 149; 154; 156
surface structure 101; 102; 107; 109; 110
surface tension 154
surface width 60
surface X-ray scattering 116;138; 141; 142; 146
surface-oxidation 269
surface-strain imaging 97
tapping mode 3
ternary alloys 300
terrace mobility 175
terrace structure 75
terraces 175
thiourea 119
three-dimensional growth 152
three-dimensional phase formation 14
thymine
  on Ag(100) 107
  on Ag(111) 107
  on Au(111) 107
Tl/Ag(111)
  adsorbate-substrate 11
  rearrangement 9
  stepped Ag(111) 1; 2; 3; 4; 7; 8; 9; 10; 11
  surface alloy 9
time correlation effects 40
time-current correlation function 53
tip
  shape 54
  coating 28
tip friction 243
tip induced interactions 129
  tip-induced 75; 81; 82; 83; 84; 85
tip-induced etching 264
Ti
  grain boundaries 237
  sputtered 225; 226; 227; 228; 229; 230; 231; 232; 233; 234; 237; 238
TiN 225; 229; 232; 233
TiO_2 225; 228; 229; 230; 231; 232; 233; 234; 237
TiO_2 films
  n-type semiconducting 237
  nitrogen implanted 233
  reduced oxide 228
  surfaces 228
TiO_{2-x}
  interface compounds 224

Ni growth 215; 216; 217; 220; 221; 222; 223; 224
Ni-nucleation 215; 216; 217; 220; 221; 222; 223; 224
roughness 215; 216; 217; 220; 221; 222; 223; 224
semiconductors 215; 216; 217; 220; 221; 222; 223; 224
Tl 88; 89
toluene-4-sulfonic acid 149; 151
tosylate 149; 151; 152; 153
transition metal complexes 125
transmission electron microscopy 54
trigonal contours 187
Triton 246
true surface area 277; 282; 286
truncated pyramidal structures 261
tunnel barrier 40
tunnel current 49; 228; 229; 235; 238
tunneling barrier height 199; 202; 205; 206; 207; 219; 223
tunneling gap 48; 52
tunneling mechanisms 195
tunneling spectroscopy
two-dimensional 150
two-dimensional 257
two-dimensional phase formation 14; 19
underpotential deposition 1; 2; 3; 5; 7; 13; 15; 19, 22, 24; 87; 88; 114; 116; 137; 139; 142; 146; 163
undersaturation 14
uracil
on Ag(100) 107
on Ag(111) 107
on Au(100) 107
on Au(100)-(hex) 107
uridine
on Au(111) 107
vacancies 190; 195; 196
vibrational coherence 37
vibrational spectroscopy 278
Volmer-Weber 17; 18; 33; 59
voltage tunneling spectra 225; 233
voltage tunneling spectroscopy 14
Watts electrolyte 164; 165
weak interaction 46
wedge structures 262
X-ray diffraction 172
X-ray photoelectron spectroscopy 190; 192; 194; 257
X-ray scattering 163
X-ray surface diffraction 75
$YBa_2Cu_3O_{7-\delta}$
AFM image 23; 24
Young's modulus 91; 92
zero-order kinetics 161